The Dissertation Committee for Sebastian Ramiro-Ramirez Certifies that this is the approved version of the following Dissertation:

INTEGRATED STRATIGRAPHIC AND PETROPHYSICAL ANALYSIS OF THE WOLFCAMP AT DELAWARE BASIN, WEST TEXAS, USA

Committee:

Peter B Flemings, Supervisor

Athma R Bhandari

Hugh C Daigle

Charles Kerans

Nicola Tisato

INTEGRATED STRATIGRAPHIC AND PETROPHYSICAL ANALYSIS OF THE WOLFCAMP AT DELAWARE BASIN, WEST TEXAS, USA

by

Sebastian Ramiro-Ramirez

Dissertation

Presented to the Faculty of the Graduate School of

The University of Texas at Austin

in Partial Fulfillment

of the Requirements

for the Degree of

Doctor of Philosophy

The University of Texas at Austin

May 2022

Dedication

A mi madre, y a todas aquellas mujeres que tuvieron que sacrificar su vida profesional para cuidar de sus hijos.

To my mom, and all those women who had to give up their professional careers to raise their children.

Acknowledgements

First, I want to express profound respect and appreciation to my supervisor Dr. Peter Flemings. His guidance during these years helped me earn invaluable skills that made me a better scientist and professional. I not only improved my technical knowledge but also learned how to thoroughly think critically about any situation that I face regularly, either professionally or personally. For that, and for many more things for which I would need several lines to describe, thank you, Peter. I must also thank Dr. Athma Bhandari for his patience, support, and devotion to teaching me how to become a better experimentalist. You have dedicated infinite time to walk me through every step in our experiments, and have always been kind and respectful with me throughout my learning curve. I would also need many more lines than these to express my gratitude to you, Athma. I would like to thank Peter Polito and Josh O'Connell for helping me with my experiments and logistics in this journey, and for their great sense of humor that made life at school much more bearable. I would also like to thank the rest of my committee members, Dr. Hugh Daigle, Dr. Charles Kerans, and Dr. Nicola Tisato for providing valuable feedback at various stages of my Ph.D.

I truly appreciate the incredible academic and personal support from Philip Guerrero at the Jackson School of Geosciences. Also, thank you to Andres Gonzalez, Reinaldo Sabbagh, and Javier Santos for making sure I did not entirely neglect my social life during my Ph.D.

Lastly, I would like to thank my parents and brothers for showing unconditional support with any decision I have made in life, and for encouraging me to explore the World. Last but not least, I thank my incredible wife Vanessa for her endless care, love, support, and patience during these (many) years as a student. I promise you, Vanessa, this is the last 'student adventure' I will have. And thank you to my dogs Thor, Unkas, and Salt for bringing me joy even in the toughest moments I have faced.

I must also acknowledge generous funding from the University of Texas Institute for Geophysics, Department of Geological Sciences, Shell, and Equinor. I also want to acknowledge

Peter Polito, Dr. Athma Bhandari, and Donnie Brooks for their immense efforts in developing the permeability and helium porosimeter setups that I used in this research project.

Abstract

INTEGRATED STRATIGRAPHIC AND PETROPHYSICAL ANALYSIS OF THE WOLFCAMP AT DELAWARE BASIN, WEST TEXAS, USA

Sebastian Ramiro-Ramirez, Ph.D.

The University of Texas at Austin, 2022

Supervisor: Peter B Flemings

Hydrocarbons stored in low-permeability reservoirs, also known as 'unconventional reservoirs', represent important energy resources worldwide. Although current technology allows their production at economic rates, there still are numerous production challenges and unknowns regarding their flow behavior. A better understanding on how fluids stored in these reservoirs are drained by the hydraulic fractures after stimulation may help to optimize completion designs and field development plans. This research is an attempt to describe such drainage behavior in the largest oil producing unconventional formation in the World. I investigated the drainage behavior in Wolfcamp reservoirs at the completion scale by integrating stratigraphic and petrophysical analyses with flow modeling. I interpreted the depositional and diagenetic processes that generated three Wolfcamp cores recovered in the central-eastern Delaware Basin, measured the porosity and permeability of distinct lithofacies, and developed simple models to describe flow in these strata. I found that most fluids (~95% of the pore volume) are stored in low-permeability (e.g., < 60 nD) mudstones that I interpreted as hemipelagics and siliciclastics turbidites. Interbedded with these deposits are the low-porosity (~5% of the pore volume) and low-permeability (e.g., < 50 nD)

carbonate lithofacies that I interpreted as gravity flow deposits and diagenetic dolomudstones. The carbonate gravity flow deposits, when dolomitized, are up to 2000 times more permeable than the other deposits and represent preferential flow pathways that drain fluids from the low-permeability strata during production. This drainage behavior increases the reservoir upscaled permeability, and therefore production rates, multiple times higher compared to a reservoir consisting of only low-permeability strata. Hence, the presence of these permeable, dolomitized, gravity flow deposits plays a critical role when producing from Wolfcamp reservoirs as they accelerate drainage. These findings are also applicable to other low-permeability formations exhibiting significant permeability heterogeneity.

Table of Contents

List of Tables

List of Figures

Chapter 1: Introduction

1.1 Background and motivation

Low-permeability formations, also known as unconventional, shale, or tight formations, represent the largest source for the oil and gas produced in the U.S. (EIA, 2021). In 2020, 2.70 billion barrels of crude oil and 29.20 tcf of gas were produced from these formations, representing 65% and 86% of the total U.S. oil and natural gas production, respectively (EIA, 2021). The Wolfcamp operational unit in the Permian Basin region of west Texas and southeast New Mexico is the most prolific low-permeability, liquid-hydrocarbon (i.e., crude oil and condensates) interval in the United States (EIA, 2022). In 2020, the average daily production in the Wolfcamp ranged between 2.3 and 2.5 million barrels, surpassing both the Eagle Ford (Texas) and the Bakken (North Dakota and Montana) formations (EIA, 2022). Outside the U.S., low-permeability formations hosting significant oil and gas reserves are also found in several countries such as Russia, China, and Argentina amongst others (EIA, 2013). Hence, hydrocarbons stored in low-permeability formations represent important hydrocarbon reserves worldwide.

The matrix permeability in low-permeability formations is typically several orders of magnitude below 1 millidarcy (e.g., Kurtoglu, 2013; Chhatre et al., 2014; Kosanke and Warren, 2016; Bhandari et al., 2019). Production rates in these formations are not economically viable unless the flow capacity of the reservoir is sufficiently increased. This is accomplished by increasing the surface area of the reservoir that is exposed to the wellbore through a combination of horizontal drilling and hydraulic fracturing techniques (Yu and Sepehrnoori, 2018; Zoback and Kohli, 2019). Although production rates rely strongly on drilling and completion designs, geologic factors such as the stratigraphic distribution of lithofacies also play a key role (e.g., Sagasti et al., 2014; Wilson et al., 2020; Euzen et al., 2021; Fraser and Pedersen, 2021).

The matrix permeability is the main rock property controlling reservoir flow behavior and productivity. It must be measured in the laboratory (e.g., in core plugs) or in the field (i.e., well tests) to describe reservoir performance and optimize field development plans (e.g., spacing between hydraulic fracturing stages, spacing between parent and child wells) (Tran et al., 2011; Kurtoglu, 2013; Yu et al., 2014; Li et al., 2015; Assady et al., 2019). However, matrix permeability is probably the most difficult rock property to measure, especially in low-permeability formations. In addition, these formations often contain multiple lithofacies with different matrix permeabilities (e.g., Kurtoglu, 2013; Kosanke and Warren, 2016; Ramiro-Ramirez et al., 2021) requiring measurements in multiple samples to characterize the vertical and areal permeability distribution. In the Wolfcamp, for example, previous core-based studies indicate the presence of drastic permeability differences between samples (i.e., k = 10 nD to 600 nD) (e.g., Rafatian and Capsan, 2015; Mathur et al., 2016; King et al., 2018; Bhandari et al., 2019). This permeability heterogeneity highlights the importance of integrating petrophysical measurements with a detailed stratigraphic interpretation to describe and predict production behavior.

The goal of this dissertation is to develop a geological and petrophysical understanding of the Wolfcamp A and Wolfcamp B stratigraphy at the bed-scale to describe the drainage behavior during production in these two units. Previous studies in the Wolfcamp focused primarily on either the geology (Moede, 2018; Kvale et al., 2020), petrophysical measurements (Mathur et al., 2016; King et al., 2018; Bhandari et al., 2019), or well testing and reservoir modeling (Zhan et al., 2018) alone. Here, I present the first integrated core-based study coupling geology, petrophysics, and reservoir modeling in the upper Wolfcamp interval at the Delaware Basin of west Texas and southeast New Mexico.

First, I define lithofacies in continuous cored intervals and interpret the depositional and diagenetic processes. Second, I determine the storage and flow properties in each lithofacies though laboratory measurements of porosity and permeability in core plugs. Third, I identify the pore-scale controls on permeability through microscopic image analysis and pore-throat size distributions in the tested samples. To finish, I conduct flow simulations in a permeability-heterogeneous layered reservoir model to describe the flow behavior and estimate upscaled permeabilities in the upper Wolfcamp.

In Chapter 2, I define lithofacies in three upper Wolfcamp cores at the inch scale using macroscopic core observations, petrographic analysis of thin sections, and geochemical analyses (X-ray fluorescence, X-ray diffraction, LECO total organic carbon). I interpret the depositional and diagenetic processes that generated each lithofacies, and documented their vertical distribution in the cores. I use these data in Chapter 3 to relate flow properties to the geology of the studied section and inform a flow model that describes the production drainage behavior in the Wolfcamp.

The results from Chapter 2 indicate that the upper Wolfcamp is stratigraphically very heterogeneous and primarily composed of hemipelagic deposits alternating with siliciclastic and calciclastic sediment gravity flow deposits and dolomitic beds that occur at varying frequencies throughout the section. In the Wolfcamp B unit, hemipelagic deposits alternate with recurrent siliciclastic fine-grained turbidites, and with sporadic carbonate turbidites and cohesive debrites. The overlying Wolfcamp A units exhibits a drastically different stratigraphy consisting only of hemipelagic deposits alternating with recurrent carbonate hybrid event beds. In both the Wolfcamp A and Wolfcamp B units, there is significant diagenetic overprint based on the presence of pervasive dolomitic intervals that I interpreted either as dolomitized carbonate flow deposits or dolomudstones.

In Chapter 3, I present the results from the porosity and liquid (dodecane) permeability measurements in core plugs extracted from the lithofacies defined in Chapter 2. In addition, I use scanning electron microscopy (SEM) images and mercury injection capillary pressure (MICP) data from the tested samples to interpret pore-scale controls on the measured permeabilities. Finally, I build a reservoir flow model consisting of two layers with drastically permeability differences to describe the production drainage behavior and estimate upscaled permeabilities in the Wolfcamp A and Wolfcamp B units. I inform this flow model with the stratigraphy and petrophysical measurements presented in Chapter 2 and Chapter 3, respectively.

The key results from Chapter 3 are that dolomitized calcareous lithofacies exhibits matrix permeabilities up to 2000 nD, whereas the remaining mudstones, dolomudstones, and calcium carbonate-bearing lithofacies have matrix permeabilities less than 60 nD. I show that such permeability contrast between lithofacies influences the production behavior in the upper Wolfcamp interval. The SEM images and MICP data indicate that interparticle pores and their throat sizes control permeability in Wolfcamp lithofacies. The flow simulations show that cross-facies flow results in focusing drainage through the permeable layers, increasing the production rates and the upscaled permeability of the system up to four times higher than if each layer was produced independently.

In Chapter 4, I expand the simulation results of the two-layer model presented in Chapter 3. I perform flow simulations using varying reservoir parameters (e.g., horizontal permeability, layer thickness) in the Wolfcamp A and Wolfcamp B models, and discuss their influence on reservoir performance.

The results from Chapter 4 demonstrate that the cross-facies flow is controlled primarily by the high-permeability layer's horizontal permeability (k_{h2}) and thickness (h_2). If one of these two parameters increase, there is less flow restriction in the high-permeability layer, and production rates and upscaled permeabilities increase.

One of the key contributions of my research is the detailed characterization of Wolfcamp A and Wolfcamp B lithofacies at the inch-scale in the Delaware Basin, and the interpretation of the depositional and diagenetic processes that formed them. I show how to discriminate between calciclastic sediment gravity flow deposits, siliciclastic sediment gravity flow deposits, and hemipelagic deposits. The lack of Wolfcamp outcrops representing a true basinal depositional setting in the Delaware Basin and the scarcity of core-based publications covering the studied section presented here represent a challenge for academia and industry to interpret the subsurface geology of the Wolfcamp. My work contributes to the fundamental understanding of these lithofacies at the bed scale to improve the interpretation of Wolfcamp deposits in the Delaware Basin.

The second key contribution is the development of a consistent understanding of permeability (in situ) and porosity of a range of distinct lithofacies through laboratory measurements. The integration of these measurements with the stratigraphy of the studied section allowed to understand that 1) most of the porosity and the hydrocarbons are in the organic rich siliceous mudstones, 2) the siliciclastic sediment gravity flow deposits are very low permeability and contain mostly water, and 3) when calciclastic sediment gravity flow deposits are dolomitized (carbonate turbidites, carbonate hybrid event beds), they have one to four orders of magnitude more permeability than the rest of lithofacies. The presence of dolomitized permeable deposits is not documented in previous Wolfcamp studies, and they have important implications on the production behavior.

The third key contribution is the development of a conceptual model whereby the dolomitized permeable deposits focus flow. This is an expansion of decades of work investigating the cross-facies flow effect on reservoir performance. My work is the first to consider cross-facies flow as a key production drainage mechanism that increase production rates and upscaled permeabilities in low-permeability formations.

The fourth key contribution is my interpretation of the pore-scale controls on permeability in Wolfcamp lithofacies. Several studies consider the porosity within the organic matter to form the most effective fluid flow pathways in low-permeability formations. However, I found that interparticle pores and their throat size distribution are major controls for liquid flow in Wolfcamp lithofacies, based on the integrated study of image analysis and petrophysical measurements. These findings illuminate potential controls on fluid flow, not only in the Wolfcamp, but also in other low-permeability formations.

1.2 FUTURE RESEARCH

The work presented here demonstrates the importance of conducting an integrative study of geology, petrophysics, and reservoir engineering to understand production behavior in the Wolfcamp. I showed that cross-facies flow between deposits with drastically different permeabilities increase the upscaled permeability in the Wolfcamp. It is highly encouraged to conduct a similar integrative approach in other unconventional formations to understand the impact of permeability heterogeneity on their production behavior and upscaled permeabilities.

In addition, the geological study in Chapter 2 is restricted to three wells distanced apart less than 15 miles. It would be beneficial to correlate the lithofacies defined in Chapter 2 beyond the study area to document their continuity in the Delaware Basin. This would help understand the source areas and areal extension of the calciclastic and siliciclastic sediment gravity flow deposits, and the continuity of the permeable dolomitized deposits. In addition, the dolomudstone lithofacies may represent important basin wide markers, which may have formed during certain geological events (e.g., sea level drop, influx of chemical ions into seawater). Hence, both a correlation beyond the study area and a more detailed diagenetic study of this lithofacies are highly encouraged.

In Chapter 3, I conducted the liquid permeability measurements using dodecane, which corresponds to the oil phase. Since Wolfcamp wells have high water cuts, it is highly encouraged to conduct additional permeability measurements using brine to investigate water vs oil mobilities in Wolfcamp lithofacies. These experiments may shed light on the reason for such high water cuts in Wolfcamp wells.

The concepts presented in this thesis can develop as a guiding process emphasizing the role of stratigraphy in the Wolfcamp and other low-permeability reservoirs worldwide. A systematic exploration and production approach that recognizes the role of high permeability layers in these reservoirs, even if they are volumetrically small, will result in better completion strategies, and therefore in better production rates and recovery factors.

REFERENCES

Assady, A., H. Jabbari, A. M. Ellafi, and B. Goudarzi, 2019, On the characterization of Bakken Formation: oscillating-pulse, pulse-decay permeability measurement & geomeachanics, U.S. Rock Mechanics/Geomechanics Symposium, New York City, New York, p. 11.

Bhandari, A. R., P. B. Flemings, S. Ramiro-Ramirez, R. Hofmann, and P. J. Polito, 2019, Gas and liquid permeability measurements in Wolfcamp samples: Fuel, p. 1026–1036.

Chhatre, S. S., S. Sinha, E. M. Braun, W. L. Esch, M. D. Determan, Q. R. Passey, S. A. Leonardi, T. E. Zirkle, A. C. Wood, J. A. Boros, and R. A. Kudva, 2014, Effect of Stress, Creep, and Fluid Type on Steady State Permeability Measurements in Tight Liquid Unconventional Reservoirs, URTeC, Denver, Colorado, p. 11.

EIA, 2013, Technically recoverable shale oil and shale gas resources: an assessment of 137 shale formations in 41 countries outside the United States, *in* U. S. D. o. Energy, ed., Washington, DC, p. 730.

EIA, 2021, Annual Energy Outlook 2021, *in* U. S. D. o. Energy, ed., Washington, DC, p. 33.

EIA, 2022, Tight oil production estimates by play.

Euzen, T., N. Watson, M. Fowler, A. Mort, and T. F. Moslow, 2021, Petroleum distribution in the Montney hybrid play: Source, carrier bed, and structural controls: AAPG Bulletin, v. 105, p. 1867-1892.

Fraser, J. A., and P. K. Pedersen, 2021, Reservoir characterization of fairways in a tight light oil play of the Upper Cretaceous Cardium Formation, west Pembina, Alberta, Canada: AAPG Bulletin, v. 105, p. 1797-1820.

King, H., M. Sansone, P. Kortunov, Y. Xu, N. Callen, S. Chhatre, H. Sahoo, and A. Buono, 2018, Microstructural Investigation of Stress-Dependent Permeability in Tight-Oil Rocks: Petrophysics, v. 59, p. 9.

Kosanke, T., and A. Warren, 2016, Geological controls on matrix permeability of the Eagle Ford Shale (Cretaceous), South Texas, U.S.A.: The Eagle Ford Shale: A renaisaance in U.S. oil production, v. AAPG Memoir 110.

Kurtoglu, B., 2013, Integrated reservoir characterization and modeling in support of enhanced oil recovery for Bakken, Colorado School of Mines, 239 p.

Kvale, E. P., C. M. Bowie, C. Flenthrope, C. Mace, J. M. Parrish, B. Price, S. Anderson, and W. A. DiMichele, 2020, Facies variability within a mixed carbonate-siliciclastic sea-floor fan (upper Wolfcamp Formation, Permian, Delaware Basin, New Mexico): AAPG Bulletin, v. 104, p. 525-563.

Li, H., B. S. Hart, M. Dawson, and E. Radjef, 2015, Characterizing the middle Bakken: laboratory measurements and rock typing of the middle Bakken Formation, Unconventional Resources Technology Conference (URTeC), San Antonio, Texas, USA, p. 13.

Mathur, A., C. H. Sondergeld, and C. S. Rai, 2016, Comparison of Steady-State and Transient Methods for Measuring Shale Permeability, SPE Low Perm Symposium, Denver, Colorado, USA, p. 22.

Moede, I. H., 2018, Lithofacies and Chemostratigraphy of the Upper Wolfcampian in the Southeastern Delaware Basin, Pecos County, Texas, The University of Texas at Austin, 114 p.

Rafatian, N., and J. Capsan, 2015, Petrophysical characterization of the pore space in Permian Wolfcamp rocks: Petrophysics, v. 56, p. 45-57.

Ramiro-Ramirez, S., P. B. Flemings, A. R. Bhandari, and O. S. Jimba, 2021, Steady-State liquid permeability measurements in samples from the Bakken Formation, Williston Basin, USA, SPE Annual Technical Conference and Exhibition, Dubai, UAE, p. 15.

Sagasti, G., A. Ortiz, D. Hryb, M. Foster, and V. Lazzari, 2014, Understanding geological heterogeneity to customize field development: An example from the Vaca Muerta unconventional play, Argentina, URTeC, Denver, Colorado, USA, p. 20.

Tran, T., P. Sinurat, and R. A. Wattenbarger, 2011, Production characteristics of the Bakken shale oil, SPE Annual Technical Conference and Exhibition, Denver, Colorado, USA, p. 14.

Wilson, R. D., J. Chitale, K. Huffman, P. Montgomery, and S. J. Prochnow, 2020, Evaluating the depositional environment, lithofacies variation, and diagenetic processes of the Wolfcamp B and lower Spraberry intervals in the Midland Basin: Implications for reservoir quality and distribution: AAPG Bulletin, v. 104, p. 1287-1321.

Yu, W., H. R. Lashgary, and K. Sepehrnoori, 2014, Simulation study of CO_2 huff-n-puff process in Bakken tight oil reservoirs, SPE Western North American and Rocky Mountain Joint Regional Meeting, Denver, Colorado, USA, p. 16.

Yu, W., and K. Sepehrnoori, 2018, Shale Gas and Tight Oil Reservoir Simulation, Gulf Professional Publishing, 432 p.

Zhan, L., P. S. Fair, R. J. Dombrowski, E. N. Quint, and R. Cao, 2018, Estimating ultralow permeability at multiple locations using simultaneous-impulse tests: A fit-for-purpose pressure-transient solution and its field application: Society of Petroleum Engineers Journal, v. 23, p. 1184-1200.

Zoback, M. D., and A. H. Kohli, 2019, Unconventional Reservoir Geomechanics: New York, NY, Cambridge University Press, 484 p.

Chapter 2: Stratigraphy of the upper Wolfcamp in central-eastern Delaware Basin, Permian Basin Region, West Texas[1]

2.1 ABSTRACT

The development of Wolfcamp reservoirs in the Delaware Basin is often challenging due to the presence of bed-scale stratigraphic heterogeneities. A thorough understanding of the subsurface distribution of lithofacies in these reservoirs is essential to identify the most prospective well landing zones and optimize field development plans. Here, I show that the upper Wolfcamp interval (Wolfcamp A and Wolfcamp B) in the central-eastern Delaware Basin consists of hemipelagic deposits alternating with siliciclastic and calciclastic sediment gravity flow deposits and dolomitic beds that occur at varying frequencies throughout the section. The vertical distribution of six lithofacies defined in three cores using macroscopic core observations, geochemical analyses, and petrographic analysis of thin sections indicate that the stratigraphy of the Wolfcamp B unit (late Wolfcampian) is significantly different to that of the overlying Wolfcamp A (early Leonardian). In the Wolfcamp B, siliciclastic fine-grained turbidites (argillaceous mudstone lithofacies) are interbedded with organically rich hemipelagic deposits (organic-rich siliceous mudstone lithofacies). Occasional carbonate turbidites (calcareous mudstone and calcareous sandstone lithofacies) and cohesive debrites (matrix-supported conglomerate lithofacies) are intercalated with hemipelagic deposits in this unit. In contrast, the Wolfcamp A records a drastic shift to a more carbonate-rich composition as recorded by recurrent

[1]The full content of this chapter was submitted to AAPG Bulletin in 2022. The citation for that publication is:

Ramiro-Ramirez, S., P. B., Flemings, and A. R., Bhandari, (*in review*), Stratigraphy of the upper Wolfcamp in central-eastern Delaware Basin, Permian Basin Region, West Texas. *AAPG Bulletin*

I designed and performed the experiments presented in that study and prepared the manuscript for publication. My co-authors are listed in order of contribution and provided support for the conceptual development of the project and manuscript preparation.

and amalgamated carbonate hybrid event beds (calcareous mudstone and calcareous sandstone lithofacies) that are intercalated with hemipelagic deposits. The stratigraphy of the upper Wolfcamp is further complicated by the presence of pervasive dolomitic horizons (dolomudstone, and dolomitic calcareous lithofacies) in both units that I interpreted to have formed diagenetically throughout burial. The identification of these dolomitic beds is important because they may represent preferential flow pathways during production. I interpret that such complex stratigraphy will ultimately control the production behavior in the upper Wolfcamp. My results and interpretations illustrate the basinal stratigraphy of the upper Wolfcamp and the depositional processes that accumulated this interval in the central-eastern Delaware Basin. My insights may serve as analogs to interpret this Wolfcamp interval in other areas of the basin.

2.2 INTRODUCTION

Low-permeability formations are often conceived as relatively homogeneous systems composed only of mudstones. Although mudstones may represent the dominant lithofacies, the occurrence of sediment gravity flow deposits sourced from proximal areas rimming the basins create bed-scale stratigraphically heterogeneous reservoirs. Petrophysical properties (e.g., porosity, permeability) may be significantly different across lithofacies, and therefore a thorough geological characterization of these reservoirs is required to describe and predict production behavior. Such characterization requires the integration of wireline logs with core descriptions and rock analyses (e.g., petrography, geochemistry, petrophysics). However, core data is often not publicly available, especially in formations that represent relatively new prospects for oil and gas production. One example corresponds to distal Wolfcamp reservoirs in the Delaware Basin.

The Wolfcamp is composed of strata deposited between Late Pennsylvanian (Missourian-Virgilian) and Early Permian (lower Leonardian) times in the Midland and Delaware basins of the

Permian Basin region (Figure 2.1) (Baumgardner et al., 2016; Sinclair et al., 2017; Fu et al., 2020). Although it is currently the most prolific low-permeability liquid hydrocarbon interval in the World, production from the Wolfcamp became significant very recently during the 2010's (EIA, 2022) with the advent of economically efficient drilling and completion techniques. Because the Wolfcamp is a relatively young prospect and it outcrops in only few locations, there is significant academic and industry interest in deciphering its subsurface geology and documenting the geological processes that formed this unit in the distal parts of the basin where the largest hydrocarbon accumulations are.

Wolfcamp lithofacies have been studied in a few locations where they are exposed, such as the Sierra Diablo, the Hueco Mountains, and the Glass Mountains (King, 1942; Ross and Ross, 2003b; Fu et al., 2020) (Figure 2.1). Wolfcamp outcrops at these locations typically correspond to lithofacies that accumulated in proximal depositional environments (e.g., organically poor dolomitic limestones in platforms and shelves) rather than distal (e.g., organically rich shales and limestones in the toe of the slope and the center of the basin) (King, 1942; Ross and Ross, 2003a; Fu et al., 2020). However, the most significant hydrocarbon production potential in the Delaware and Midland basins is in the distal lithofacies (Potter et al., 2020), which differ geologically and petrophysically from their proximal equivalents. Hence, we rely on the study of subsurface data (e.g., cores and wireline logs) to document the distribution, continuity, and physical properties of the most prospective lithofacies in the Wolfcamp.

There are few published core-based studies of Wolfcamp basinal lithofacies in the Delaware Basin (Figure 2.1). Loucks et al. (1985) identified multiple lithofacies that they interpreted as carbonate debrites and turbidites alternating with suspension deposits in the northern part of the basin (Figure 2.1); they inferred that the Northwestern shelf sourced the carbonate gravity-flow deposits. Moede (2018) identified lithofacies that he interpreted as debrites and density flow deposits overlaying a siliciclastic-dominated sandy turbidite unit in the southeastern Delaware Basin (Figure 2.1). Thompson et al. (2018) interpreted siliciclastic and calciclastic lithofacies to be formed by turbidity currents and debris flows in the central Delaware Basin, nearby my study area. More recently, Kvale et al. (2020) identified carbonate-bearing lithofacies that they interpreted as hybrid event beds and debrites in the northeastern Delaware Basin (Figure 2.1); they interpreted these deposits to form in distinct parts of a sea-floor fan sourced from the northeast. Price et al. (2021) also interpreted siliciclastic and calciclastic lithofacies in Wolfcamp cores to record sediment gravity flows sourced from the northwest. In all these studies, the authors describe how sediment flow deposits are typically capped with organic-rich hemipelagic deposits, which indicates a return to background pelagic sedimentation. This heterogeneous distribution of lithofacies at various locations and depth intervals in the Delaware Basin emphasizes the importance of understanding the stratigraphic architecture of the Wolfcamp to inform completion and production strategies at different parts of the basin.

In this paper, I define lithofacies observed in three cores spanning the Wolfcamp A and Wolfcamp B units in the central-eastern Delaware Basin (green circles, Figure 2.1) using macroscopic core observations, geochemical analyses of rock samples, and petrographic study of thin sections. I interpret the depositional environment of these lithofacies based on their sedimentary structures, textures, bounding surfaces, and composition. I identify siliciclastic, clay-dominated (~50% clays on average) lithofacies that records turbidite deposition, has a low organic content, and has not been documented previously in detail in the studied Wolfcamp interval. I also identify pervasive regional dolomitization within specific lithofacies that is identifiable through core analysis. I then show how these lithofacies can be mapped from log data. Lastly, I describe how the distribution of these lithofacies changes upward through the stratigraphic section. One fundamental distinction between the Wolfcamp B and Wolfcamp A units is that the Wolfcamp B has a significant fraction of siliciclastic turbidites, which are essentially low organic content mudstones and of a different source area. The results of this paper contribute to the understanding of the depositional and diagenetic processes that generate the observed bed-scale stratigraphic heterogeneity in cores and well logs in the Wolfcamp A and Wolfcamp B units at the Delaware Basin.

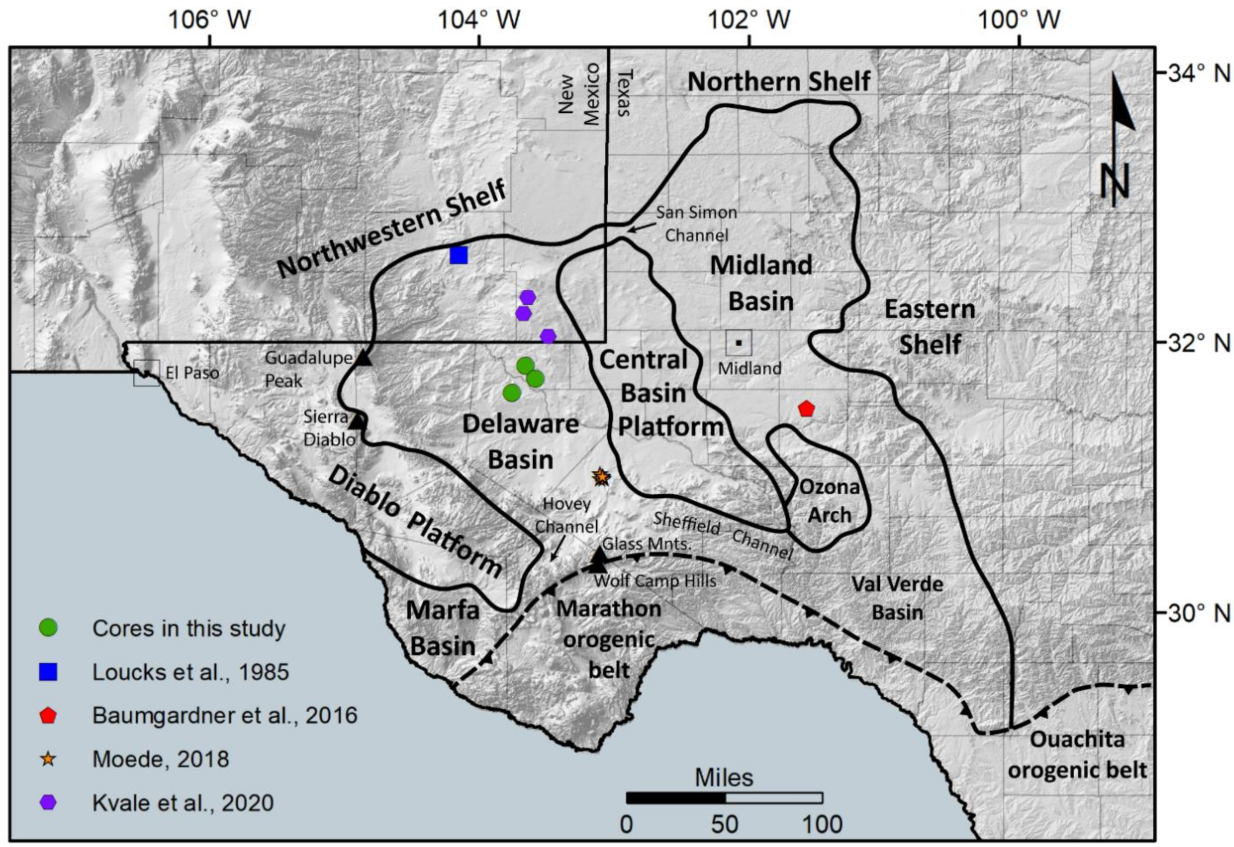

Figure 2.1. Modern topography in west Texas and southeast New Mexico with key components of the Permian Basin region during Early Permian (Late Wolfcampian to Early Leonardian) overlain.

The location of cores used in this study (green circles) and additional cores described in the literature are shown. Figure derived from Hunt and Fitchen (1999), Dutton et al. (2005), and Fu et al. (2020).

2.3 GEOLOGIC SETTING

The Permian Basin region is in the foreland of the Marathon-Ouachita orogenic belt (Figure 2.1). It extends over 115,000 mi^2 (~300,000 km^2) of west Texas and southeast New Mexico (Galley, 1958). The collision of Laurentia and Gondwana on the North American margin during the Early Pennsylvanian-Early Permian formed several intraforeland NW-SE trending sub-basins (e.g., Delaware Basin, Midland basin) rimmed by structural highs (e.g., Diablo Platform, Central Basin Platform), which, in time, became carbonate platforms (Frenzel et al., 1988; Shumaker, 1992; Yang and Dorobek, 1995; Wahlman and Tasker, 2013) (Figure 2.1). After the initial continental collision, subsidence continued in the Permian Basin region at variable rates (Yang and Dorobek, 1995; Ewing, 2019). In the Delaware Basin, subsidence rates peaked during the Wolfcampian stage (Early Permian) and then slowed down gradually throughout the rest of the Permian (Yang and Dorobek, 1995; Sinclair, 2007; Ewing, 2019).

Throughout most of Permian time, deep-water marine conditions prevailed in the Delaware Basin, whereas shallow water conditions were present in the uplifted areas adjacent to the basin (King, 1942). High-frequency glacioeustatic sea-level fluctuations occurred during the Pennsylvanian-Permian times (Ross and Ross, 1987, 2003a, b; Wahlman and Tasker, 2013). Three major sea-level lowstands are inferred from basinwide unconformities: 1) just above the Wolfcamp D and Wolfcamp C boundary; 2) at the boundary between Wolfcamp C and Wolfcamp B, known as the “mid-Wolfcampian unconformity” (MWU, Figure 2.2); and 3) at the boundary between Wolfcamp B and Wolfcamp A, Figure 2.2) (Ross and Ross, 2003b; Wahlman and Tasker, 2013) (Figure 2.2). Concurrently, northward tectonic drift caused the climate to shift from subhumid during Wolfcamp D deposition, to semiarid with intermittently seasonal dry/wet conditions during Wolfcamp C and Wolfcamp B deposition, to conditions that are more arid during Wolfcamp A deposition (Parrish, 1993; Ross and Ross, 2003a; Tabor et al., 2008; Wahlman and Tasker, 2013).

2.4 STUDY AREA AND STRATIGRAPHY

My study area is in the central-eastern Delaware Basin, within 50 mi (~80 km) of the western edge of the Central Basin Platform and north of the (Figure 2.3). The Wolfcamp strata in this area are among the thickest in the Permian Basin (Yang and Dorobek, 1995; Ewing, 2019; Fu et al., 2020), and the depth to the top of the Wolfcamp is deeper (~11,000 ft) (~3,300 m) than most locations in the basin (Moede, 2018; Ruppel, 2019).

The Wolfcamp interval in the Midland Basin is typically subdivided into four operational units (see Baumgardner et al., 2016): Wolfcamp D (Late Pennsylvanian); Wolfcamp C (Early Wolfcampian); Wolfcamp B (Late Wolfcampian); and Wolfcamp A (Early Leonardian). I followed this nomenclature and defined the Wolfcamp tops in my wells based on a gamma-ray and deep resistivity wireline log correlation with the O. L. Greer 2 well (Figure 2.2) located in the Midland Basin (Figure 2.1). The top of the Wolfcamp A is defined by a high-resistivity shale located immediately beneath a thick (150 ft to 200 ft) (~45 m to ~60 m), low-resistivity, sandy interval, which corresponds to Wolfcamp X & Y sands (Kvale et al., 2020). The Wolfcamp A contains several high-resistivity, low gamma-ray, carbonate beds separated by thin, high gamma-ray mudstone deposits (Figure 2.2). The boundary between the Wolfcamp A and Wolfcamp B units is at the base of a well-defined high-resistivity carbonate bed. Overall, the Wolfcamp B unit exhibits lower deep resistivity and higher gamma-ray values than the Wolfcamp A (Figure 2.2). Based on my well log correlation, I estimate the studied section extends down to the Wolfcamp B unit of the O.L. Greer 2 well in Baumgardner et al. (2016).

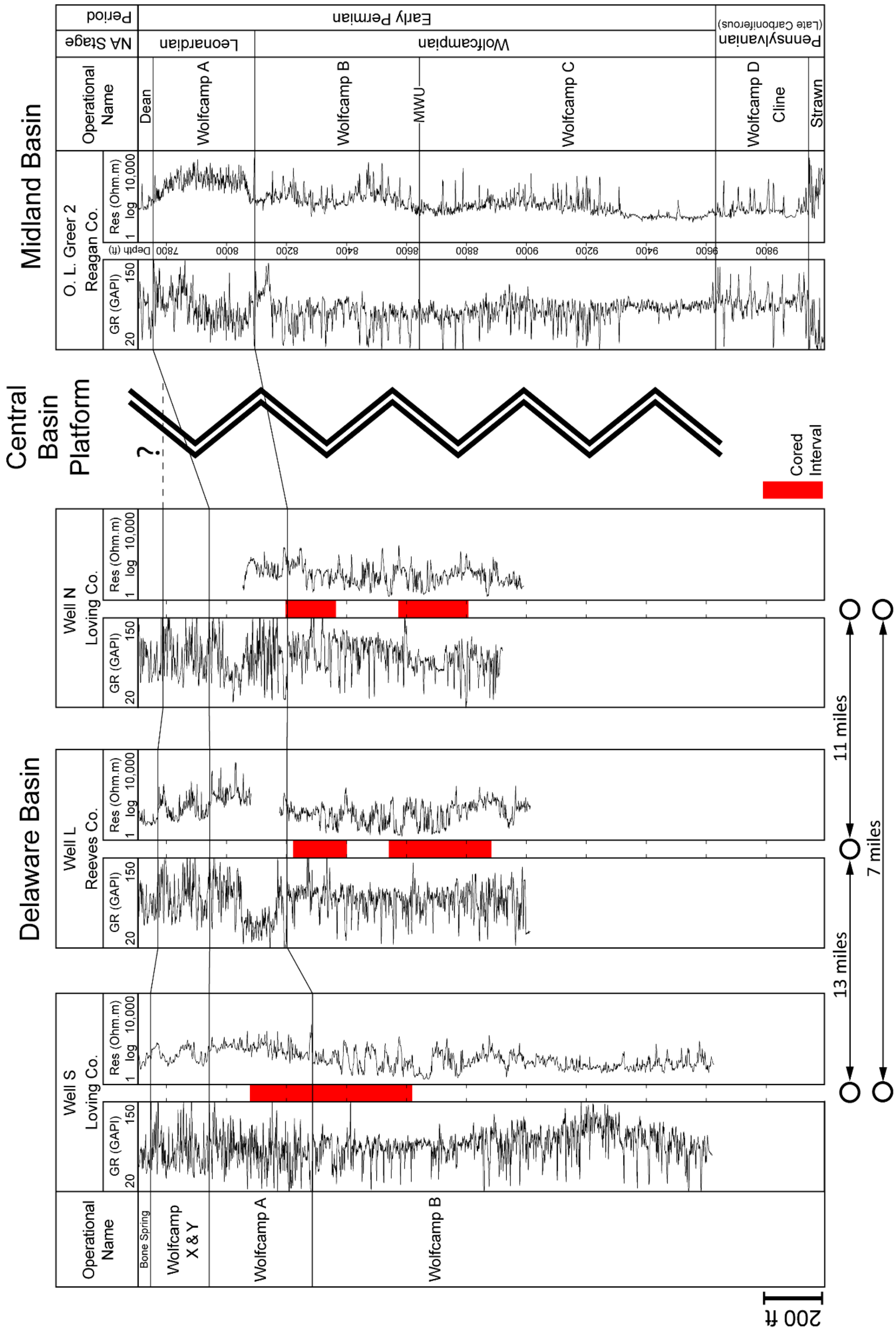

Midland Basin
Central Basin Platform
Delaware Basin
O. L. Greer 2
Reagan Co.
Well N
Loving Co.
Well L
Reeves Co.
Well S
Loving Co.
GR (GAPI)
20
150
Res (Ohm.m)
1
log
10,000
Depth (ft)
7800
8000
8200
8400
8600
8800
9000
9200
9400
9600
9800
Operational Name
NA Stage
Period
Early Permian
Leonardian
Wolfcampian
Pennsylvanian
(Late Carboniferous)
Dean
Wolfcamp A
Wolfcamp B
MWU
Wolfcamp C
Wolfcamp D
Cline
Strawn
Bone Spring
Wolfcamp X & Y
?
Cored Interval
13 miles
11 miles
7 miles
200 ft

Figure 2.2. West (left)-East (right) cross-section of wells used in this work showing correlation to Wolfcamp operational units in the O. L. Greer 2 well (Baumgardner et al., 2016) in the Midland Basin (Figure 2.1).

Detailed location of Well S, Well L, and Well N is in Figure 2.3.Vertical red bars in each well represent the cored intervals used in this work. The cored intervals comprise 1451 total linear ft) (~440 m) spanning ~750 ft (~230 m) of the Wolfcamp A and Wolfcamp B units. Horizontal distance between wells not to scale. MWU = mid-Wolfcampian unconformity. GR = gamma-ray; Res = deep resistivity in log scale.

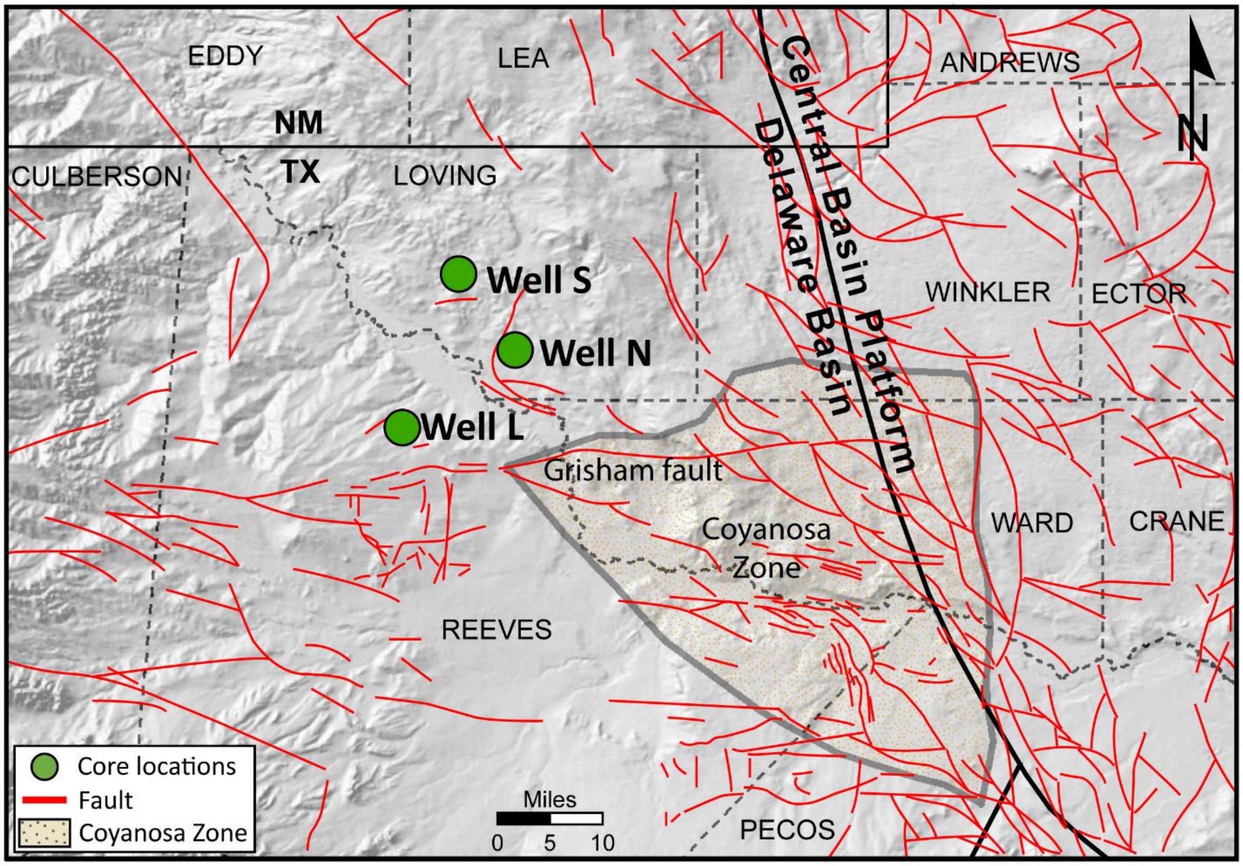

Figure 2.3. Detailed map showing locations of my study cores and the nearby basement-rooted faults.

Basement-rooted faults mapped from Horne et al. (2021). Coyanosa Zone mapped from (Ewing, 2019). The Grisham Fault is also referred to as the Mid-Basin fault by Shumaker (1992).

2.5 Dataset and methods

Three conventional cores of the Wolfcamp A and Wolfcamp B units (see red rectangles, Figure 2.2) were slabbed and photographed under plain light and ultraviolet (UV). The bulk mineralogy and total organic carbon (TOC) content were determined by analyzing rock samples with X-ray diffraction (XRD) and LECO TOC techniques, respectively. 183 XRD and 183 LECO TOC samples were analyzed in Well L; 111 XRD and 74 LECO TOC samples were analyzed in Well N; and 107 XRD samples were analyzed in Well S. The texture and composition of rock samples in Well N were characterized from 36 thin sections. These data were integrated with macroscopic core observations, XRD-mineralogy and LECO TOC to define lithofacies.

I interpreted each lithofacies in the cored intervals at the inch scale. XRD and LECO TOC analyses were not feasible to conduct at such a small scale. Therefore, I modeled the mineralogy and TOC content of the cores using their elemental composition. The core-slabbed surfaces were scanned with XRF handheld devices to estimate the concentration of thirty elements every two inches. I then used this elemental composition to estimate the calcite, dolomite, quartz, illite, and TOC contents at each XRF-scan point in the core.

I integrated the sedimentary structures, bounding surfaces, texture, and composition (mineralogy, TOC) in each lithofacies to interpret the depositional or diagenetic processes that generated them. Lastly, I depth-calibrated the core dataset to conventional wireline log depths to determine the characteristic wireline log response (e.g., gamma-ray, deep resistivity, neutron porosity) exhibited by each deposit.

2.5.1 Lithofacies classification

Wolfcamp rocks contain varying abundances of calciclastic and siliciclastic sediments, and therefore it is challenging to classify them by schemes designed for carbonates (e.g., Dunham, 1962; Folk, 1962; Embry and Klovan, 1971) or siliciclastics (e.g., McBride, 1963; Folk, 1968) alone. I named my lithofacies based on the dominant grain size present and added modifiers to describe characteristic attributes such as mineralogy or organic content. I described the roundness of particles according to (Krumbein and Sloss, 1963), and the degree of particle sorting from (Longiaru, 1987).

"Mudstones" refer to matrix-supported sedimentary rocks composed of 50 vol.% or more of clay and silt size (<62.5 μm) sediments (Lazar et al., 2015) as observed in thin section. "Sandstones" refer to grain-supported sedimentary rocks of more than 50 vol.% sand-size (62.5 μm - 2 mm, Wentworth, 1922) sediments as observed in thin section. For mudstones and sandstones, I add the modifier 'siliceous', 'argillaceous', or 'calcareous' if quartz, clay, or calcite are their primary mineral components, respectively. I add the modifier 'dolomitic' when the XRD-determined dolomite content is ≥12 wt.%. "Conglomerate" refers to rocks that have more than 10 vol.% gravel-sized (>2 mm, Wentworth, 1922) components as observed in thin section or in core. Finally, "dolomudstone" refers to rocks consisting of over ~30 wt.% XRD-determined dolomite exhibiting a crystalline texture in thin section.

2.5.2 Compositional analysis

I measured the elemental composition with X-Ray Fluorescence (XRF). I then estimated the mineral content based on the molar ratio of elements with a mineral formula like that presented by Algeo et al. (2007) and Nance and Rowe (2015). In the studied interval, dolomite, calcite, quartz, and illite account for over 75 wt.% on average of the bulk mineralogy, based on the XRD bulk mineralogy analysis. Therefore, I used the XRF-measured elemental concentration of magnesium (Mg), calcium (Ca), silicon (Si), and aluminum (Al) to estimate the content in those four minerals at each XRF-scan point. I detail my approach in Appendix 2.A. The XRF-modeled dolomite, calcite, and quartz strongly correlate with the XRD-determined mineralogy (Figure 2.A1A,B,D). However, the correlation is weaker for illite (Figure 2.A1C). Therefore, the uncertainty for the illite estimation is higher than that in the other three minerals.

I cross-plotted all the elements with the available LECO TOC measurements to estimate the TOC content from XRF data. I found that nickel (Ni) exhibits the best correlation ($R^2 = 0.63$) amongst all elements, which was also observed by Driskill et al. (2018) in the upper Wolfcamp and Bone Spring intervals in the Delaware Basin. I estimated the TOC content using linear regression of the XRF-measured Ni vs LECO TOC measurements. I detail my approach in Appendix 2.B.

2.5.3 Depth calibration

I correlated the core data to the wireline log data. I generated a synthetic gamma-ray log (GR_{synth}) that I generated with the XRF-measured thorium (Th), uranium (U), and potassium (K) concentrations:

$$GR_{synth} \text{ (API units)} = 4*Th \text{ (ppm)} + 8*U \text{ (ppm)} + 16*K \text{ (wt. \%)} \quad \text{Eq. 2.1}$$

Eq. 2.1 is from Ellis and Singer (2007). I applied a moving weighted regression (Peltier, 2019) to the GR_{synth} curve (red curve, Figure 2.4) using a smoothing parameter (α) of 0.01 to generate a lower frequency GR curve (black curve, Figure 2.4). I used this curve to correlate the core data to the wireline log (green curve, Figure 2.4). I had to perform the depth calibration at multiple depths, probably because the core recovery was not 100%.

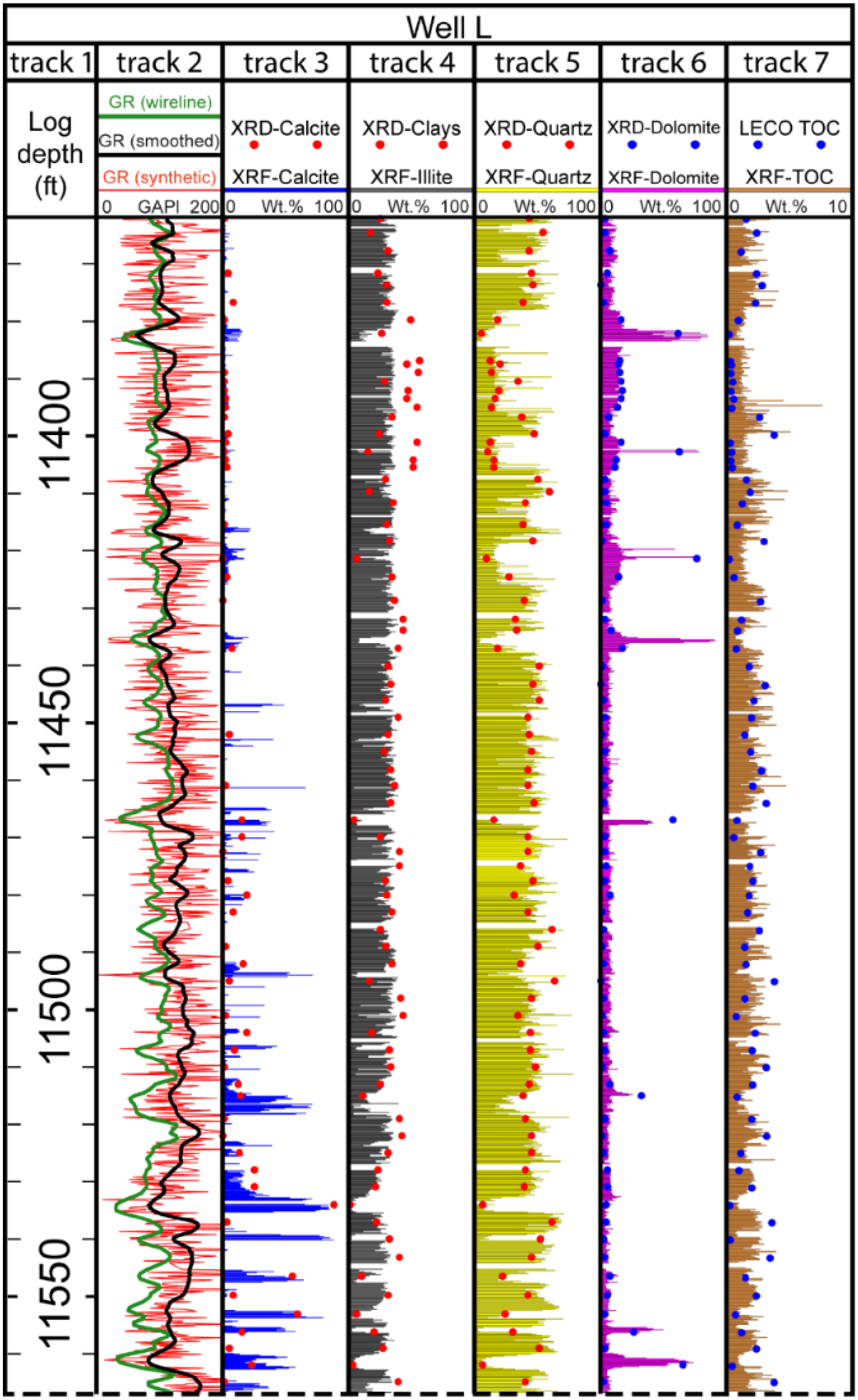

Well L
track 1
track 2
track 3
track 4
track 5
track 6
track 7
Log depth (ft)
GR (wireline)
GR (smoothed)
GR (synthetic)
0 GAPI 200
XRD-Calcite
XRF-Calcite
0 Wt.% 100
XRD-Clays
XRF-Illite
0 Wt.% 100
XRD-Quartz
XRF-Quartz
0 Wt.% 100
XRD-Dolomite
XRF-Dolomite
0 Wt.% 100
LECO TOC
XRF-TOC
0 Wt.% 10
11400
11450
11500
11550

Figure 2.4: Example of core data shifted to wireline log depth using synthetic gamma-ray and wireline gamma-ray logs.

Track 1: wireline log depth. Track 2: synthetic gamma-ray curve generated with XRF core elemental data (red), smoothed synthetic gamma-ray (black), and wireline gamma-ray (green). Track 3: XRF-modeled calcite (blue) and XRD-calcite (red dot). Track 4: XRF-modeled illite (grey) and XRD-clays (red dot), which includes illite/smectite mix layer, illite/mica, and chlorite. Track 5: XRF-modeled quartz (yellow) and XRD-quartz (red dot). Track 6: XRF-modeled dolomite (magenta) and XRD-dolomite (blue dot). Track 7: XRF-modeled TOC (brown) and LECO TOC (blue dot). The shown depth interval is from the Wolfcamp B, Well L.

2.6 RESULTS

2.6.1 Lithofacies description

Lithofacies 1: Organic-rich siliceous mudstone

The organic-rich siliceous mudstone is a dark grey to nearly black mudstone (Figure 2.5A) dominated by quartz (42.9 wt.%), clay (29.7 wt.%), and feldspar (12.3 wt.%) (Table 2.1). The quartz is composed of microcrystalline quartz cement, biogenic silica (e.g., silicified radiolarians, siliceous sponges, agglutinated benthic foraminifera), and detrital quartz. Detrital quartz consists of angular to subangular, moderately sorted, silt-sized grains (Figure 2.6A). Radiolarians are typically silicified but may also be calcitized or dolomitized. The test chambers of agglutinated benthic foraminifera are frequently collapsed, probably due to compaction. This lithofacies has the highest LECO TOC content (2.07 wt.%, Table 2.1) in the studied interval. The organic matter occurs either as elongated, bed-parallel flattened lenses, or as particles with well-defined, curved-to-straight edges that are probably debris of plants (e.g., woody material). The texture is generally massive but can have millimeter-thick planar laminations composed of silt-sized quartz and interstitial clays interbedded with more clay-rich layers. The upper and lower boundaries of this lithofacies are generally abrupt. However, the lower boundary can also be in gradational contact with the underlying calcareous mudstone lithofacies. Bioturbation is occasionally present, and bedding-parallel, thin (<1-inch thick) calcite-cemented fractures are common.

Table 2.1. Normalized average bulk X-ray diffraction (XRD) mineralogy and LECO total organic carbon (TOC) content by lithofacies.

Values are in weight percent (wt.%). n = number of samples used to calculate average contents. Dolomite includes Mg-dolomite and ankerite. Clays include illite, smectite-illite mixed layer, chlorite, and mica. Feldspars include K-feldspars and plagioclase. 'Others' may consist of pyrite, apatite, siderite, halite and/or anatase.

#	*Lithofacies*	*Quartz*	*Feldspars*	*Calcite*	*Dolomite*	*IS/S-ML*	*Chlorite*	*Pyrite*	*Others*	*TOC*
1	Organic-rich siliceous mudstone n_{XRD} = 259, n_{TOC} = 169	42.9	12.3	6.7	3.9	27.0	2.7	1.9	0.6	2.07
2	Argillaceous mudstone n_{XRD} = 56, n_{TOC} = 35	21.5	13.9	5.1	8.6	45.8	2.6	1.4	0.2	0.97
3a	Calcareous mudstone n_{XRD} = 31, n_{TOC} = 13	33.6	7.2	30.0	6.8	17.0	0.9	1.8	0.9	1.85
3b	Dolomitic calcareous mudstone n_{XRD} = 17, n_{TOC} = 13	18.4	6.7	12.8	51.5	7.8	0.5	1.0	0.1	1.21
4a	Calcareous sandstone n_{XRD} = 19, n_{TOC} = 9	30.3	4.4	50.0	6.6	5.6	0.4	1.5	0.6	0.63
4b	Dolomitic calcareous sandstone n_{XRD} = 8, n_{TOC} = 5	16.0	4.1	25.5	49.6	3.4	0.3	0.4	0.2	0.50
5	Matrix-supported conglomerate n_{XRD} = 17, n_{TOC} = 13	30.4	7.1	36.5	9.8	12.5	0.5	1.4	0.7	1.01
6	Dolomudstone n_{XRD} = 23, n_{TOC} =10	7.8	4.6	3.2	63.2	17.9	1.6	0.9	0.4	0.42

Lithofacies 2: Argillaceous mudstone

The argillaceous mudstone is light grey (Figure 2.5B) and dominated by clays (48.4 wt. %) and varying amounts of quartz (21.5 wt.%) and feldspars (13.9 wt.%) (Table 2.1). The quartz is primarily detrital, and is finer-grained, slightly better sorted, and less abundant (Figure 2.6B) than the detrital quartz in the organic-rich siliceous mudstone. Its TOC content (0.97 wt.%) (Table 2.1) is approximately half that in the organic-rich siliceous mudstone. Fossils are rare and consist primarily of silicified radiolarians. Pyritized oval-shaped to flattened aggregates (yellow arrows, Figure 2.6B) and highly-compacted clay-aggregates (red arrows, Figure 2.6B) are common. The radiolarians and aggregates have their long axis oriented parallel to the bedding plane. The texture is generally massive, although planar laminations, lenticular laminations, and convoluted bedding are relatively common at the base. This lithofacies is typically in sharp top and bottom contact with the organic-rich siliceous mudstone and in gradual transition with the dolomudstone lithofacies. In a few cases, the upper contact is sharp and erosive with the calcareous sandstone lithofacies and with the matrix-supported conglomerate lithofacies. The argillaceous mudstone lithofacies grades upwards from silt-dominated at the bottom to clay-sized towards the middle and top. Bioturbation typically occurs towards the top of the deposits.

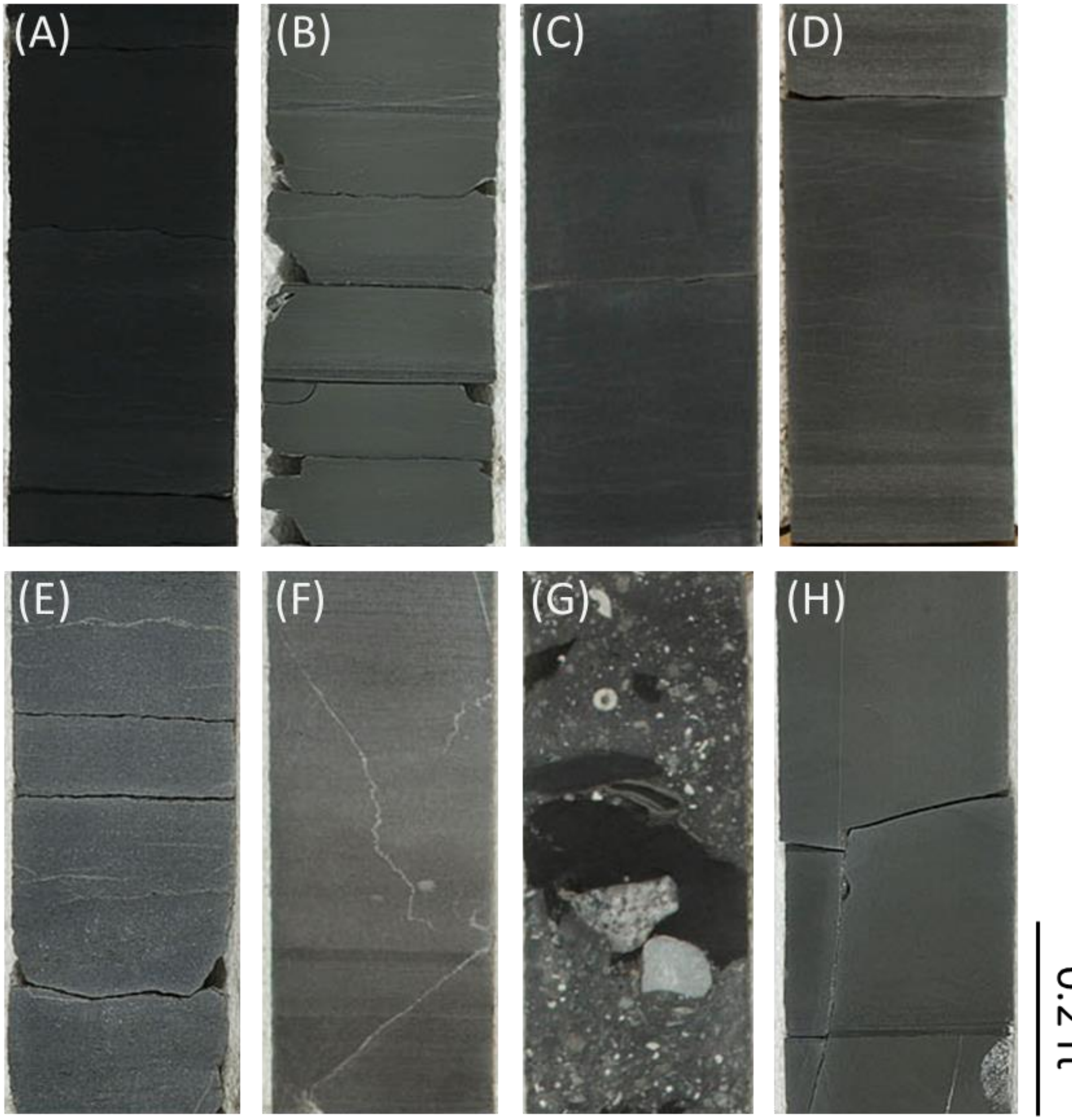

Figure 2.5. Plain light core photographs of upper Wolfcamp lithofacies.

(A) organic-rich siliceous mudstone. (B) Argillaceous mudstone. (C) Calcareous mudstone. (D) Dolomitic calcareous mudstone. (E) Calcareous sandstone. (F) Dolomitic calcareous sandstone (G) Matrix-supported conglomerate. (H) Dolomudstone.

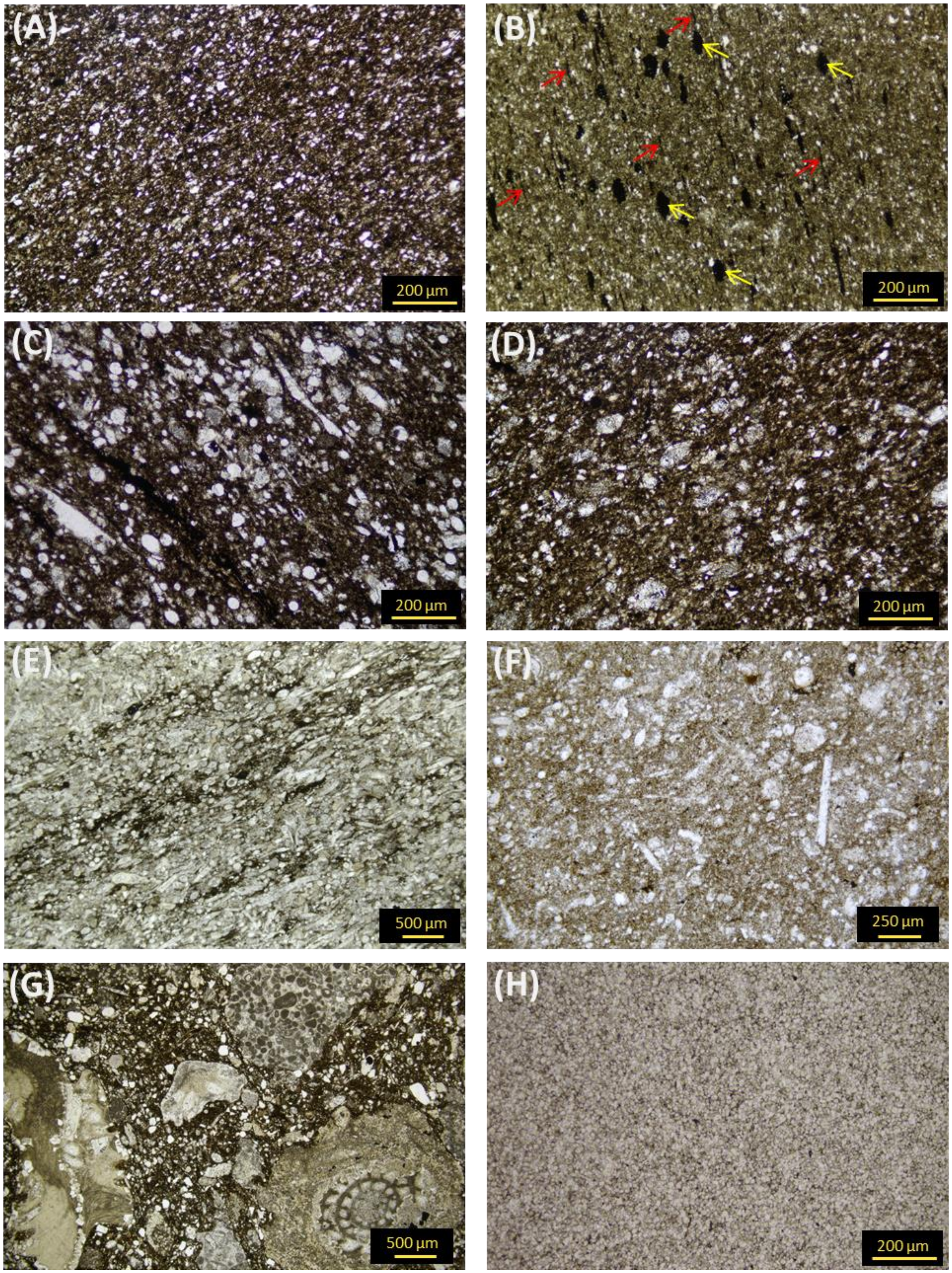
(A)
200 µm
(B)
200 µm
(C)
200 µm
(D)
200 µm
(E)
500 µm
(F)
250 µm
(G)
500 µm
(H)
200 µm

Figure 2.6. Transmitted light photomicrographs of upper Wolfcamp lithofacies.

(A) Organic-rich siliceous mudstone lithofacies with abundant detrital quartz (white grains) dispersed throughout the organic- and clay-rich matrix. (B) Argillaceous mudstone lithofacies with oriented pyritized oval-shaped aggregates (yellow arrows) and flattened organic matter lenses (?) (red arrows). (C) Calcareous mudstone lithofacies has a matrix-supported texture with carbonate fossils, undifferentiated carbonate bioclasts and detrital quartz floating in a clay-rich matrix. (D) Dolomitic calcareous mudstone showing a similar texture to the calcareous mudstone but with dolomitized carbonate fossils. (E) Calcareous sandstone lithofacies has a grain-supported texture with few clay-rich bands. (F) Dolomitic calcareous sandstone has a similar texture to the calcareous sandstone, but it is dolomitized. (G) Matrix-supported conglomerate lithofacies has carbonate bioclasts, lithoclasts, and silt-sized detrital quartz floating in a clay-rich matrix. (H) Dolomudstone lithofacies has a massive texture consisting of tightly packed dolomite crystals; see Figure 2.7B for high-magnification view of the dolomite crystals.

Lithofacies 3a: Calcareous mudstone

The calcareous mudstone is dark grey (Figure 2.5C) and mainly composed of quartz (33.6 wt.%), silt-sized calcium carbonate bioclasts (30.0 wt.%), and clays (17.9 wt. %) (Table 2.1). The silica may occur as detrital grains, biogenic grains, and microcrystalline quartz cement. The TOC content (1.85 wt.%) (Table 2.1) is slightly lower than that that in the organic-rich siliceous mudstone. Fossils include calcispheres, silicified and calcitized radiolarians, bivalve shells, calcitized and silicified sponge spicules, agglutinated benthic foraminifera, and abraded equinoderm plates (Figure 2.6C). Fossils with a high aspect ratio (e.g., sponge spicules) show preferential orientation parallel to the bedding plane. This lithofacies is generally massive but can exhibit millimeter-thick planar laminations. Its basal contact is typically gradational with the calcareous sandstone lithofacies or sharp with the organic-rich siliceous mudstone. Its upper contact generally is gradational with the overlying organic-rich siliceous mudstone, although it is sharp in a few cases. When dolomitic, I classified the calcareous mudstone as Lithofacies 3b: Dolomitic calcareous mudstone.

Lithofacies 3b: Dolomitic calcareous mudstone

This lithofacies (Figure 2.5D) is a calcareous mudstone with dolomite content greater than 12 wt.% (Table 2.1). Dolomite occurs as both dolomitized bioclasts (Figure 2.6D) and dolomite rhombic crystals (Figure 2.7A). The dolomite crystals exhibit a pronounced zonation characterized by ferroan rims surrounding a magnesium-rich core. Dolomitic microfossils are also ferroan and frequently exhibit dolomite overgrowths. Most dolomite crystals and dolomitized microfossils exhibit nano- to micrometer-size intraparticle pores.

Lithofacies 4a: Calcareous sandstone

The calcareous sandstone (Figure 2.5E) is a grain-supported carbonate primarily composed of very-fine sand-size calcium carbonate bioclasts and carbonate cement (50.0 wt.%). It contains varying amounts of silt-sized detrital quartz, biogenic silica, and quartz cement (30.3 wt.%) (Table 2.1). The clay (6.0 wt.%) and TOC (0.63 wt.%) contents are very low (Table 2.1). Carbonate bioclasts consist of calcispheres, equinoid spines and plates, sponge fragments (up to ~2 mm in the long axis), fusulinids, and bivalves' shells (Figure 2.6E). Radiolarians and sponge spicules may either be silicified or calcitized. Sorting is poor to moderate and grains may be oriented parallel to the bedding plane, indicating bedload transport. This lithofacies can be massive, planar-laminated or convolute-bedded. It typically has a sharp basal contact either with the organic-rich siliceous mudstone or with the calcareous mudstone lithofacies. In rare cases, the basal contact is sharp and erosive with the argillaceous mudstone lithofacies. The top contact is typically gradational with the overlying calcareous mudstone lithofacies. When dolomitic, I classified the calcareous sandstone as Lithofacies 4b: Dolomitic calcareous sandstone.

Lithofacies 4b: Dolomitic calcareous sandstone

The dolomitic calcareous sandstone (Figure 2.5D) is a calcareous sandstone with more than 12 wt.% dolomite (Table 2.1). Although dolomitized, this lithofacies preserves a texture like the calcareous sandstone lithofacies (Figure 2.6F), and it may exhibit a brown or tan color in core.

Lithofacies 5: Matrix-supported conglomerate

The matrix-supported conglomerate is composed of silt- to sand-size carbonate bioclasts, millimeter- to centimeter-sized lithoclasts of carbonate or mud composition, and detrital quartz dispersed throughout a clay-rich matrix (Figure 2.5G). Over 10 vol.% of these constituents are larger than 2 mm in the long axis. Some lithoclasts even exceed the diameter of the core. The primary mineral components in this lithofacies are calcite (36.5 wt.%), quartz (30.4 wt.%), and clays (13.0 wt.%) (Table 2.1). The quartz is mostly detrital and consists of subangular, very poorly sorted, silt- to sand-sized grains (Figure 2.6G). However, microcrystalline quartz cement is also common. Fossils include sponge fragments, sponge spicules, equinoderm plates and spines, fusulinid foraminifera, brachiopod shell fragments, rugose corals, thin bivalves' shells, and calcispheres. The organic content in this lithofacies is low (1.01 wt.%) (Table 2.1). The matrix-supported conglomerate consistently exhibits massive and non-gradational texture. It typically shows sharp top and bottom contacts with the organic-rich siliceous mudstone lithofacies. In rare cases, it is in sharp bottom contact with the argillaceous mudstone lithofacies.

Lithofacies 6: Dolomudstone

The dolomudstone is a structureless (Figure 2.5H), very fine crystalline (Figure 2.6H, Figure 2.7A) carbonate predominantly composed of dolomite (63.2 wt.%) and clays (19.5 wt.%) (Table 2.1). It has a similar color to the argillaceous mudstone lithofacies, and it is easily recognizable under UV light because it glows. This lithofacies exhibits a planar-euhedral texture (Sibley and Gregg, 1987), which consists of a mosaic of tightly packed (Figure 2.6F) unimodal euhedral rhombic dolomite crystals. Clays occupy the intercrystalline pore space, and the edge of the dolomite crystals exhibit low iron content (Figure 2.7B). The dolomudstone has the lowest organic content (0.42 wt.%) (Table 2.1) amongst all lithofacies in the studied interval. Neither fossils, nor fossil ghosts were recognized in this lithofacies. It is typically massive, although traces of millimeter to sub-millimeter scale laminations are visible in some thin sections. Some core intervals show signs of bioturbation. The dolomudstone top and bottom contacts are always in gradational contact with the argillaceous mudstone lithofacies.

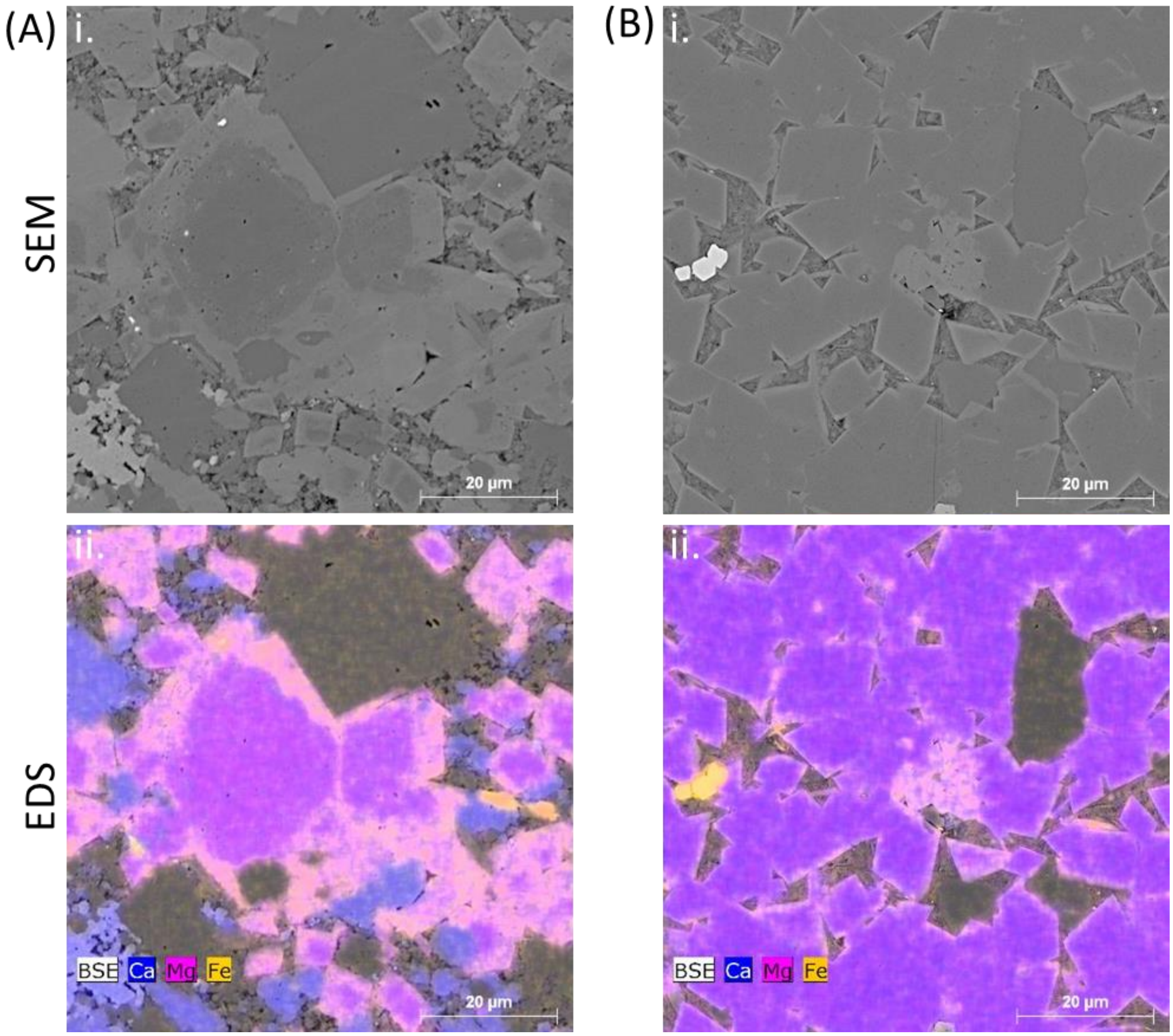

Figure 2.7. SEM and EDS maps of dolomitic lithofacies.

(A) SEM and EDS maps of dolomitic calcareous mudstone showing dolomite crystals with their rims enriched in iron (yellow) and their core rich in magnesium (magenta). (B) SEM and EDS maps of dolomudstone lithofacies showing a tightly packed texture of dolomite crystals (magenta) with the intercrystalline volume occupied primarily by clays. The dolomite crystals in the dolomudstone have low iron content (yellow) in their rims. SEM and EDS map images are courtesy of Dr. Robert M. Reed.

2.6.2 Lithofacies interpretation

Lithofacies 1: Organic-rich siliceous mudstone

I interpreted that this lithofacies records settling through the water column of suspended living organisms (e.g., radiolarians), and terrigenous sediments transported from the shelves to the basin by currents or river discharges (McCave, 1972; Stow and Piper, 1984; Stow and Tabrez, 1998; Henrich and Huneke, 2011; Stow and Smillie, 2020). The silicon (Si) and zircon (Zr) elements do not exhibit a clear negative or positive correlation (Figure 2.8A). This indicates that quartz in this lithofacies was derived from both biogenic (e.g., radiolarians, sponge spicules) and terrestrial (e.g., silt-size detrital quartz) sources (Ratcliffe et al., 2012), which is characteristic of hemipelagic deposits. The high TOC content suggests that this lithofacies accumulated predominantly during periods of high organic productivity, rapid sedimentation, and/or low bioturbation activity within a poorly-oxygenated and low-energy deep marine environment. The presence of benthonic fauna (e.g., agglutinated foraminifera) may suggest periods of higher oxygen levels at the seafloor (Wilson et al., 2020).

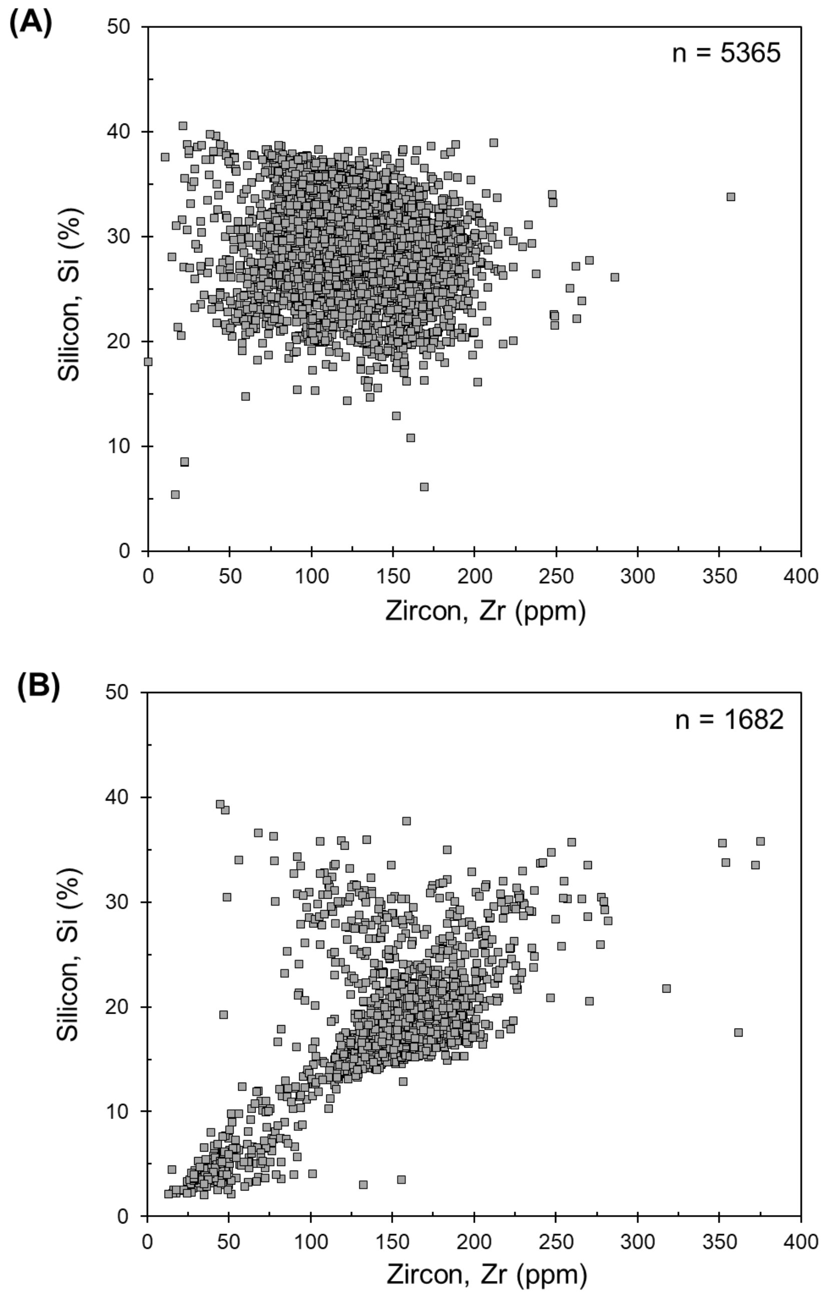

Figure 2.8. Zircon (Zr) versus silicon (Si) binary plot from the organic-rich siliceous mudstone and argillaceous mudstone lithofacies.

(A) Organic-rich siliceous mudstone lithofacies. (B) Argillaceous mudstone lithofacies. According to Ratcliffe et al. (2012), silicon is derived from a terrestrial source when it increases with increasing Zr, whereas an inverse correlation between Si and Zr indicates a biogenic source for the silicon. The elemental concentration of Si and Zr were measured on the slabbed surface of the cores. n = number of XRF data points.

Lithofacies 2: Argillaceous mudstone

I interpret that the argillaceous mudstone records deposition from fine-grained turbidity currents based on the normally graded texture, the presence of cross-bedding at the base, preferential orientation of elongated particles (i.e., clay aggregates), an abrupt basal contact, and clay- to silt-dominated particle size (Figure 2.9A). The overall positive correlation between silicon (Si) and zircon (Zr) in this lithofacies (Figure 2.8B) indicates that quartz was derive predominantly from terrestrial sources (Ratcliffe et al., 2012).

Figure 2.9B is an interpreted type example of the argillaceous mudstone lithofacies and its turbidite intervals. The cross-bedding at the base records tractional movement of the coarse fraction transported by the turbidity current. The overlying convoluted bedding and the irregular bedding indicate rapid sediment deposition from the turbulent flow (Piper, 1972). As the turbidity current waned, the finest sediments settled and formed the homogeneous upper sequences. I interpret that the top of the turbidite sequence is homogenous because the grain size distribution of the last sediments to deposit was fairly uniform. Micro-bioturbation near the upper surface suggests that a relatively low-energy environment followed deposition of the turbidite. The top contact is typically sharp with the organic-rich siliceous mudstone lithofacies, suggesting that the turbidite must have deposited very rapidly for the transition with the overlying hemipelagic deposits not to be gradual. This rapid deposition may be possible when clays flocculate while in suspension (Piper, 1972; Manning et al., 2017).

The argillaceous mudstone is similar to the ‘fine-grained turbidites’ described by Stow and Shanmugam (1980) and Stow and Piper (1984). I interpret the ‘T’ classification of Stow and Shanmugam (1980) in the individual components of my fine-grained turbidite (Figure 2.9C). This lithofacies has not been previously documented in the upper Wolfcamp interval at the Delaware Basin.

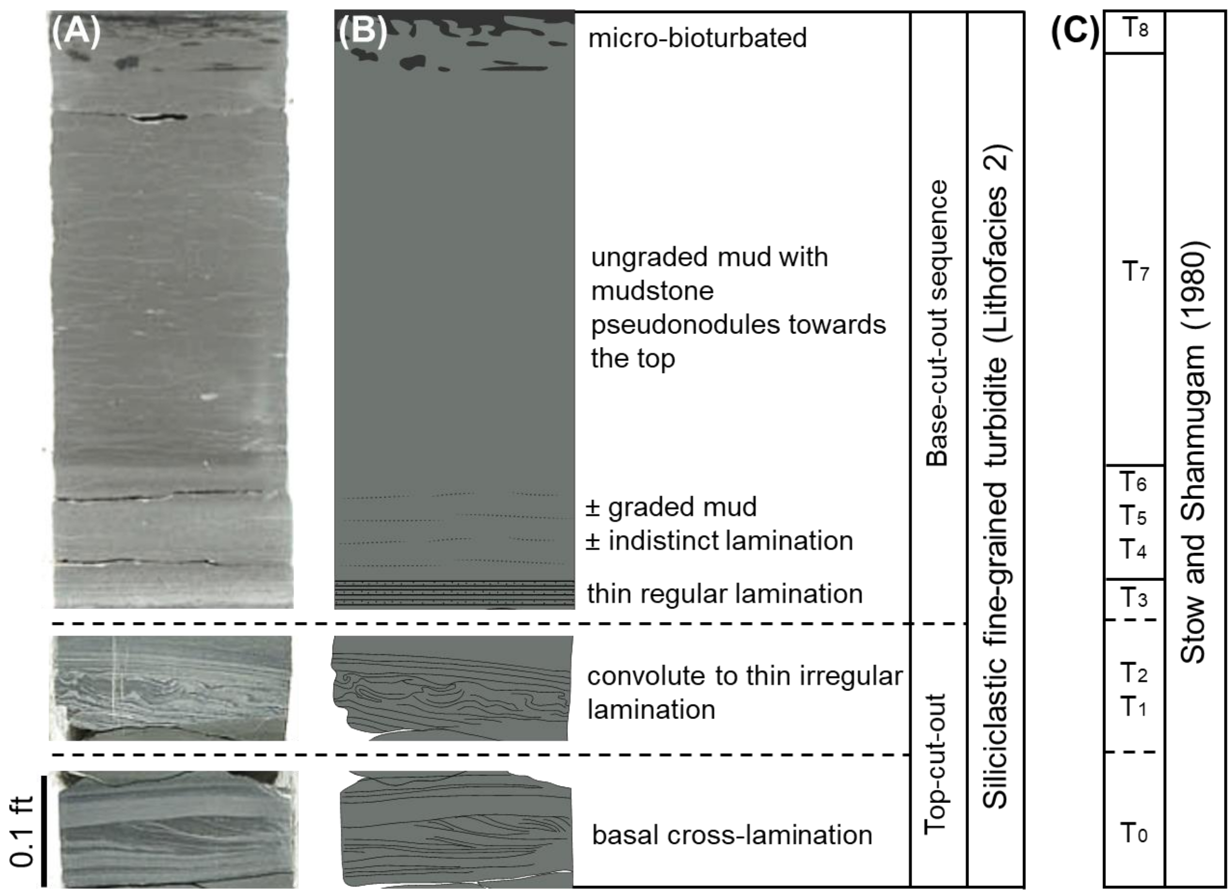

Figure 2.9. Fine grained turbidite.

(A) Composite photograph (plain light) of three different levels in the core (separated by dashed lines) showing the ideal sequence of structures of a siliciclastic fine-grained turbidite (Lithofacies 2). Core intervals are from the Wolfcamp B unit (B) Line-drawing interpretation of core photographs in (A) with interpreted sedimentary features. . I did not find examples of this fully preserved sequence but found the individual components illustrated (i.e., top- and base-cut-out sequences) which I superimpose here. (C) Interpreted sequence of ‘T’ divisions of Stow and Shanmugam’s (1980) fine-grained turbidites.

Lithofacies 3a and 4a: Calcareous mudstone and calcareous sandstone

I interpret that the calcareous mudstone and the calcareous sandstone record deposition from turbidity currents based on their sharp bottom contact, normally graded textures, and sequence of sedimentary structures. In some instances, I interpret that turbidity currents probably transitioned to laminar flow and formed a sequence of deposits similar to the hybrid event beds described by Haughton et al. (2009).

Carbonate turbidites

A single carbonate turbidite deposit is composed of a massive- to planar-laminated calcareous sandstone that grades upwards into convolute-bedded to planar-laminated calcareous sandstone alternating with calcareous mudstone (Figure 2.10). This grades upwards into massive calcareous mudstone and the organic-rich siliceous mudstone, interpreted to record hemipelagic sedimentation. The boundary between the turbidite and the overlying hemipelagic deposition is difficult to delineate. This lithofacies progression is similar to Bouma's (1962) model.

The coarse-grained calcareous sandstone represents the most energetic part of the flow (Bouma's Ta, Figure 2.10). Its poorly graded texture, absence of bedforms, and low matrix mud content suggest that it was deposited from high-density turbidity currents (Talling et al., 2012). Thereafter, rates of sediment fallout decrease and near-bed layers are reworked by traction to form planar laminations in the calcareous sandstone lithofacies (Bouma's Tb) (Talling et al., 2012). The sediment concentration and fallout rates continue decreasing within the flow and fluid turbulence becomes the dominant sediment support mechanism, resulting in ripple cross-laminations (Bouma's Tc) (Talling et al., 2012). An upward flow of water from the underlying deposits due to sediment loading probably generated the convolute cross-lamination. This is followed by the deposition of the laminated calcareous sandstone to calcareous mudstone interval (Bouma's Td) from a low-density turbidity current (Talling et al., 2012). Lastly, there is suspension fallout of the finest sediments transported by the low-velocity dilute tail of the turbidity current. Deposits generated during this late-stage of the flow are the massive calcareous mudstone (Bouma’s Te) grading upwards into organic-rich siliceous mudstone, which records the return to background hemipelagic sedimentation.

The carbonate turbidites described above are mostly present in the Wolfcamp B unit. Although I found some turbidites preserving the complete Bouma sequence, they commonly occur as incomplete intervals throughout the core. Deposits showing only the Ta-c intervals probably represent deposition of the turbidite along channels or in an unconfined setting such as lobes or the peripheral submarine fan fringe environment (Payros and Pujalte, 2008; Kane et al., 2017). In contrast, deposits consisting of Td-e intervals may have accumulated within the channel, or in an unconfined setting such as lobes or on the marginal levees by overspilling of the turbulent cloud (Payros and Pujalte, 2008).

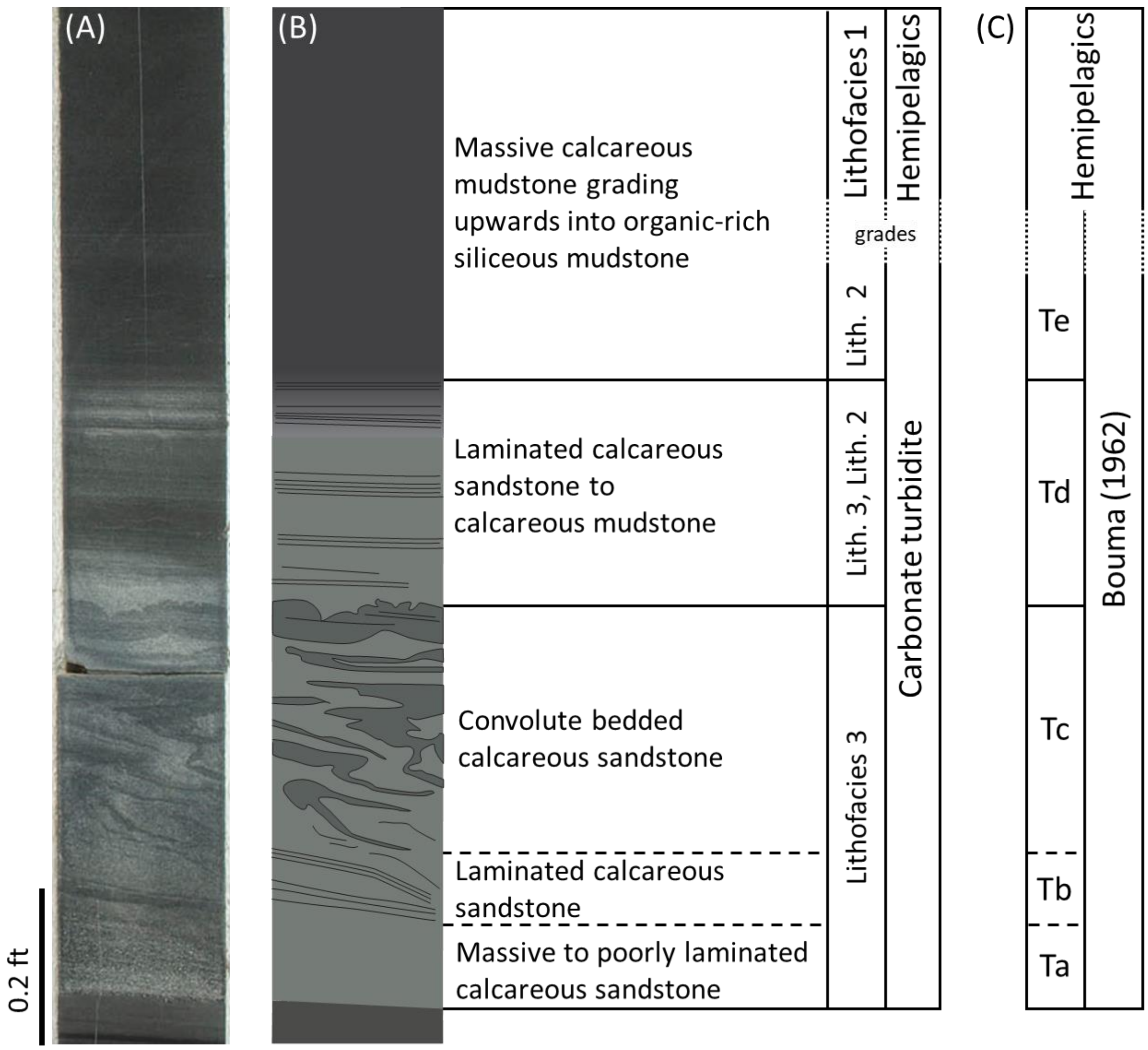

Figure 2.10. Carbonate turbidite.

(A) Plain light core photograph of carbonate turbidite deposit in Wolfcamp B unit. (B) Schematic photograph with interpreted features and sequence of lithofacies. (C) Interpreted Bouma's (1962) 'T' divisions.

Carbonate hybrid event beds (HEBs)

Hybrid event beds (HEBs) record a transition from turbulent flow to laminar flow (Haughton et al., 2009). In my cores, the carbonate HEBs exhibit four internal divisions (Figure 2.11). At the base, a massive calcareous sandstone is overlain by a layered interval of calcareous mudstone (darker bands) alternating with calcareous sandstone (lighter bands). This interval is overlain by a massive calcareous mudstone with scattered pseudonodules that are presumably composed of coarser (e.g., sand-sized) sediments. The carbonate HEB sequence grades upwards into massive organic-rich siliceous mudstone, which I interpret to record hemipelagic sedimentation.

In Figure 2.11, the structureless calcareous sandstone interval at the base is inferred to be deposited from high-density turbidity currents (see H1 of Haughton et al. (2009)). Immediately above, the banded interval of calcareous sandstone and calcareous mudstone records a transition from turbulent to laminar flow due to an increase in clay content within the flow (see H2 of Haughton et al. (2009)). When the clay concentration is such that fluid turbulence is suppressed, the flow becomes laminar and the massive calcareous mudstone is accumulated (see H3 of Haughton et al. (2009)). The flow becomes turbulent again and generates massive deposits of calcareous mudstone that grade upwards into the organic-rich siliceous mudstone lithofacies (hemipelagics) (see H5 of Haughton et al. (2009)). The Haughton's (2009) H4 division is absent in my carbonate HEBs; Kvale et al. (2020) did not observed this interval either in Wolfcamp carbonate HEBs.

HEBs are found in deep-water siliciclastic systems (e.g., Haughton et al., 2009; Hodgson, 2009; Kane et al., 2017; Spychala et al., 2017) and in mixed calciclastic-siliciclastic systems, such as the Wolfcamp (e.g., Driskill et al., 2018; Kvale et al., 2020). In my cores, I found the most carbonate HEBs in the Wolfcamp A unit. Their high recurrence and degree of amalgamation suggest that my cores' location represent the medial and distal frontal fringe environments of deep-marine lobes in a calciclastic or mixed-siliciclastic submarine fan system (Kane and Pontén, 2012; Spychala et al., 2017; Kvale et al., 2020).

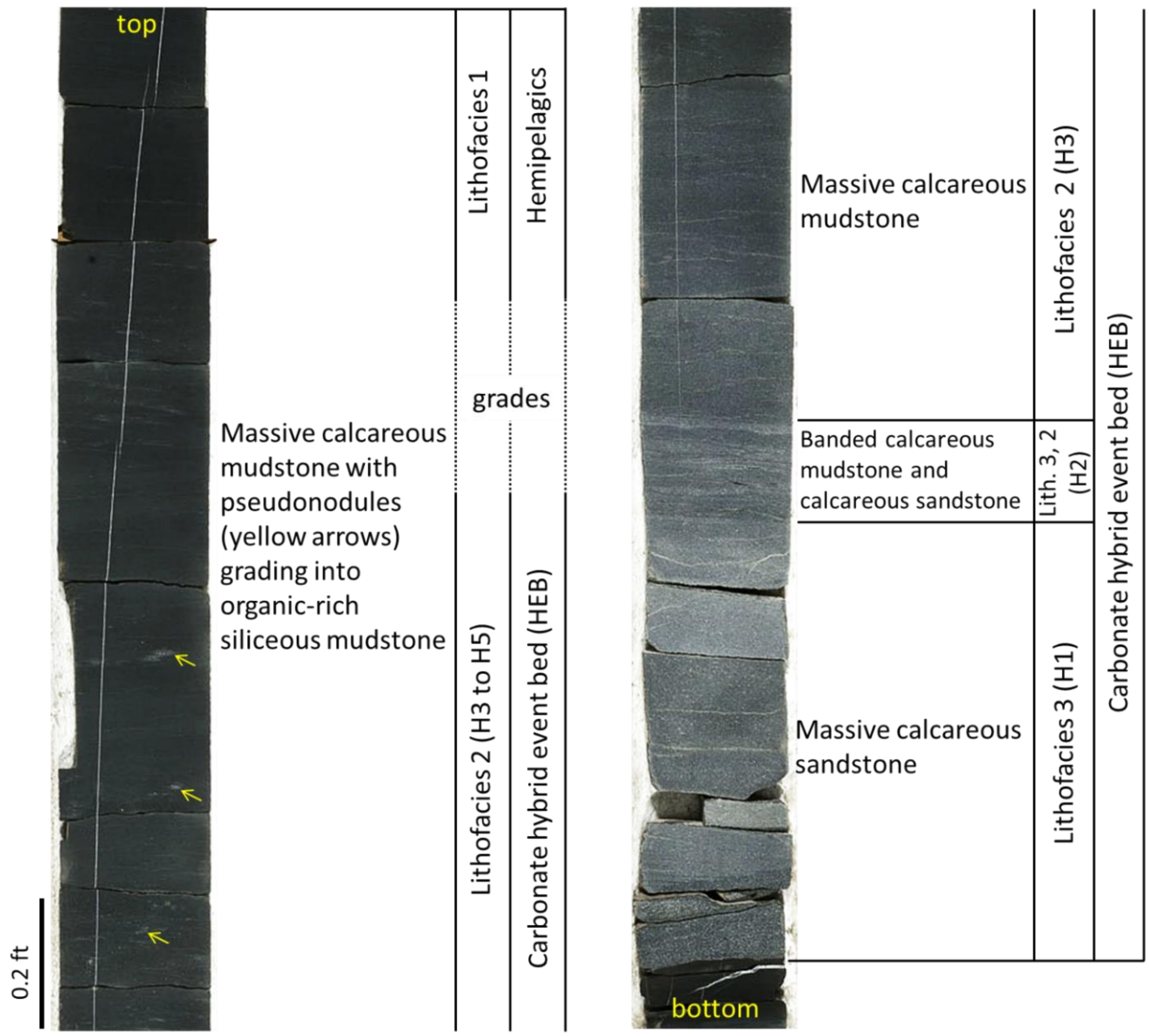

Figure 2.11. Carbonate hybrid event beds.

Core photograph showing carbonate hybrid event bed (HEB) with interpreted features and lithofacies in Wolfcamp A, well S. My interpreted Haughton's (2009) 'H' divisions are in brackets next to the lithofacies number.

Lithofacies 3b, 4b: Dolomitic calcareous mudstone and dolomitic calcareous sandstone

I interpret that the dolomitic calcareous mudstone and the dolomitic calcareous sandstone record dolomitization of the calcareous mudstone and calcareous sandstone lithofacies, respectively. I made this interpretation based on the similarity in texture, microfossils and sedimentary structures observed in thin section and core between the dolomitic and non-dolomitic lithofacies (Figure 2.12). Dolomitization of the carbonate lithofacies may have occurred regionally (e.g., > 10 mi) based on the apparent correlation of individual dolomitized deposits correlate across my three wells (see Chapter 3).

The dolomite in the dolomitic calcareous mudstone and dolomitic calcareous sandstone exhibits both early- and late-diagenetic features. The non-ferroan core of the dolomite crystals indicates that it possibly formed by direct precipitation in the pore space or by replacing calcium carbonate precursors (e.g., micrite) during early-diagenesis (Mazzullo, 2000; Dobber and Goldstein, 2020). The increase in iron content in dolomite crystals (Figure 2.7A) and widespread replacement of carbonate microfossils by iron-rich dolomite is interpreted as late-diagenetic features by several authors (McHargue and Price, 1982; Tucker and Wright, 1990; Flügel, 2013; Dobber and Goldstein, 2020). Hence, I infer the dolomite was geochemically altered and progressively replaced by iron-rich dolomite throughout burial. In addition, the intraparticle pores within dolomite crystals and within dolomitized microfossils indicate that dissolution of the dolomite occurred at some stage during burial.

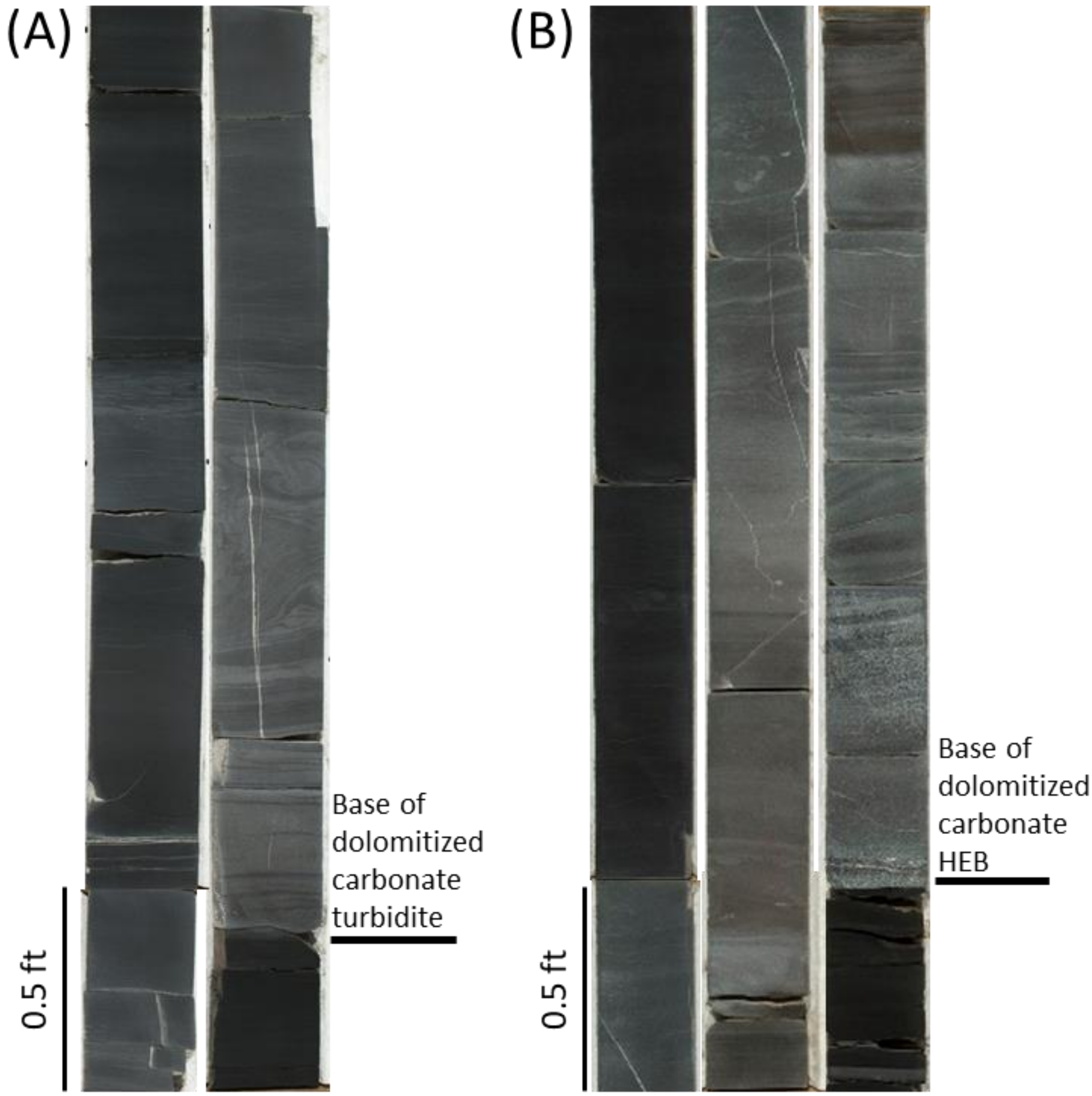

Figure 2.12. Dolomitized carbonate sediment gravity flow deposits.

Plain light core photographs of dolomitized carbonate sediment gravity flow deposits that preserve the original sedimentary structures. (A) Photograph of dolomitized carbonate turbidite. (B) Photograph of dolomitized carbonate HEB. Bottom of the core is in the lower right and the top is in the upper left.

Lithofacies 5: Matrix-supported conglomerate

The matrix-supported conglomerate records deposition from cohesive debris flows based on the non-gradational texture, very poor sorting, lack of sedimentary structures, clay-rich matrix, and sharp top and basal contacts with other lithofacies (Figure 2.13). The co-existence of centimeter-size clasts and sand- to silt-size grains within the same deposit indicates a high degree of cohesiveness of the clay-rich matrix.

Cohesive debrites in my cores probably record shelf-edge collapse episodes due to active faulting or shelf and slope instabilities during sea-level lowstands, and they may have been transported through channels (Payros and Pujalte, 2008; Kvale et al., 2020) prior to deposition.

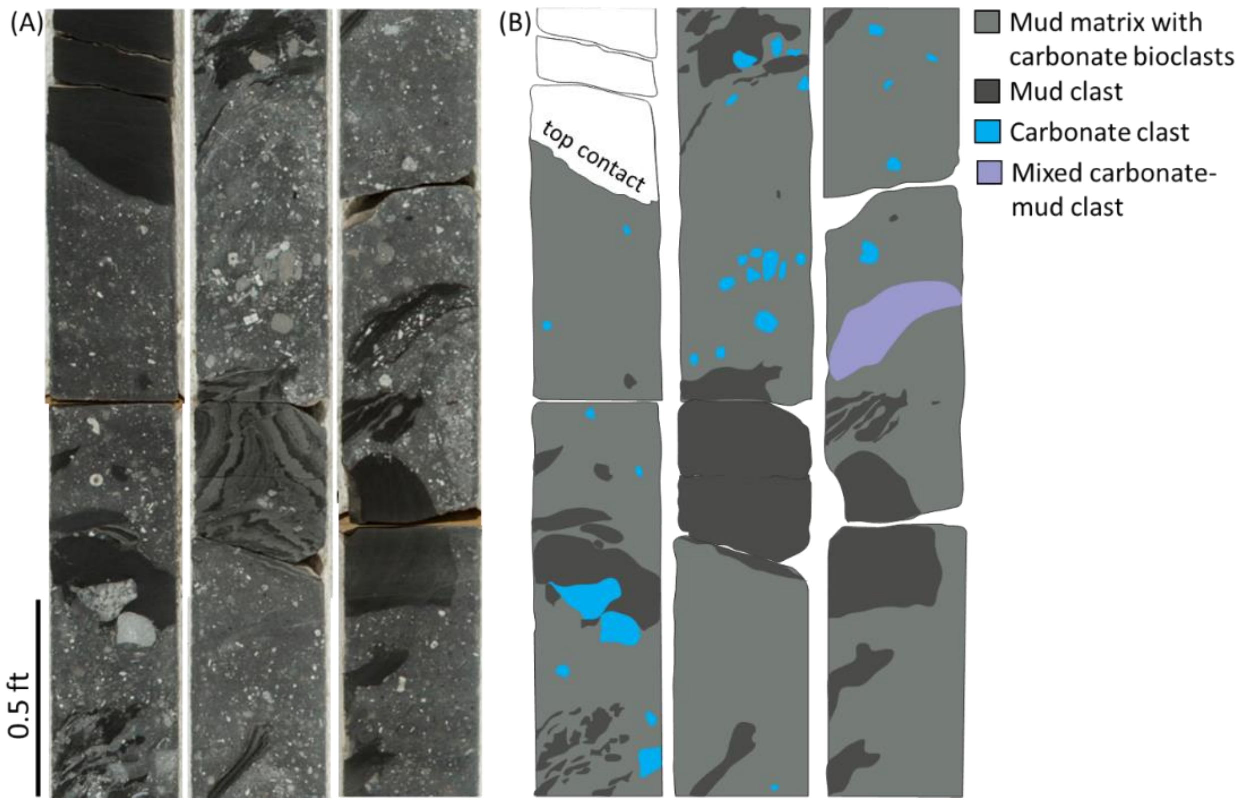

Figure 2.13. Cohesive debrite.

(A) Plain light core photograph of cohesive debrite in Wolfcamp B unit. (B) Schematic of photograph with interpreted features including mud clasts (dark grey), carbonate clasts (blue), and mixed carbonate-mud clasts (violet) floating in a clay-rich matrix (grey). The cohesive debrite is typically in sharp top and bottom contact with organic-rich siliceous silty mudstone lithofacies. I only show the top contact in this figure. Bottom of the core is in the lower right and the top is in the upper left.

Lithofacies 6: Dolomudstone

I interpreted the dolomudstone to record early diagenetic dolomitization of micrite or very fine carbonate debris at or near the seafloor based on its planar texture and low iron content (Tucker and Wright, 1990; Machel, 2004). Petrographically, the dolomite crystals in this lithofacies are similar to the early-burial Rd3 dolomite described by Dobber and Goldstein (2020) in Wolfcamp cores at the Delaware Basin. This early-burial interpretation is may be supported by the presence of rip-up dolomudstone clasts in the upper parts of a cohesive debrite unit (Figure 2.14A); dolomitization may have occurred before the debris flow event and before complete lithification of the seafloor deposits for the dolomudstone clasts to be incorporated into the debris flow (Figure 2.14B). The relatively high clay content in the dolomudstone and its close association with the argillaceous mudstone lithofacies suggest that the dolomudstone probably formed during or immediately after deposition of the siliciclastic turbidites.

This penecontemporaneous dolomite may have been formed through the mediation of microbes (Machel, 2004) as described in the ‘organogenic’ model (Baker and Burns, 1985; Compton, 1988a; Mazzullo, 2000). The dolomudstone has similar characteristics to the organogenic dolomites; they are typically fine crystalline (e.g., <10 µm) nonstoichiometric (e.g., more calcium than magnesium) cements with low iron content because of concurrent pyrite precipitation (Mazzullo, 2000). Their nonstoichiometric nature (calcium surplus) may explain why my XRF-mineral model overestimates the calcite content in the dolomudstone intervals (e.g., Well S, Depth: 12,150 ft, Figure 2.15A) compared to the calcite content measured with XRD (Table 2.1).

2.6.3 Lithofacies distribution in the upper Wolfcamp

Figure 2.15A shows the vertical distribution of lithofacies in the Wolfcamp B unit. The lower part consists of organic-rich siliceous mudstone (hemipelagics) alternating with occasional calcareous mudstones and calcareous sandstones (carbonate turbidites) and rare thin deposits of matrix-supported conglomerates (cohesive debrites). The middle part is primarily composed of organic-rich siliceous mudstone alternating with argillaceous mudstone (siliciclastic fine-grained turbidites) and rare calcareous mudstones and calcareous sandstones. The dolomudstone is interbedded with the argillaceous mudstone. The upper part of the unit contains thick matrix-supported conglomerates alternating with organic-rich siliceous mudstones and rare calcareous mudstone and calcareous sandstones. The majority of the calcareous mudstone and calcareous sandstone lithofacies in the Wolfcamp B unit are dolomitic.

Figure 2.15B shows the vertical distribution of lithofacies in the Wolfcamp A unit. It is composed of calcareous mudstone and calcareous sandstone lithofacies (carbonate hybrid event beds) and organic-rich siliceous mudstone (hemipelagics). Some of the calcareous mudstone and calcareous sandstones are dolomitic.

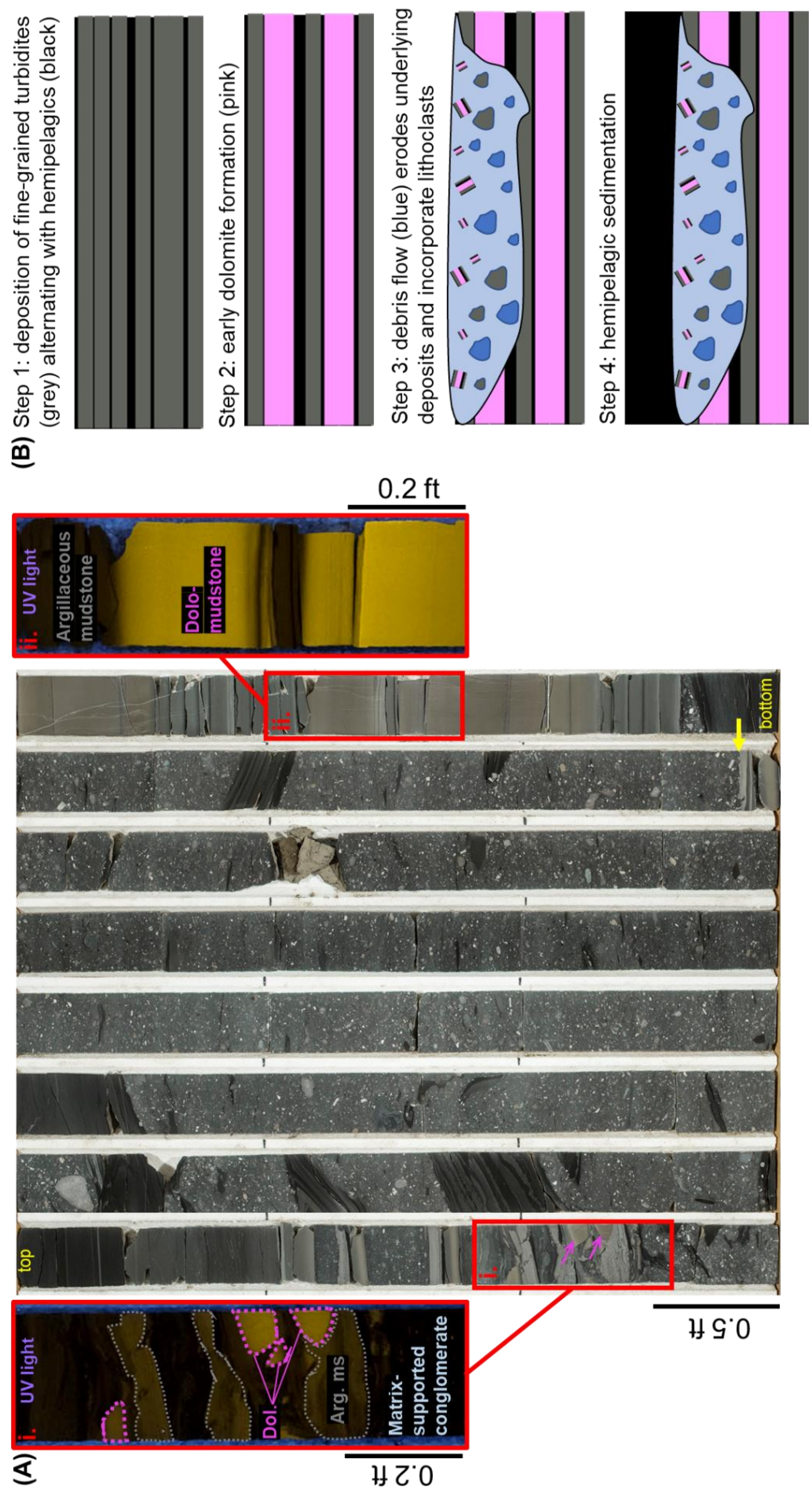

(A)
i.
UV light
Dol.
Arg. ms
Matrix-supported conglomerate
0.2 ft
top
bottom
0.5 ft
ii.
UV light
Argillaceous mudstone
Dolo-mudstone
0.2 ft
(B)
Step 1: deposition of fine-grained turbidites (grey) alternating with hemipelagics (black)
Step 2: early dolomite formation (pink)
Step 3: debris flow (blue) erodes underlying deposits and incorporate lithoclasts
Step 4: hemipelagic sedimentation

Figure 2.14. Evidence of early dolomite formation in the Wolfcamp B unit, Well N.

(A) Plain light photograph showing entire cohesive debrite unit in sharp and erosive bottom contact with siliciclastic turbidite (yellow arrow) and zoomed-in UV light photographs of the areas highlighted in red in the plain light photographs. The argillaceous mudstone is intercalated with dolomudstone layers, which glow under UV light (see zoomed-in image on the top right). The top of the cohesive debrite unit has both dolomudstone and argillaceous mudstone lithoclasts intermixed with the matrix-supported conglomerate (see zoomed-in image on the top left). Bottom of the core is in the lower right and the top is in the upper left. (B) Interpretation of events leading to the presence of dolomudstone clasts in the upper parts of the cohesive debrite in (A).

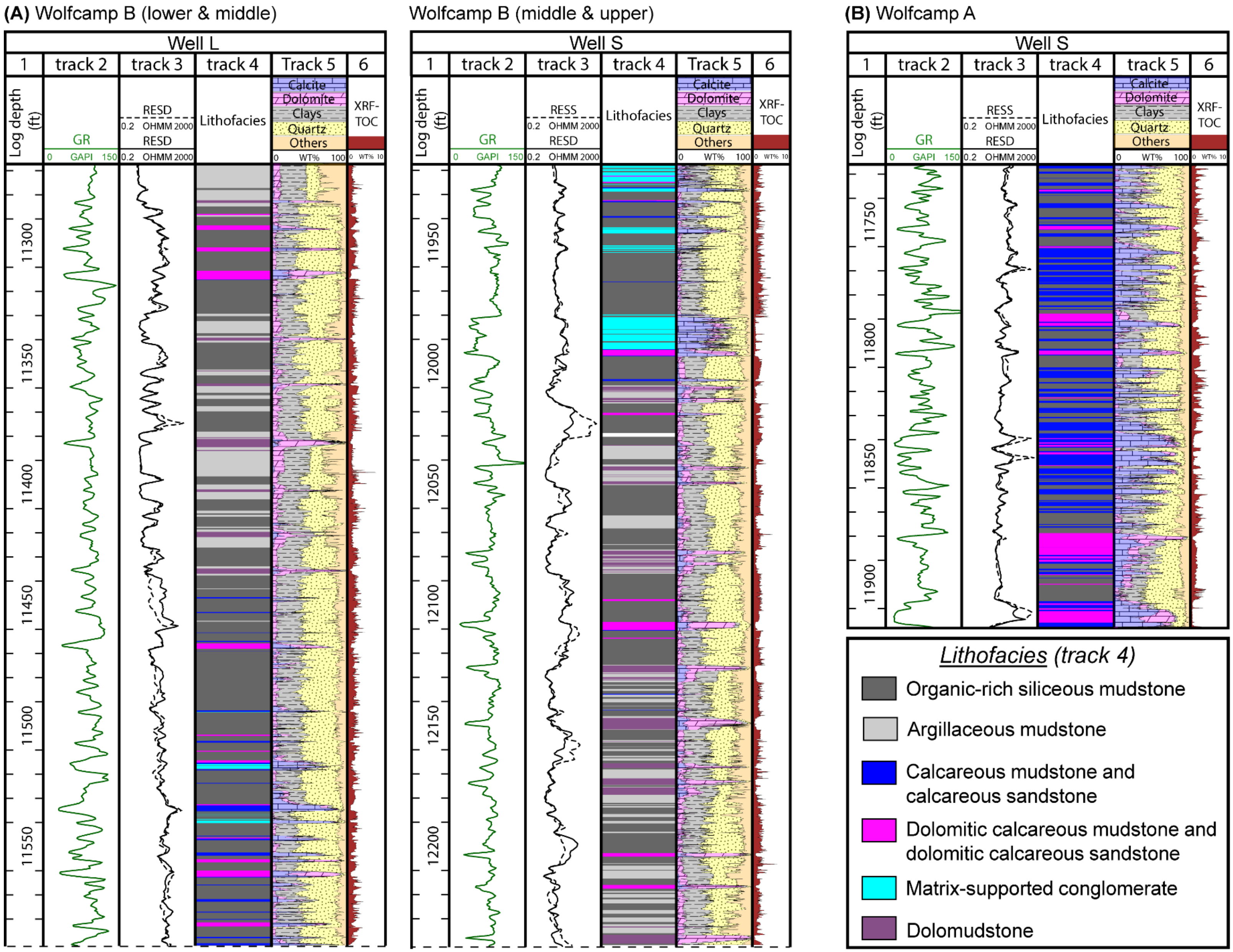
(A) Wolfcamp B (lower & middle)
Well L
Wolfcamp B (middle & upper)
Well S
(B) Wolfcamp A
Well S
1
track 2
track 3
track 4
Track 5
track 5
6
Log depth (ft)
GR
0 GAPI 150
RESD
RESS
0.2 OHMM 2000
RESD
0.2 OHMM 2000
Lithofacies
Calcite
Dolomite
Clays
Quartz
Others
0 WT% 100
XRF-TOC
0 WT% 10
11300
11350
11400
11450
11500
11550
11950
12000
12050
12100
12150
12200
11750
11800
11850
11900
Lithofacies (track 4)
Organic-rich siliceous mudstone
Argillaceous mudstone
Calcareous mudstone and calcareous sandstone
Dolomitic calcareous mudstone and dolomitic calcareous sandstone
Matrix-supported conglomerate
Dolomudstone

Figure 2.15. Vertical distribution of lithofacies.

(A) (left) Distribution of lithofacies in the lower-to-middle Wolfcamp B unit, Well L, and (right) distribution of lithofacies in the middle-to-upper Wolfcamp B, Well S. (B) Distribution of lithofacies in the Wolfcamp A unit, Well S. Both the calcareous mudstone and calcareous sandstone lithofacies are represented by the same blue color because they are typically in gradational contact and their boundary is difficult to define at the scale of this figure. The cored intervals in each well are represented in Figure 2.2. Track 1: Log depth; track 2: gamma-ray; track 3: deep resistivity (solid line) and shallow resistivity (dashed line); track 4: interpreted lithofacies in core; track 5: modeled mineralogy from XRF elemental data; track 6: modeled TOC content from XRF elemental data.

2.6.4 Lithofacies electric log response

The organic-rich siliceous mudstone and the argillaceous mudstone lithofacies have similar gamma-ray and bulk density values (track 2 and track 7, Figure 2.16A). However, the argillaceous mudstone has lower resistivity and higher neutron porosity than the organic-rich siliceous mudstone (track 3 and track 7, Figure 2.16A). The lower resistivity of the argillaceous mudstone may result from its lower fraction of organic matter (track 6, Figure 2.16A), and possibly a higher water saturation. The higher neutron porosity values in the argillaceous mudstone may be due to its higher clay content (Ellis and Singer, 2007). In high-frequency successions of these two mudstones, the wireline log records the physical properties of the argillaceous mudstone because the organic-rich siliceous mudstone layers are too thin (< 1 in.) to be distinguished by logs. The dolomudstone lithofacies has a sharply higher gamma-ray and bulk density and lower neutron porosity response than the argillaceous mudstone (Figure 2.16A).

The calcareous mudstone and calcareous sandstone lithofacies have lower gamma-ray, higher bulk density and lower neutron porosity than the organic-rich siliceous mudstone (track 2 and track 7, Figure 2.16B). In the Wolfcamp B, the dolomitic calcareous mudstone and dolomitic calcareous sandstone sub-lithofacies may exhibit a slightly higher bulk density and faster compressional and shear wave travel times than their non-dolomitic counterparts. However, these dolomitic sub-lithofacies are more difficult to define in the Wolfcamp A unit because it is richer in carbonates. Compared to the dolomudstone, the dolomitic calcareous mudstone and dolomitic calcareous sandstone have higher resistivity and slightly lower neutron porosity values (Figure 2.16A).

Lastly, the matrix supported conglomerate lithofacies has a similar wireline log response as the calcareous mudstone and calcareous sandstone lithofacies. However, it shows a characteristic cylinder-shaped pattern in the gamma-ray (e.g., Well S, Depth: 11,990 ft, Figure 2.15A) and sonic curves when it forms thick deposits (e.g., over 10 ft thick). This cylinder-shaped pattern may be due to both the sharp top and bottom contacts with the organic-rich siliceous mudstone lithofacies and the non-graded texture.

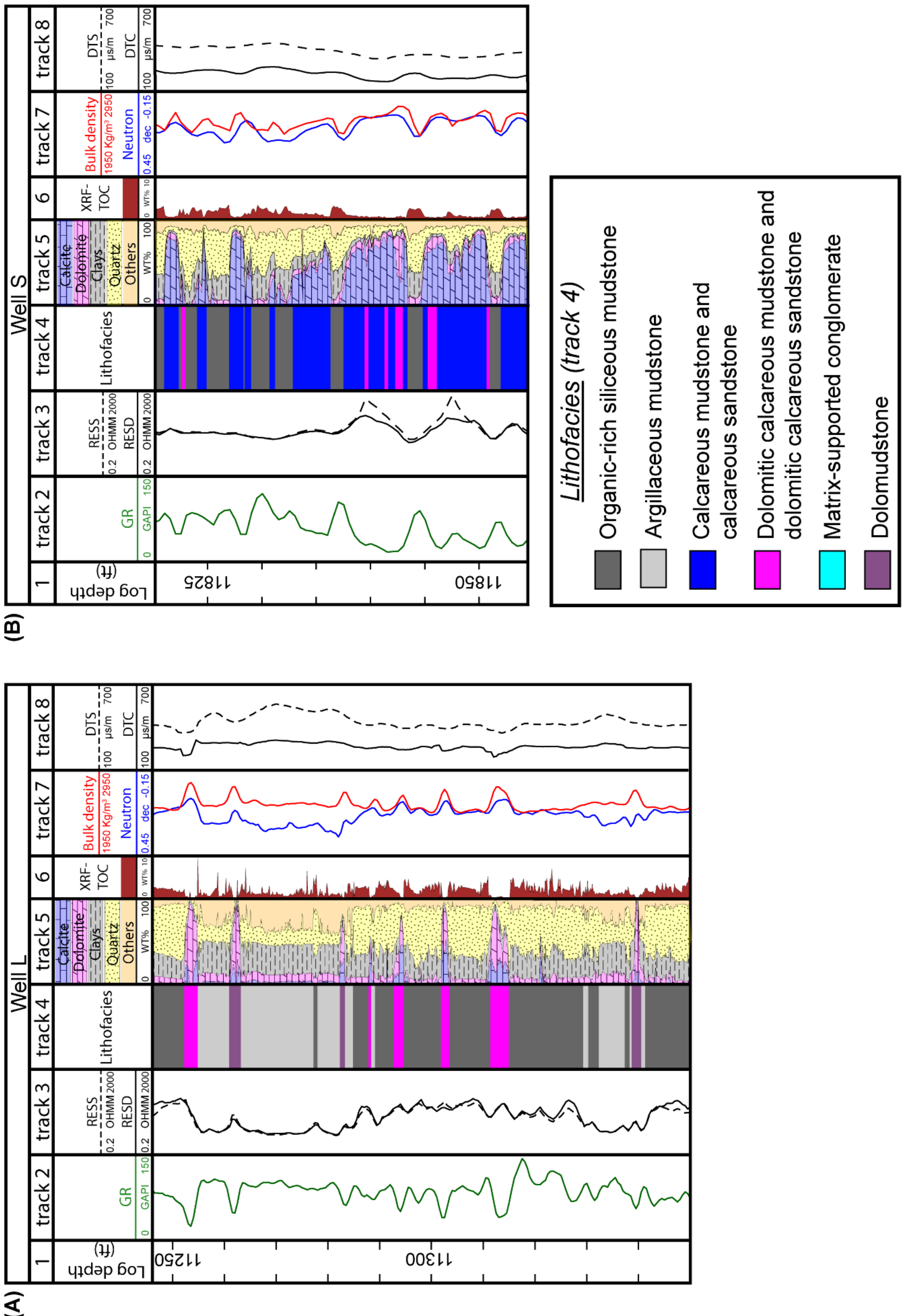
(A)
Well L
(B)
Well S
track 1
Log depth (ft)
track 2
GR
0 GAPI 150
track 3
RESS
0.2 OHMM 2000
RESD
0.2 OHMM 2000
track 4
Lithofacies
track 5
Calcite
Dolomite
Clays
Quartz
Others
0 WT% 100
6
XRF-TOC
0 WT% 10
track 7
Bulk density
1950 Kg/m³ 2950
Neutron
0.45 dec -0.15
track 8
DTS
100 μs/m 700
DTC
100 μs/m 700
11250
11300
11825
11850
Lithofacies (track 4)
Organic-rich siliceous mudstone
Argillaceous mudstone
Calcareous mudstone and calcareous sandstone
Dolomitic calcareous mudstone and dolomitic calcareous sandstone
Matrix-supported conglomerate
Dolomudstone

Figure 2.16. Detailed view of lithofacies distribution.

(A) Detailed view of lithofacies distribution in depth interval of the Wolfcamp B unit, Well L. (B) Expanded view of lithofacies distribution in depth interval of the Wolfcamp A unit, Well S. Track 1: Log depth; track 2: gamma-ray; track 3: deep resistivity (solid line) and shallow resistivity (dashed line); track 4: interpreted lithofacies in core; track 5: modeled mineralogy from XRF elemental data; track 6: modeled TOC content from XRF elemental data; track 7: bulk density (red) and neutron porosity (blue); track 8: compressional sonic slowness (solid line) and shear sonic slowness (dashed line).

2.7 DISCUSSION

2.7.1 Depositional model for Wolfcamp B and Wolfcamp A

Background hemipelagic sedimentation deposited the organic-rich siliceous mudstone pervasively during deposition of both the Wolfcamp B and the Wolfcamp A units. Concurrently, sediment gravity flows (Figure 2.17), sourced from uplifted areas adjacent to the Delaware Basin, interrupted hemipelagic sedimentation. In the Wolfcamp B unit, recurrent siliciclastic turbidites resulted in the accumulation of the argillaceous mudstone, and occasional carbonate turbidites and cohesive debrites resulted in the accumulation of the calcareous mudstone and calcareous sandstone, and matrix-supported conglomerate, respectively. In contrast, the main flow deposits in the Wolfcamp A unit are carbonate hybrid event beds (HEBs), recorded by the calcareous mudstone and calcareous sandstone lithofacies.

After deposition of the siliciclastic turbidites and the carbonate turbidites, dolomite started to precipitate in their pore spaces. In the carbonate turbidites, dolomite also replaced the calcium carbonate bioclasts and micritic matrix. Throughout burial, the permeability of the dolomitic carbonate turbidites was sufficiently preserved for subsurface fluids to circulate through the rock. These fluids altered the composition of the early dolomite and also formed intraparticle pores within dolomite crystals and within dolomitized microfossils.

2.7.2 Paleogeography

The fine-grained turbidites are dominated by siliciclastic sediments and they are the most frequent flow deposit in the Wolfcamp B unit; these were most likely sourced from an area capable of producing siliciclastic sediments in large quantities. I infer that the Marathon thrust area is a probable source for these turbidites (Figure 2.17), based on previous studies indicating that siliciclastic sediments in Permian deposits likely had their origin in the Delaware Basin's southern areas (Hickman et al., 2009; Soreghan and Soreghan, 2013; Xie et al., 2019; Liu and Stockli, 2020; Soto-Kerans et al., 2020).

In contrast, I interpret the carbonate turbidites and carbonate HEBs to be sourced from a different area. The high carbonate fossil content in these deposits suggest that carbonate platforms with shallow water fauna are probable sources. During Wolfcamp B deposition (late Wolfcampian), the Northwestern Shelf and the Diablo Platform probably were the only carbonate platforms that were adjacent to the Delaware Basin (Frenzel et al., 1988; Fu et al., 2020). Most of the Central Basin Platform's western wedge was an emergent part of the uplift during all of Wolfcampian time (Frenzel et al., 1988), although it became a carbonate platform during the Leonardian time (Ruppel, 2020). Hence, I hypothesize that the Wolfcamp B's carbonate turbidites were sourced from Northwestern Shelf or the Diablo Platform, whereas the Northwestern Shelf or the Central Basin Platform were the most likely sources for the Wolfcamp A's carbonate HEBs (Figure 2.17). The cohesive debrites in the Wolfcamp B contain similar fossils to those found in the carbonate turbidites, suggesting that they were also sourced either from the Northwestern Shelf or the Diablo Platform (Figure 2.17). The existing correlations of Wolfcamp A's carbonate deposits nearby my study area (Kvale et al., 2020) also indicate that carbonate deposits in this unit were likely sourced from the northeast. However, given the data available, it is also possible that the Diablo Platform and the southern Delaware Basin were possible source areas for the carbonate deposits in the Wolfcamp A unit.

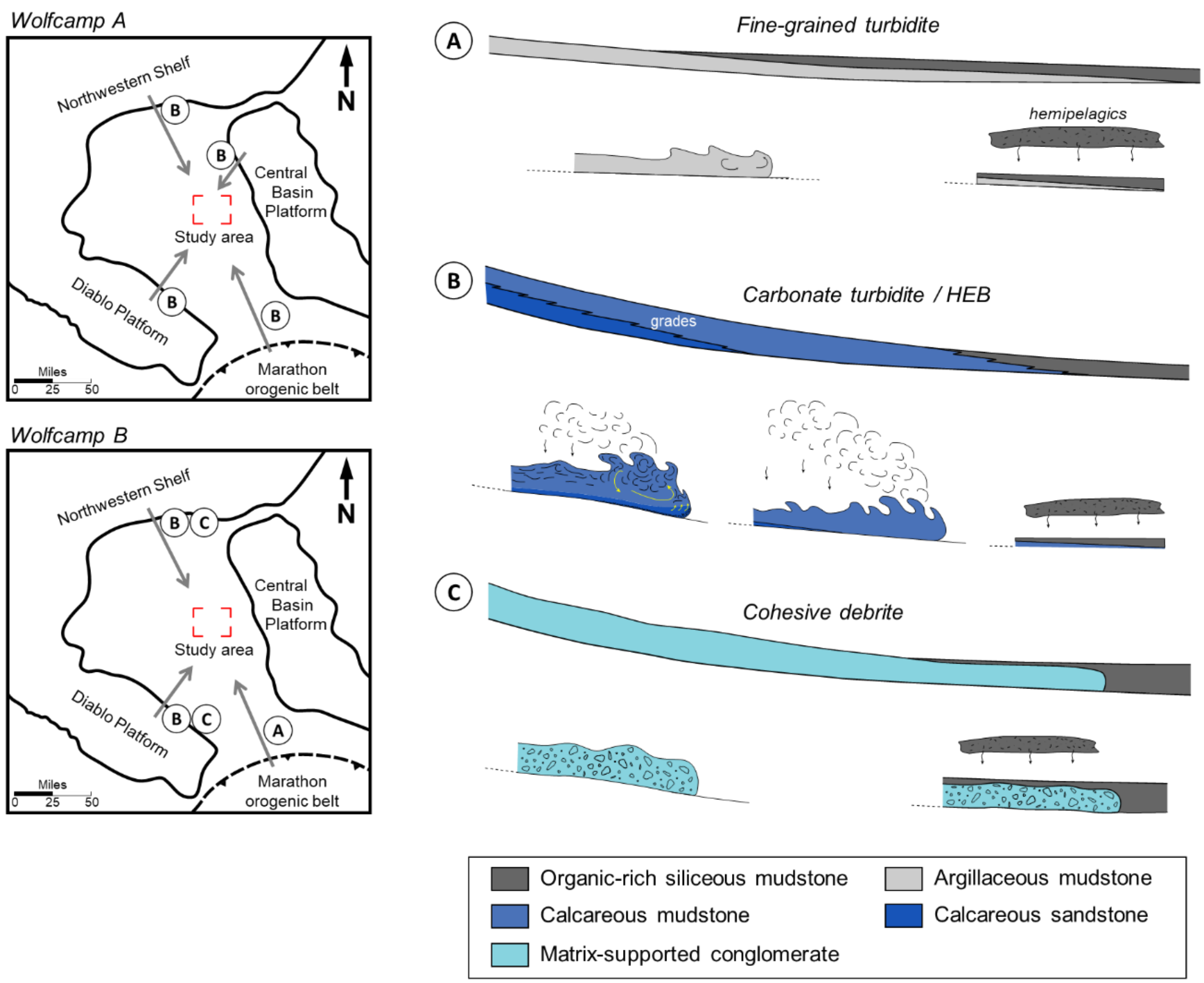

Figure 2.17. Schematic of the Delaware Basin showing possible source areas for the flow deposits found in my cores during the accumulation of the Wolfcamp B and Wolfcamp A units.

Fine grained turbidites (A), carbonate turbidites and carbonate hybrid event beds (HEBs) (B), and cohesive debrites were accumulated by separate flow events. Hemipelagic sedimentation occurs after deposition or contemporaneous with it.

2.7.3 Stratigraphic architecture

The lower Wolfcamp B (Figure 2.18A) is characterized by thick (up to 27 ft) (~8 m) and laterally continuous deposits of organic rich siliceous mudstones that alternate with sporadic thin (< 5 ft.) (~1.5 m) dolomitic calcareous mudstones and dolomitic calcareous sandstones, and rare matrix-supported conglomerates. This records the interplay between carbonate turbidite flows and occasional debris flows and hemipelagic sedimentation. Most carbonate turbidites in this interval are dolomitized, and they are correlative between wells. In contrast, the matrix-supported conglomerates are laterally discontinuous and very thin (< 1 ft) (~0.3 m).

In the middle-to-upper Wolfcamp B (Figure 2.18A), laterally continuous argillaceous mudstone alternates with thin (e.g., < 1 in.) (~2.54 cm) organic-rich siliceous mudstones, forming high-frequency sequences up to 20 ft (~6 m) thick (Figure 2.19). Laterally continuous dolomudstone occurs as thin layers (< 3 ft. thick) (~1 m) within these sequences (Figure 2.19). The dolomitic calcareous mudstone and dolomitic calcareous sandstone are less frequent in this Wolfcamp B interval and they are mostly interbedded with the organic-rich siliceous mudstone. The matrix-supported conglomerate in the upper ~ 200 ft (~60 m) of the Wolfcamp B unit in Well S and Well N forms laterally discontinuous, thick deposits (up to 15 ft) (~5 m) intercalated with organic-rich siliceous mudstone. This succession records cohesive debris flows that originated by destabilization of the carbonate platform edges, and return to hemipelagic sedimentation after deposition.

The Wolfcamp A unit contains thicker (up to 8 ft) (~2.5 m) and more frequent calcareous mudstone and calcareous sandstone deposits (Figure 2.18B) compared to the Wolfcamp B (Figure 2.18A). Many of these deposits are dolomitic, and they either alternate with organic-rich siliceous mudstone or are amalgamated (Figure 2.20).

Organic-rich siliceous mudstone recording hemipelagic deposition make up 50% or more of the thickness in both the Wolfcamp A and Wolfcamp B (Figure 2.18B). In addition, argillaceous mudstone, which records fine-grained turbidite deposition, is responsible for 20% of the Wolfcamp B but is not present in the Wolfcamp A. In contrast, only about 5% of the Wolfcamp B is composed of calcareous mudstone or sandstone, whereas approximately 50% of the Wolfcamp A is composed of this lithofacies.

As described in Chapter 3, the organic rich siliceous mudstone contains both the majority of the pore volume and the majority of the liquid hydrocarbons in the field area. As a result, this is thought to be the major reservoir for hydrocarbons. In contrast, the argillaceous mudstone is both very low permeability and contains a very high water saturation. In Chapter 3, I describe how the calcareous mudstone and sandstone lithofacies can have much higher permeability than the organic-rich siliceous mudstone and propose that these beds act as carrier beds during production.

2.7.4 Dolomite-bearing intervals

The dolomudstone and dolomitized carbonate flow deposits occur every 20 ft (~6 m) to 30 ft (~9 m) apart in the Wolfcamp B unit, although in some cases they may occur every 5 ft (~1.5 m). The relatively constant frequency of these dolomitic deposits and their apparent lateral correlation between wells suggests that dolomite formation may record a field-to-basin wide cyclicity, such as sea-level fluctuations or climatic cycles (e.g., glacial, interglacial) that condition oceanic circulations. Cycles marked by dolomitic horizons were also found in the Pennsylvanian Wolfcamp D unit of the Midland Basin (McGlue et al., 2015; Reis et al., 2019), or in the Monterrey Formation of the Santa Maria basin (Compton, 1988b). Dolomitic intervals also occur in the Wolfcamp A unit, but they do not exhibit any type of cyclicity.

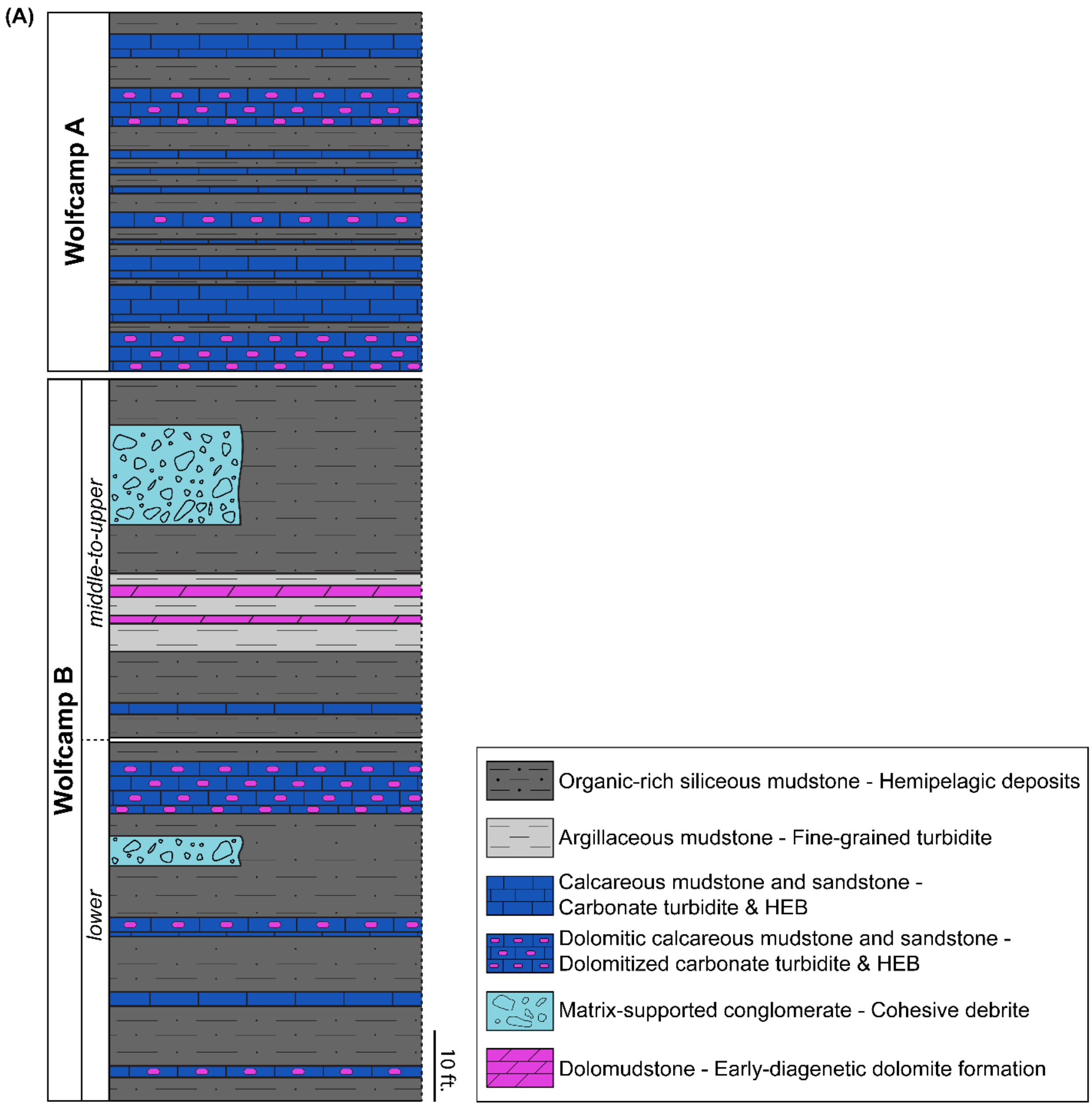
(A)
Wolfcamp A
Wolfcamp B
middle-to-upper
lower
10 ft.
Organic-rich siliceous mudstone - Hemipelagic deposits
Argillaceous mudstone - Fine-grained turbidite
Calcareous mudstone and sandstone - Carbonate turbidite & HEB
Dolomitic calcareous mudstone and sandstone - Dolomitized carbonate turbidite & HEB
Matrix-supported conglomerate - Cohesive debrite
Dolomudstone - Early-diagenetic dolomite formation

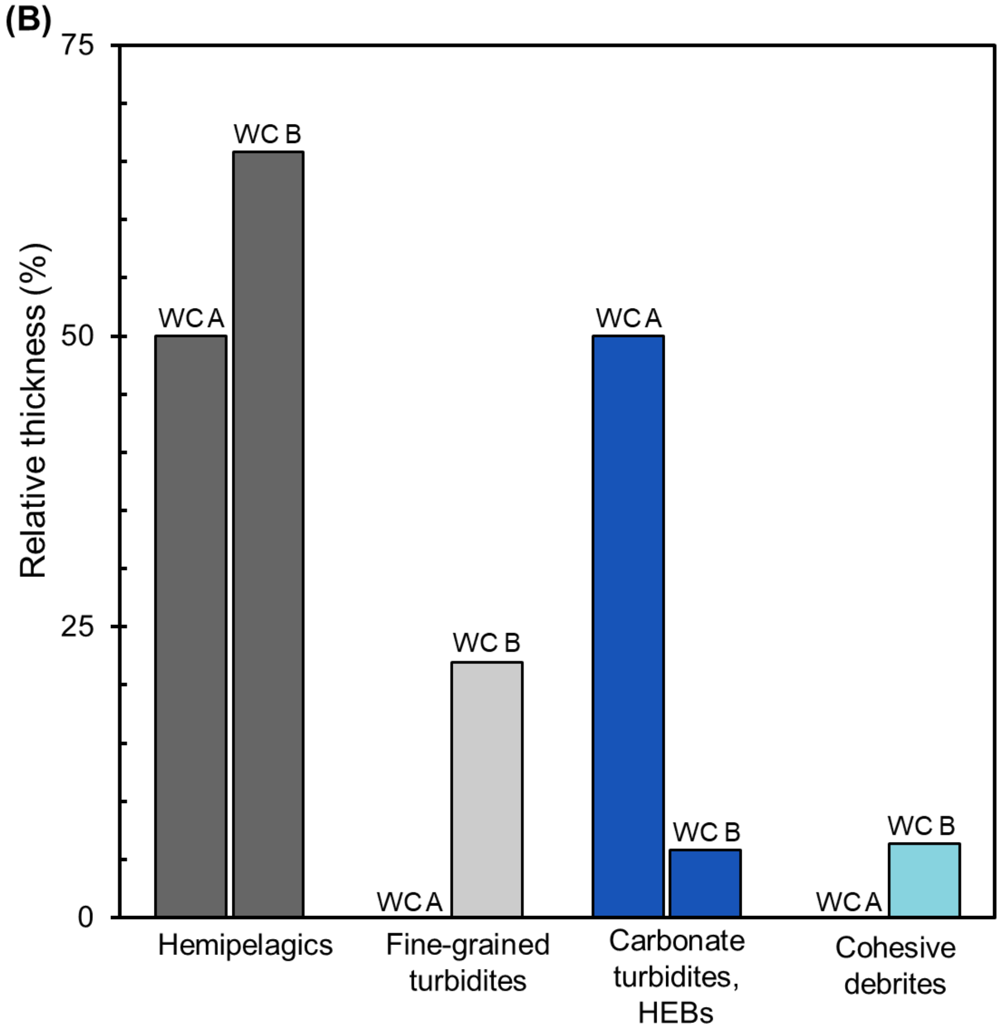

Figure 2.18. Characteristic stratigraphy in upper Wolfcamp interval and relative thickness of deposits.

(A) Characteristic stratigraphic architecture of the Wolfcamp A (left), middle-to-upper section of the Wolfcamp B (middle) and lower section of Wolfcamp B (right). The carbonate turbidites in the Wolfcamp B are typically dolomitized, whereas the carbonate hybrid event beds are dolomitized only in some instances. (B) Bar chart showing the relative thickness of hemipelagics and interpreted flow deposits in the Wolfcamp A (WC A) and Wolfcamp B (WC B) units based on non-overlapping cored intervals (Figure 2.3) in the three wells.

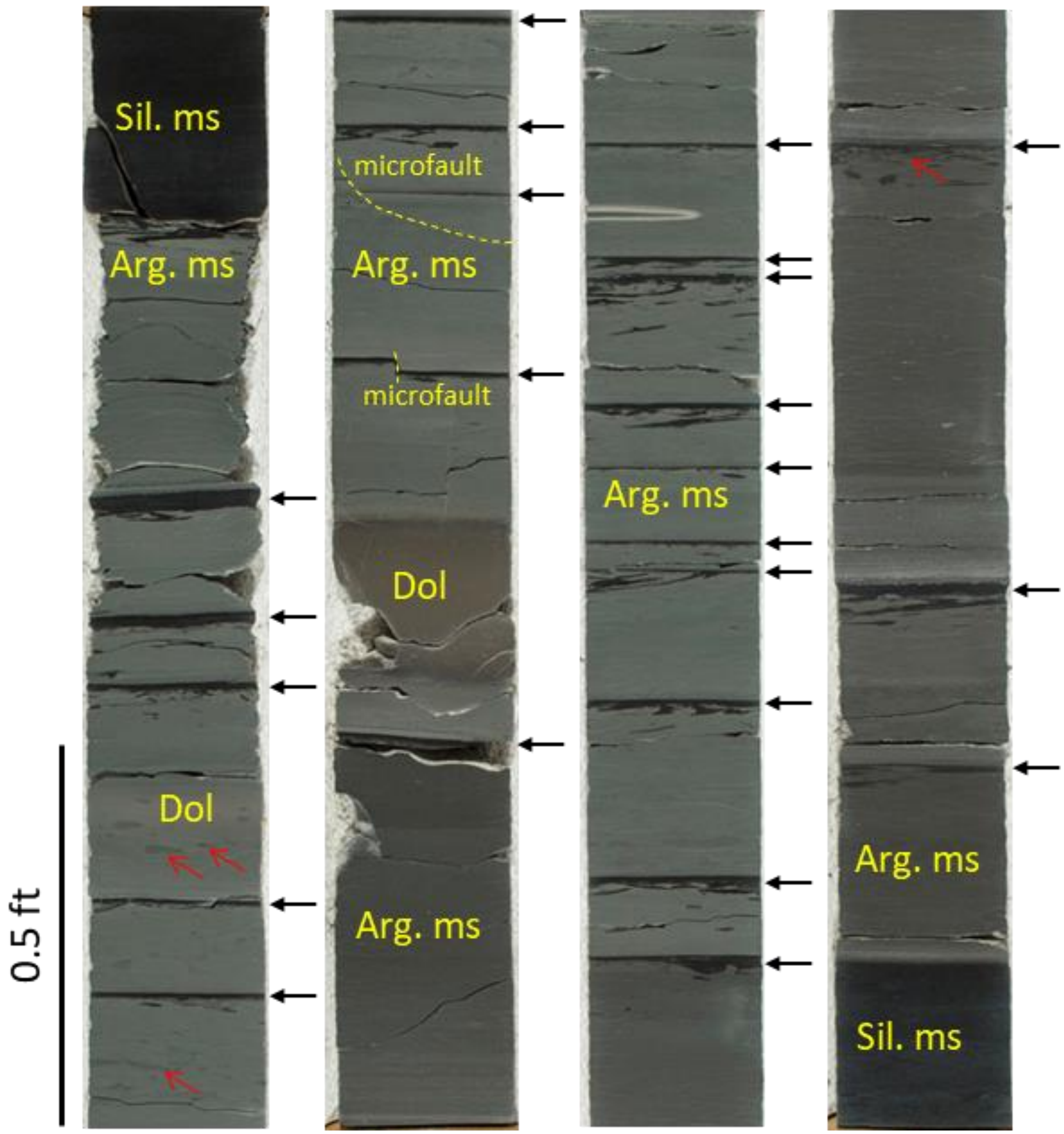

Figure 2.19. Succession of siliciclastic fine-grained turbidites alternating with hemipelagic deposits.

Plain light core photograph showing high-frequency succession of siliciclastic turbidites (argillaceous mudstone, light grey to greenish color, Arg. ms) alternating with much thinner layers of hemipelagic deposits (organic-rich siliceous silty mudstone, black color, Sil. ms) in the Wolfcamp B unit, well N. Black arrows point to thin hemipelagic deposits. Dolomitic intervals (dolomudstone, tanned color, Dol) are common in this type of succession. Red arrows indicate examples of bioturbation. Bottom of the core is in the lower right and the top is in the upper left.

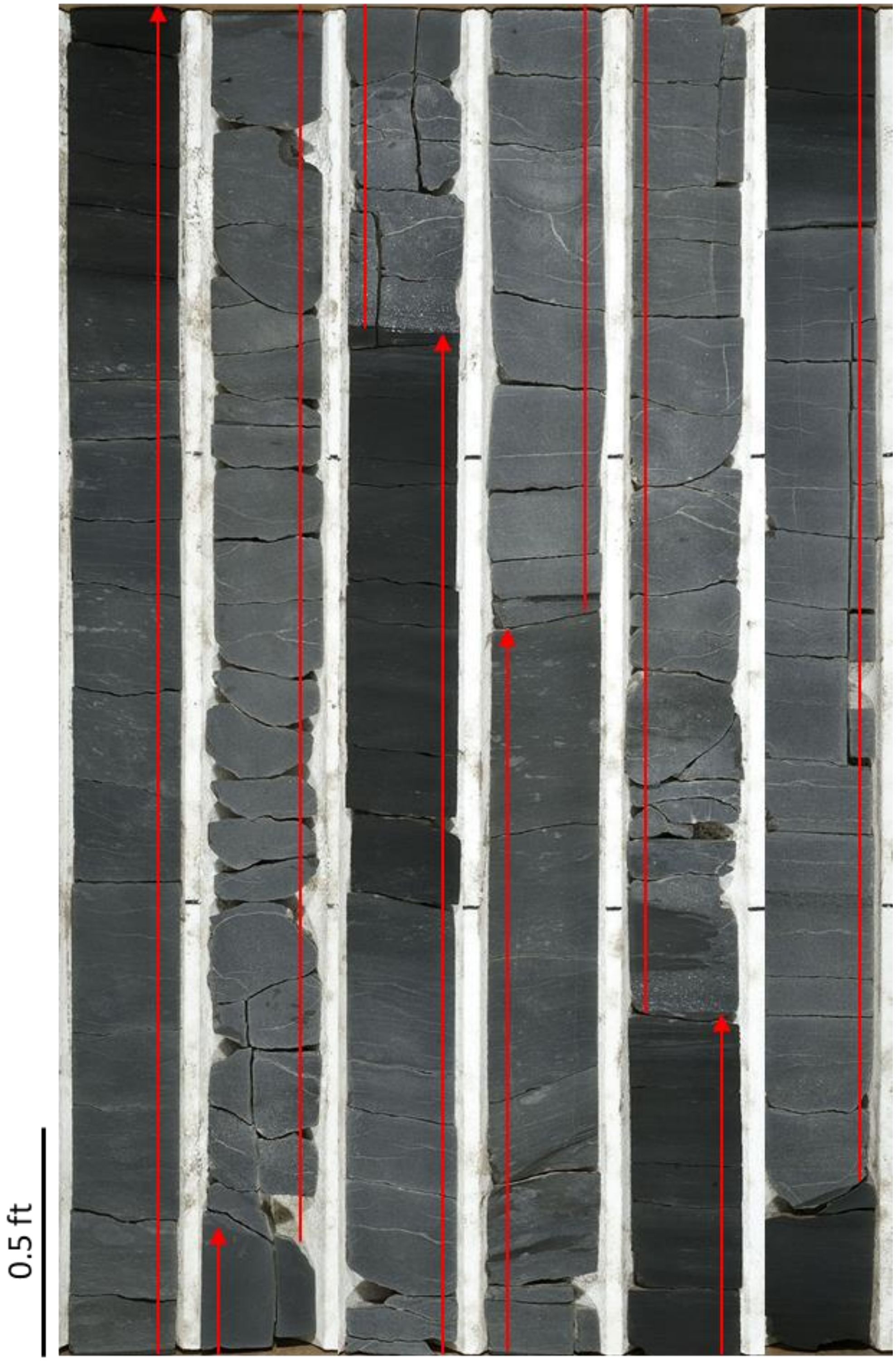

Figure 2.20. Amalgamated carbonate hybrid event beds.

Example of interpreted carbonate hybrid event beds (HEBs) exhibiting certain degree of amalgamation in the Wolfcamp A, Well S. Red arrows indicate single HEBs. Bottom of the core is in the lower right and the top is in the upper left.

2.8 CONCLUSIONS

I defined six lithofacies in three upper Wolfcamp cores recovered in the central-eastern Delaware Basin based on core observations integrated with geochemical rock analyses and thin section petrography. Both the Wolfcamp B (late Wolfcampian) and Wolfcamp A (early Leonardian) units are composed of 50% or more of the thickness of organic-rich siliceous mudstone lithofacies, that I interpreted to record suspension settling of hemipelagic sediments. This hemipelagic sedimentation was interrupted periodically by diverse kinds of siliciclastic and calciclastic sediment gravity flows sourced from uplifted areas adjacent to the Delaware Basin.

The Wolfcamp B unit (late Wolfcampian) is dominated by organic-rich siliceous mudstones (66%) and frequent clay-rich and organically poor argillaceous mudstones (22%) that I interpreted as siliciclastic turbidites. The calcareous mudstone and sandstone lithofacies, interpreted as carbonate turbidites, occur occasionally throughout this unit (6%). The matrix-supported conglomerates, interpreted as cohesive debrites, are rare (6%) and occur mostly in the uppermost part of the section. In contrast, the Wolfcamp A is composed mostly of organic-rich siliceous mudstones (50%) alternating with calcareous mudstones and sandstones (50%), that I interpreted as carbonate hybrid event beds.

Pervasive diagenesis occurred in the study area based on the presence of recurrent dolomitic intervals in both Wolfcamp units. These intervals are either a) the dolomudstone lithofacies, that I interpreted was formed immediately after deposition of the siliciclastic fine-grained turbidite, or b) the dolomitic calcareous mudstone and dolomitic calcareous sandstone lithofacies, interpreted to be formed by dolomitization of carbonate turbidites and hybrid event beds throughout burial. Permeability studies in the Wolfcamp indicate that these dolomitized carbonate flow deposits act as carrier beds during production.

ACKNOWLEDGEMENTS

I thank Shell for funding this research under the SUTUR (Shell-UT Unconventional Research) agreement. I am grateful to Dr. Robert Dombrowski and Dr. Ronny Hofmann for guidance and fruitful discussions, and Brian Driskill and Adenike Tokan-Lawal for their technical and logistical support throughout this project. I also thank Equinor for providing additional funding for this research under the University of Texas - Equinor Fellows Program. Discussions regarding Wolfcamp geology and depositional processes in the Permian Basin with Dr. Xavier Janson and Buddy Price were especially useful. I also thank Dr. Robert Reed for providing the SEM images and Evan Sivil for conducting the XRF measurements of the cores. I am also grateful to Dr. Eric Prokocki for discussions regarding depositional processes.

APPENDIX 2.A

Mineral model

I estimate the mineral contents based on the stoichiometric relationships or molar ratios between elements within the same mineral formula. Based on that relationship between elements, I use the XRF-elemental composition of the core to estimate the content of each mineral. In my model, I estimate the contents of dolomite, calcite, illite, and quartz.

I estimated the dolomite content with Eq. 2.A1. The molar ratio of magnesium in dolomite is $Mg/CaMg(CO_3)_2$ equals 13.19 % assuming a Ca:Mg ratio of 50:50. Thus the weight percent of dolomite is:

$$Dolomite = \frac{Mg_{measured\ with\ XRF\ (\%)}}{13.19} x100 \qquad \text{Eq. 2.A1}$$

The molar ratio of calcium in dolomite is $Ca/CaMg(CO_3)_2 = 21.74$ %. Therefore, the weight percent of calcium is determined with Eq. 2.A2:

$$Ca_{in\ dolomite} = \frac{XRF\ estimated\ dolomite\ (\%)\ x\ 21.74}{100} \qquad \text{Eq. 2.A2}$$

To estimate the weight percent of calcite, I subtracted the calcium present in the dolomite from the total calcium measured with XRF, where the molar ratio of Ca in calcite ($Ca{:}CaCO_3$) is 40 % (Eq. 2.A3):

$$Calcite \ = \frac{Ca_{\,measured\ with\ XRF\ (\%)} - Ca_{\,in\ dolomite\ (\%)}}{40} x100 \qquad \text{Eq. 2.A3}$$

I assume that all clays are illite because the XRD analyses indicate only minor contents in illite-smectite mixed-layer (average ~4 wt.%) and chlorite (average ~ 3 wt.%). The aluminum molar ratio in the illite formula presented by (Rieder et al., 1998) is $Al/K_{0.65}Al_{2.0}(Al_{0.65}\,Si_{3.35}\,O_{10})(OH)_2$ = 18.60 %. Thus, the weight percent of illite is calculated with Eq. 2.A4:

$$Illite = \frac{Al_{\,measured\ with\ XRF\ (\%)}}{18.60} x100 \qquad \text{Eq. 2.A4}$$

I calculate the amount of silicon in the illite in Eq. 2.A5, assuming a molar ratio of silicon in illite of $Si/K_{0.65}Al_{2.0}(Al_{0.65}\,Si_{3.35}\,O_{10})(OH)_2$ = 24.44 %.

$$Si_{\,in\ illite} = \frac{XRF\ estimated\ illite\ (\%)\ x\ 24.44}{100} \qquad \text{Eq. 2.A5}$$

I subtract the silicon in the illite from the total measured with XRF to estimate quartz content using Eq. 2.A6. The denominator corresponds to the Si in the quartz formula, which is Si/SiO_2 = 46.70 %:

$$Quartz \ = \frac{Si_{\,measured\ with\ XRF\ (\%)} - Si_{\,in\ XRF\ estimated\ illite\ (\%)}}{46.70} x100 \qquad \text{Eq. 2.A6}$$

In my calculations, I used the following atomic masses: H = 1.01 u; C = 12.01 u; O = 16.00 u; Mg = 24.305 u; Al = 26.98 u; Si = 28.08 u; K = 39.10 u; and Ca = 40.08 u.

Figure 2.A1 shows the correlation between the XRF-modeled mineralogy and the XRD-determined mineralogy for each mineral. The XRF-modeled dolomite shows the highest correlation coefficient (R^2) with the XRD-measured dolomite amongst all four minerals (R^2 = 0.82,

Figure 2.A1A). XRF-modeled calcite (Figure 2.A1B) and quartz (Figure 2.A1D) also exhibit a relatively strong correlation with their corresponding XRD-determined mineralogy (R^2 = 0.79), whereas illite has the weakest correlation (R^2 = 0.62, Figure 2.A1C). Thus, my XRF-modeled illite tends to underestimate the illite content in intervals where the XRD-measured illite is very high (e.g., 11380-11410 ft, Figure 2.4). The underestimation of the illite content with my model could be due to: (a) the XRD-determined mineralogy is higher than XRF-modeled illite because it includes not only illite but also illite-smectite mixed layer, chlorite, and micas, (b) the stoichiometric relationship between elements in the illite mineral equation that I used is such that it underestimates illite content, or (c) the XRD-determined mineralogy overestimated the illite content.

Despite these discrepancies between XRF-modeled mineralogy and XRD-determined mineralogy, I consider that my XRF-modeled mineral contents provide an acceptable estimation of the bulk mineralogic composition of the core at each XRF-scan point.

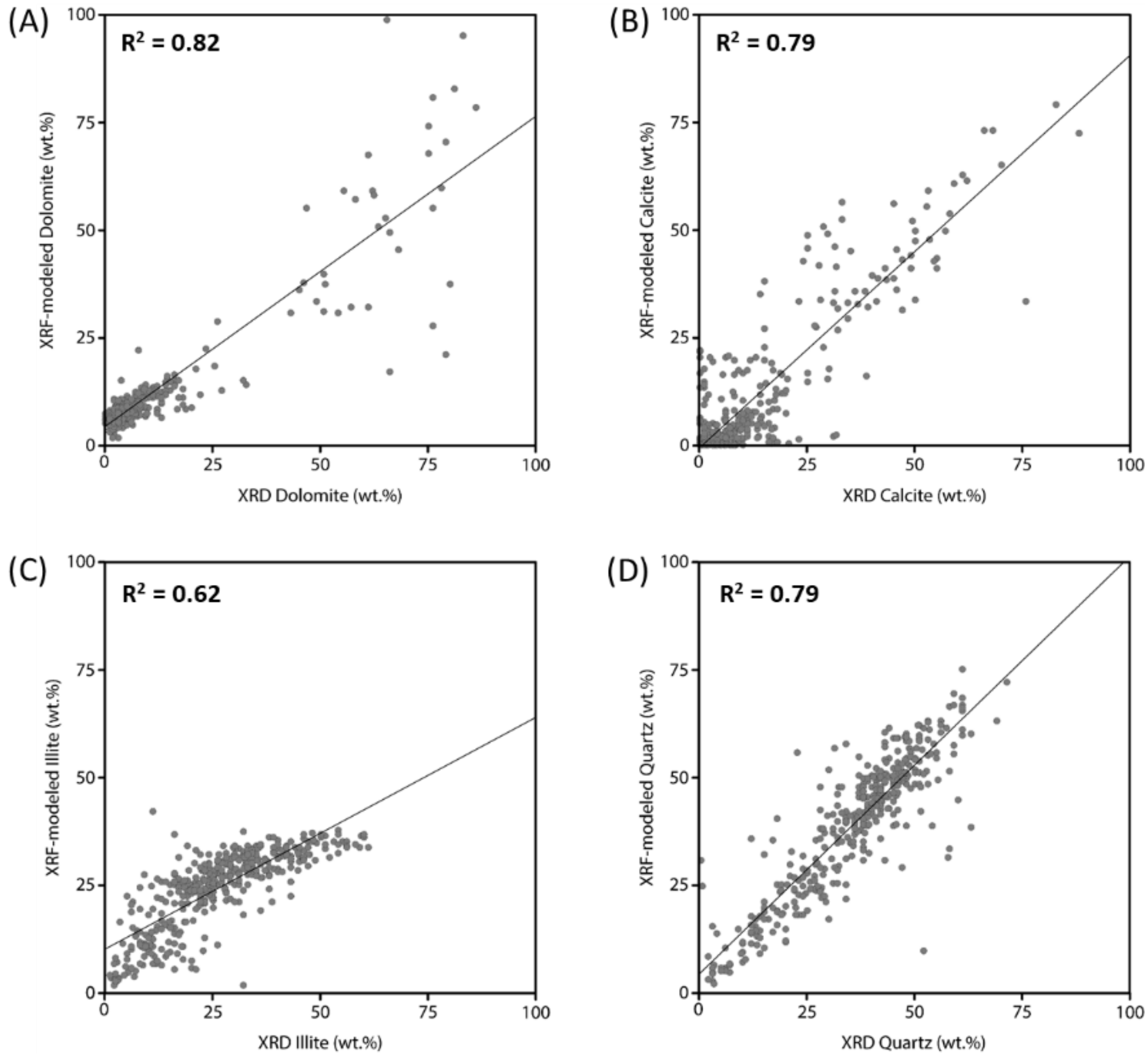

Figure 2.A1. XRF modeled mineralogy versus XRD-determined mineralogy crossplots with regression line and coefficient of determination (R^2).

(A) Dolomite. (B) Calcite. (C) Illite. (D) Quartz.

APPENDIX 2.B

TOC model

I estimate the TOC based on the relationship between LECO TOC measurements in rock samples and elements measured with XRF. I correlated the LECO TOC measurements with all elements measured with XRF to find which element gave the strongest R^2. In my cores, I found that nickel showed the best correlation (R^2 = 0.63, Figure 2.B1A). I used the equation of the regression line (Eq. 2.B1) to estimate the TOC content at each XRF-scan point.

The correlation between XRF-modeled TOC and LECO TOC measurements in core samples had an acceptable value (R^2 = 0.56, Figure 2.B1B). Although this correlation is weaker than observed in the XRF-estimated mineralogy, I interpret that it provides a good semi-quantitative assessment of the organic content in my lithofacies. It also provides reliable trends to identify which deposits the TOC content increases (e.g., hemipelagic deposits) or decreases (e.g., carbonate sediment gravity flows).

$$TOC\ estimated\ (wt.\%) = 0.046 * Ni_{measured\ with\ XRF\ (ppm)} \qquad \text{Eq. 2.B1}$$

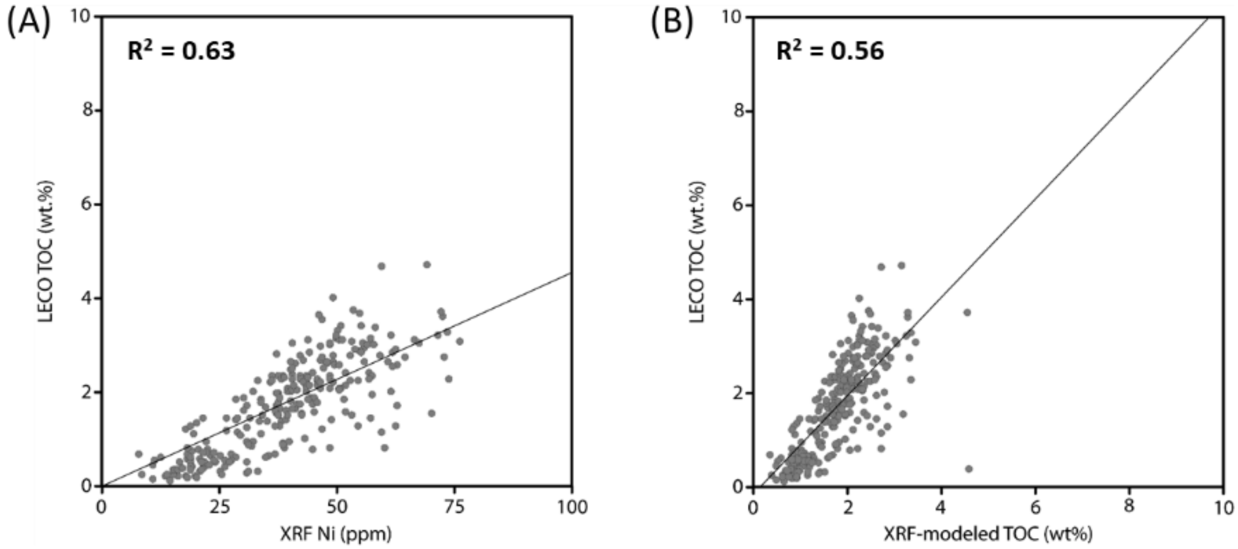

Figure 2.B1. LECO TOC content versus XRF-measured nickel (Ni) and XRF modeled TOC crossplots with regression line and coefficient of determination (R^2).

(A) Crossplot showing the correlation between the XRF-measured Ni versus the LECO TOC from core measurement. (B) Crossplot showing the correlation between LECO TOC core measurements and XRF-modeled TOC with regression equation obtained from correlation in (A).

REFERENCES

Algeo, T. J., R. Hannigan, H. Rowe, M. Brookfield, A. Baud, L. Krystyn, and B. B. Ellwood, 2007, Sequencing events across the Permian–Triassic boundary, Guryul Ravine (Kashmir, India): Palaeogeography, Palaeoclimatology, Palaeoecology, v. 252, p. 328–346.

Baker, P. A., and S. J. Burns, 1985, Ocurrence and formation of dolomite in organic-rich continental margin sediments: AAPG Bulletin, v. 69, p. 1917-1930.

Baumgardner, R. W., Jr, H. S. Hamlin, and H. D. Rowe, 2016, Lithofacies of the Wolfcamp and Lower Leonard Intervals, Southern Midland Basin, Texas, *in* P. Eichhubl, ed., Report of Investigations, Austin, Texas, Bureau of Economic Geology, p. 67.

Compton, J. S., 1988a, Degree of supersaturation and precipitation of organigenic dolomite: Geology, v. 16, p. 318-321.

Compton, J. S., 1988b, Sediment composition and precipitation of dolomite and pyrite in the Neogene Monterey and Sisquoc formations, Santa Maria basin Area, California: Sedimentology and Geochemistry of Dolsotones, SEPM Special Publication, p. 53-64.

Dobber, A. W., and r. H. Goldstein, 2020, Diagenetic Controls on Reservoir Character of the Lower Permian Wolfcamp and Bone Spring Formations in the Delaware Basin, West Texas, URTeC, Austin, Texas, USA, p. 23.

Driskill, B., J. Pickering, and H. Rowe, 2018, Interpretation of High Resolution XRF data from the Bone Spring and Upper Wolfcamp, Delaware Basin, USA, Unconventional Resources Technology Conference (URTeC), Houston, TX, p. 28.

Dunham, R. J., 1962, Classification of carbonate rocks according to depositional texture, *in* W. E. Ham, ed., Classification of Carbonate Rocks-a symposium, v. 1: Tulsa, OK, AAPG, p. 108-121.

Dutton, S. P., E. M. Kim, R. F. Broadhead, W. D. Raatz, C. L. Breton, S. C. Ruppel, and C. Kerans, 2005, Play analysis and leading-edge oil-reservoir development methods in the Permian basin: Increased recovery through advanced technologies: AAPG Bulletin, v. 89, p. 553-576.

EIA, 2022, Tight oil production estimates by play.

Ellis, D. V., and J. M. Singer, 2007, Well Logging for Earth Scientists, 2nd ed., Springer, 692 p.

Embry, A. F., and J. E. Klovan, 1971, A Late Devonian reeftrack on northeastern Banks Island, N.W.T.: Bulletin of Canadian Petroleum Geology, v. 19, p. 730-781.

Ewing, T. E., 2019, Tectonics of the West Texas (Permian) Basin - Origins, Structural Geology, Subsidence, and Later Modification: Anatomy of a Paleozoic basin: the Permian Basin, USA, v. 1: Austin, TX, Bureau of Economic Geology; American Association of Petroleum Geologists, 399 p.

Flügel, E., 2013, Microfacies of carbonate rocks: analysis, interpretation and application, Springer Science & Business Media, 984 p.

Folk, R. L., 1962, Spectral subdivision of limestone types, *in* W. E. Ham, ed., Classification of Carbonate rocks-a symposium: AAPG Memoir, v. 1: Tulsa, OK, AAPG, p. 62-84.

Folk, R. L., 1968, Petrology of Sedimentary Rocks: Austin: University of Texas Publication, p. 170.

Frenzel, H. N., R. R. Bloomer, R. B. Cline, J. M. Cys, J. E. Galley, W. R. Gibson, J. M. Hills, W. E. King, W. R. Seager, F. E. Kottlowski, S. Thompson III, G. C. Luff, B. T. Pearson, and D. C. Van Siclen, 1988, The Permian Basin region, *in* L. L. Sloss, ed., The Geology of North America: Sedimentary Cover - North American Craton: US, v. D-2: Boulder, Colorado, The Geological Society of America, p. 261-306.

Fu, Q., R. W. Baumgardner, Jr, and H. S. Hamlin, 2020, Early Permian (Wolfcampian) succession in the Permian Basin: icehouse platform, slope carbonates, and basinal mudrocks, *in* S. C. Ruppel, ed., Anatomy of a Paleozoic basin: the Permian Basin, USA, v. 2, The University of Texas at Austin, Bureau of Economic Geology Report of Investigations 285; AAPG Memoir 118, p. 185-226.

Galley, J. E., 1958, Oil and geology in the Permian Basin of Texas and New Mexico: Habitat of oil, American Association of Petroleum Geologists.

Haughton, P., C. Davis, W. McCaffrey, and S. Barker, 2009, Hybrid sediment gravity flow deposits – Classification, origin and significance: Marine and Petroleum Geology, v. 26, p. 1900-1918.

Henrich, R., and H. Huneke, 2011, Hemipelagic advection and periplatform sedimentation: Developments in Sedimentology, v. 63, p. 353-396.

Hickman, R. G., r. J. Varga, and R. M. Altany, 2009, Structural style of the Marathon thrust belt, West Texas: Journal of Structural Geology, v. 31, p. 900-909.

Hodgson, D. M., 2009, Distribution and origin of hybrid beds in sand-rich submarine fans of the Tanqua depocentre, Karoo Basin, South Africa: Marine and Petroleum Geology, v. 26, p. 1940-1956.

Horne, E. A., P. H. Hennings, and C. K. Zahm, 2021, Basement-rooted faults of the Delaware Basin and Central Basin Platform, Permian Basin, West Texas and southeastern New Mexico, *in* O. A. Callahan, and P. Eichbul, eds., The geologic basement of Texas: a volume in honor of Peter T. Flawn: Bureau of Economic Geology Report of Investigations, v. No. 286: Austin, TX, The University of Texas, p. 40.

Hunt, D., and W. M. Fitchen, 1999, Compaction and the dynamics of carbonate-platform develoment: insights from the Permian Delaware and Midland basins, southeast New Mexico and west Texas, U.S.A., *in* P. M. Harris, A. H. Saller, and J. A. Simo, eds., Advances in carbonate sequence stratigraphy: application to reservoirs, outcrops and models, SEPM Special Publication No. 63, p. 75-106.

Kane, I. A., and A. S. M. Pontén, 2012, Submarine transitional flow deposits in the Paleogene Gulf of Mexico: Geology, v. 40, p. 1119-1122.

Kane, I. A., A. S. M. Pontén, B. Vangdal, J. T. Eggenhuisen, D. M. Hodgson, and Y. T. Spychala, 2017, The stratigraphic record and processes of turbidity current transformation across deep-marine lobes: Sedimentology, v. 64, p. 1236-1273.

King, P. B., 1942, Permian of West Texas and Southeastern New Mexico: Part 1: AAPG Bulletin, v. 26, p. 115.

Krumbein, W. C., and L. L. Sloss, 1963, Stratigraphy and Sedimentation, v. 2nd Edition: San Francisco, CA, USA, W.H. Freeman and Co., 660 p.

Kvale, E. P., C. M. Bowie, C. Flenthrope, C. Mace, J. M. Parrish, B. Price, S. Anderson, and W. A. DiMichele, 2020, Facies variability within a mixed carbonate-siliciclastic sea-floor fan (upper Wolfcamp Formation, Permian, Delaware Basin, New Mexico): AAPG Bulletin, v. 104, p. 525-563.

Lazar, O. R., K. M. Bohacs, J. H. S. Macquaker, J. Schieber, and T. M. Demko, 2015, Capturing key attributes of fine-grained sedimentary rocks in outcrops, cores, and thin sections: nomenclature and description guidelines: Journal of Sedimentary Research, v. 85, p. 230-246.

Liu, L., and D. F. Stockli, 2020, U-Pb ages of detrital zircons in lower Permian sandstone and siltstone of the Permian Basin, west Texas, USA: Evidence of dominant Gondwanan and peri-Gondwanan sediment input to Laurentia: GSA Bulletin, v. 132, p. 245-262.

Longiaru, S., 1987, Visual comparators for estimating the degree of sorting from plane and thin section: Journal of Sedimentary Petrology, v. 57, p. 4.

Loucks, R. G., A. A. Brown, C. W. Achauer, and D. A. Budd, 1985, Carbonate Gravity-Flow Sedimentation of Low-Angle Slopes off the Wolfcampian Northwest Shelf of the Delaware Basin: SEPM Deep Water Carbonates, p. 56-92.

Machel, H. G., 2004, Concepts and models of dolomitization: a critical reappraisal, *in* C. J. R. Braithwaite, G. Rizzi, and G. Darke, eds., The Geometry and petrogenesis of dolomite hydrocarbon reservoirs, v. 235: London, Geological Society Special Publications, p. 7-63.

Manning, A. J., R. J. S. Whitehouse, and R. J. Uncles, 2017, Suspended particulate matter: the measurement of flocs, *in* R. J. Uncles, and S. Mitchell, eds., Estuarine and Coastal Hydrography and Sediment Transport: Cambridge, Cambridge University Press., p. 211-260.

Mazzullo, J. M., 2000, Organogenic dolomitization in peritidal to deep-sea sediments: Journal of Sedimentary Research, v. 70, p. 10-23.

McBride, E. F., 1963, A classification of common sandstone: Journal of Sedimentary Petrology, v. 33, p. 664-669.

McCave, I. N., 1972, Transport and escape of fine-grained sediment from shelf areas, *in* D. J. P. Swift, D. Duane, and O. H. Pilkey, eds., Shelf Sediment Transport: Stroundsburg, Pa, Dowden, Hutchinson & Ross, Inc., p. 225-248.

McGlue, M. M., P. W. Baldwin, L. Waite, O. P. Woodruff, and P. T. Ryan, 2015, Preliminary geologic and chemostratigraphic analysis of the Wolfcamp D shale, Midland Basin, West Texas, URTeC, San Antonio, Texas, USA, p. 5.

McHargue, T. R., and R. C. Price, 1982, Dolomite from clay in argillaceous or shale-associated marine carbonates: Journal of Sedimentary Petrology, v. 52, p. 873-886.

Moede, I. H., 2018, Lithofacies and Chemostratigraphy of the Upper Wolfcampian in the Southeastern Delaware Basin, Pecos County, Texas, The University of Texas at Austin, 114 p.

Nance, H. S., and H. Rowe, 2015, Eustatic controls on stratigraphy, chemostratigraphy, and water mass evolution preserved in a Lower Permian mudrock succession, Delaware Basin, west Texas, USA: Interpretation, v. 3, p. 11-25.

Parrish, J. T., 1993, Climate of the supercontinent Pangea: Journal of Geology, v. 101, p. 19.

Payros, A., and V. Pujalte, 2008, Calciclastic submarine fans: An integrated overview: Earth-Science Reviews, v. 86, p. 203-246.

Peltier, J., 2019, Peltier Tech Blog, https://peltiertech.com/.

Piper, D. J. W., 1972, Turbidite origin of some laminated mudstones: Geological Magazine, v. 109, p. 115 - 126.

Potter, E. C., M. P. Walsh, C. L. Breton, C. Lemons, and R. C. Reedy, 2020, Oil and gas production, Permian Basin: a giant conventional oil province being transformed by shale oil production, *in* C. Ruppel, ed., Anatomy of a Paleozoic basin: the Permian Basin, USA, v. 2, The University of Texas at Austin, Bureau of Economic Geology Report of Investigations 285; AAPG Memoir 118, p. 497-526.

Price, B., R. Dommisse, and X. Janson, 2021, Linking Depositional Environment Interpretations and Stratal Architecture to Source Rock Richness and Mechanical Property Distribution in the Delaware Basin, Unconventional Resources Technology Conference (URTeC), Houston, Texas, USA, p. 12.

Ratcliffe, K., M. Wright, and D. Spain, 2012, Unconventional methods for unconventional plays: using elemental data to understand shale resource plays, Part 2: PESA News Resources, p. 55-60.

Reis, A., A. M. Erhardt, M. M. McGlue, and L. Waite, 2019, Evaluating the effects of diagenesis on the $\delta^{13}C$ and $\delta^{18}O$ compositions of carbonates in a mud-rich depositional environment: A case study from the Midland Basin, USA: Chemical Geology, v. 524, p. 196-212.

Rieder, M., G. Cavazzini, Y. D'Yakonov, V. A. Frank-Kamenetskii, G. Gottardi, S. Guggenheim, P. V. Koval', G. Muller, A. M. R. Neiva, E. W. Radoslovich, J.-L. Robert, F. P. Sassi, H. Takeda, Z. Weiss, and D. R. Wones, 1998, Nomenclature of the Micas: The Canadian Mineralogist, v. 36, p. 41-48.

Ross, C. A., and J. Ross, R. P., 1987, Late Paleozoic sea levels and depositional sequences: Cushman Foundation for Foraminiferal Research, v. Special Publication 24, p. 13.

Ross, C. A., and J. Ross, R. P., 2003a, Fusulinid sequence evolution and sequence extinction in Wolfcampian and Leonardian Series (Lower Permian), Glass Mountains, West Texas: Revista Italiana di Paleontologia e Stratigrafia, v. 109, p. 26.

Ross, C. A., and J. Ross, R. P., 2003b, Sequence evolution and sequence extinction: fusulinid biostratigraphy and species-level recognition of depositional sequences, Lower Permian, Glass Mountains, West Texas, U.S.A.: Society for Sedimentary Geology, p. 44.

Ruppel, S. C., 2019, Anatomy of a Paleozoic basin: the Permian Basin, USA: introduction, overview, and evolution, *in* S. C. Ruppel, ed., Anatomy of a Paleozoic basin: the Permian Basin, USA: Bureau of Economic Geology Report of Investigations 285; AAPG Memoir 118, v. 1, The University of Texas at Austin, p. 1-27.

Ruppel, S. C., 2020, Lower Permian (Leonardian) platform carbonate succession: deposition and diagenesis during a waning icehouse period, *in* S. C. Ruppel, ed., Anatomy of a Paleozoic basin: the Permian Basin, USA, v. 2, The University of Texas at Austin, Bureau of Economic Geology Report of Investigations 285; AAPG Memoir 118, p. 227-282.

Shumaker, R. C., 1992, Paleozoic Structure of the Central Basin Uplift and Adjacent Delaware Basin, West Texas: AAPG Bulletin, v. 76, p. 1804-1824.

Sibley, D. F., and J. M. Gregg, 1987, Classification of dolomite rock textures: Journal of Sedimentary Petrology, v. 57, p. 967-975.

Sinclair, S., L. Crespo, L. Waite, K. Smith, and C. Leslie, 2017, Resource assessment in the northern Midland Basin: Detailed mapping of Late Pennsylvanian, Wolfcampian, and Early Leonardian margins and flooding surfaces using well logs and seismic data, URTeC, Austin, Texas, USA, p. 13.

Sinclair, T. D., 2007, The generation and continued existence of overpressure in the Delaware Basin, Texas: Doctoral thesis, Durham University, 314 p.

Soreghan, G. S., and M. J. Soreghan, 2013, Tracing clastic delivery to the Permian Delaware Basin, U.S.A.: implications for paleogeography and circulation in westernmost equatorial Pangea: Journal of Sedimentary Research, v. 83, p. 786-802.

Soto-Kerans, G. M., D. F. Stockli, X. Janson, T. F. Lawton, and J. A. Covault, 2020, Orogen proximal sedimentation in the Permian foreland basin: Geosphere, v. 16, p. 567-593.

Spychala, Y. T., D. M. Hodgson, A. Prélat, I. A. Kane, S. S. Flint, and N. P. Mountney, 2017, Frontal and lateral submarine lobe fringes: comparing sedimentary facies, architecture and flow processes: Journal of Sedimentary Research, v. 87, p. 75-96.

Stow, D., and Z. Smillie, 2020, Distinguishing between Deep-Water Sediment Facies: Turbidites, Contourites and Hemipelagites: Geosciences, v. 10, p. 43.

Stow, D. A. V., and D. J. W. Piper, 1984, Deep-water fine-grained sediments: facies models: Geological Society, London, Special Publications, v. 15, p. 611-646.

Stow, D. A. V., and G. Shanmugam, 1980, Sequence of structures in fine-grained turbidites: somparison of recent deep-sea and ancient flysch sediments: Sedimentary Geology, p. 23-42.

Stow, D. A. V., and A. R. Tabrez, 1998, Hemipelagites: processes, facies and model: Geological Society, London, Special Publications, v. 129, p. 317-337.

Tabor, N. J., I. P. Montañez, C. R. Scotese, C. J. Poulsen, G. H. Mack, C. R. Fielding, T. D. Frank, and J. L. Isbell, 2008, Paleosol archives of environmental and climatic history in paleotropical western Pangea during the latest Pennsylvanian through Early Permian, Resolving the Late Paleozoic Ice Age in Time and Space, v. 441, Geological Society of America, p. 0.

Talling, P. J., D. G. Masson, E. J. Sumner, and G. Malgesini, 2012, Subaqueous sediment density flows: depositional processes and deposit types: Sedimentology, v. 59, p. 1937-2003.

Thompson, M., P. Desjardins, J. Pickering, and B. Driskill, 2018, An integrated view of the petrology, sedimentology, and sequence stratigraphy of the Wolfcamp Formation, Delaware Basin, Texas, URTeC, Houston, Texas, p. 8.

Tucker, M. E., and V. P. Wright, 1990, Carbonate Sedimentology, Blackwell Scientific Publications, 482 p.

Wahlman, G. P., and D. R. Tasker, 2013, Lower Permian (Wolfcampian) Carbonate Shelf-Margin and Slope Facies, Central Basin Platform and Hueco Mountains, Permian Basin, West Texas, USA: SEPM Special Publication, p. 305-333.

Wentworth, C. K., 1922, A scale of grade and class terms of clastic sediments: Journal of Geology, v. 30, p. 377-392.

Wilson, R. D., J. Chitale, K. Huffman, P. Montgomery, and S. J. Prochnow, 2020, Evaluating the depositional environment, lithofacies variation, and diagenetic processes of the Wolfcamp B and lower Spraberry intervals in the Midland Basin: Implications for reservoir quality and distribution: AAPG Bulletin, v. 104, p. 1287-1321.

Xie, X., J. M. Anthony, and A. B. Busbey, 2019, Provenance of Permian Delaware Mountain Group, central and southern Delaware Basin, and implications of sediment dispersal pathway near the southwestern terminus of Pangea: International Geology Review, v. 61, p. 361-380.

Yang, K.-M., and S. L. Dorobek, 1995, The Permian Basin of West Texas and New Mexico: Tectonic History of a "Composite" Foreland Basin and its Effects on Stratigraphic Development: SEPM Special Publication, p. 149-174.

Chapter 3: Permeability of upper Wolfcamp lithofacies and implications for production in the Delaware Basin, Permian Basin Region, West Texas, USA[2]

3.1 Abstract

Drainage behavior in low-permeability reservoirs at the completion scale is often interpreted to be controlled by the presence of hydraulic and natural fractures. However, the presence of permeability heterogeneity due to lithofacies variability in these reservoirs has not been previously explored as a plausible mechanism controlling drainage. Here, I demonstrate that the presence of lithofacies that are up to 2000 times more permeable than others in the upper Wolfcamp interval in the central-eastern Delaware Basin increase the upscaled reservoir permeability and production rates multiple times higher than a reservoir composed of only low-permeability mudstones. I conducted steady-state liquid (dodecane) permeability measurements in 30 horizontal core plugs extracted from six upper Wolfcamp lithofacies. The dolomitized calcareous lithofacies exhibit effective permeabilities to dodecane (oil phase) up to 2000 nD, whereas the remaining mudstones, dolomudstones, and calcium carbonate-bearing lithofacies have effective permeabilities less than 60 nD. The interpreted stratigraphy of the studied section indicates that the permeable lithofacies are dolomitized calciclastic sediment gravity flow deposits with variable thicknesses (2 inches to 9 feet). These deposits are interspersed with the low-permeability strata that dominate the studied section. I constructed a simplified layered model consisting of a high-permeability dolomitic layer and a low-permeability layer to examine the

---

[2]The full content of this chapter was submitted to AAPG Bulletin in 2022. The citation for that publication is:

Ramiro-Ramirez, S., A. R., Bhandari, P. B., Flemings, and R. M., Reed (*in review*), Permeability of upper Wolfcamp lithofacies and implications for production in the Delaware Basin, Permian Basin Region, West Texas, USA. *AAPG Bulletin.*

I designed and performed the experiments presented in that study and prepared the manuscript for publication. My co-authors are listed in order of contribution and provided support for the conceptual development of the project and manuscript preparation.

production behavior in the studied interval through simulations. I show that cross-facies flow results in focusing drainage through the permeable layer, increasing the upscaled permeability and production rates of the system up to four times higher than a reservoir composed of only low-permeability strata. Thus, I interpret that permeability heterogeneity plays a critical role in production drainage behavior in the upper Wolfcamp interval. Other low-permeability formations exhibiting similar permeability heterogeneity structure may behave similarly to the Wolfcamp interval described here.

3.2 Introduction

The Wolfcamp operational unit in the Permian Basin region of west Texas and southeast New Mexico is the most prolific low-permeability, liquid-hydrocarbon (i.e., crude oil and condensates) onshore producing interval in the United States (EIA, 2022). In 2020, the average daily production in the Wolfcamp ranged between 2.3 and 2.5 million bbl., surpassing both the Eagle Ford (Texas) and the Bakken (North Dakota and Montana) formations (EIA, 2022). Hydrocarbons are produced at such economic rates from these low-permeability formations by combining horizontal drilling with multistage hydraulic fracturing techniques (Yu and Sepehrnoori, 2018; Zoback and Kohli, 2019). The long lateral lengths of horizontal wells and the artificial fracture network created in the rock increase the surface area of the reservoir exposed to the wellbore, resulting in economically viable production rates. In addition to operational factors, the stratigraphic architecture and subsequent distribution of geological and petrophysical rock properties play a significant role in primary production from low-permeability reservoirs (Sagasti et al., 2014; Wilson et al., 2020; Euzen et al., 2021; Fraser and Pedersen, 2021).

Low-permeability reservoirs are often dominated by fine-grained, organic-rich lithofacies (e.g., mudstones) that have matrix permeabilities ranging from 1 to 30 nD (Vermylen, 2011;

Bhandari et al., 2018; Bhandari et al., 2019). However, reservoir simulation models often require upscaled permeabilities that are higher than those measured in core plugs from these lithofacies to history-match production. For example Patzek et al. (2013) found that an upscaled permeability of 500 nD in early production and 50 nD in late production times were required in Barnett Shale reservoirs even though estimates of the rock permeability was ~3 nD.

It has been suggested that the stimulation process alone (i.e., hydraulic fracturing) may increase the reservoir upscaled permeability by, for instance, reopening of pre-existing natural fractures in the reservoir (Patzek et al., 2013) or creating of a complex secondary hydraulic fracture network (Mohan et al., 2013). However, a range of studies have recently suggested that only a small fraction of natural fractures reactivate during stimulation (Male et al., 2021), and for what little fracture reactivation there is, it may not be enough to transfer fluids to the wellbore at significant rates (Salem et al., 2022). Also, cores obtained from stimulated reservoir intervals in the Wolfcamp (Gale et al., 2018; Gale et al., 2021) and Eagle Ford (Raterman et al., 2018) formations do not exhibit the development of complex secondary fractures. Hence, the upscaled permeabilities in these reservoirs may increase due to geological factors not previously considered.

An opposite interpretation is the presence of significant permeability heterogeneity in the reservoir due to stratigraphic layering of multiple lithofacies with different fabric and pore systems, and therefore different matrix permeabilities. During production, the more permeable lithofacies may drain fluids from the less permeable strata through cross-facies flow (Katz and Tek, 1961; Pendergrass and Berry, 1962; Russell and Prats, 1962; Park, 1989; Phillips, 1991; Kuhl, 2003) and laterally into the hydraulic fracture. This drainage behavior may increase the upscaled permeability of the hydraulically fractured intervals multiple times. Such behavior is possible in low-permeability formations because they often contain multiple lithofacies with different matrix permeabilities (e.g., Kurtoglu, 2013; Kosanke and Warren, 2016; Ramiro-Ramirez et al., 2021). In the Wolfcamp, previous core-based studies indicate the presence of drastic permeability heterogeneity (i.e., k = 10 nD to 600 nD) (e.g., Rafatian and Capsan, 2015; Mathur et al., 2016; King et al., 2018; Bhandari et al., 2019). However, these studies provide a limited geological context for the tested samples. Hence, the reported permeabilities cannot be related to the stratigraphy of the Wolfcamp to study their effect on the upscaled permeabilities.

In this study, I systematically measure the porosity and permeability of all lithofacies (see Chapter 2) in the Wolfcamp A and Wolfcamp B units of the Delaware Basin. I suggest that the major oil reservoir is the volumetrically dominant organic-rich siliceous mudstone lithofacies which has a permeability in the order of 20 nD. However, I also find that dolomitized carbonate flow deposits have much higher permeabilities up to 2000 nD. I present a flow model to illustrate how the high-permeability deposits play a role in drainage of the reservoir resulting in a much higher upscaled permeability. My work also illustrates why there has been more success in the Wolfcamp A, where high-permeability layers are more abundant, than in the Wolfcamp B. Nonetheless, there are intervals within the Wolfcamp B that may be significant economic targets.

I begin by measuring the porosity and permeability in core plugs extracted from upper Wolfcamp lithofacies. Then, I interpret the lithofacies control on permeability based on petrographic and petrophysical analyses of the pore system in the tested samples. Lastly, I perform flow simulations in a layered reservoir model and discuss the impact of the permeability heterogeneity on the upscaled permeabilities in the upper Wolfcamp interval.

3.3 Geological Overview

In my study area (Figure 3.1), I defined six upper Wolfcamp lithofacies and interpreted the depositional processes associated with them (see Chapter 2) (Table 3.1). They studied the upper

Wolfcamp as the interval comprising the Wolfcamp B (late Wolfcampian) and the overlying Wolfcamp A (early Leonardian) units (Figure 3.2). I summarize those results below.

The lower part of the Wolfcamp B unit (Figure 3.3) is dominated by organic-rich siliceous mudstone (Lithofacies 1, Table 3.1). This mudstone is interpreted to record hemipelagic deposition. It is interbedded occasionally with laterally continuous calcareous mudstone (Lithofacies 3a, Table 3.1) and calcareous sandstone (Lithofacies 4a, Table 3.1), which are interpreted to record deposition from carbonate turbidites. When dolomitic, these two lithofacies are sub-classified into dolomitic calcareous mudstone (Lithofacies 3b, Table 3.1) and dolomitic calcareous sandstone (Lithofacies 4b, Table 3.1), and they are interpreted as dolomitized carbonate turbidites. Matrix-supported conglomerates (Lithofacies 5, Table 3.1) are interpreted as cohesive debrites; they are rare and form very thin deposits in this interval.

In the middle-to-upper parts of the Wolfcamp B unit (Figure 3.3), the organic-rich siliceous mudstone is interbedded with laterally continuous argillaceous mudstone (Lithofacies 2, Table 3.1), which is interpreted to record siliciclastic turbidites. This mudstone has higher clay content, lower total organic carbon (TOC), and is finer-grained than the organic-rich siliceous mudstone (Lithofacies 1). Dolomudstone (Lithofacies 6, Table 3.1) is always associated with the argillaceous mudstone and is interpreted to have formed by early diagenetic dolomite precipitation. The calcareous mudstone and calcareous sandstone lithofacies occur only occasionally in this interval, and they are usually dolomitized. The matrix-supported conglomerate is found towards the uppermost part of the unit, forming thick, laterally discontinuous deposits alternating with the organic-rich siliceous mudstone.

The overlying Wolfcamp A unit is quite different from the Wolfcamp B unit. The organic-rich siliceous mudstone alternates with frequent calcareous mudstone and calcareous sandstone lithofacies (Figure 3.3), interpreted as carbonate hybrid event beds. In addition, the calcareous mudstone and calcareous sandstone lithofacies are often dolomitized in this unit.

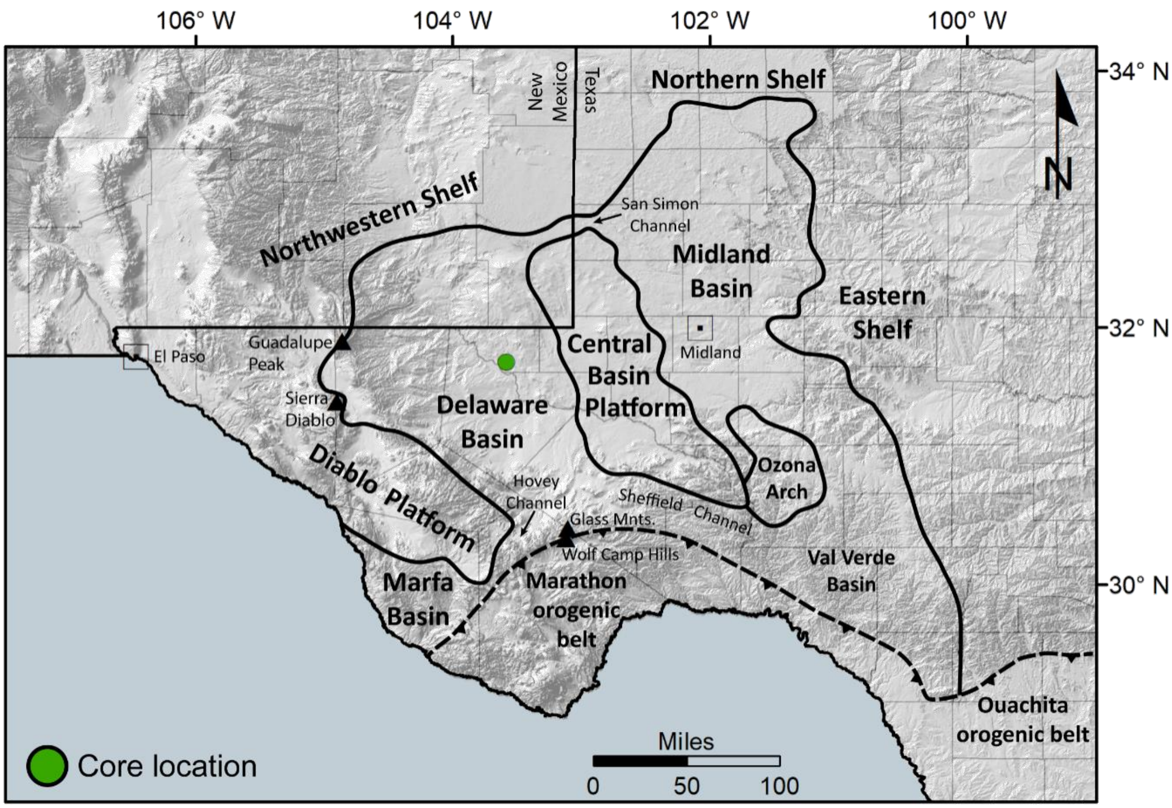

Figure 3.1: Modern topography in west Texas and southeast New Mexico with key components of the Permian Basin region during Early Permian (Late Wolfcampian to Early Leonardian) overlain.

Map of the Permian Basin region showing the location of studied core (green circle) in the central-eastern Delaware Basin (green circle). Figure derived from Hunt and Fitchen (1999), Dutton et al. (2005), and Fu et al. (2020).

Table 3.1. Lithofacies in the upper Wolfcamp interval and interpreted deposits from Chapter 2.

#	*Lithofacies*	*Interpretation*
1	Organic-rich siliceous mudstone	Hemipelagic
2	Argillaceous mudstone	Siliciclastic turbidite
3a	Calcareous mudstone	Carbonate turbidite and hybrid event bed (HEB)
3b	Dolomitic calcareous mudstone	Dolomitized carbonate turbidite and HEB
4a	Calcareous sandstone	Carbonate turbidite and HEB
4b	Dolomitic calcareous sandstone	Dolomitized carbonate turbidite and HEB
5	Matrix-supported conglomerate	Cohesive debrite
6	Dolomudstone	Early diagenetic dolomite formation

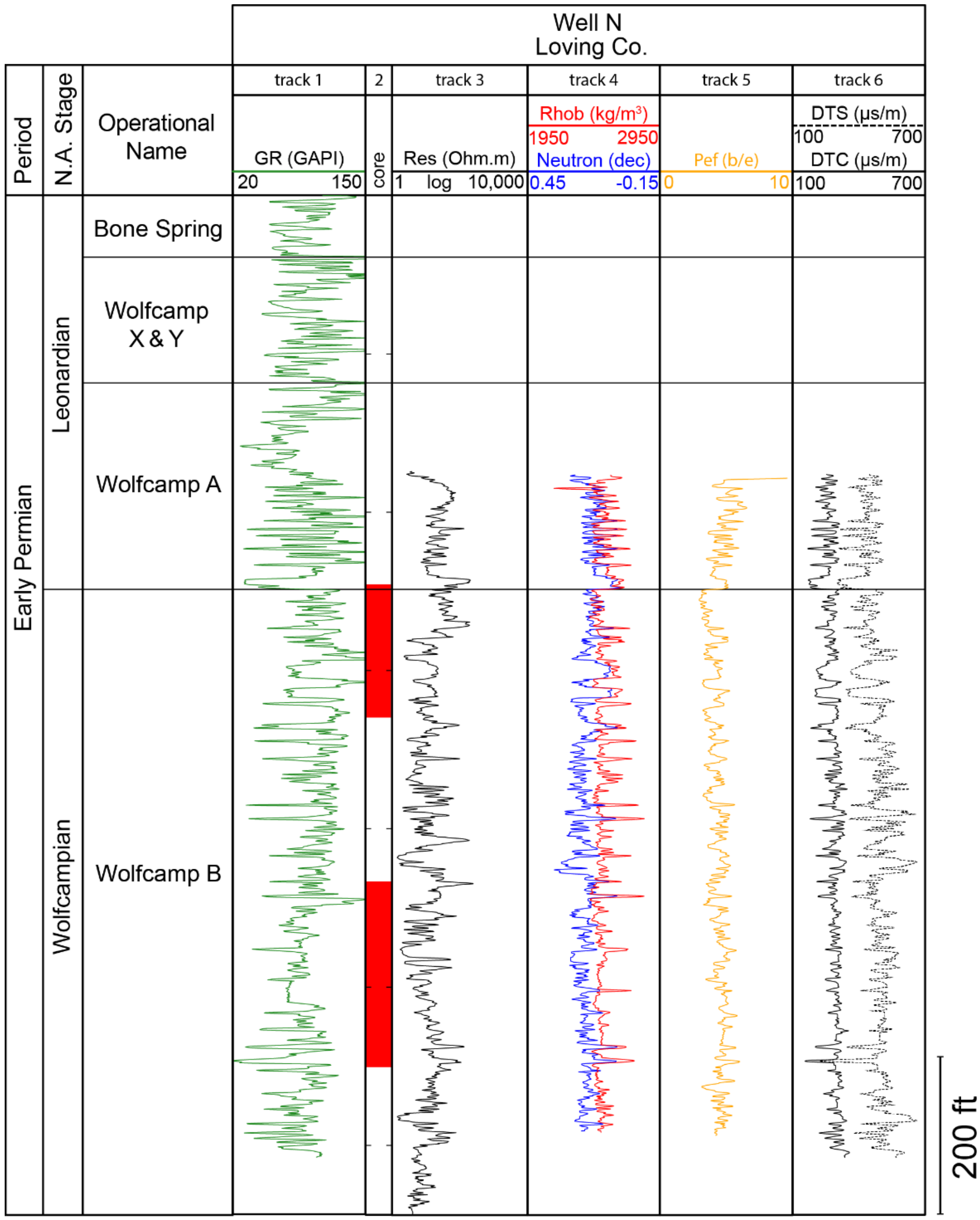

Figure 3.2: Wireline log curves of Well N and cored intervals (indicated by red bars) studied here.

In Chapter 2, I provide more details about the Wolfcamp operational units. Track 1: gamma ray. Track 2: cored interval (red). Track 3: deep resistivity. Track 4: bulk density (red) and neutron porosity (blue). Track 5: photoelectric effect. Track 6: shear slowness (dashed line) and compressional slowness (solid line). N.A. = North America.

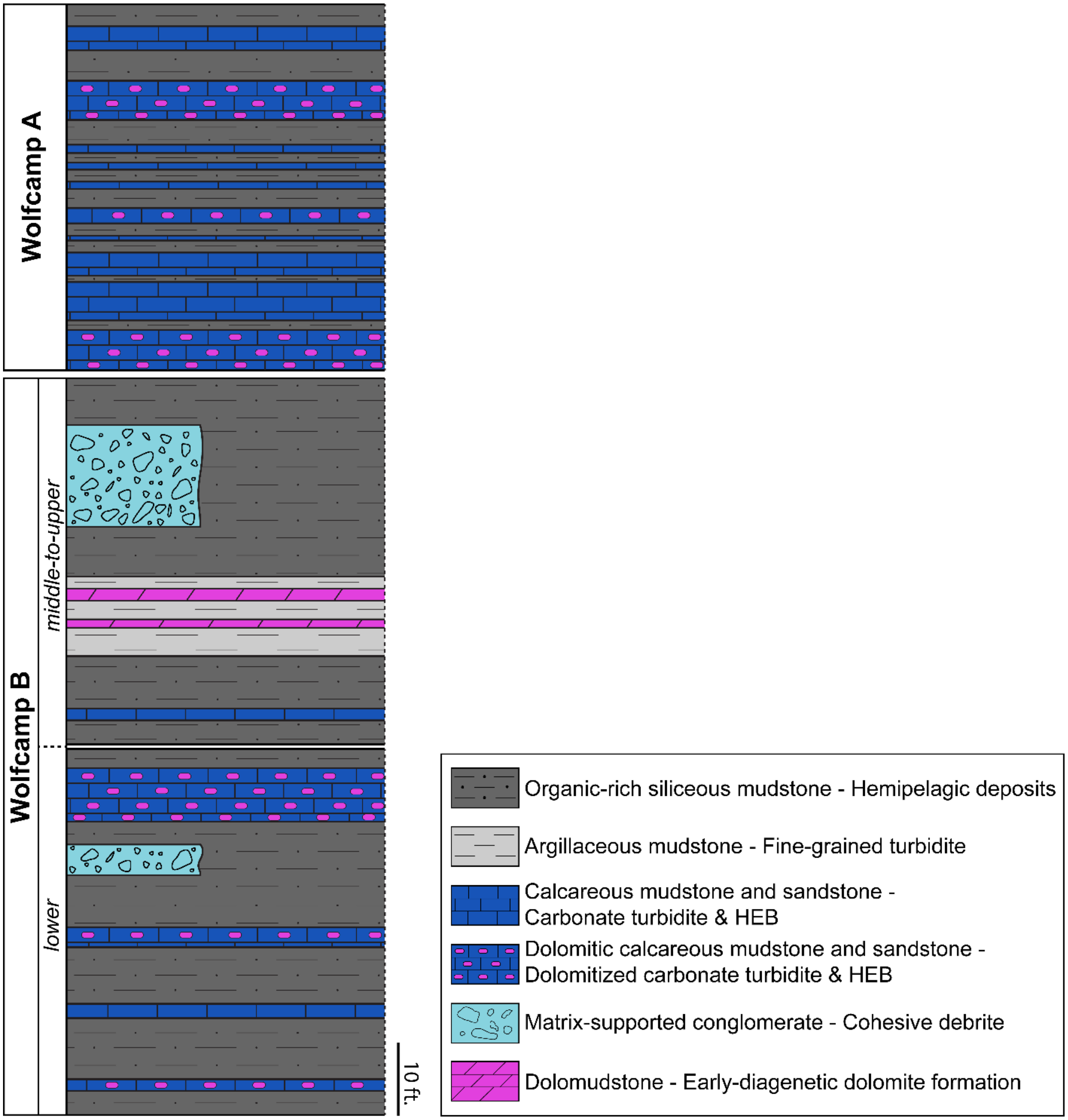

Figure 3.3. Characteristic stratigraphic architecture of the lower (bottom) and middle-to-upper (middle) sections of the Wolfcamp B unit, and Wolfcamp A unit (top).

3.4 MATERIALS AND METHODS

3.4.1 Samples

I extracted core plugs from a vertical core that spans 403 ft of the Wolfcamp B unit in the Delaware Basin (Figure 3.1, Figure 3.2). The core was slabbed and photographed, immediately preserved in aluminum foil followed by plastic film, and sealed in wax.

To choose sampling locations, I first defined the lithofacies in the core at the inch-scale (see Chapter 2) and then selected the best core depths to extract high quality, unfractured, specimens. I recovered 90 core plugs with a diameter of either 1.5 in (3.81 cm) or 1.0 in (2.54 cm), and with their long axis oriented either parallel or normal to the bedding plane. The plugs were cored using humidified nitrogen as coolant to avoid fluid interaction with the rock components (e.g., water with expansive clays). I preserved the core plugs in plastic film and aluminum foil, and stored them in plastic containers.

The quality of the extracted core plugs was variable. I selected core plugs for permeability measurement from each lithofacies that had no open fractures visible to the naked eye. I acquired high-resolution X-ray Micro-Computed Tomography (micro-CT) images of these core plugs to assess the presence of natural fractures and artificial microfractures (e.g., coring induced).

I measured the total porosity in 40 core plugs by combining helium porosimetry (HeP) and nuclear magnetic resonance (NMR) techniques. I measured the liquid permeability to dodecane in 30 of those core plugs at varying effective stress conditions using the steady-state technique. Appendix 3.A details the dimensions, mineralogy, and TOC content of the tested core plugs.

3.4.2 Porosity

I measured the total porosity in my core plugs at ‘as received’ conditions. Thus, I did not perform any core cleaning or oven drying. I obtained the total porosity by summing the helium porosity ($\emptyset_{He}$) and the nuclear magnetic resonance porosity ($\emptyset_{NMR}$) (e.g., Rydzy et al., 2016; Romero-Sarmiento et al., 2017):

$$\emptyset_{total} = \emptyset_{He} + \emptyset_{NMR} \ . \qquad \text{Eq. 3.1}$$

The helium porosity ($\emptyset_{He}$) is the pore volume accessible by helium gas divided by the bulk volume of the sample. The nuclear magnetic resonance porosity ($\emptyset_{NMR}$) is the pore volume occupied by the structural and remnant in-situ liquids (formation water, clay-bound water, and liquid hydrocarbons) divided by the bulk volume of the sample. I document the experimental procedures and equipment used to measure the porosity in Appendix 3.B.

3.4.3 Permeability

Experimental setup

I performed my permeability measurements in four identical permeability test cells equipped with a dual-cylinder Quizix® Q5000 pump and a dual-cylinder Quizix® QX-10K pump to control the upstream and downstream pore fluid pressures in the core plug, respectively. A second dual-cylinder Quizix® QX-10K controls the confining axial and radial confining pressures applied on the core plug. The pore fluid pressures are measured with pressure transducers installed at both ends of the core holder. The schematic of my apparatus was given previously by Bhandari et al. (2019).

The permeability test cells were leak-tested. The leaks were ~1e-6 ml/min, on average. The temperature (T) inside the cell was actively controlled to remain constant at T = 30 ± 0.1°C (max fluctuation) during the permeability experiments. I conducted my permeability experiments using dodecane, $C_{12}H_{26}$ (CAS# 112-40-3), which is a liquid alkane hydrocarbon that is miscible with crude oil, but it is immiscible with water.

Test program

My test program consists of two saturation stages followed by six steady-state liquid permeability tests at varying confining pressure (P_c) conditions (2000 psi to 9500 psi) [13.79 MPa to 65.50 MPa] while maintaining the pore pressure (P_p) at approximately 1000 psi [6.89 MPa] (Figure 3.4). The radial and axial confining pressures were applied equally on the core plug during my permeability tests, and therefore I tested the samples at isostatic confining stress conditions. I assume the pore pressure to be the arithmetic average of the upstream pressure and the downstream pressure.

I conducted the first saturation stage by drawing a vacuum on the sample inside a vacuum chamber, and then flooding dodecane until the sample is fully submerged in the liquid. The core plug remains at these conditions for 24 hr. (Figure 3.4). The second saturation stage consists of high-pressure saturation of the core plug inside the permeability cell, according to the procedure described in Bhandari et al. (2019). I next ramp the confining pressure to 6500 psi, and then I decrease it to 5500 psi and to 2000 psi to conduct the first (Test 1) and second (Test 2) steady-state liquid permeability tests, respectively (Figure 3.4). I conduct the ensuing permeability tests at the confining pressures of 5500 psi (Test 3), 9500 psi (Test 4), 5500 psi (Test 5), and 2000 psi (Test 6) (Figure 3.4). Between tests, I change P_c at a constant rate of 25 psi/min [0.17 MPa/min] while setting the P_p constant at 950 psia on both sides of the core plug. In addition, I let the sample stabilize at the new confining pressure condition for 24 hr. before conducting the permeability test.

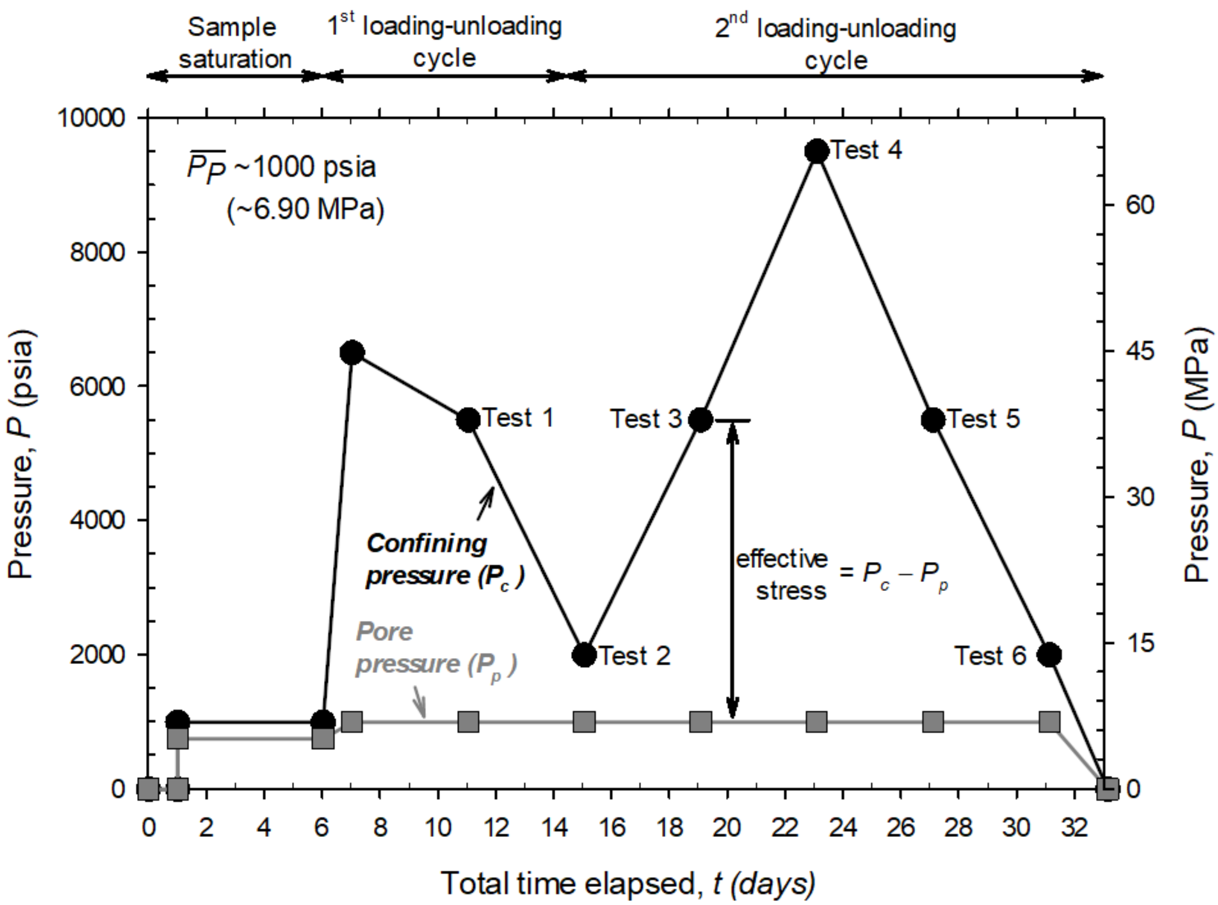

Figure 3.4: Permeability test program consisting of a sample saturation stage followed by two loading-unloading confining pressure cycles.

The stead-state permeability tests are conducted at isostatic (vertical = horizontal) confining stress condition. The effective stress is the confining pressure (P_c) minus the pore pressure (P_c). The average total time to complete the test program is ~30 days per sample.

Steady-state liquid (dodecane) permeability

I conducted liquid steady-state permeability tests at each confining stress condition indicated in Figure 3.4 (Test 1 to Test 6). I injected dodecane at constant flow rate (*q*) at the upstream side of the core plug while maintaining the pressure constant in the downstream side to generate a pressure differential of ΔP = 100 psi ± 20 psi across the sample. By injecting dodecane at constant *q*, I avoid any pore pressure instabilities (e.g., pressure oscillations or 'hunting effect') that may occur if both upstream and downstream pumps were operated to maintain a constant pressure, and I can also monitor on real time when the steady-state conditions are reached (i.e., when ΔP = constant due to steady flow across the sample). Since the permeability of the sample is unknown at every new confining pressure condition, I first need to estimate the *q* required to generate a pressure differential of ΔP = 100 psi ± 20 psi, and then run the permeability tests with the estimated *q*. The experimental protocol is as follows:

<u>Step 1 – Estimation of upstream (injection) flow rate (*q*)</u>: I inject dodecane through the upstream side of the core plug at a constant pore pressure of 1050 psi while maintaining the pore pressure constant on the downstream side at 950 psi. I record the upstream and downstream pressures (Figure 3.5A) and the volume change of the pump cylinders (Figure 3.5B) for ~12-24 hr. I then interpret that the slope of the injected pore volume (solid line, Figure 3.5B) corresponds to the approximate flow rate (*q*) at which dodecane flows across the sample.

<u>Step 2 – Estimation of permeability (*k*)</u>: I inject dodecane through the upstream side of the core plug at a constant *q* estimated in Step 1 to generate ΔP = 100 psi while maintaining the pore pressure in the downstream side constant at 950 psi (Figure 3.5A). I continue this test until the ΔP is approximately constant over time, which typically takes over 12 hr. I then calculate the permeability (*k*) of the core plug using Darcy's law (Eq. 3.2):

$$k = -\frac{q}{A}\frac{\mu L}{\Delta P},$$ Eq. 3.2

where μ is the viscosity of dodecane at the average pore pressure, and A and L are the cross-sectional area and the length of the core plug, respectively. Since I tested my samples at 'as received' conditions, the calculated k corresponds to the effective permeability to dodecane (i.e., effective permeability to the oil phase).

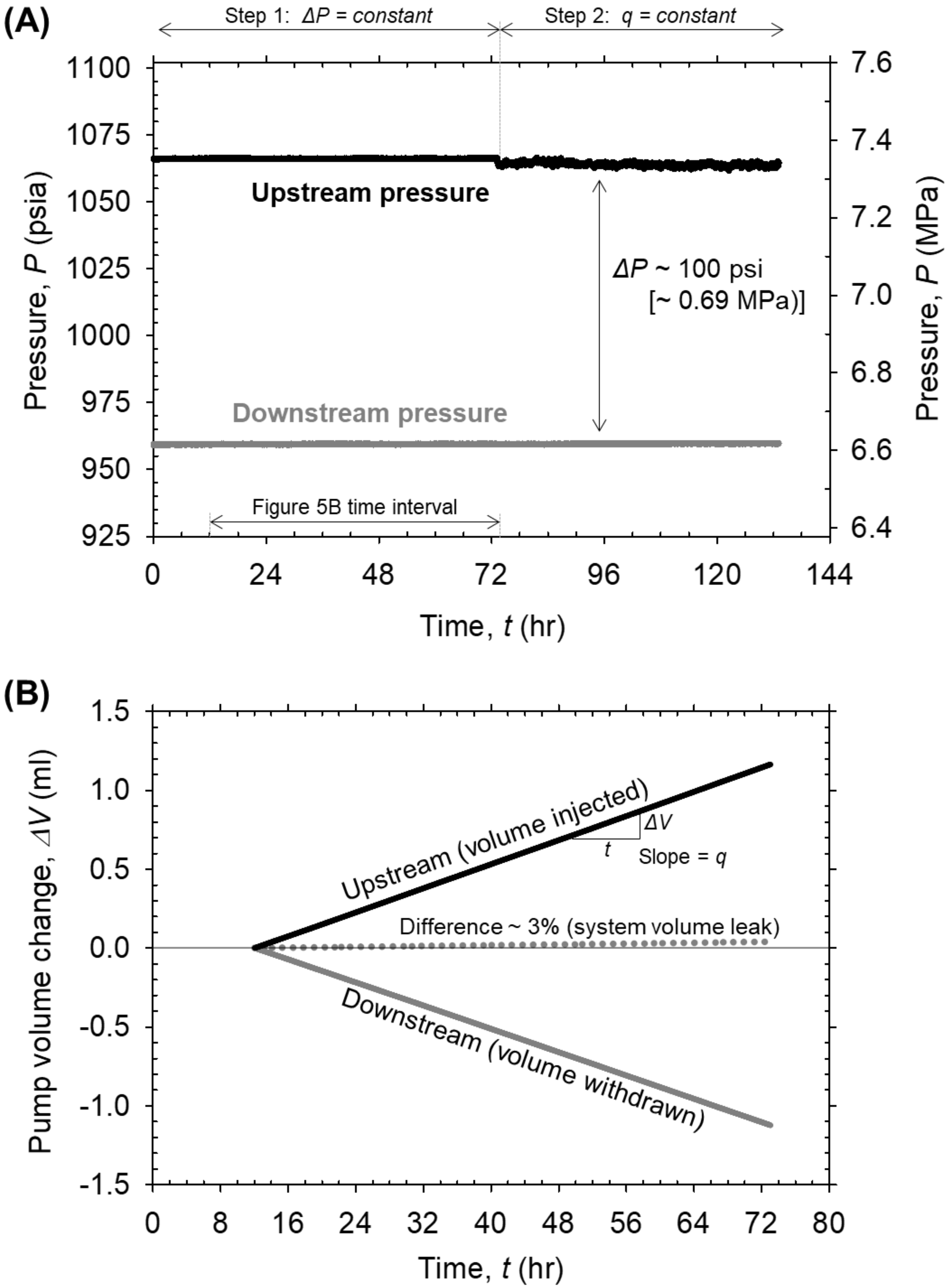
(A)
Step 1: ΔP = constant
Step 2: q = constant
Pressure, P (psia)
Pressure, P (MPa)
1100
1075
1050
1025
1000
975
950
925
7.6
7.4
7.2
7.0
6.8
6.6
6.4
Upstream pressure
ΔP ~ 100 psi
[~ 0.69 MPa)]
Downstream pressure
Figure 5B time interval
0
24
48
72
96
120
144
Time, t (hr)
(B)
Pump volume change, ΔV (ml)
1.5
1.0
0.5
0.0
-0.5
-1.0
-1.5
Upstream (volume injected)
ΔV
t
Slope = q
Difference ~ 3% (system volume leak)
Downstream (volume withdrawn)
0
8
16
24
32
40
48
56
64
72
80
Time, t (hr)

Figure 3.5. Example of data recorded during a steady-state permeability test.

(A) Evolution of the upstream (black) and downstream (grey) pressures recorded by the pressure transducers located at the inlet and the outlet of the core holder during Step 1 (ΔP = constant) and Step 2 (q = constant). The difference between the upstream and downstream pressures corresponds to the pressure differential (ΔP) that I use to compute the permeability using Darcy's law. (B) Data recorded during Step 1 (ΔP = constant) in Figure 3.5A. The solid black curve shows the volume of dodecane injected at constant flow rate by the upstream pump. The solid grey curve shows the volume withdrawn by the downstream pump. The slope of the volume injected in the upstream side corresponds to the flow rate (q) that I use to conduct the second steady-state permeability measurement. The difference between the volume injected upstream and the volume withdrawn downstream corresponds to the volume leaked in the system during the permeability test (dotted grey). In this test, the cumulative leak was ~3% of the injected volume. Data after 12 hr. of flow is shown here. Data shown is from Sample PN 3-108.

3.4.4 Petrographic characterization

I characterized the texture and pore types with a field emission scanning electron microscope (FE-SEM). A ~ 5 mm-side cube of rock was sub-sampled from each core plug. The sub-sampled cubes were argon-ion-beam milled to prepare a flat surface (~ 1.5 mm by ~0.5 mm in size) for imaging; this sample preparation technique eased the identification of real pores versus artifacts (Loucks et al., 2009).

Backscattered-electron (BSE-SEM) images (Camp and Wawak, 2013) and energy dispersive X-ray spectrometry (EDS) (Huang et al., 2003; Curtis et al., 2010) maps were acquired. I used these images to interpret the mineral phases (e.g., dolomite, quartz), document the organic matter distribution, and characterize the pore types. I use "organic matter" as a generic term to classify any organic compound identified petrographically. I did not distinguish between organic matter types (e.g., kerogen or macerals, bitumen, solid bitumen, oil, and pyrobitumen) (Jarvie et al., 2007; Bernard et al., 2012a; Milliken et al., 2014) because this was not possible with SEM petrography alone (Mastalerz et al., 2018).

3.5 EXPERIMENTAL RESULTS

3.5.1 Total porosity

The organic-rich siliceous mudstone and the argillaceous mudstone lithofacies together have a median total porosity of 12.4% whereas the carbonate lithofacies, taken together, have a median total porosity of 3.5% (Figure 3.6). I estimate the fraction of the pore space that lies within the mudstones with Eq. 3.3:

$$Fractional\ pore\ volume\ in\ mudstone = \frac{\phi_{ms} * h_{ms}}{(\phi_{ms} * h_{ms}) + (\phi_c * h_c)}. \qquad \text{Eq. 3.3}$$

h_{ms} and h_c are the total thickness of the mudstone and carbonate respectively and $\varnothing_{ms}$ and $\varnothing_c$ are the median total porosity of the mudstones and carbonates respectively. The siliciclastic mudstones (Figure 3.7A) comprise 82 % of the total thickness of all the core studied in the Wolfcamp A and Wolfcamp B (see Chapter 2); thus h_{ms} = 0.82 and h_c = 0.18. The total porosities are 12.4% and 3.5% for the mudstone and carbonates as stated above. I find that 94 % of the total pore volume is in siliciclastic mudstones (Figure 3.7B) with the remaining 6% present in the carbonates.

The median nuclear magnetic resonance porosity ($\varnothing_{NMR}$), a measure of the liquid-filled porosity, is 90% in the argillaceous mudstone (Figure 3.7B). This indicates that 90% of the pore fluid is liquid in these samples. This lithofacies also has low electrical resistivity in wireline logs (see Chapter 2) and we interpret that it has a very high water saturation. Thompson et al. (2018) also found very high water saturations in similar clay-rich lithofacies in the Wolfcamp B. We interpret that the liquid loss is small because the pore fluid is mostly water (thus less evaporation), because there is little effective porosity (the water is immobile), and because a large fraction of the pore water is clay-bound. The median nuclear magnetic resonance porosity of the organic-rich siliceous mudstone lithofacies is 60% (Figure 3.7B). Its resistivity is much higher than that of the argillaceous mudstone (see Chapter 2). I interpret that this lithofacies is saturated with both liquid hydrocarbons and water. Thompson et al. (2018) and Zhang et al. (2021) indicate that organic-rich siliceous mudstones in the Wolfcamp A and Wolfcamp B units has significant oil saturations.

The median liquid-filled porosity is 70% in the carbonate lithofacies, indicating that they also have a high liquid saturation. The resistivities in carbonate lithofacies (except the dolomudstone) are in general similar or higher than those in the organic-rich siliceous mudstone lithofacies (see Chapter 2). This high resistivity is partly due to their carbonate-rich composition and low clay content. However, this high-resistivity may also indicate that carbonate lithofacies have a significant fraction of their pore volume saturated with liquid hydrocarbons. Thompson et al. (2018) found that carbonate lithofacies have low water saturations in the Wolfcamp A and Wolfcamp B, and Zhang et al. (2021) showed that Wolfcamp A's carbonate lithofacies may act as reservoirs for the oil expelled by the adjacent organic-rich siliceous mudstones.

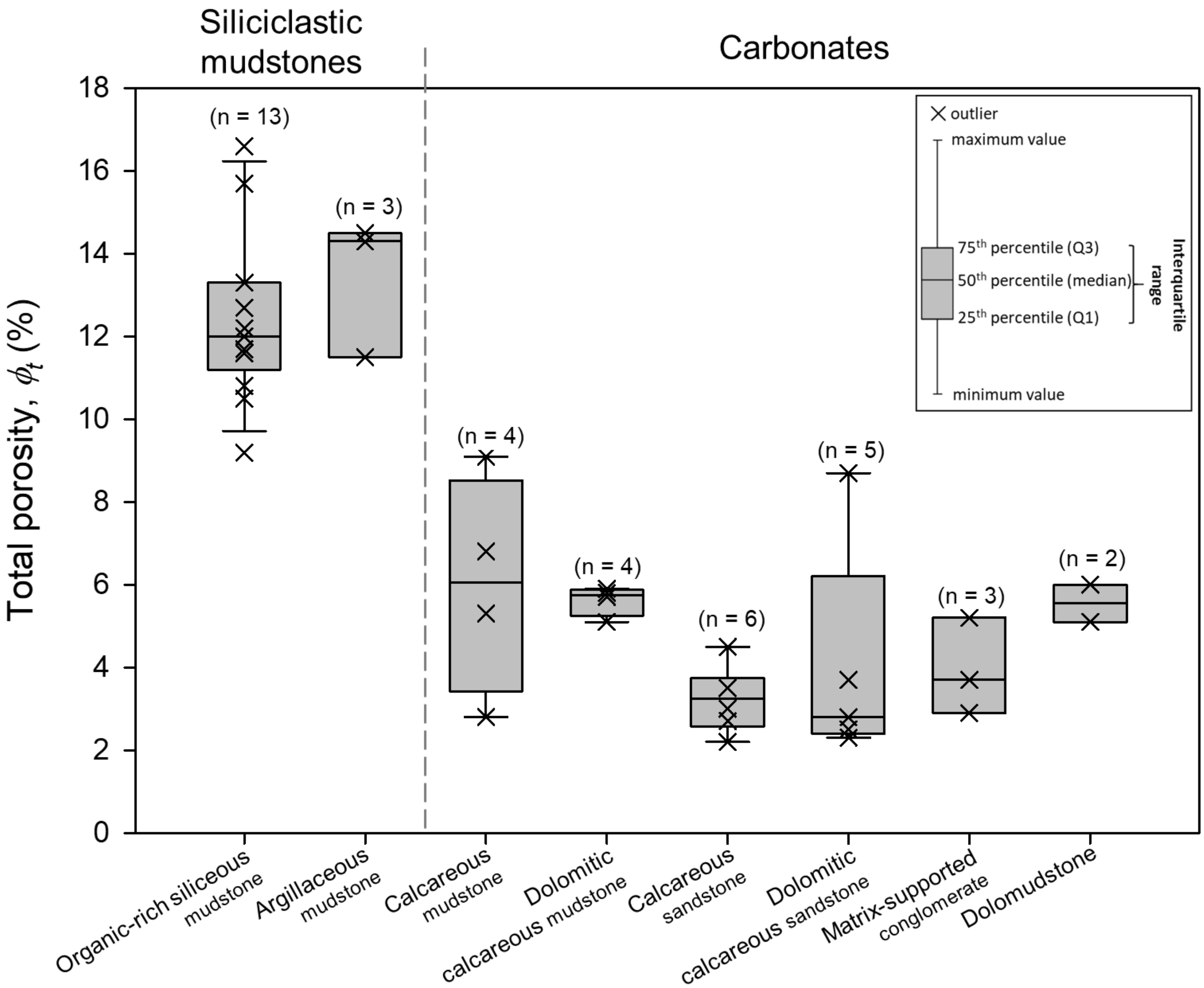

Figure 3.6: Total porosity (ϕ_t) of all samples measured by lithofacies.

The median total porosity value of all mudstones is 12.4% whereas that of the carbonates is 3.5%. For each lithofacies, the top and bottom lines represent the maximum and minimum values, respectively. The top and bottom edges of the grey box mark the first and third percentiles, respectively. The median value is the horizontal line within the box. Values that fall beyond the lower limit (25 percentile – 1.5*interquartile range) and the upper limit (75 percentile + 1.5*interquartile range) represent extremes. Total porosity is the sum of both the helium-derived porosity (ϕ_{He}) and the NMR derived porosity (ϕ_{NMR}) (see Table 3.A1).

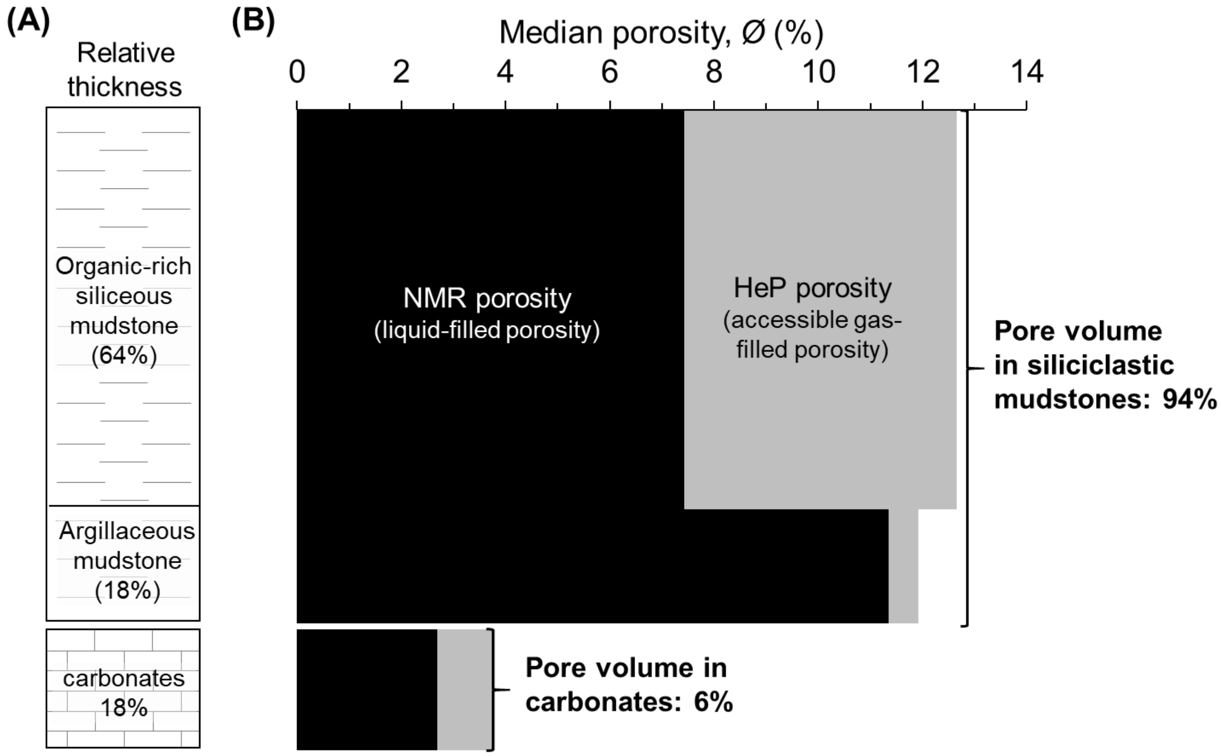

Figure 3.7: Weight averaged pore volume by lithofacies in the upper Wolfcamp interval.

(A) Relative thickness of siliciclastic mudstones and carbonates in the studied Wolfcamp interval. (B) Median NMR porosity (black area) and helium porosity (grey area) in tested samples from siliciclastic mudstones (n = 17 samples) and carbonates (n = 23 samples) lithofacies. The thickness of the bars is proportional to the relative thickness of each lithofacies according to (A).

3.5.2 Permeability

I discuss my effective permeability measurements to dodecane (oil phase) in detail with one experiment on the organic-rich siliceous mudstone and one experiment on the dolomitic calcareous mudstone. I then review how to interpret the matrix permeability from these experiments. I then estimate the in-situ permeability for all of my tested samples and thereby describe the permeability of individual lithofacies.

Permeability-stress behavior and its interpretation

The initial permeability of the organic-rich siliceous mudstone sample is 148 nD (Test 1) at an effective stress (i.e., $Pc - Pp$) of 4500 psi (squares, Figure 3.8). This permeability increases to 521 nD (Test 2) when unloaded to 1000 psi. When re-loaded to 8500 psi effective stress (Test 4), the permeability drops to 22 nD. During the final unloading segment of the test, the permeability is 29 nD (Test 5) and 151 nD (Test 6) at effective stresses of 4500 psi and 2000 psi, respectively. The permeability at 1000 and 4500 psi effective stresses is much higher before being loaded to 8500 psi than it is after being loaded (Figure 3.8). Clearly, the permeability is dependent on the stress history of the experiment: it exhibits hysteresis.

This behavior has been described previously for the organic-rich siliceous mudstone samples from the Wolfcamp by Bhandari et al. (2019). Bhandari et al. attribute the permeability hysteresis to damage done to the rock by the coring and sample preparation process; this is termed sample disturbance. Specifically, microfractures are created by disturbance and during experimental loading these samples are closed. For instance, in sample PN3-108 there is one bedding-parallel microfracture that traverses ¾ of the sample length (Figure 3.9A) that I interpret to be caused by sample disturbance. I infer that this microfracture was open during the first part of the test program (Test 1-3, Figure 3.8). At increasing effective stress, the microfracture closes and the permeability decreased. When unloaded from Test 4 to Test 5 (Figure 3.8), the permeability increases only by ~ 30 %, suggesting that the microfracture probably remains mostly closed. Further unloading to Test 6 results in a permeability increase of ~ 400 %, which I interpret to be due to a partial reopening of the microfracture.

The permeability hysteresis observed in sample PN3-108 (Figure 3.8) is characteristic of additional core plugs that I tested from this lithofacies (Table 3.A1). These samples also exhibited artificial microfractures in micro-CT images. Significant permeability hysteresis is also reported in organic-rich lithofacies from the Wolfcamp (Bhandari et al., 2019), Eagle Ford (Bhandari et al., 2018), Niobrara (Teklu et al., 2018), Montney (Rydzy et al., 2016), and Vaca Muerta (Chhatre et al., 2015) formations.

For samples that exhibit significant permeability hysteresis, I interpret that to estimate the in-situ permeability under steady flow, the fractures must be closed. Therefore, the most reasonable estimate of the matrix permeability are the measurements made after the sample has been loaded to 8500 psi effective stress. In the ensuing section, I plot the permeability measurements made after the sample is loaded to 8500 psi and then after the sample is unloaded from this point to 4500 psi. Bhandari et al. (2018) used a dual permeability model and a pulsed decay permeability experiment on an Eagle Ford sample to illustrate that this approach successfully captured the matrix permeability.

The initial permeability of the dolomitic calcareous sandstone is 2054 nD (Test 1) at an effective stress of 4500 psi (circles, Figure 3.8). This permeability remains almost constant throughout the rest of the test program. When the effective stress is increased from 1000 psi (Test 2) to 8500 psi (Test 4), the permeability decreases by ~5%. This permeability loss almost completely recovered in Test 5 and Test 6. Hence, the dolomitic calcareous sandstone has systematically higher permeabilities than the mudstone, and it behaves almost perfectly elastically.

I attribute the minimal change in permeability with stress and the negligible permeability hysteresis throughout the test program to better sample quality. The micro-CT images of the tested core plug (Figure 3.9B) show that the sample is intact. In general, the micro-CT images acquired on additional tested core plugs from the dolomitic calcareous sandstone and other carbonate lithofacies show less microfractures than the organic-rich siliceous mudstone core plugs. Hence, lithofacies with high carbonate content tend to preserve their integrity during coring, resulting in little or no permeability hysteresis.

The samples were loaded in the laboratory to much higher effective stresses than are inferred to be present today in the study area (shaded region, Fig 3.8). This is because there is significant overpressure at this location. The in situ mean effective stress (σ'_m) is estimated by:

$$\sigma'_m = \frac{(\sigma_v - P_p) + 2(\sigma_h - P_p)}{3}, \qquad \text{Eq. 3.4}$$

where σ_v is the overburden stress, and σ_{hmin} is the least principal stress, and P_p is the pore pressure. Eq. 3.4 assumes that one of the principal stresses is vertical and that the two horizontal stresses are equal. The average overburden gradient is 1.075 psi/ft and was determined from integration of density log data. The least principal stress was calculated from regional studies of the fracture gradient and it lies at an average gradient of 0.86 psi/ft and 0.95 psi/ft, depending on the depth of the samples. The average overpressure gradient ranges from 0.79 psi/ft to 0.90 psi/ft. Based on these estimates, the mean effective stress for the shallowest sample (PN2-2, Table 3.A1) and the deepest sample (PN6-118, Table 3.A1) is 1665 psi and 1038 psi, respectively. This is an estimate of the present-day effective stress but the sample may have been loaded to much higher stresses in the past because significant erosion has occurred in the Permian Basin (Sinclair, 2007).

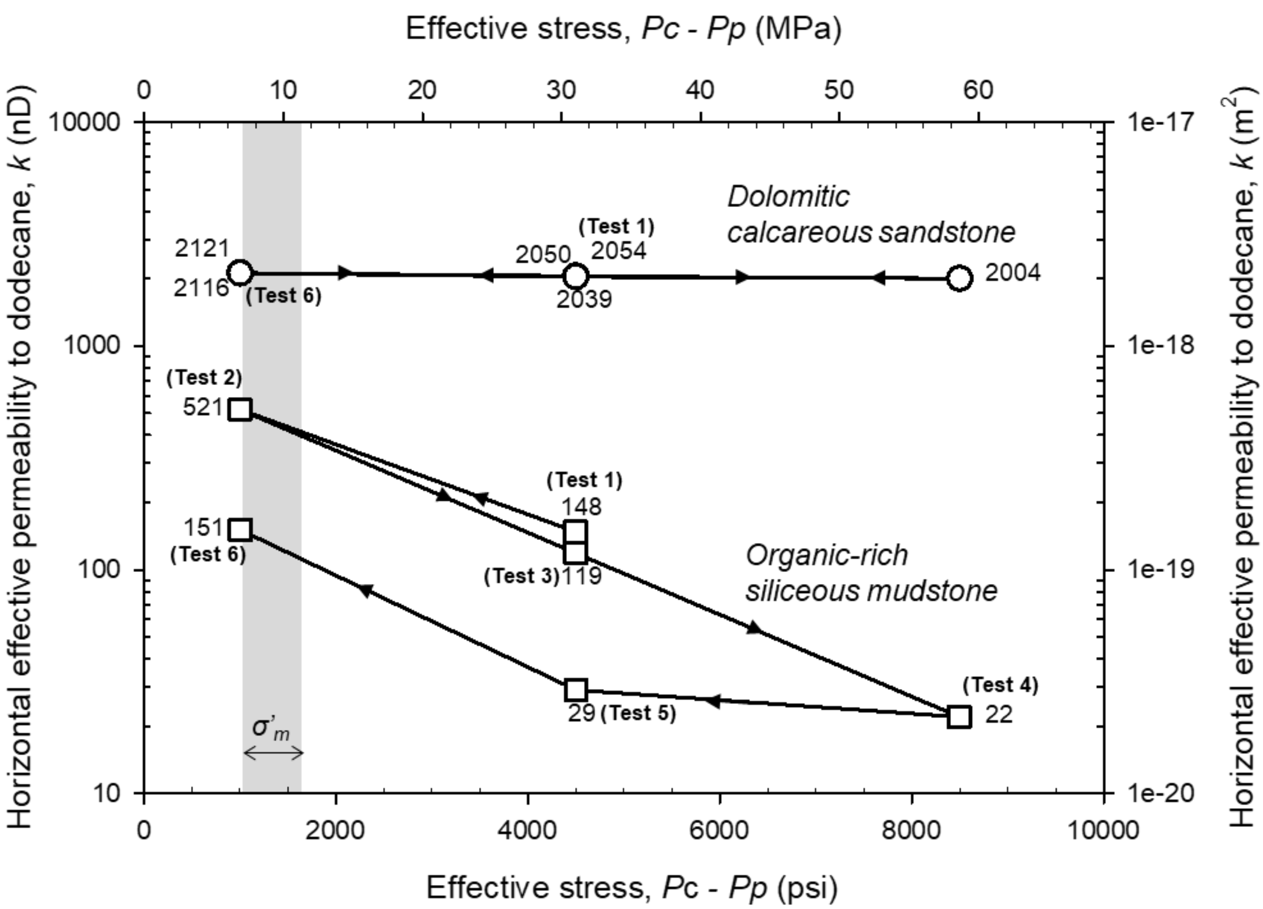

Figure 3.8: Plot showing the horizontal permeability to dodecane measured in samples from the organic-rich siliceous mudstone (squares) and dolomitic calcareous sandstone (circles) lithofacies (as examples) at the effective stress conditions specified in my test program (Figure 3.4).

The arrows indicate the loading and unloading confining pressure paths. The vertical grey-shaded rectangle represents the upper bound (1665 psi) [11.48 MPa] and lower bound (1038 psi) [7.16 MPa] of the in-situ mean effective stress (σ'_m) for the depths of the samples tested in this work.

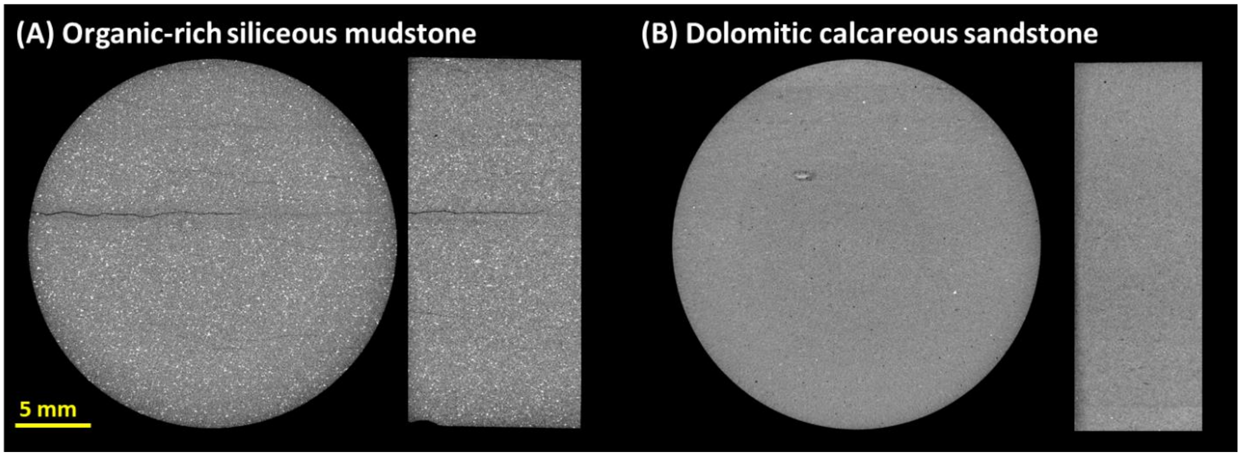

Figure 3.9: Micro-CT cross-sectional views of core plugs acquired after sample preparation and before conducting the permeability tests.

(A) Organic-rich siliceous mudstone sample (PN 3-108) exhibiting one artificial microfracture. (B) Dolomitic calcareous sandstone sample (PN D-17) is intact. Images correspond to diametrical (left) and longitudinal (right) cross-sections. The samples were CT scanned without confinement. Voxel size is ~ 25 micrometers.

Matrix permeability by lithofacies

Figure 3.10 summarizes all of the permeabilities measured at 8500 psi and then after unloading from 8500 psi to 4500 psi. As described above, these values are interpreted to be the best measure of the in-situ matrix permeability.

The organic-rich siliceous mudstone comprises 65% of the thickness of the studied section and 74% of the pore volume (Figure 3.7, Table 3.A1). Its permeability ranges from 5 to 57 nD with a median value of 21 nD (Table 3.2). The permeabilities measured in Sample PN3-108 at 8500 psi (22 nD) and 4500 psi (29 nD) (Figure 3.8, Table 3.A1) are very similar to the permeability of 32 nD determined by Zhan et al. (2018) from well tests conducted in a 25-ft Wolfcamp B interval of organic-rich siliceous mudstone strata in this region of the Delaware Basin. This supports the interpretation that our measurement protocol is capturing the in-situ matrix permeabilities.

The argillaceous mudstone is the second mudstone lithofacies and comprises 18% of the stratigraphic thickness and 20% of the pore volume (Figure 3.7, Table 3.A1). It is the least permeable lithofacies (k_{median} < 1 nD, Table 3.2). I interpret that this lithofacies is both very fine grained and largely, if not totally, water saturated. Thus, permeability measurements attempting to measure permeability to dodecane are expected to be very low.

The carbonates as a whole comprise only 18% of the section and 6% of the pore volume (Figure 3.7, Table 3.A1). Their permeabilities have a fairly wide range. All of the non-dolomitic lithofacies have median permeabilities of less than 40 nD (Table 3.2). The calcareous mudstone and the matrix-supported conglomerate have permeabilities that are in the same range as the organic-rich siliceous mudstone (38 nD, 30 nD, and 21 nD, respectively) (Table 3.2). The calcareous sandstone and dolomudstone lithofacies have both much lower median permeabilities of 3 nD (Table 3.2). However, what is striking is that the calcareous mudstone and the calcareous sandstone lithofacies, when dolomitic (i.e., dolomitic calcareous mudstone, dolomitic calcareous sandstone), have systematically higher permeabilities than the rest of lithofacies. The median permeabilities (k_{median}) are 216 nD and 904 nD in the dolomitic calcareous mudstone and dolomitic calcareous sandstone lithofacies, respectively (Table 3.2).

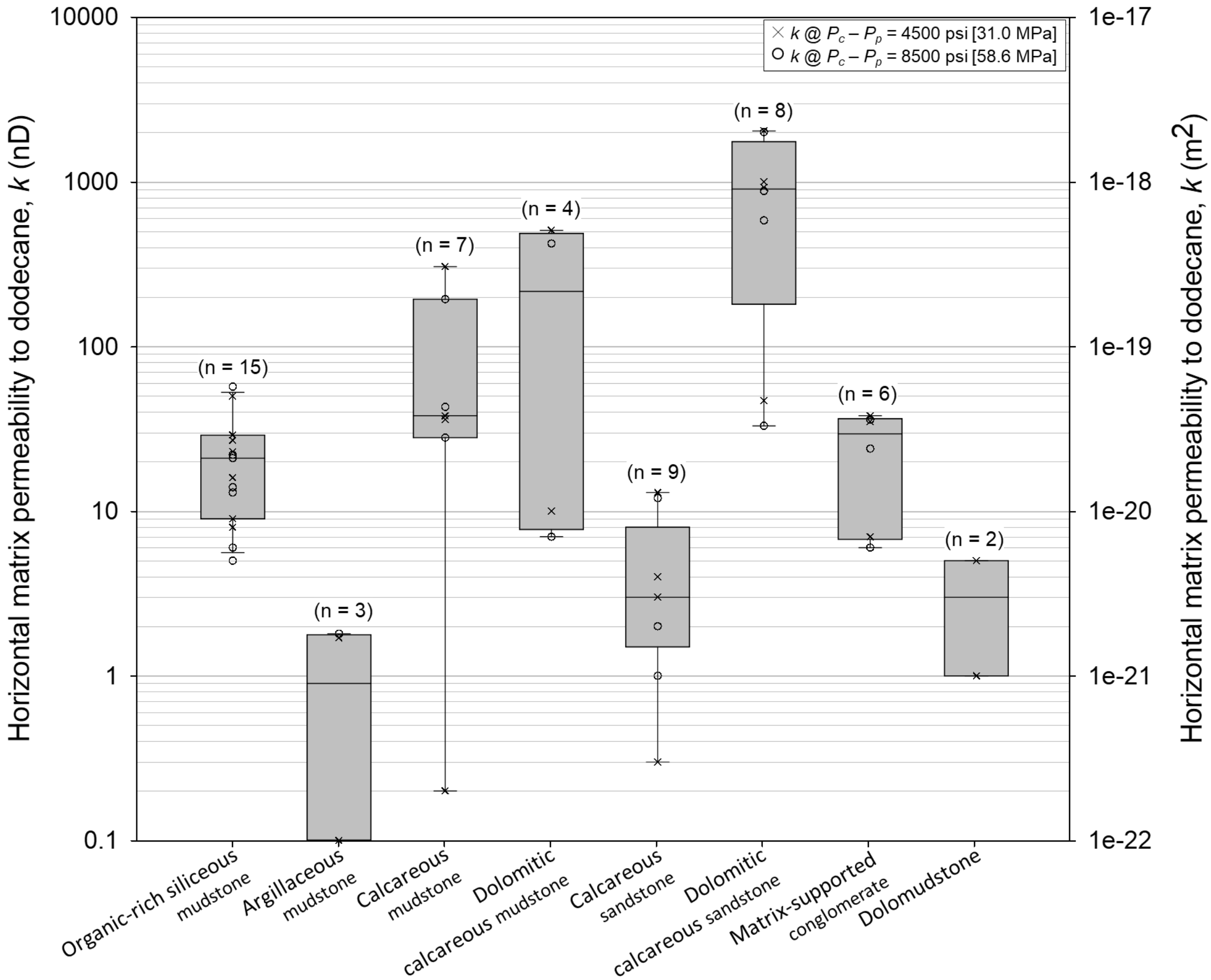

Figure 3.10. Horizontal permeability to dodecane (k) of all samples measured by lithofacies.

For each lithofacies, the top and bottom lines represent the maximum and minimum values, respectively. The top and bottom edges of the grey box mark the first and third percentiles, respectively. The median value is the horizontal line within the box. Values that fall beyond the lower limit (25 percentile-1.5*interquartile range) and the upper limit (75 percentile+1.5*interquartile range) represent extremes. The 'n' represents the number of permeability measurements conducted at $Pc – Pp$ = 4500 psi (cross) and $Pc – Pp$ = 8500 psi (circles) per lithofacies.

Table 3.2. Summary of minimum (k_{min}), maximum (k_{max}), and median (k_{median}) horizontal permeabilities to dodecane measured by lithofacies.

Lithofacies	k_{min} (nD)	k_{max} (nD)	k_{median} (nD)
Organic-rich siliceous mudstone	5	57	21
Argillaceous mudstone	< 0.1	2	< 1
Calcareous mudstone	< 1	306	38
Dolomitic calcareous mudstone	7	508	216
Calcareous sandstone	< 1	13	3
Dolomitic calcareous sandstone	33	2039	904
Matrix-supported conglomerate	6	38	30
Dolomudstone	1	5	3

3.5.3 Pore scale controls on permeability

I now explore the pore scale characteristics of each lithofacies that may contribute to the permeability that is observed.

Organic-rich siliceous mudstone

The organic-rich siliceous mudstone is primarily composed of clay- to silt-sized detrital, biogenic, and microcrystalline quartz within a clay-rich matrix (Figure 3.11A). The organic matter occurs as micrometer-sized detrital particles (Figure 3.11A) and occupying the interparticle pores between grains (Figure 3.11B). A rigid framework of silt-sized grains and clays often encloses the organic matter (Figure 3.11C, D).

This lithofacies has abundant interparticle pores between clays and quartz microcrystals, and between other clay- to silt-size particles (Figure 3.11E). I calculated the equivalent circular diameter (D_{eq}) of the pores by measuring the pore area in the SEM images using ImageJ and computing its equivalent diameter (assuming it has a circular section). Most pores have an equivalent diameter smaller than 300 nm. I observed some larger interparticle pores with an equivalent diameter up to 2,000 nm; these are often associated with potassium feldspars (Figure 3.11F). I interpret these larger pores were formed by partial dissolution of the potassium feldspars. The intraparticle pores occur primarily within the organic matter (Figure 3.11C, D). These are irregular ellipsoids; their D_{eq} ranges from 300 nm (Figure 3.11C) to less than 50 nm (Figure 3.11D). Similar organic matter pores have been observed in other formations and are interpreted to have formed during thermal maturation of organic matter (Loucks et al., 2009; Passey et al., 2010; Schieber, 2010; Bernard et al., 2012b; Curtis et al., 2012). Intraparticle pores within clay aggregates, micas, and other rock components are also present, but they are not volumetrically significant.

I interpret the size of interparticle pores controls permeability in this lithofacies. I tested eight organic-rich siliceous mudstone samples and found that the permeability varied from 5 to 57 nD (Figure 3.10, Table 3.2). Two of the organic-rich siliceous mudstone samples with the highest permeability (Sample PN3-33 and Sample PN6-75, Table A.1) have the largest interparticle pores (micrometer-sized), as observed on their SEM images. I interpret that fluid flow occurs primarily through interparticle pores in this lithofacies.

The TOC content in Sample PN 3-108 (k = 22 nD to 29 nD, Figure 3.8 and Table 3.A2). is 2.12 wt.%, or ~ 4.20 vol.%, assuming a weight-to-volume conversion factor of approximately two (Jarvie et al., 2007; Loucks et al., 2009). I estimate the porosity within the organic matter to be up to 50 % (e.g., Figure 3.11C, D); thus, ~2% of the sample's bulk volume is porosity within the organic matter. Given that the actual porosity is 13.3% (Figure 3.6), I infer most pore volume is within interparticle pores. This supports my interpretation that the interparticle pores and their size are responsible for most permeability in this lithofacies. Bohacs et al. (2013) also suggested that large (e.g., 1 μm to 2 μm) inter- and intra-particle pores are likely required in low-permeability formations to produce liquid hydrocarbons at economic rates.

The mercury injection capillary pressure (MICP) data experiments support the interpretation that samples with larger interparticle pores have higher permeability (Figure 3.12A, B). For example, Sample PN3-108 which has a higher measured permeability (k = 22 nD to 29 nD) than Sample PN5-12 (k = 6 nD to 9 nD), exhibited a lower displacement pressure (P_{de}) of 8626 psi and a larger modal pore throat diameter (D_t) of 13 nm than Sample PN5-12 (P_{de} = 12791 psi; D_t = 11 nm).

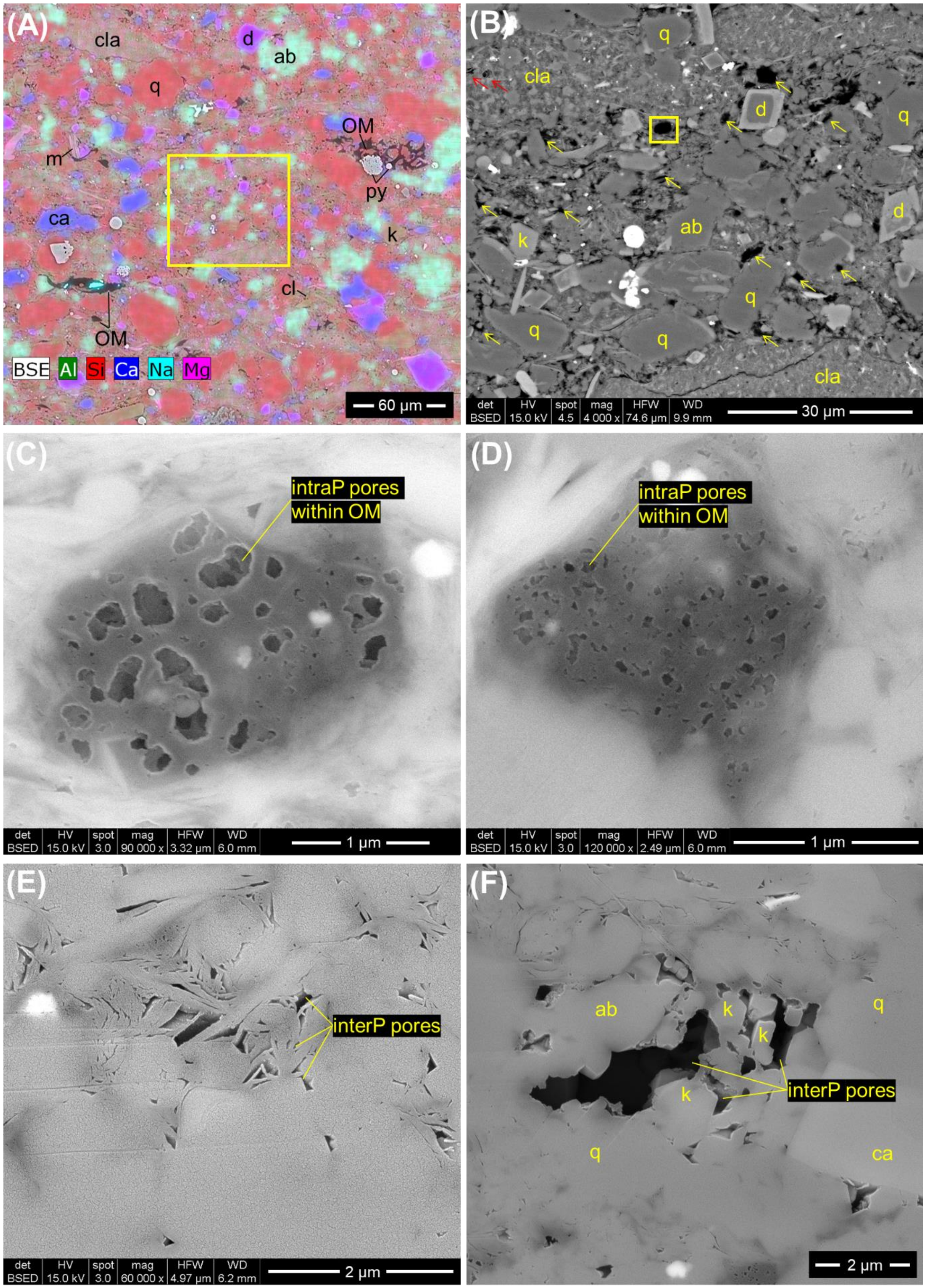

(A)
cla
d
ab
q
OM
m
py
ca
k
cl
OM
BSE Al Si Ca Na Mg
60 µm
(B)
q
cla
d
q
ab
k
d
q
q
q
cla
det BSED HV 15.0 kV spot 4.5 mag 4 000 x HFW 74.6 µm WD 9.9 mm
30 µm
(C)
intraP pores within OM
det BSED HV 15.0 kV spot 3.0 mag 90 000 x HFW 3.32 µm WD 6.0 mm
1 µm
(D)
intraP pores within OM
det BSED HV 15.0 kV spot 3.0 mag 120 000 x HFW 2.49 µm WD 6.0 mm
1 µm
(E)
interP pores
det BSED HV 15.0 kV spot 3.0 mag 60 000 x HFW 4.97 µm WD 6.2 mm
2 µm
(F)
ab
k
k
q
k
interP pores
q
ca
2 µm

Figure 3.11: Organic-rich siliceous silty mudstone lithofacies: FE-SEM images of Ar-ion milled sample.

(A) Low magnification color EDS elemental map (aluminum is green, silicon is red, calcium is dark blue, sodium is aqua, and magnesium is magenta) superimposed on BSE SEM image showing silt quartz (q), albite (ab), dolomite (d), calcite (ca), clays (cl), clay-mineral aggregate (cla), mica (m), potassium feldspar (k), pyrite (py) and organic matter (OM). Sample PN3-108. (B) Enlargement of yellow-framed area in (A). Organic matter is filling most pores between clay- to silt-sized matrix components (yellow arrows). (C) Enlargement of yellow-framed area in (B) showing porous organic matter particle enclosed by clays and other rigid grains in the matrix. (D) Image showing intraparticle pores within the organic matter. (E) Image showing interparticle pores between clays and other grains. Sample PN6-75. (F) Image of interparticle pore between potassium feldspars (k), albite (ab), and quartz (q). I interpret that the dissolution the potassium feldspar formed this pore. The potassium feldspar grains shown in the image correspond to the non-dissolved areas of the mineral. Sample PN6-75. det = detector; BSED = back-scattered electron detector; HV = high voltage (accelerating voltage); spot = spot size; mag = magnification; HFW = horizontal frame width; WD = working distance.

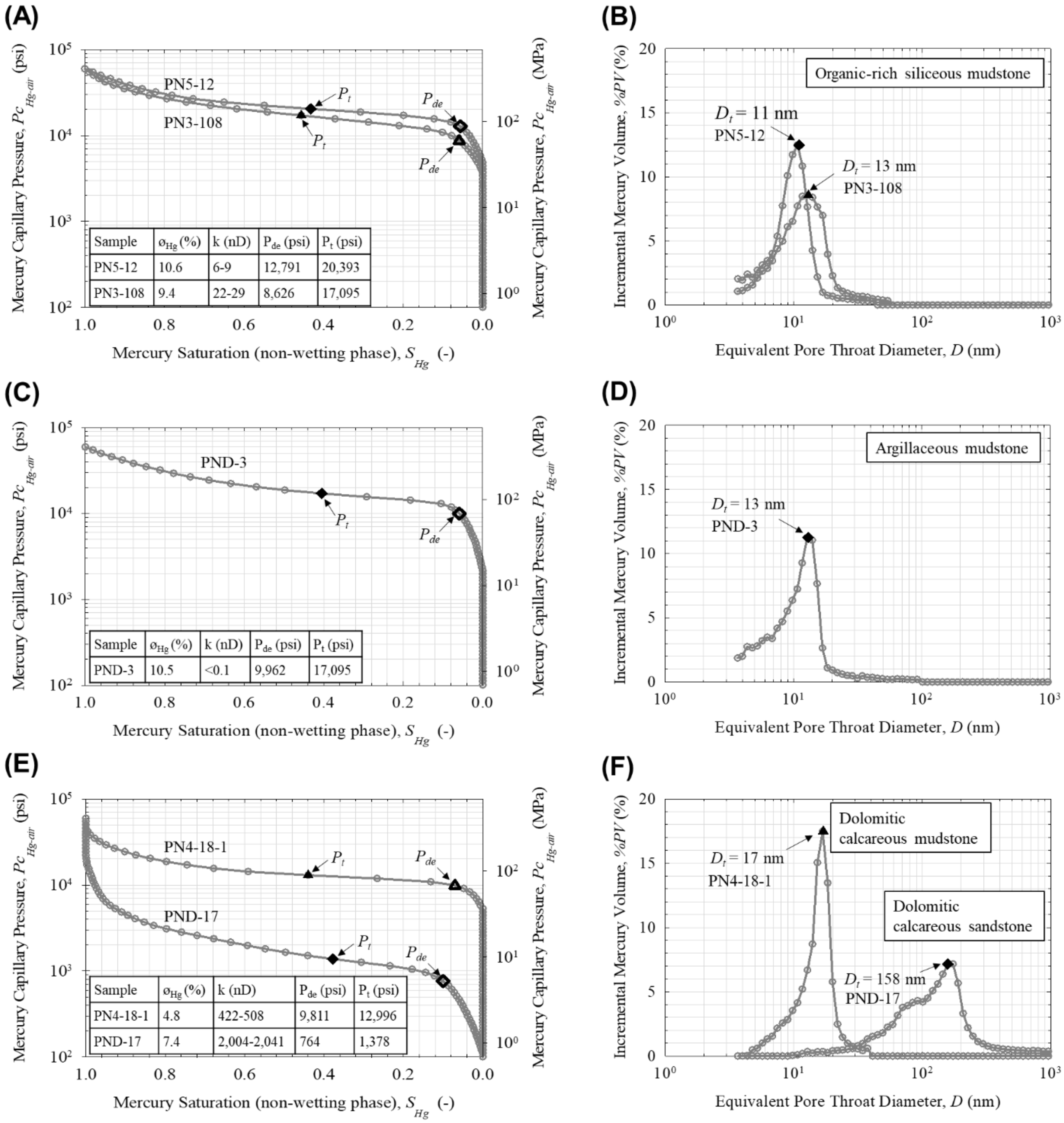

Sample	ϕ_{Hg} (%)	k (nD)	P_{de} (psi)	P_t (psi)
PN5-12	10.6	6-9	12,791	20,393
PN3-108	9.4	22-29	8,626	17,095

Sample	ϕ_{Hg} (%)	k (nD)	P_{de} (psi)	P_t (psi)
PND-3	10.5	<0.1	9,962	17,095

Sample	ϕ_{Hg} (%)	k (nD)	P_{de} (psi)	P_t (psi)
PN4-18-1	4.8	422-508	9,811	12,996
PND-17	7.4	2,004-2,041	764	1,378

Figure 3.12. Drainage capillary pressure and pore throat size distribution curves in samples tested for permeability.

(A) & (B) Organic-rich siliceous mudstone samples PN5-12 (k = 6 nD to 9 nD) and PN3-108 (k = 22 nD to 29 nD). (C) & (D) Sample PND-3 (k < 1 nD) from the argillaceous mudstone lithofacies. (E), (F) Sample PN4-18-1 (k = 422 nD to 508 nD) from the dolomitic calcareous mudstone lithofacies, and Sample PND-17 (k = 2004 nD to 2041 nD) from the dolomitic calcareous sandstone lithofacies. Curves were obtained using MICP measurements on whole sample in PN5-12, and crushed samples in PN3-108, PND-3, PN4-18-1, and PND-17. PV = pore volume, $Ø_{Hg}$ = MICP porosity, D_t = threshold diameter, k = permeability to dodecane, P_t = threshold pressure, and P_{de} = extrapolated displacement pressure determined from a hyperbolic fit to the displacement curve and its projection to a horizontal asymptote (see Thomeer, 1960).

Argillaceous mudstone

The argillaceous mudstone lithofacies is primarily composed of clays and clay- to silt-sized detrital quartz and dolomite crystals (Figure 3.13A, B). The organic matter is scattered throughout the matrix (Figure 3.13C) or mixed with clays (Figure 3.13D). This lithofacies has lower TOC content, higher clay content (~ 45 wt.%, Appendix 3.A), finer-grained detrital quartz, and lacks microcrystalline quartz cement relative to the organic-rich siliceous mudstone lithofacies.

Interparticle pores between clays (Figure 3.13E) dominate the pore system in this lithofacies. Their equivalent diameter (D_{eq}) is typically smaller than 300 nm. They generally have a polygonal shape with straight edges between randomly oriented clay-platelets (Figure 3.13F). Interparticle pores between clays and other grains (Figure 3.13E) and intraparticle pores within the organic matter (Figure 3.13C,D) are less abundant than the interparticle pores between clays. Therefore, I infer that fluid flow occurs primarily through the interparticle pores between clays.

The measured permeability of this lithofacies is extremely low (k = 0.1 nD to 2 nD, Figure 3.10) compared to the organic-rich siliceous mudstone permeability (k = 8 nD to 57 nD, Figure 3.10). However, the MICP data (Figure 12C, D) show the pore throat size distributions are almost similar for these two lithofacies. The displacement pressure in this mudstone is smaller (P_{de} = 9,962 psi, Figure 3.12C), and the modal pore throat size is slightly larger (D_t = 13 nm, Figure 3.12D) than in the organic-rich siliceous mudstone (Sample PN5-12, P_{de} = 12,791 psi, D_t = 11 nm, k = 6 nD to 9 nD, Figure 3.12A,B). I infer that my measured permeability to dodecane for the argillaceous mudstone is extremely low because there is a significant water saturation in the sample. The pore volume in the argillaceous mudstone sample is ~80% liquid-saturated (Figure 3.6). I interpret the majority of this liquid to be water, based on the low resistivity of this lithofacies (see Chapter 2). Since I use dodecane (oil phase) to measure permeability, and the water saturation is high, the effective permeability to dodecane is low.

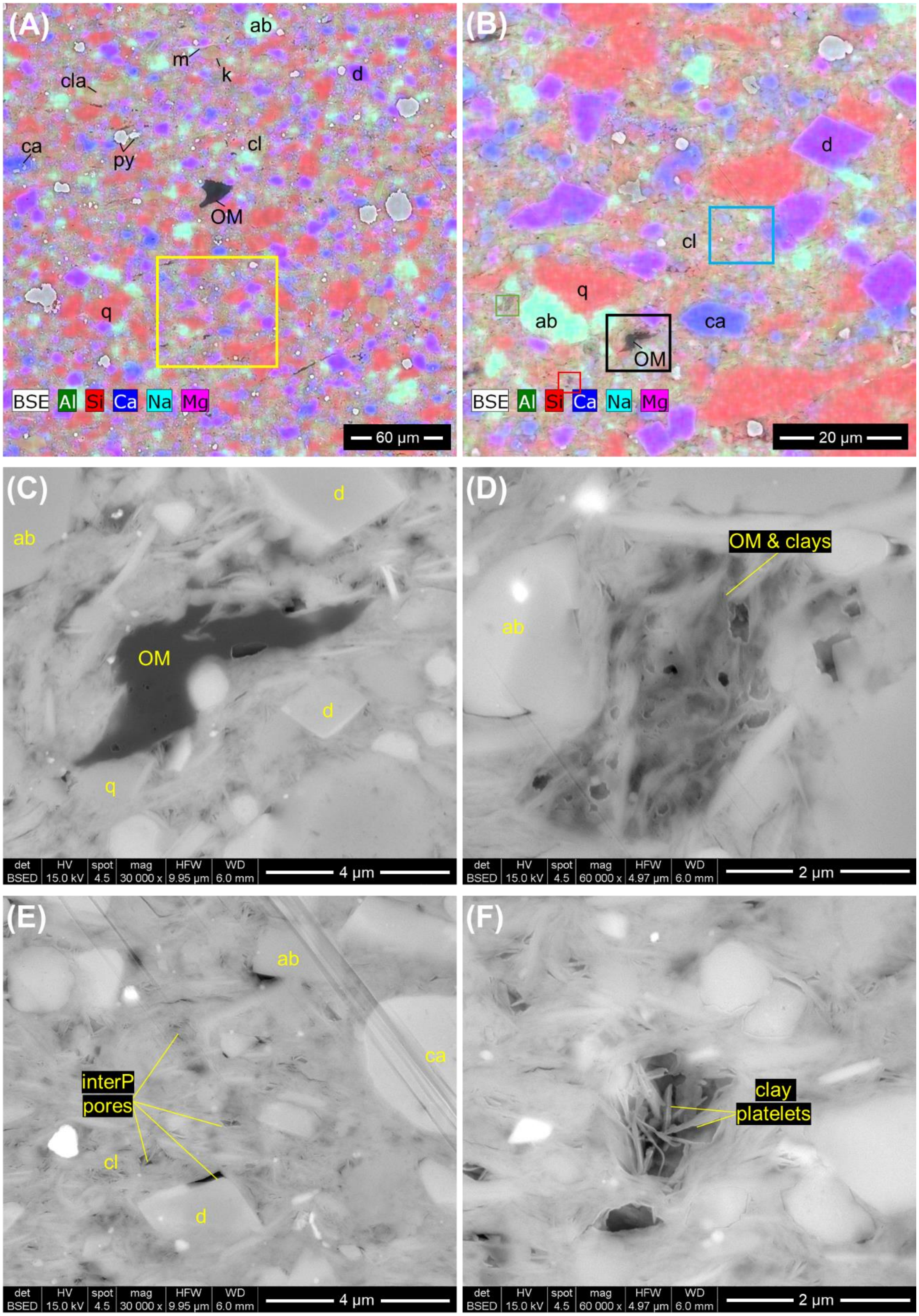
(A)
ab
m
k
d
cla
ca
py
cl
OM
q
BSE Al Si Ca Na Mg
60 µm
(B)
d
cl
q
ab
ca
OM
BSE Al Si Ca Na Mg
20 µm
(C)
d
ab
OM
d
q
det BSED HV 15.0 kV spot 4.5 mag 30 000 x HFW 9.95 µm WD 6.0 mm
4 µm
(D)
OM & clays
ab
det BSED HV 15.0 kV spot 4.5 mag 60 000 x HFW 4.97 µm WD 6.0 mm
2 µm
(E)
ab
ca
interP pores
cl
d
det BSED HV 15.0 kV spot 4.5 mag 30 000 x HFW 9.95 µm WD 6.0 mm
4 µm
(F)
clay platelets
det BSED HV 15.0 kV spot 4.5 mag 60 000 x HFW 4.97 µm WD 6.0 mm
2 µm

Figure 3.13: Argillaceous mudstone lithofacies: FE-SEM images of Ar-ion milled sample.

(A) Low magnification color EDS elemental map (aluminum is green, silicon is red, calcium is dark blue, sodium is aqua, and magnesium is magenta) superimposed on BSE SEM image showing silt quartz (q), albite (ab), dolomite (d), calcite (ca), clays (cl), mica (m), potassium feldspar (k), pyrite (py) and organic matter (OM). (B) Enlargement of yellow-framed area in (A) showing that clays dominate the composition of this lithofacies. Clay- to silt-sized grains of detrital quartz and dolomite crystals are scattered throughout the rock. (C) Enlargement of black-framed area in (B) showing deformed organic matter particle surrounded by clays and other grains in the matrix. This organic matter particle has only a few intraparticle pores. (D) Enlargement of green-framed area in (B) showing porous organic matter intermixed with abundant clays. (E) Enlargement of blue-framed area in (B) showing nanometer-sized interparticle pores between clays, and between clays and other grains. (F) Enlargement of red-framed area in (B) showing interparticle pores between randomly orientated clays. All images are from Sample PND-3. det = detector; BSED = back-scattered electron detector; HV = high voltage (accelerating voltage); spot = spot size; mag = magnification; HFW = horizontal frame width; WD = working distance.

Dolomitic calcareous mudstone and dolomitic calcareous sandstone

The dolomitic calcareous mudstone and dolomitic calcareous sandstone lithofacies are composed of dolomite rhombic crystals and dolomitized microfossils separated by detrital and microcrystalline quartz and other grains (Figure 3.14A, Figure 3.15A,C). The dolomitic calcareous sandstone has microfossils larger than 62.5 µm, low clay content (e.g., < 7 wt.%, Table A.2), and is located in the lower-to-middle parts of the dolomitized carbonate flow deposit (see Chapter 2). In contrast, the dolomitic calcareous mudstone generally has microfossils smaller than 62.5 µm, higher clay content (e.g., > 9 wt.%, Table A.2), and is located in the middle-to-upper parts of dolomitized flow deposit (see Chapter 2).

Both lithofacies have a similar pore system consisting of intraparticle pores within dolomitized microfossils and dolomite crystals and interparticle pores between quartz microcrystals and other grains. Intraparticle pores within dolomitized microfossils exhibit irregular polygonal shapes with straight margins (Figure 3.14A-D, Figure 3.15A,B). Their equivalent diameter (D_{eq}) is up to 18,000 nm. These pores may host migrated organic matter (Figure 3.15B), indicating they were most likely connected to the effective pore volume during hydrocarbon migration. The intraparticle pores within dolomite crystals have a D_{eq} typically smaller than 500 nm. The intraparticle pores within dolomitized microfossils pores were probably formed by dissolution, whereas the intraparticle pores within dolomite crystals are fluid inclusions, dissolution pores, or both. The interparticle pores dominate the pore system in these two lithofacies. They are predominantly between quartz microcrystals (Figure 3.14E,F, Figure 3.15E,F), and some are filled with porous organic matter. Their D_{eq} is typically up to 1,000 nm. In the calcareous sandstone lithofacies, interparticle pores between dolomite crystals and quartz exhibit D_{eq} up to 40,000 nm (Figure 3.14D). These larger pores resemble cavities, and there are no signs of collapse into them.

I interpret that the pore system observed in the dolomitic calcareous mudstone and dolomitic calcareous sandstone developed in the following manner. First, dolomite replacement occurred in the carbonate flow deposit during shallow burial, based on the formation temperatures of 30˚C to 50˚C estimated by Dobber and Goldstein (2020) in similar Wolfcamp dolomite to those observed petrographically here. This early dolomitization may be explained by the organogenic model (Mazzullo, 2000). Precipitation of microcrystalline quartz in the interparticle pores of the carbonate flow deposit also occurred during shallow burial. The microcrystalline quartz prevented compaction of the deposit throughout burial, and the effective porosity and permeability were preserved. Second, late-stage iron-rich dolomitization occurred, as evidenced by the presence of a) iron-rich zones surrounding or completely replacing a magnesium-rich core in dolomite crystals, and b) the iron-rich dolomite composition of the microfossils (Figure 3.16). Finally, fluids lacking magnesium or acidified pore waters entered the dolomitized carbonate deposit and partially dissolved the dolomitized microfossils, forming the intraparticle pores. During this stage, the micrometer-scale interparticle pores in the dolomitic calcareous sandstone may have formed by complete dissolution of dolomitized microfossils or by progressive dissolution and enlargement of former pores that connected to high-permeability pathways in the rock. Fredd and Fogler (1998) describe a similar pore growth mechanism by which the flow and reaction of certain fluids (e.g., acids) with carbonate porous media results in formation of highly conductive flow channels (i.e., wormholes).

I observe the larger pore throats in the dolomitic calcareous sandstone result in the higher measured permeabilities. The permeabilities of dolomitic calcareous mudstone samples are between 7 nD and 508 nD with a median value of 216 nD, whereas samples from the dolomitic calcareous sandstone have permeabilities between 33 nD and 2041 nD with a median value of 904 nD (Figure 3.10). The dolomitic calcareous sandstone sample PND-17 (k = 2004 nD to 2041 nD, Table A1.1) has a lower displacement pressure (P_{de} = 764 psi, Figure 3.12E), larger modal pore throat diameter (D_t = 158 nm, Figure 3.12F), and broader pore throat size distribution than the dolomitic calcareous mudstone sample PN4-18-1 (k = 422 nD to 508 nD, P_{de} = 9,811 psi, D_t = 17 nm, Figure 3.12E,F).

It is interesting to compare Sample PN4-18-1 and sample PN3-108 (dolomitic calcareous mudstone vs. organic-rich siliceous mudstone). Sample PN 4-18-1 is ~20 times more permeable (k = 422 nD to 508 nD, Table 3.A1) and ~2 times less porous ($Ø_t$ = 5.9 %, Table 3.A1) than Sample PN3-108 (k = 22 nD to 29 nD, $Ø_t$ = 13.3%, Table 3.A1). In addition, Sample PN4-18-1 has a slightly higher P_{de} (9811 psi, Figure 3.12E) and D_t (17 nm, Figure 3.12F) than Sample PN3-108 (P_{de} = 8626 psi and D_t = 13 nm, Figure 3.12A, B). I interpret that, despite its low porosity, the dolomitic calcareous mudstone has a higher volume of larger pore throats that are similar in size (D_t = 17 nm at incremental mercury volume of 17.5%) than the organic-rich siliceous mudstone (D_t = 13 nm at incremental mercury volume of 8.5%), resulting in a higher measured permeability. I infer that these pore throats correspond to the interparticle pores between quartz microcrystals (Figure 3.14E, F), suggesting that a pervasive precipitation of microcrystalline quartz formed a more effectively connected interparticle pore volume than that in the organic-rich siliceous mudstone. These data further support my interpretation that the interparticle pore volume is a primary control for permeability.

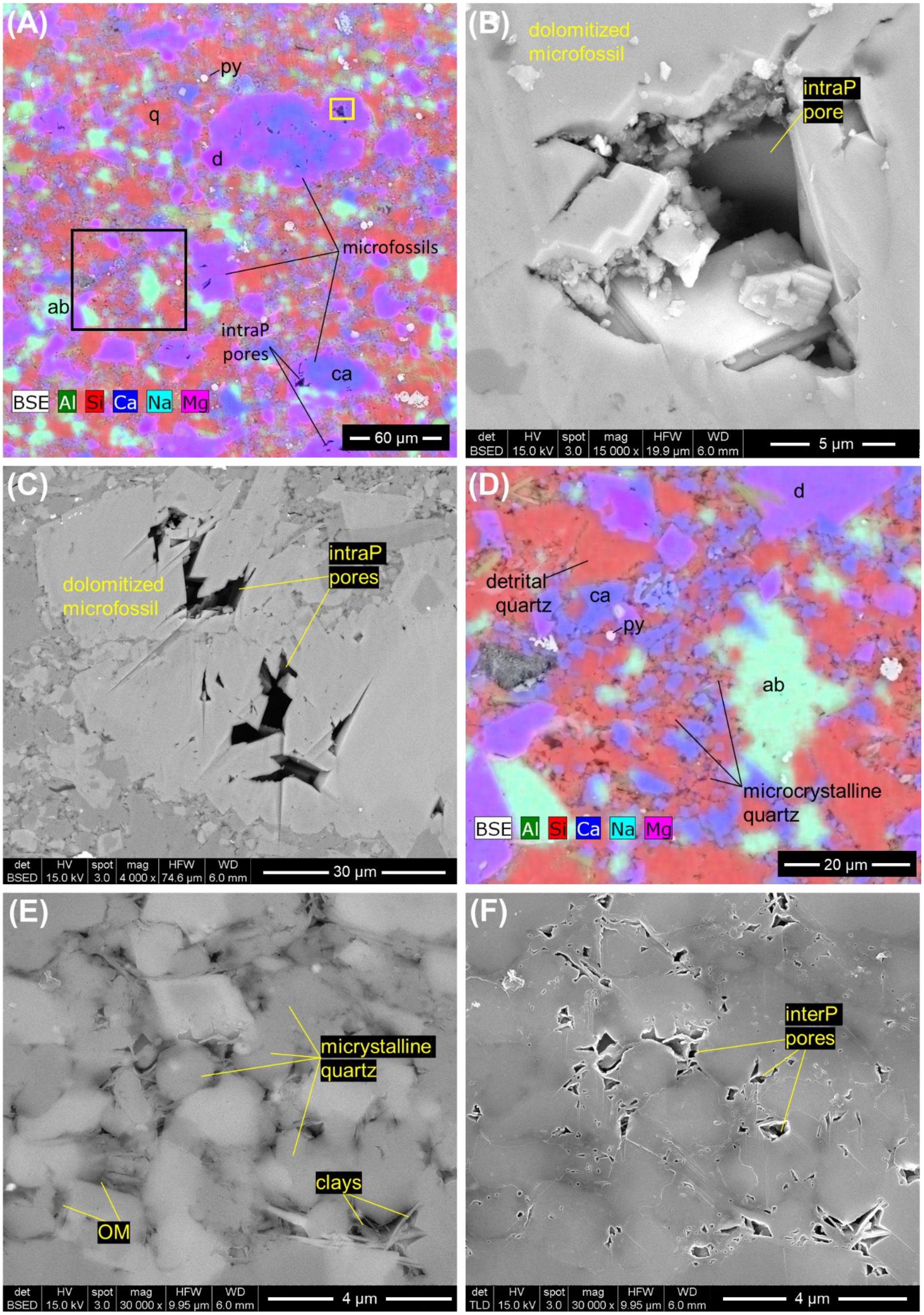

(A)
py
q
d
microfossils
ab
intraP
pores
ca
BSE
Al
Si
Ca
Na
Mg
60 µm
(B)
dolomitized
microfossil
intraP
pore
det BSED
HV 15.0 kV
spot 3.0
mag 15 000 x
HFW 19.9 µm
WD 6.0 mm
5 µm
(C)
dolomitized
microfossil
intraP
pores
det BSED
HV 15.0 kV
spot 3.0
mag 4 000 x
HFW 74.6 µm
WD 6.0 mm
30 µm
(D)
d
detrital
quartz
ca
py
ab
microcrystalline
quartz
BSE
Al
Si
Ca
Na
Mg
20 µm
(E)
micrystalline
quartz
clays
OM
det BSED
HV 15.0 kV
spot 3.0
mag 30 000 x
HFW 9.95 µm
WD 6.0 mm
4 µm
(F)
interP
pores
det TLD
HV 15.0 kV
spot 3.0
mag 30 000 x
HFW 9.95 µm
WD 6.0 mm
4 µm

Figure 3.14: Dolomitic calcareous mudstone lithofacies: FE-SEM images of Ar-ion milled samples.

(A) Low magnification color EDS elemental map (aluminum is green, silicon is red, calcium is dark blue, sodium is aqua, and magnesium is magenta) superimposed on BSE SEM image showing quartz (q), albite (ab), dolomite (d), calcite (ca), and pyrite (py). Dolomite occurs as rhombic crystals or as dolomitized microfossils with micrometer-sized intraparticle pores. Sample PN4-18-1. (B) Enlargement of yellow-framed area in (A) showing micrometer-sized intraparticle pore within dolomitized microfossil. (C) Polygonal intraparticle pore within dolomitized microfossil. Sample PN4-18-1. (D) Enlargement of black-framed area in (A) showing clay-sized quartz microcrystals mixed with silt-sized detrital quartz and other clay- to silt-sized rock components. Sample PN4-18-1. (E) High magnification image showing clay-sized microcrystalline quartz and other clay-sized grains. Porous organic matter is filling some of interparticle pores. Sample PN4-18-1. (F) TLD image showing interparticle pores between microcrystalline quartz and other grain components. Same field of view as Figure 3.14E. det = detector; BSED = back-scattered electron detector; TLD = through-lens detector; HV = high voltage (accelerating voltage); spot = spot size; mag = magnification; HFW = horizontal frame width; WD = working distance.

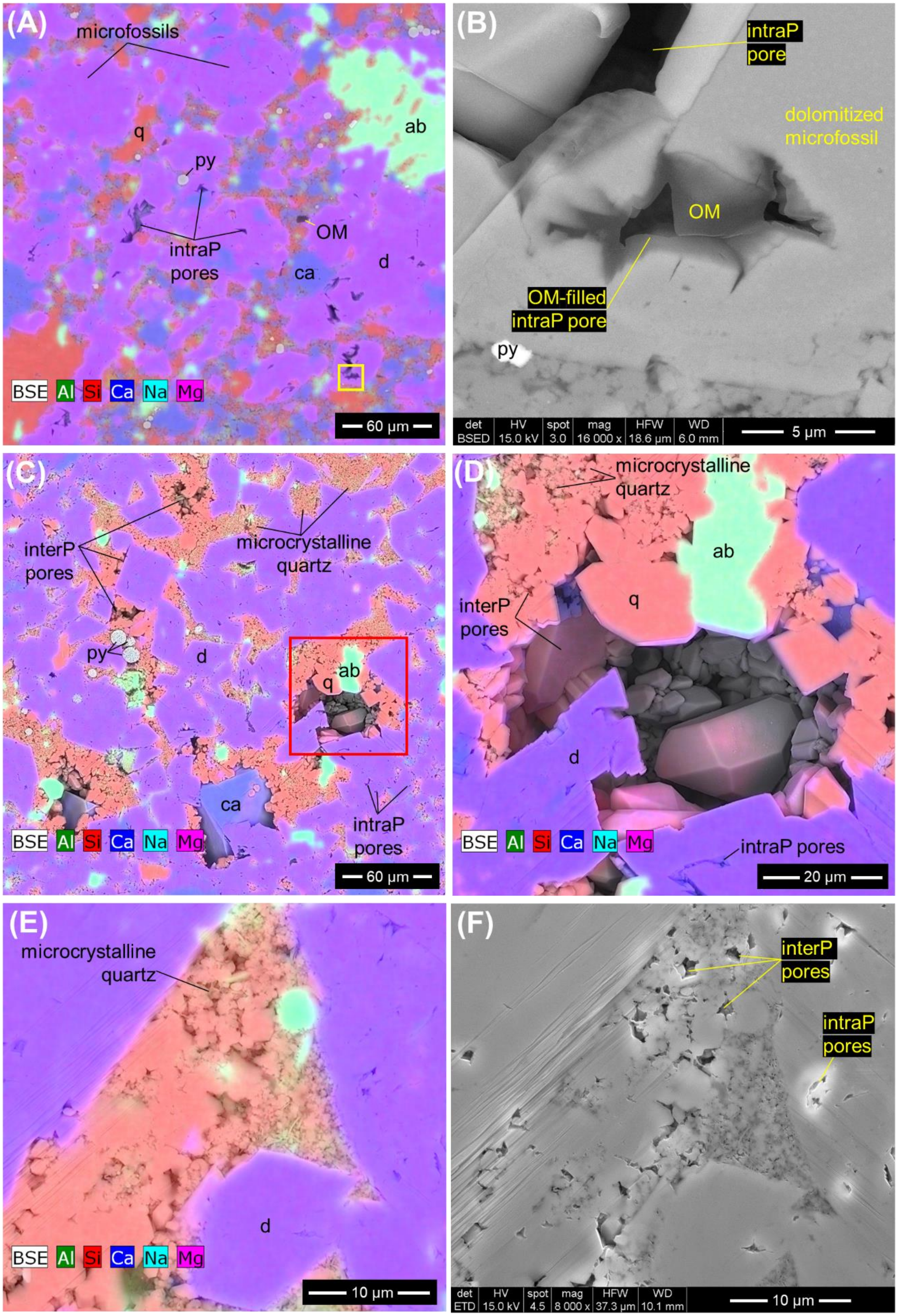
(A)
microfossils
q
py
ab
intraP
pores
OM
ca
d
BSE Al Si Ca Na Mg
60 μm
(B)
intraP
pore
dolomitized
microfossil
OM
OM-filled
intraP pore
py
det BSED HV 15.0 kV spot 3.0 mag 16 000 x HFW 18.6 μm WD 6.0 mm
5 μm
(C)
interP
pores
microcrystalline
quartz
py
d
q
ab
ca
intraP
pores
BSE Al Si Ca Na Mg
60 μm
(D)
microcrystalline
quartz
ab
q
interP
pores
d
intraP pores
BSE Al Si Ca Na Mg
20 μm
(E)
microcrystalline
quartz
d
BSE Al Si Ca Na Mg
10 μm
(F)
interP
pores
intraP
pores
det ETD HV 15.0 kV spot 4.5 mag 8 000 x HFW 37.3 μm WD 10.1 mm
10 μm

Figure 3.15: Dolomitic calcareous sandstone lithofacies: FE-SEM images of Ar-ion milled samples.

(A) Low magnification color EDS elemental map (aluminum is green, silicon is red, calcium is dark blue, sodium is aqua, and magnesium is magenta) superimposed on BSE SEM image showing quartz (q), albite (ab), dolomite (d), calcite (ca), pyrite (py), and micrometer-size intraparticle pores (intraP) within dolomitized microfossils. Sample PN6-36. (B) Enlargement of yellow-framed area in (A) showing intraparticle pore within dolomitized microfossil filled with organic matter (OM). (C) Low magnification color EDS elemental map superimposed on BSE SEM image showing silt quartz (q), microcrystalline quartz, albite (ab), dolomite (d), calcite (ca), pyrite (py), intraparticle pores (intraP) within dolomite crystals, and micrometer-size interparticle pores (interP) between dolomite and quartz. Sample PND-17. (D) Enlargement of red-framed area in (C) showing micrometer-size interP pores between dolomite crystals and quartz, sub-micrometer size interP between quartz microcrystals, and intraP pores within dolomite crystal. (E) High magnification view of microcrystalline quartz between dolomite crystals. Sample PND-17. (F) ETD image showing interparticle pores between quartz microcrystals and intraparticle pores within dolomite crystals. Same field of view as Figure 3.15E. det = detector; BSED = back-scattered electron detector; ETD = Everhart-Thornley detector; HV = high voltage (accelerating voltage); spot = spot size; mag = magnification; HFW = horizontal frame width; WD = working distance.

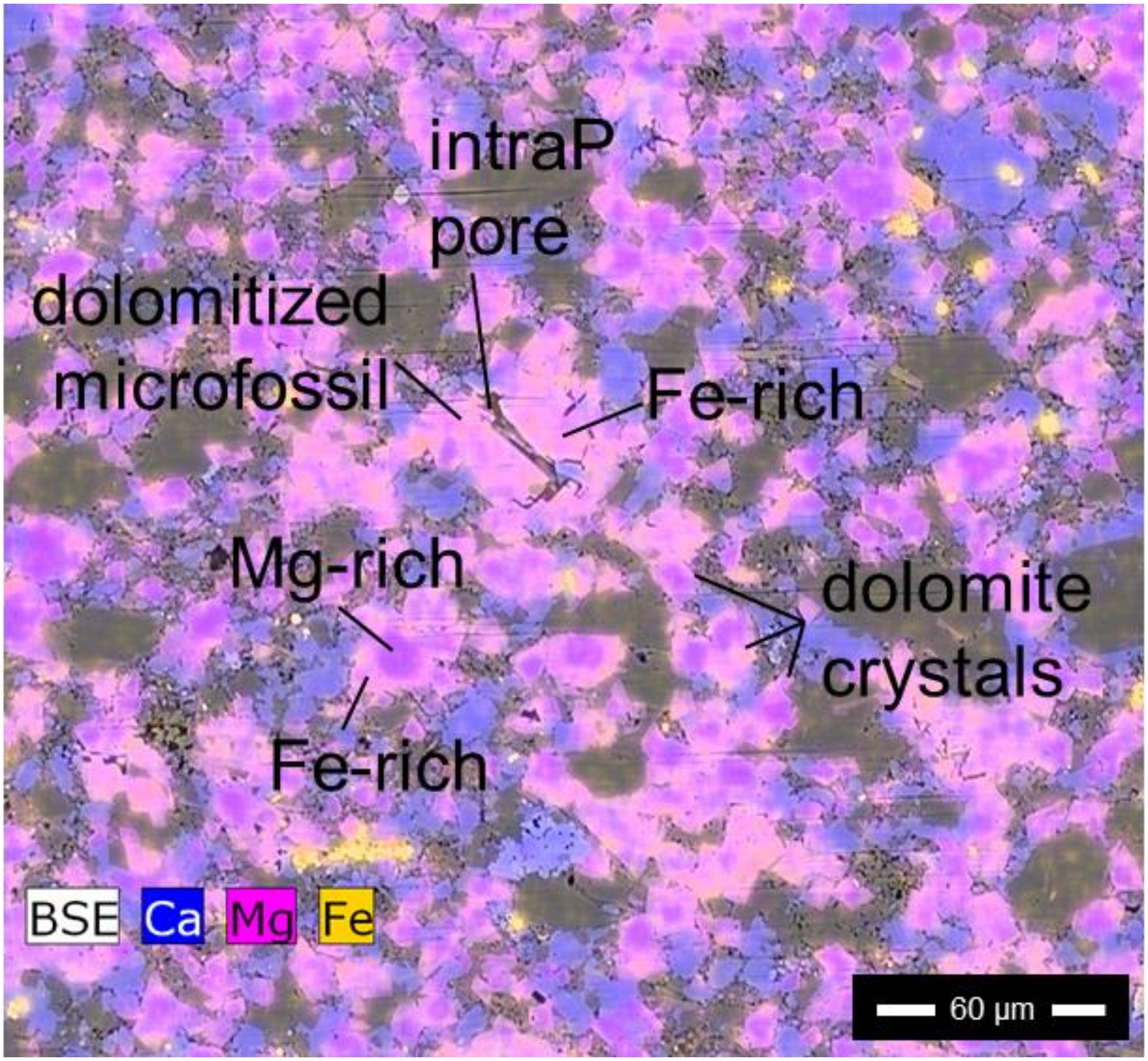

Figure 3.16: Color EDS elemental map (calcium is dark blue, magnesium is magenta, and iron is yellow) superimposed on FE-SEM BSE image of Ar-ion milled sample from dolomitic calcareous mudstone lithofacies showing iron-rich dolomite rims surrounding a magnesium-rich core in dolomite crystals, and iron-rich dolomitized microfossils. Sample PN2-52.

3.6 FLOW MODEL IN WOLFCAMP STRATA

3.6.1 Permeability distribution in the upper Wolfcamp

I document a significant variation of permeability in the upper Wolfcamp lithofacies Figure 3.10.

The calcareous mudstone and calcareous sandstone lithofacies, when dolomitized, have median permeabilities of 216 nD and 904 nD (Figure 3.10). These are the highest permeabilities present of all lithofacies in the Wolfcamp. I interpret that it is possible to correlate these dolomitic lithofacies between the three wells in some intervals of the Wolfcamp B based on both log and core character. For example, Figure 3.17 shows a dolomitized carbonate turbidite present at Well L and Well N. Based on the log signature, I correlate this bed to the Well S, where no core is present. This correlation suggests that some of these deposits may extend over several miles (e.g., 12 miles). In turn, this implies that dolomitization may have occurred at the regional scale. In the Wolfcamp A, the dolomitic calcareous mudstone and dolomitic calcareous sandstone are more frequent than in the Wolfcamp B and are often amalgamated. It is not possible to confidently correlate individual dolomitized beds in this unit (see Chapter 2).

The strata between the permeable dolomitic calcareous mudstone and dolomitic calcareous sandstone lithofacies are less permeable (i.e., $k < 60$ nD). The organic-rich siliceous mudstone is the dominant lithofacies (Figure 3.7) and it has a median permeability of 21 nD (Figure 3.10). The argillaceous mudstone is the second most common lithofacies (Figure 3.7), although it is only present in the Wolfcamp B unit. Its median permeability is less than 1 nD, and it is often interbedded with the dolomudstone lithofacies, which has a median permeability of 3 nD (Figure 3.10). The calcareous mudstone and calcareous sandstone lithofacies occur sporadically in the Wolfcamp B unit and much more frequently in the Wolfcamp A unit. Their median permeabilities are 38 nD and 3 nD (Figure 3.10), respectively. Finally, the matrix-supported conglomerate is mostly restricted to the uppermost section of the Wolfcamp B unit, and it has a median permeability of 30 nD (Figure 3.10).

Based on these observations, I describe the upper Wolfcamp as a system composed of relatively thin permeable dolomitized carbonate deposits (k = 216 nD to 904 nD) interbedded with much thicker low-permeability strata (k < 60 nD) (Figure 3.18). I infer that beds are laterally continuous at the scale of 100 feet, which is a typical spacing between hydraulic fractures (e.g., Weijermars et al., 2020). In this environment, hydraulic fractures will intersect one or more of these permeable beds.

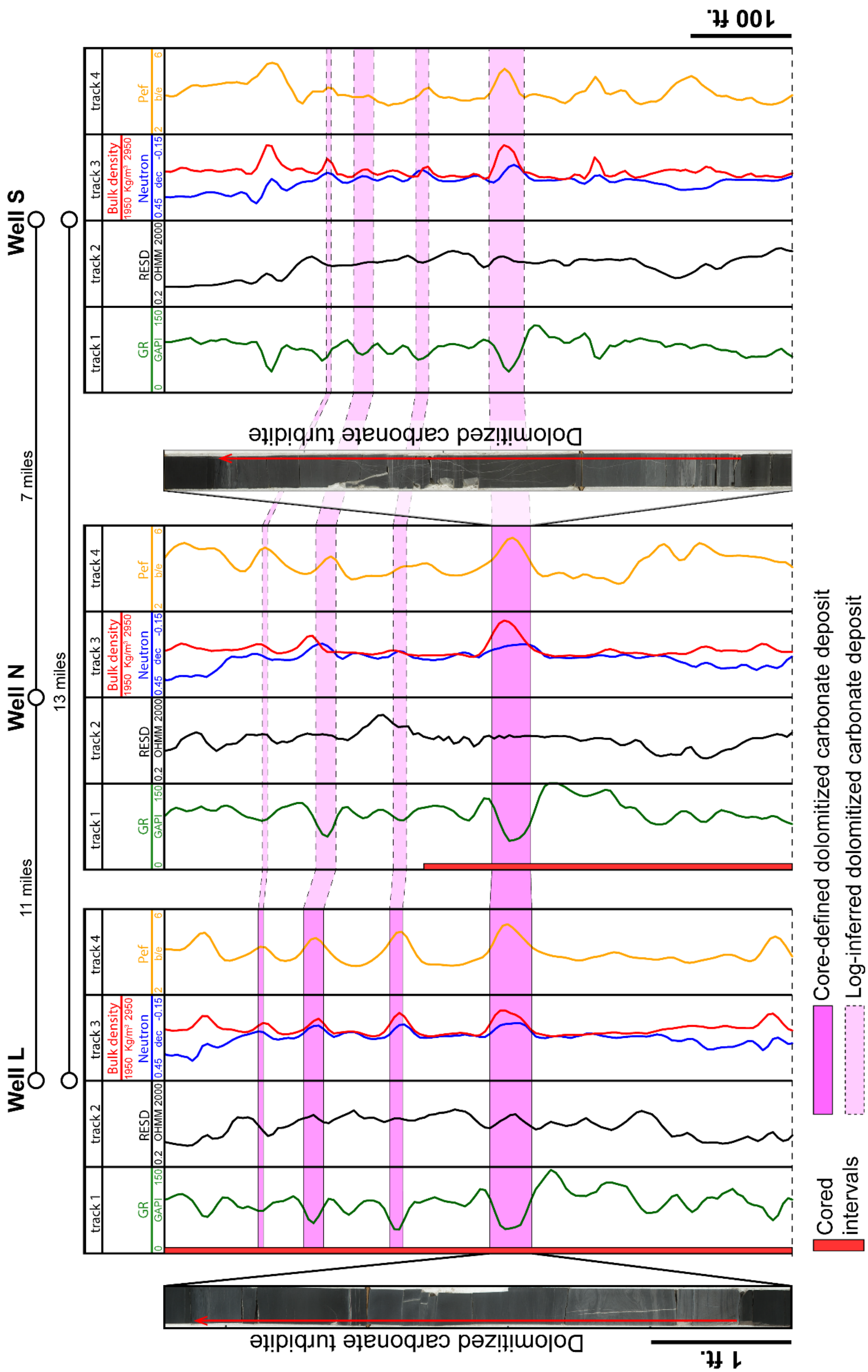
Well L
Well N
Well S
11 miles
7 miles
13 miles
track 1
GR
GAPI
0
150
track 2
RESD
OHMM
0.2
2000
track 3
Bulk density
1950 Kg/m³ 2950
Neutron
0.45 dec -0.15
track 4
Pef
b/e
2
6
Dolomitized carbonate turbidite
Dolomitized carbonate turbidite
1 ft.
100 ft.
Cored intervals
Core-defined dolomitized carbonate deposit
Log-inferred dolomitized carbonate deposit

Figure 3.17. Correlated dolomitic calcareous mudstone and dolomitic calcareous sandstone lithofacies (dolomitized carbonate deposits) across Well L, Well S, and Well N in the depth interval of Wolfcamp B unit.

Dark magenta represents dolomitized carbonate flow deposits defined in core, and the light magenta represents the inferred correlation of these deposits. The distance between Well L and Well S is 13 miles, between Well L and Well N is 11 miles, and between Well N and well S is 7 miles. See Chapter 2 for well locations. Track 1: gamma ray (green), cored interval (red vertical bar). Track 2: deep resistivity (black). Track 3: bulk density (red) and neutron porosity (blue). Track 4: photoelectric effect.

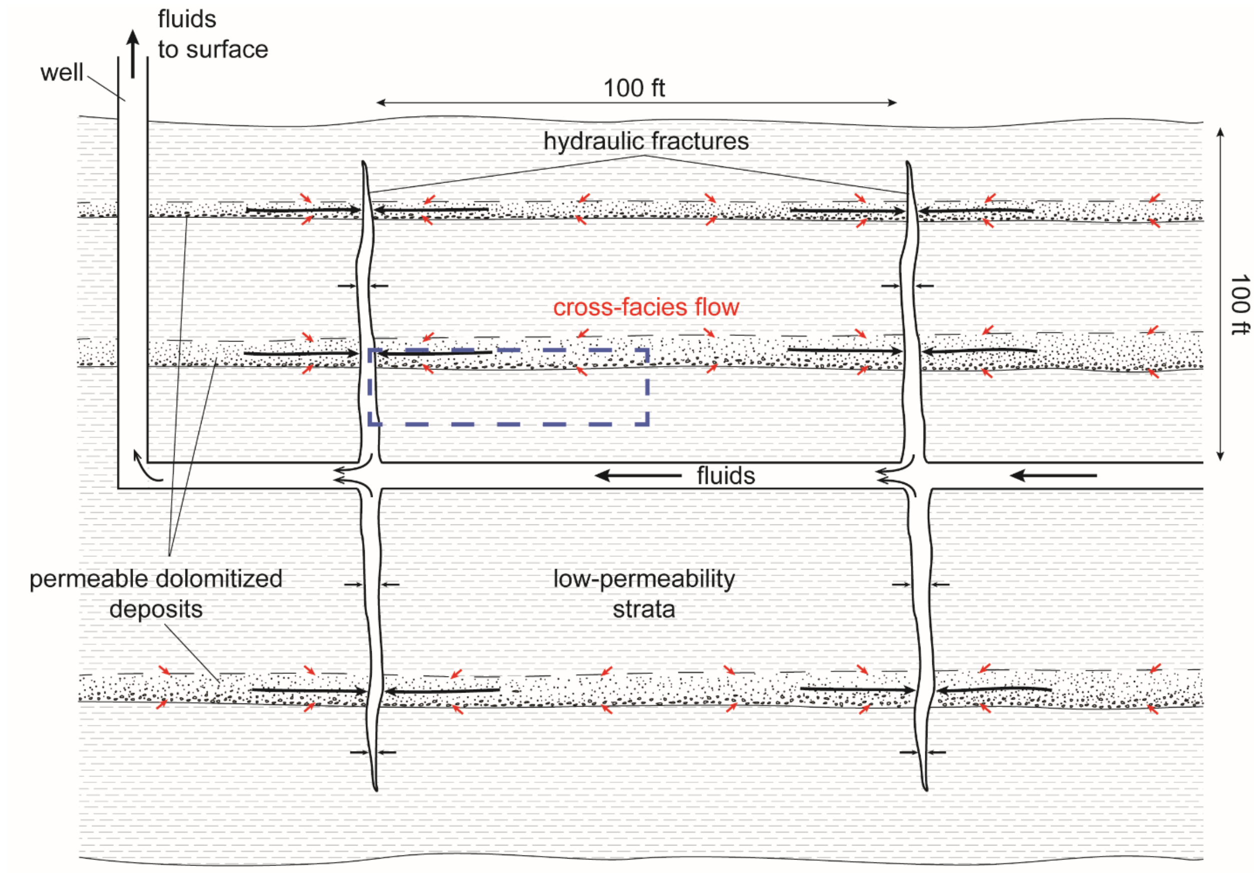

Figure 3.18: Hydrostratigraphic model of the Wolfcamp showing a horizontal well and two hydraulic fractures spaced out 100 ft.

I represent each stage by a single planar hydraulic fracture. The horizontal layers represent the permeable dolomitized carbonate flow deposits. The strata between these permeable layers correspond to the low-permeability organic-rich siliceous mudstones. Hydraulic fractures intersect both the high- and low-permeability layers; during production, the more permeable layers drain fluids from the mudstones due to cross-facies flow. The blue rectangle represents the model domain described in Figure 3.20. The thickness of permeable flow deposits and width of hydraulic fractures and well are not to scale.

3.6.2 Net to gross of dolomitized carbonate deposits

The number, thickness, and distribution of the dolomitized carbonate deposits will have a strong impact on the drainage of the reservoir because of their high permeability. In the Wolfcamp B unit, these deposits have an average thickness of 1.3 ft and are separated by low-permeability strata which average thickness is 22.0 ft (Figure 3.19A). In general, the net to gross (*NG*) profile of dolomitized carbonate deposits to low-permeability strata is less than 0.1 in this unit (Figure 3.19B). However, certain intervals have a higher frequency of permeable deposits, resulting in *NG* > 0.1. In the Wolfcamp A unit, the dolomitized carbonate deposits are thicker (average thickness is 2.8 ft) and more frequent (average thickness of low-permeability strata is 13.5 ft) than in the Wolfcamp B (Figure 3.19A). This translates into a higher net to gross, typically more than 0.1 (Figure 3.19B).

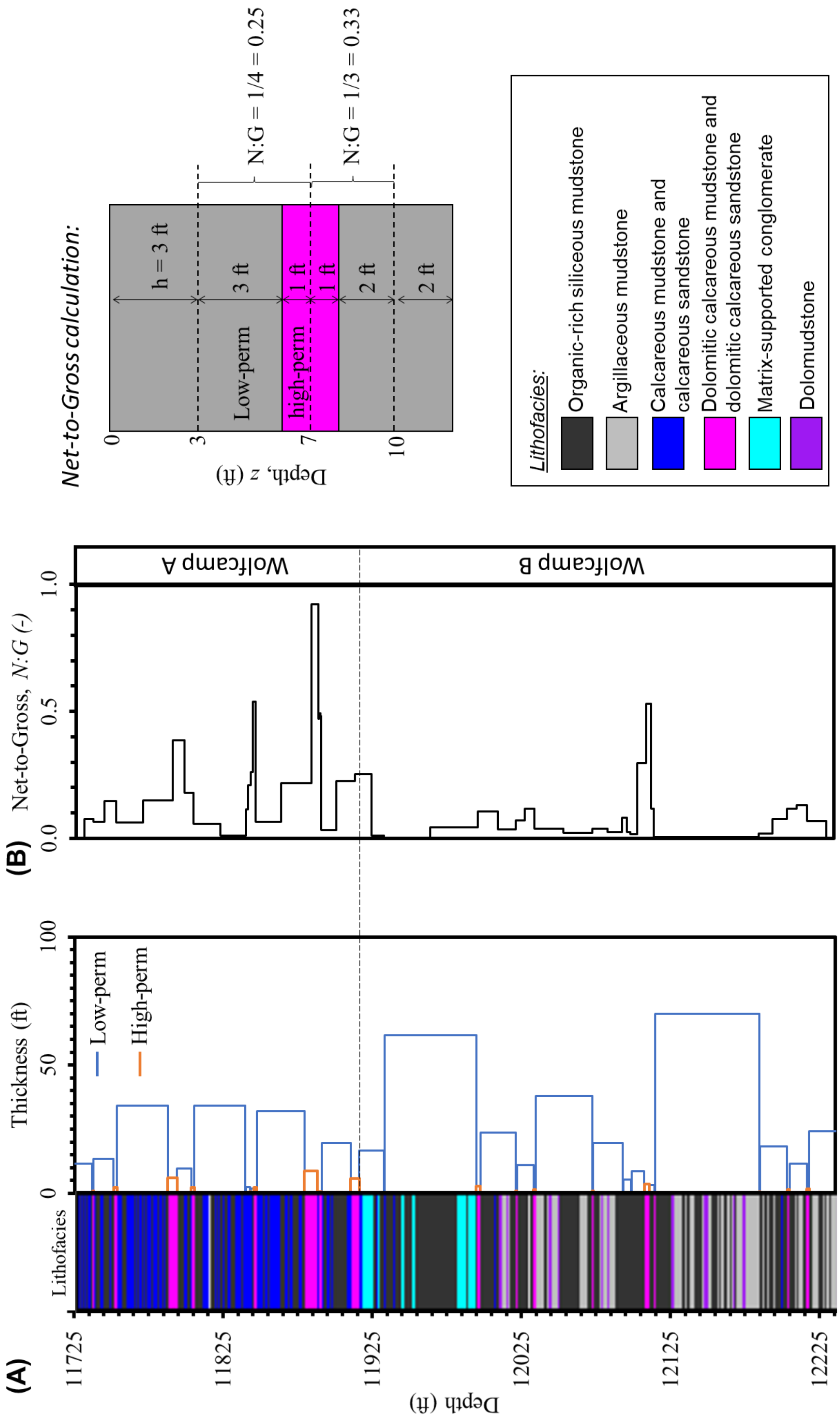

(A)
Depth (ft)
11725
11825
11925
12025
12125
12225
Lithofacies
Thickness (ft)
0
50
100
Low-perm
High-perm
(B)
Net-to-Gross, N:G (-)
0.0
0.5
1.0
Wolfcamp A
Wolfcamp B
Net-to-Gross calculation:
Depth, z (ft)
h = 3 ft
3 ft
1 ft
1 ft
2 ft
2 ft
Low-perm
high-perm
N:G = 1/4 = 0.25
N:G = 1/3 = 0.33
Lithofacies:
Organic-rich siliceous mudstone
Argillaceous mudstone
Calcareous mudstone and calcareous sandstone
Dolomitic calcareous mudstone and dolomitic calcareous sandstone
Matrix-supported conglomerate
Dolomudstone

Figure 3.19. Lithofacies distribution, thickness, and the net-to-gross ratio of the high-permeability layers in the upper Wolfcamp.

(A) Lithofacies distribution and thickness of low-permeability deposits (blue line) and dolomitized carbonate deposits with high-permeability (orange line) in the Wolfcamp B and Wolfcamp A units. The permeable deposits are the dolomitic calcareous mudstone and dolomitic calcareous sandstone lithofacies (magenta). (B) Net-to-Gross (NG) profile of high-permeability deposits to low-permeability strata. The NG was calculated using half the thickness of the deposits.

3.6.3 Flow model and drainage behavior

Model description

I constructed a model (Figure 3.20) to simulate the flow behavior during production of a reservoir with stratigraphic permeability heterogeneity such as envisioned in Figure 3.17. I consider low permeability layers of constant thickness interbedded with high permeability layers of constant thickness. Under these conditions, it is appropriate to extract a single domain (red dashed lines, Figure 3.20A) and model this system with no flow boundaries at the top, right side, and base with all flow occurring into the fracture. This simplification is possible because of the symmetry of the problem: there is no flow at the top, base, and right side because at these interfaces the pressure gradient will be zero.

I assume 1) single phase flow; 2) gravity effects are negligible; 3) flow follows Darcy's Law, 4) the bulk rock is incompressible; 5) the fluid properties are constant; 6) properties are homogenous in each layer; and 7) permeability is anisotropic along the horizontal axis.

The flow behavior is described by Equation 3.5:

$$\frac{\partial P}{\partial t} = \frac{1}{\emptyset \mu c_f}\left(\frac{\partial}{\partial x}\left(k\frac{\partial P}{\partial x}\right) + \frac{\partial}{\partial y}\left(k\frac{\partial P}{\partial y}\right)\right), \qquad \text{Eq. 3.5}$$

where P = fluid pressure, t = time, k = matrix permeability, $\emptyset$ = rock porosity, μ = fluid viscosity, and c_f = fluid compressibility.

The model has a domain of length L that is composed of two layers of thickness h_1 and h_2 (Figure 3.20.B). Layer 1 represents the high-porosity low-permeability organic-rich siliceous mudstone and Layer 2 represents the permeable dolomitized carbonate deposits. There is no flow across the top, bottom, and right boundaries. Pressure at the left boundary is fixed to simulate the interface between the hydraulic fracture and the reservoir. The initial pressure of the reservoir is

P_i. At t<0, the pressure at the left boundary is P_i. At t>0, the pressure at the boundary is decreased to Pf. Pf represents the pressure that the well is drawn down to during production.

The length of the model domain (L) is assumed to equal 50 feet. I chose values of porosity, and permeability based on my measurements of the Wolfcamp lithofacies (Table 3.3). Layer 1 is assumed to have the median porosity (0.12) and median permeability (20 nD) of the organic-rich siliceous mudstone (Table 3.3). Layer 2 is assumed to have the median porosity (0.05) and median permeability (560 nD) of the dolomitic calcareous lithofacies (Table 3.3). I assume the vertical permeability is 10 times less than the horizontal permeability in each layer (Table 3.3), based on my vertical and horizontal permeability measurements in two contiguous vertical and horizontal core plugs from the organic-rich siliceous mudstone lithofacies (Samples PN5-12 and PN5-12V, PN6-75 and PN6-75V, Table 3.A.1).

The average thickness of the high-permeability dolomitized carbonates in the Wolfcamp A is 2.8 ft and the average thickness of the low-permeability strata is 13.5 ft. In the Wolfcamp B, the average thickness of the high-permeability dolomitized carbonates is 1.3 ft whereas the average thickness of the low-permeability strata is 22.0 ft. I assumed the height of each layer in the model is half the average bed thickness (Figure 3.20B). Hence, the thickness of the low-permeability and high-permeability layers in the Wolfcamp A are h_1 = 6.7 ft and h_2 = 1.4 ft, respectively. In the Wolfcamp B, the thickness of the low-permeability and high-permeability layers are h_1 = 11.0 ft and h_2 = 0.6 ft, respectively. Table 3.3 summarizes the model parameters for Wolfcamp A and Wolfcamp B.

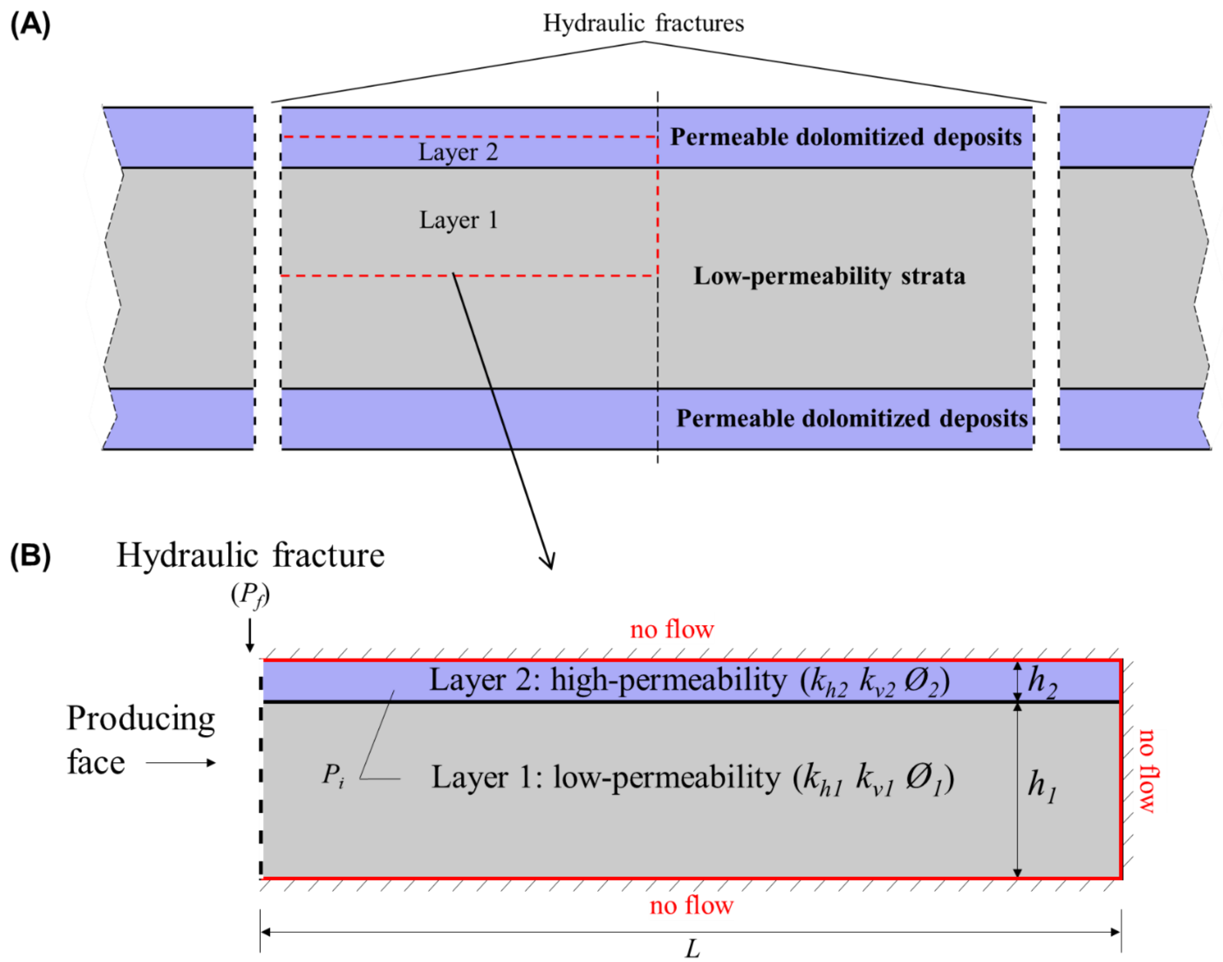

Figure 3.20: Schematic of layered model.

(A) The layered modeled consists of high-permeability layers interbedded with low-permeability strata. (B) The modeled domain is composed of a high-permeability layer (blue) and low-permeability layer (gray). I model half the thickness of each layer. The length (L) of the model is half the distance between hydraulic fractures.

Table 3.3. Model parameters.

Parameter		Wolfcamp A	Wolfcamp B
Model length	L	50 ft	
Layer 1 thickness	h_1	6.7 ft	11.0 ft
Layer 2 thickness	h_2	1.4 ft	0.6 ft
Layer 1 horizontal permeability	k_{h1}	20 nD	
Layer 1 vertical permeability	k_{v1}	0.1 k_{h1}	
Layer 2 horizontal permeability	k_{h2}	560 nD	
Layer 2 vertical permeability	k_{v2}	0.1 k_{h2}	
Layer 1 porosity	$Ø_1$	0.12	
Layer 2 porosity	$Ø_2$	0.05	
Initial reservoir pressure	P_i	6,000 psi	
Pressure at the fracture	P_f	3,000 psi	
Fluid density[1]	ρ_f	725 kg/m^3	
Fluid viscosity[1]	μ	6.6 e-4 Pa.s	
Fluid compressibility[1]	c_f	1.55 e-9 1/Pa	

[1]Wolfcamp crude oil properties at 4500 psi (Mavor, 2014).

Simulation results

Figure 3.21 represents the pressure evolution and flow orientation and magnitude (white arrows) at three different time slices of the simulations conducted in the Wolfcamp A model. Initially, the pressure in both layers is P_i = 6,000 psi. With time, the pressure dissipates in both Layer 1 and Layer 2 as fluids are produced at the left boundary. However, the pressure dissipates faster in Layer 2 than Layer 1 (e.g. t = 0.1 years), generating a vertical pressure gradient between both layers. Significant amounts of flow are diverted upwards into the high permeability Layer 2 (e.g. t = 1 year). These fluids are then transported horizontally towards the fracture. The pressure in the low-permeability Layer 1 continues dissipating in both the horizontal and vertical directions until the pressure in the entire reservoir equilibrates with P_f. Not surprisingly, at any particular time the pressure is more depleted near the fracture face (left) than on the no-flow boundary at the far right.

The amount of flow across the left boundary is plotted in Figure 3.22. This is represented with a dimensionless recovery factor (*RF*):

$$RF\ (t) = \frac{Q}{V_{\Delta P}}, \qquad \text{Eq. 3.6}$$

where Q is the cumulative produced pore volume, and $V_{\Delta P}$ is the producible pore volume given by:

$$V_{\Delta P} = c_f\, \Delta P\, V_p\ , \qquad \text{Eq. 3.7}$$

where $\Delta P = P_i - P_f$, and V_p is the total pore volume of the reservoir. When the pore pressure in the domain is equal to the fracture pressure, the recovery factor is 100%. The horizontal axis represents the square root of time. In this plot, the production decline is proportional to the inverse of the square root of time (1/√t) when the production profile is a straight line, whereas production declines exponentially when the production profile deviates from the straight line. We see that production starts declining proportionally to 1/√t in this space, whereas in late time the production slows down during exponential decline (black curve, Figure 3.22).

The production rate is faster for the modeled system than for the case where there is no cross-facies flow (i.e., lower bound) (red curve, Figure 3.22). 50% of the reserves are recovered (*RF* = 50%) almost four times faster with cross-facies flow compared with the model with no cross-facies flow. The production rate for the modeled system is lower than the case where the permeability of the upper layer is very large (e.g., $k_{h2} = 10^9$ nD). This represents the maximum rate at which the low permeability rock could be produced (i.e., upper bound) (grey curve, Figure 3.22). A recovery factor of 50% is reached after ~ 1 year of production time, compared to ~2 years required when the high-permeability layer is less permeable.

Finally, given the modeled production behavior, I interpret what permeability throughout the reservoir (i.e., upscaled permeability) would produce similar production results. I estimated this permeability by performing flow simulations in a homogeneous model with equal permeability in both layers, and same dimensions and equivalent pore volume as the two-layer model. The production with cross-facies flow requires an upscaled permeability of 74 nD (green dashed curve, Figure 3.23). This upscaled permeability is almost four times higher than the permeability in a model consisting of only low-permeability strata (i.e., 20 nD).

I repeated these simulations in a model that has the Wolfcamp B dimensions (Table 3.3) to compare its production performance with the Wolfcamp A. The results indicate that the Wolfcamp B model required an upscaled permeability of 40 nD (Figure 3.22), which is lower than that in the Wolfcamp A (k_{ups} = 74 nD), but it is still twice the upscaled permeability in a model consisting of only low-permeability strata (k_{ups} = 20 nD) (Figure 3.23).

The increase of the low-permeability layer's thickness (h_1), while setting the high-permeability layer's thickness (h_2) constant, results in slower production rates (Figure 3.23). The system's upscaled permeability is 74 nD at h_1, and then it progressively approaches 20 nD when the h_1 thickness is increased. Hence, the upscaled permeabilities, and therefore the production rates, approach the behavior of a model consisting of only mudstones when the net to gross thickness of the high-permeability layer to the low-permeability strata decreases.

In these simulations, I have assumed that the hydraulic fractures (i.e., producing face at the left boundary) are infinitely conductive. Thus, all fluids produced at the fracture face are transported to the wellbore without any flow restriction, and therefore production rates are controlled by the upscaled reservoir permeability. However, if hydraulic fractures are not infinitely conductive, production rates may be controlled by the fracture permeability when smaller than the upscaled reservoir permeability.

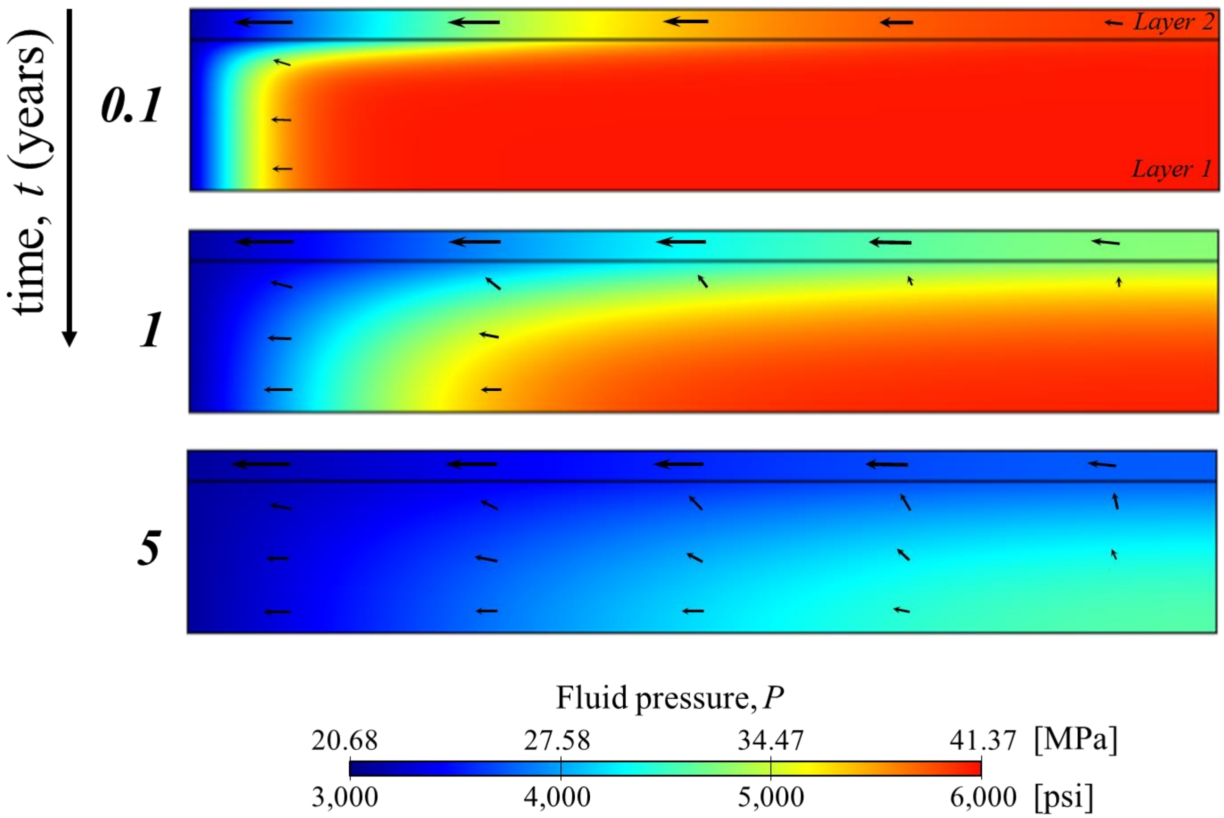

Figure 3.21. Example of pressure evolution within each layer's domain at t = 0.1, 1, and 5 years. The arrows show the orientation and magnitude of the flow in logarithmic scale.

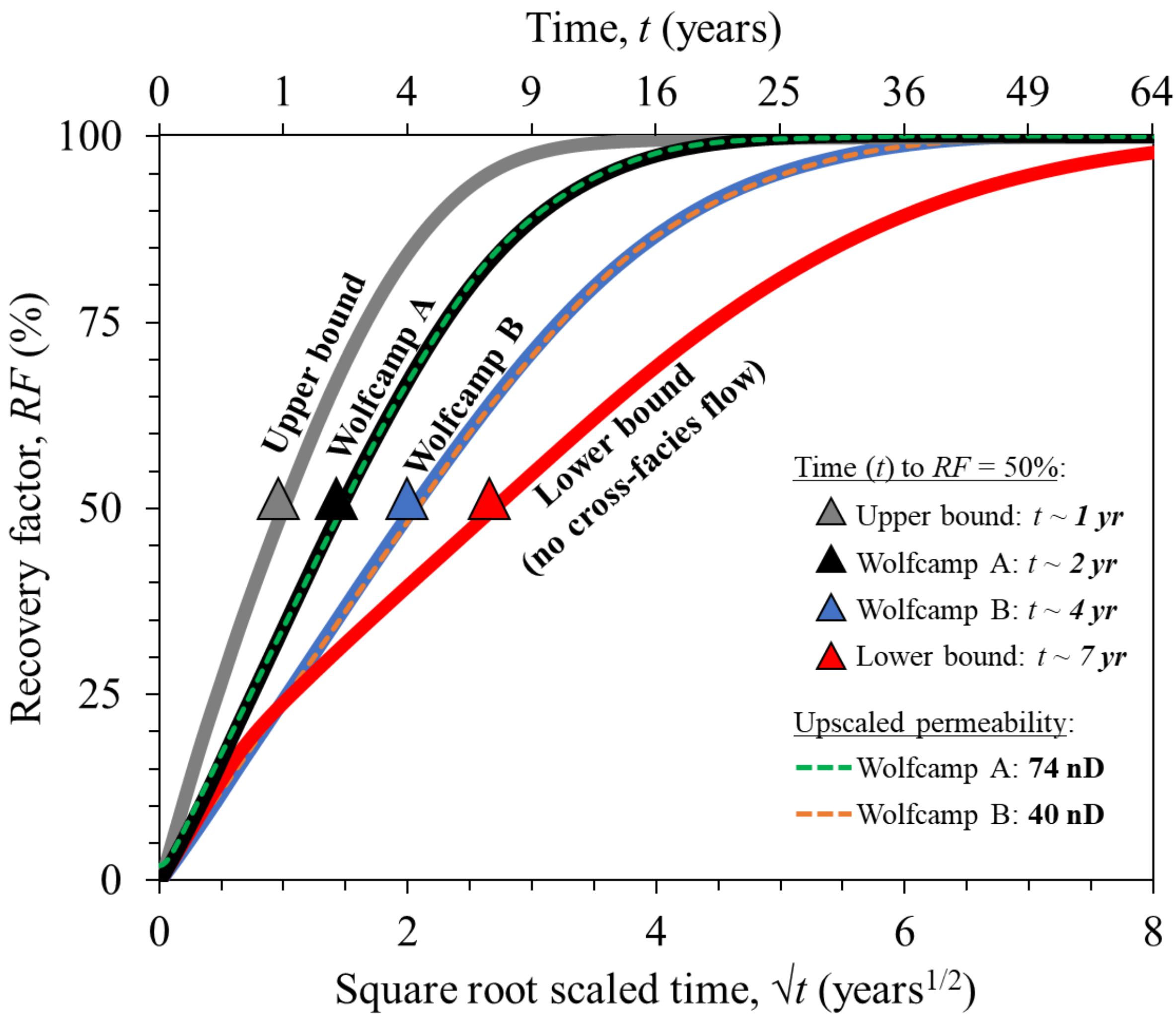

Figure 3.22: Flow simulation results for the layered model.

The black curve is the production when there is cross-facies flow in Wolfcamp A model. The red curve is the production when there is no cross-facies flow, and it represents the lower bound performance in the Wolfcamp A model. The grey curve is the production when there is cross-facies flow, and the permeability in the high-permeability layer is very high (i.e., k_{h2} = 10^9 nD); it represents the upper bound performance in the Wolfcamp A model. The blue curve is the production when there is cross-facies flow in the Wolfcamp B model. The dashed lines represent the matched production behavior in the Wolfcamp A (green) and Wolfcamp B (orange) using a single upscaled permeability in a homogeneous model. The recovery factor (*RF*) is the cumulative produced pore volume over the maximum producible pore volume for the given model parameters. The recovery factor is 100% when the pore pressure in the domain equilibrates with the pressure in the fracture.

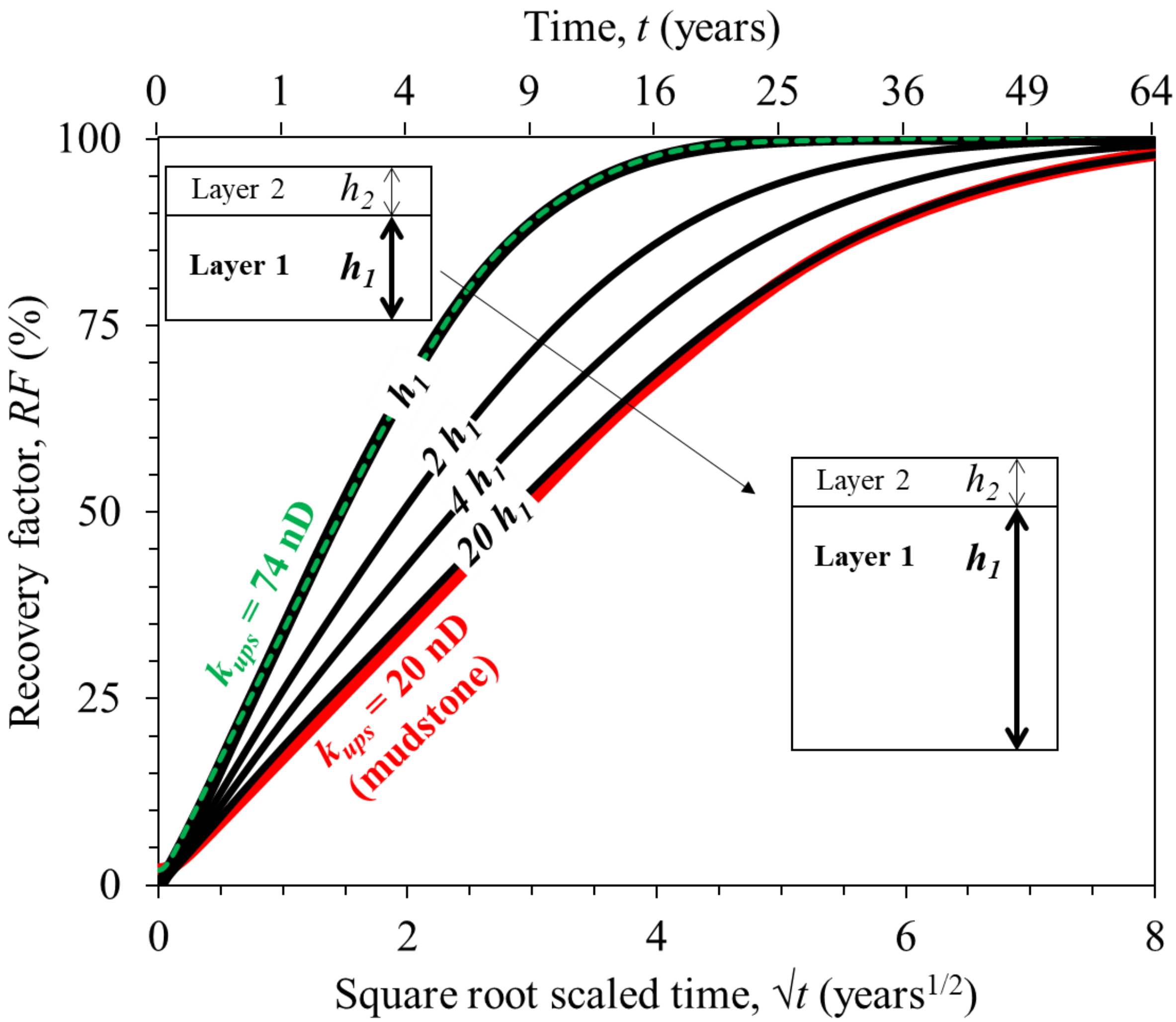

Figure 3.23: Simulation results for layered model with increasing low-permeability layer's thickness (h_1). Production behavior is matched using a single upscaled permeability in homogeneous model.

The dashed green line represents the matched production behavior in the Wolfcamp A homogeneous model with an upscaled permeability of 74 nD. The red curve is the production in a homogeneous model composed on only low-permeability strata with an upscaled permeability (k_{ups}) of 20 nD. The production rates decrease at increasing the h_1. The upscaled permeability approaches 20 nD as h_1 increases. The recovery factor (RF) is the cumulative produced pore volume over the maximum producible pore volume for the given model parameters. The recovery factor is 100% when the pore pressure in the domain equilibrates with the pressure in the fracture.

Table 3.4. Production time (t) required to achieve a recovery factor of RF = 50%, and upscaled permeabilities (k_{ups}) required to match production in the lower bound, simulated production, and upper bound performance on the Wolfcamp A and Wolfcamp B models.

The recovery factor (RF) is the cumulative produced pore volume over the maximum producible pore volume for the given model parameters.

	Wolfcamp A		Wolfcamp B	
	Time (t) to RF = 50% (years)	k_{ups} (nD)	Time (t) to RF = 50% (years)	k_{ups} (nD)
No cross-facies flow, Lower bound	7.3	20	8.2	20
Cross-facies flow	2.2	74	4.2	40
Cross-facies flow, Upper bound	1.0	190	2.0	110

3.7 DISCUSSION

This work further resolves a growing conceptual view of Wolfcamp reservoirs in distal portions of the Delaware Basin. These reservoirs are dominated volumetrically by high-TOC organic rich siliceous mudstones and low-TOC clay-rich argillaceous mudstones. Our analysis would suggest that a significant oil saturation is stored in the siliceous mudstones, whereas the argillaceous mudstones are mostly saturated with water. These findings coincide with observations made in other recent work (Thompson et al., 2018; Zhang et al., 2021). The organic-rich siliceous mudstone and the argillaceous mudstone are volumetrically the dominant lithofacies in Wolfcamp reservoirs and have the highest porosity. Thus, they represent 94% of the total pore volume in the studied section. In contrast, the carbonate gravity flow deposits are much lower porosity, and have in general a lower TOC. We interpret, and it is supported by others (Thompson et al., 2018; Zhang et al., 2021), that the hydrocarbon saturations are relatively high in these deposits.

Our permeability measurements show that when the carbonate gravity flow deposits are dolomitized, there can be a remarkable permeability that is as much as 2000 times greater than the organic rich siliceous mudstone and argillaceous mudstone. Such high permeability is due to dissolution, either partial or total, of carbonate grains. The interparticle pores between quartz microcrystals also seem to contribute to permeability in these lithofacies. It is remarkable the high permeability of the dolomitized carbonate gravity flow deposits despite their low porosity. The mercury injection capillary pressure data clearly suggests that pores in these deposits form well connected pore systems.

A simple reservoir model shows that these permeable dolomitized carbonate flow deposits will act as drainage pathways during production when intersected by hydraulic fractures. The high liquid saturation, but low pore volume within the dolomitized carbonate deposits will be rapidly produced and thereafter, these permeable layers will act as conduits to drain the less permeable strata. This results in reservoir upscaled permeabilities that are higher (e.g., ~ 4 times higher) than a reservoir composed of only organic-rich siliceous mudstones.

It is important to note that the permeability of 560 nD that I used for the high-permeability layer in this model may be underestimated. The maximum permeability of samples from the dolomitic calcareous mudstone and dolomitic calcareous sandstone lithofacies is up to 2000 nD. Hence, we can expect higher upscaled permeabilities, and therefore faster production rates closer to the upped bound performance when layers with such high permeabilities are produced.

Taken together, these observations point to a system where during production, the permeable layers act as carrier beds to drain the major hydrocarbon reservoir, which is the organic rich siliceous mudstone itself.

The observations described above can inform completion strategies. For example, production will be faster when hydraulic fractures intersect permeable dolomitized carbonate flow deposits interbedded with relatively thin organic-rich siliceous mudstone layers. In addition, intervals with high net to gross of the permeable deposits should be reservoir stimulation targets as they will yield better production rates. Thus, this may be used as a tool to target the most optimal landing zones. In this study, it is clear that the Wolfcamp A unit will be potentially more productive than the Wolfcamp B because the net to gross is higher.

Another aspect to consider is that, if hydraulic fractures are not infinitely conductive, then production rates would be controlled by the fracture permeability if it were lower than the upscaled reservoir permeability. In this scenario, there is limited impact of the high-permeability layers on production rates, and more hydraulic fractures per lateral length in the horizontal well may be needed.

At the broadest level, this work reminds us of the fundamental importance of understanding the lithologic and flow behavior of strata at the meter scale, and perhaps smaller. It suggests that, although volumetrically small, permeable carrier beds have a major influence on the production behavior: they increase the upscaled permeability of the system due to cross-facies flow. This view may also reconcile the fact that reservoir simulation models, to history-match production rates, often require much higher permeabilities that than those measured in the laboratory for the dominant lithofacies (e.g., Mohan et al., 2013; Patzek et al., 2013; Defeu et al., 2018; Parsegov et al., 2018). It is often assumed that reservoir upscaled permeability is high due to the development of complex hydraulic fracture networks (e.g., dendritic) that intersect and reopen natural fractures during stimulation. However, examination of slant cores retrieved from hydraulically fractured reservoirs (Gale et al., 2018; Raterman et al., 2018; Gale et al., 2021; Male et al., 2021) and vertical cores from producing reservoir intervals (Salem et al., 2022) seem to contradict that assumption. Here, we show cross-facies flow is an opposite production drainage mechanism that increases the upscaled permeabilities in Wolfcamp A and Wolfcamp B reservoirs. Although this study focuses in the Wolfcamp, this drainage behavior may also occur in other low-permeability reservoirs.

Finally, a problem not explored in depth here is the implications of this drainage behavior for parent-child wells. If the permeable layers extend beyond individual hydraulic fractures in a completed interval, then we would expect drainage to extend outward from a particular well to other prospective landing zones for child wells. In this case, the parent well would drain relatively rapidly from the mudstone adjacent to the permeable bed over a large distance. Any additional child wells drilled and completed within the same interval would encounter mudstones that were partially depleted, resulting in slower production rates.

3.8 CONCLUSIONS

Based on the results presented in this paper, I make the following conclusions:

1. There is significant porosity and permeability heterogeneity in the upper Wolfcamp (Wolfcamp B, Wolfcamp A) interval of the central-eastern Delaware Basin:
   - Most fluids (~95 % of the pore volume) are stored in the organic-rich siliceous mudstone and argillaceous mudstone deposits. This implies that most fluids produced in the Wolfcamp originate in mudstone lithofacies.
   - The matrix permeability to dodecane (oil-phase) of most lithofacies is below 60 nD; contrastingly, the dolomitic calcareous mudstone and dolomitic calcareous sandstone lithofacies exhibit permeabilities up to 2000 nD
2. The interparticle pores control permeability in upper Wolfcamp lithofacies. Lithofacies with larger pore throats correlate with higher permeability.
3. My permeability measurements, when combined with geological information, indicate that fluids production occurs primarily via high-permeability layers. These permeable layers are dolomitized carbonate-flow deposits, that may be laterally continuous e.g., >10 mi) based on well correlations; the permeable dolomitic calcareous mudstone and dolomitic calcareous sandstone samples are representative of these deposits.
4. My simulations indicate that cross-facies flow is the most probable drainage mechanism during production in a Wolfcamp interval with significant permeability heterogeneity structure (permeabilities ranging from 1 nD to 2000 nD). Cross-facies flow increases the reservoir upscaled permeability by ~4 times compared to a system composed of only low-permeability mudstones.

5. Reservoir models in the Wolfcamp should account for the presence of permeable layers to describe well performance and design field development plans (e.g., optimal landing zones, spacing between hydraulic fractures, well spacing).

ACKNOWLEDGEMENTS

I thank Shell for funding this research under the SUTUR (Shell-UT Unconventional Research) agreement. I am grateful to Dr. Robert Dombrowski and Dr. Ronny Hofmann for guidance and fruitful discussions, and Brian Driskill and Adenike Tokan-Lawal for their technical and logistical support throughout this project. I also thank Robert Baumgardner for his initial core descriptions and Evan Sivil for conducting the XRF measurements of the cores. I also thank Equinor for providing additional funding for this research under the University of Texas - Equinor Fellows Program. Lastly, I thank NSF for supporting the University of Texas High-Resolution X-ray Computed Tomography Facility (UTCT) through the grant EAR-1762458.

APPENDIX 3.A

Characterization details of tested core plugs

Table 3.A1. Summary of samples tested.

Summary of samples tested, including sample ID, lithofacies, sample depth and orientation (H = horizontal, V = vertical), dimensions of the core plug (D = diameter, L = length), helium porosity (Φ_{He}), NMR porosity (Φ_{NMR}), and liquid permeability to dodecane (k) measured at the 4500 psi and 8500 psi effective stresses (i.e., $P_c - P_p$).

Sample ID		Lithofacies	Sample Depth (ft)	Sample Orientation	D (mm)	L (mm)	Φ_{He} (%)	Φ_{NMR} (%)	k (nD) at Pc- Pp = 4500 psi	k (nD) at Pc- Pp = 8500 psi
PN2-46*	1	Organic-rich siliceous mudstone	11274.20	H	38.09	17.50	6.4 ± 0.9	5.2	--	--
PN2-46B	1	Organic-rich siliceous mudstone	11274.20	H	38.10	18.10	6.0 ± 0.9	6.0	--	--
PN3-33	1	Organic-rich siliceous mudstone	11311.05	H	38.18	18.49	1.1 ± 0.4	8.1	50 ± 3	57 ± 6
PN3-39	1	Organic-rich siliceous mudstone	11317.00	H	25.34	21.14	4.9 ± 0.5	5.9	8 ± 5	5 ± 4
PN3-92	1	Organic-rich siliceous mudstone	11370.30	H	38.11	18.93	3.6 ± 0.8	8.0	16 ± 2	14 ± 2
PN3-108	1	Organic-rich siliceous mudstone	11386.60	H	38.10	16.81	5.9 ± 1.0	7.4	29 ± 6	22 ± 5
PN4-11V	1	Organic-rich siliceous mudstone	11617.95	V	38.22	14.06	5.4 ± 1.1	12.2	96 ± 4	82 ± 4
PN4-15	1	Organic-rich siliceous mudstone	11621.25	H	38.45	19.73	7.6 ± 1.2	n/a	23	13
PN5-12	1	Organic-rich siliceous mudstone	11669.10	H	38.24	16.58	7.1 ± 1.5	9.5	9 ± 3	7 ± 3
PN5-12V	1	Organic-rich siliceous mudstone	11669.20	V	38.08	19.28	4.0 ± 0.8	9.3	1	--
PN5-50	1	Organic-rich siliceous mudstone	11707.90	H	38.45	17.38	6.1 ± 0.3	9.7	35	--
PN6-3	1	Organic-rich siliceous mudstone	11726.15	H	38.31	16.77	5.2 ± 1.0	7.5	--	--
PN6-75	1	Organic-rich siliceous mudstone	11798.50	H	38.30	18.80	4.4 ± 0.5	7.2	29	21
PN6-75V	1	Organic-rich siliceous mudstone	11798.40	V	37.84	17.58	4.9 ± 0.8	5.6	2	--
PN D-3	2	Argillaceous mudstone	11380.45	H	38.00	11.11	3.1 ± 1.4	11.4	<0.1	--
PN D-11	2	Argillaceous mudstone	11701.10	H	38.06	17.12	0.3 ± 0.9	13.9	--	--
PN D-14	2	Argillaceous mudstone	11729.40	H	38.11	18.26	0.6 ± 0.9	10.9	2	2
PN D-6	3a	Calcareous mudstone	11650.45	H	38.13	16.67	0.3 ± 1.0	2.5	<1	--
PN6-93	3a	Calcareous mudstone	11816.20	H	38.19	15.26	2.4 ± 1.1	3.0	38	43
PN6-113	3a	Calcareous mudstone	11836.25	H	38.24	18.17	3.7 ± 0.9	3.1	306 ± 14	194 ± 9
PN6-118	3a	Calcareous mudstone	11841.50	H	38.23	19.05	4.1 ± 0.9	5.0	36	28
PN2-52	3b	Dolomitic calcareous mudstone	11280.35	H	38.04	18.05	1.7 ± 0.9	5.8	--	--
PN D-4	3b	Dolomitic calcareous mudstone	11614.10	H	38.09	15.23	0.9 ± 1.0	4.8	10	7
PN4-10	3b	Dolomitic calcareous mudstone	11616.50	H	38.22	13.24	2.3 ± 1.2	2.8	--	--

PN4-18-1	3b	Dolomitic calcareous mudstone	11624.70	H	38.22	19.37	2.2 ± 0.8	3.7	508 ± 21	422 ± 40
PN D-15	3b	Dolomitic calcareous mudstone	11773.80	H	--	--	--	--	--	--
PN2-2	4a	Calcareous sandstone	11230.40	H	38.02	18.51	1.0 ± 0.9	2.5	13 ± 1	12 ± 1
PN2-3	4a	Calcareous sandstone	11231.75	H	38.12	19.06	1.8 ± 0.4	1.7	--	--
PN2-51	4a	Calcareous sandstone	11279.45	H	38.03	16.76	1.6 ± 1.1	1.3	4 ± 0.5	2 ± 1
PN6-69	4a	Calcareous sandstone	11792.55	H	25.56	15.78	0.9 ± 0.3	3.6	<1	--
PN6-78	4a	Calcareous sandstone	11801.80	H	38.21	16.78	0.4 ± 0.9	2.7	3	2
PN6-108	4a	Calcareous sandstone	11831.21	H	38.22	17.06	0.0 ± 1.0	2.2	3 ± 1	1 ± 0.5
PN D-1	4b	Dolomitic calcareous sandstone	11281.25	H	38.10	15.37	0.0 ± 1.1	2.3	47 ± 2	33
PN6-36	4b	Dolomitic calcareous sandstone	11759.00	H	38.26	19.08	0.7 ± 0.9	2.0	1003	583
PN6-36B*	4b	Dolomitic calcareous sandstone	11759.00	H	38.29	14.53	1.2 ± 1.2	2.4	--	--
PN D-16-1	4b	Dolomitic calcareous sandstone	11817.20	H	38.13	14.57	0.0 ± 1.1	2.5	900	880
PN D-17	4b	Dolomitic calcareous sandstone	11819.50	H	38.06	14.19	4.7 ± 1.1	4.1	2041 ± 90	2004
PN2-30	5	Matrix-supported conglomerate	11258.30	H	38.08	15.45	0.4 ± 1.0	2.9	35 ± 8	24 ± 7
PN3-54	5	Matrix-supported conglomerate	11332.50	H	38.16	16.91	2.0 ± 1.0	1.7	38 ± 6	36 ± 6
PN3-90	5	Matrix-supported conglomerate	11368.85	H	38.17	18.56	2.4 ± 0.9	2.9	7 ± 1	6 ± 2
PN3-64	6	Dolomudstone	11342.35	H	38.04	23.68	0.0 ± 0.7	5.1	1	--
PN D-2	6	Dolomudstone	11377.50	H	38.06	16.06	1.0 ± 1.0	5.0	5	--

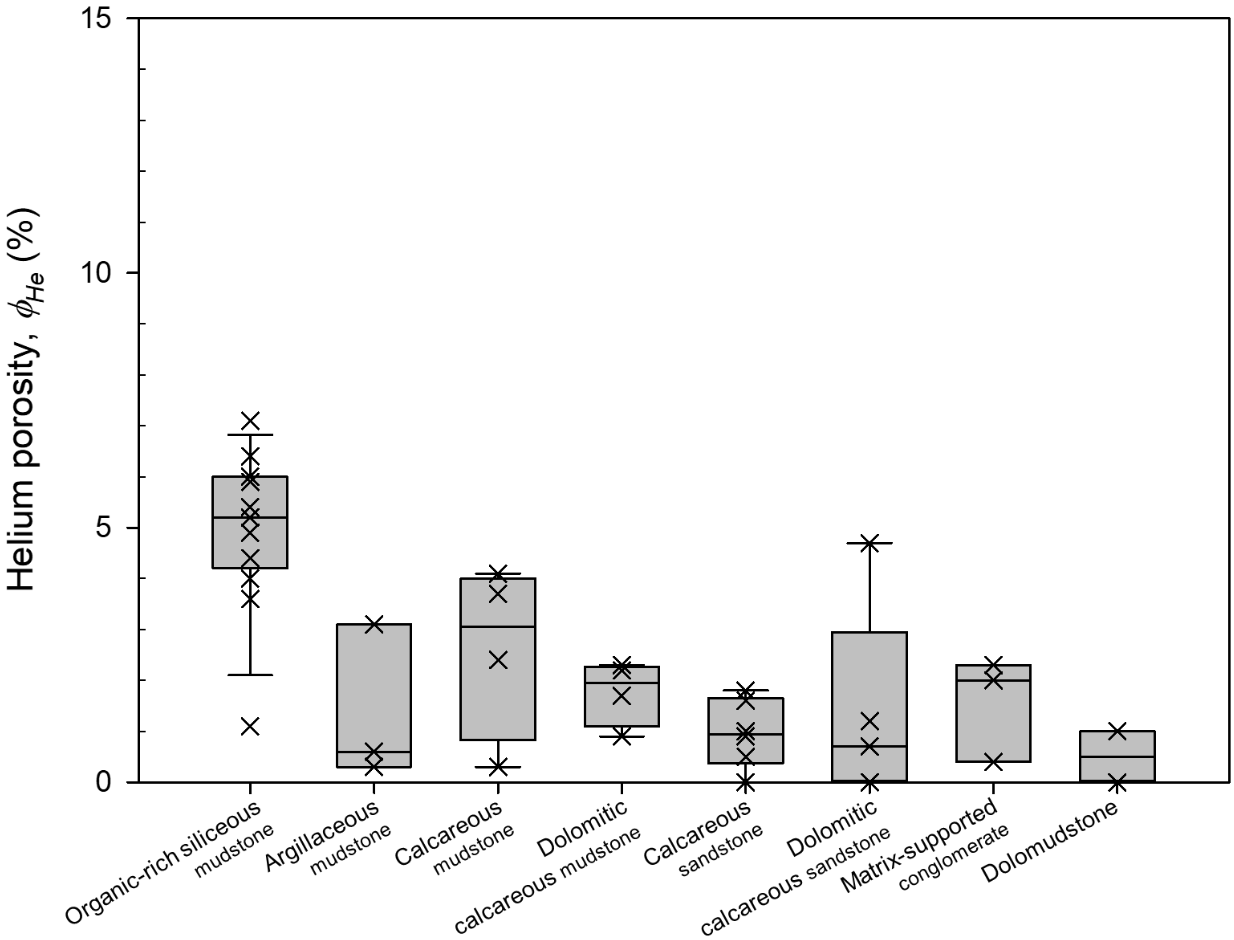

Figure 3.A1. Helium porosity (ϕ_{He}) of all samples measured by lithofacies.

For each lithofacies, the top and bottom lines represent the maximum and minimum values, respectively. The top and bottom edges of the grey box mark the first and third percentiles, respectively. The median value is the horizontal line within the box. See Table 3.A1 for the measured ϕ_{He} in each sample.

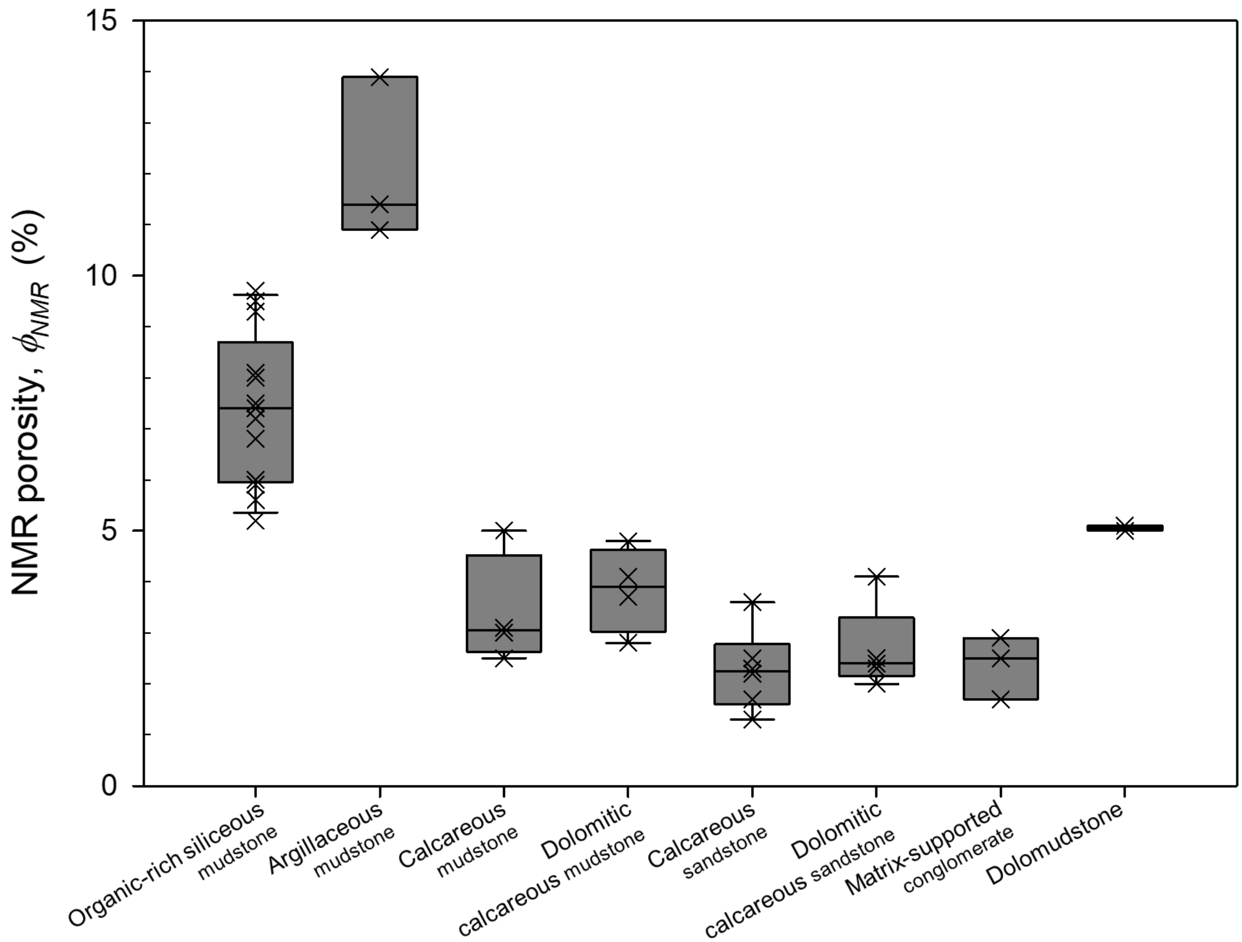

Figure 3.A2. Nuclear magnetic resonance porosity (ϕ_{NMR}) of all samples measured by lithofacies.

For each lithofacies, the top and bottom lines represent the maximum and minimum values, respectively. The top and bottom edges of the grey box mark the first and third percentiles, respectively. The median value is the horizontal line within the box. See Table 3.A1 for the measured ϕ_{NMR} in each sample.

Table 3.A2. Summary of normalized TOC content and bulk XRPD-mineralogy by sample, in wt. %, and vitrinite reflectance (VR), in %Ro.

Sample ID		Lithofacies	TOC [a]	Quartz [b]	K-Feldspar [b]	Plagioclase [b]	Calcite [b]	Dolomite [b]	Ankerite [b]	Siderite [b]	Anatase [b]	Apatite [b]	IS/S-ML [b]	Chlorite [b]	Pyrite [b]	VR [c]
PN2-46*	1	Organic-rich siliceous mudstone	1.57	49.5	0.8	8.6	7.6	1.3	5.9	0.0	0.0	0.7	21.9	0.8	1.2	0.97
PN2-46B	1	Organic-rich siliceous mudstone	--	--	--	--	--	--	--	--	--	--	--	--	--	--
PN3-33	1	Organic-rich siliceous mudstone	1.82	40.2	2.2	14.3	6.5	1.2	1.0	0.0	0.3	0.0	29.2	1.5	2.0	--
PN3-39	1	Organic-rich siliceous mudstone	0.34	53.7	2.8	10.9	7.4	1.1	2.1	0.0	0.2	0.0	19.4	1.1	1.0	1.12
PN3-92	1	Organic-rich siliceous mudstone	2.07	28.4	1.0	10.1	20.0	3.0	2.3	0.9	0.0	0.0	28.4	2.3	1.7	1.16
PN3-108	1	Organic-rich siliceous mudstone	2.11	37.2	1.0	12.4	8.8	0.7	2.0	0.0	0.0	0.9	30.6	2.4	1.9	1.00
PN4-11V	1	Organic-rich siliceous mudstone	1.76	33.5	1.4	15.7	14.2	2.2	2.2	0.1	0.3	0.0	25.7	0.4	2.6	--
PN4-15	1	Organic-rich siliceous mudstone	1.67	56.6	1.0	11.1	2.1	0.7	0.7	0.0	0.3	0.0	23.3	1.1	1.5	1.34
PN5-12	1	Organic-rich siliceous mudstone	2.01	38.6	2.0	11.8	4.0	1.4	1.8	0.0	0.3	0.0	33.5	3.4	1.3	1.54
PN5-12V	1	Organic-rich siliceous mudstone	--	--	--	--	--	--	--	--	--	--	--	--	--	--
PN5-50	1	Organic-rich siliceous mudstone	1.54	52.1	2.3	6.9	2.0	0.1	0.1	0.0	0.0	0.0	26.5	8.0	0.6	1.12
PN6-3	1	Organic-rich siliceous mudstone	2.23	44.7	1.4	11.8	0.6	0.4	1.1	0.0	0.0	0.0	33.1	2.4	2.2	1.04
PN6-75	1	Organic-rich siliceous mudstone	1.86	45.2	0.6	7.2	14.0	2.1	2.6	0.0	0.2	0.0	24.5	0.0	1.7	1.21
PN6-75V	1	Organic-rich siliceous mudstone	--	--	--	--	--	--	--	--	--	--	--	--	--	--
PN D-3	2	Argillaceous mudstone	0.64	23.8	0.0	8.0	11.0	3.5	5.5	0.0	0.0	0.2	44.4	1.2	1.7	--
PN D-11	2	Argillaceous mudstone	--	--	--	--	--	--	--	--	--	--	--	--	--	--
PN D-14	2	Argillaceous mudstone	--	--	--	--	--	--	--	--	--	--	--	--	--	--
PN D-6	3a	Calcareous mudstone	0.57	38.9	0.0	14.0	29.8	2.1	6.0	0.0	0.0	0.2	6.6	1.1	0.9	--
PN6-93	3a	Calcareous mudstone	1.09	35.0	0.5	4.3	41.1	1.3	6.0	0.2	0.1	0.0	9.5	0.0	0.9	--
PN6-113	3a	Calcareous mudstone	1.26	27.6	0.0	3.7	48.8	1.9	4.2	0.3	0.0	0.0	10.8	0.4	1.0	--
PN6-118	3a	Calcareous mudstone	1.20	58.6	1.4	5.9	13.8	0.3	0.7	0.0	0.2	0.0	16.1	0.2	1.6	1.46
PN2-52	3b	Dolomitic calcareous mudstone	0.93	27.2	0.0	6.3	26.8	5.9	19.5	0.0	0.0	1.2	11.6	0.0	0.6	--
PN D-4	3b	Dolomitic calcareous mudstone	0.95	19.2	0.0	6.8	30.8	8.0	15.3	0.0	0.0	0.2	17.1	0.7	0.9	--
PN4-10	3b	Dolomitic calcareous mudstone	0.58	34.3	0.7	7.6	34.3	3.4	8.2	0.3	0.0	0.0	9.5	0.3	0.8	--
PN4-18-1	3b	Dolomitic calcareous mudstone	1.16	39.6	0.0	12.7	15.3	5.0	9.1	0.5	0.1	0.0	12.8	1.8	1.9	--
PN D-15	3b	Dolomitic calcareous mudstone	1.40	37.8	0.0	6.4	10.9	5.9	10.8	0.0	0.0	0.3	22.2	3.2	1.1	--
PN2-2	4a	Calcareous sandstone	0.36	24.8	0.0	5.0	58.1	1.4	4.9	0.3	0.0	0.0	4.7	0.2	0.3	--
PN2-3	4a	Calcareous sandstone	0.61	32.3	0.5	5.3	45.4	0.8	9.1	0.0	0.1	0.0	5.1	0.0	0.7	0.94
PN2-51	4a	Calcareous sandstone	0.36	18.9	0.0	4.1	70.0	0.2	2.4	0.4	0.0	0.0	2.4	0.9	0.4	--
PN6-69	4a	Calcareous sandstone	0.26	55.5	0.0	3.1	34.5	0.8	1.0	0.0	0.1	0.0	2.9	0.2	1.7	--
PN6-78	4a	Calcareous sandstone	0.61	22.4	0.0	3.3	60.9	1.7	4.8	0.0	0.0	0.1	5.5	0.2	0.4	--
PN6-108	4a	Calcareous sandstone	0.56	28.6	0.0	2.4	61.7	0.4	1.0	0.2	0.0	0.0	4.5	0.2	0.5	--
PN D-1	4b	Dolomitic calcareous sandstone	0.50	10.9	0.0	3.2	31.5	13.8	35.2	0.0	0.0	0.3	4.5	0.0	0.2	--
PN6-36	4b	Dolomitic calcareous sandstone	0.45	20.2	0.0	5.7	33.0	4.1	28.6	0.0	0.1	0.0	6.7	0.0	1.2	1.37

PN6-36B*	4b	Dolomitic calcareous sandstone	--	--	--	--	--	--	--	--	--	--	--	--	--	--
PN D-16-1	4b	Dolomitic calcareous sandstone	--	--	--	--	--	--	--	--	--	--	--	--	--	--
PN D-17	4b	Dolomitic calcareous sandstone	0.67	20.2	0.0	2.5	24.1	29.2	21.3	0.0	0.0	0.0	1.6	0.5	0.0	--
PN2-30	5	Matrix-supported conglomerate	1.57	47.9	0.9	8.3	16.8	2.0	3.8	0.0	0.0	2.0	14.6	1.2	0.9	--
PN3-54	5	Matrix-supported conglomerate	0.71	28.3	0.9	8.7	43.3	0.4	7.4	0.0	0.1	0.0	9.4	0.0	0.7	--
PN3-90	5	Matrix-supported conglomerate	0.73	31.3	0.1	8.2	39.0	1.8	6.3	0.3	0.0	0.0	11.0	0.7	0.6	--
PN3-64	6	Dolomudstone	0.16	7.0	0.5	2.5	2.1	61.6	13.4	0.7	0.0	0.0	11.7	0.2	0.2	--
PN D-2	6	Dolomudstone	0.12	7.2	0.0	1.6	0.3	41.1	35.1	0.0	0.0	0.0	14.6	0.0	0.0	--

[a] Determined using LECO TOC analyzer by GeoMark Research Limited.

[b] Determined with X-ray powder diffraction (XRPD) analyses by The James Hutton Institute. The bulk samples were wet ground (in ethanol) in a McCrone mill and spray dried to produce random powders. The bulk XRPD patterns were recorded from 4-75°2θ using Copper Kα radiation. Quantitative analysis was done by a normalized full pattern reference intensity ratio (RIR) method. The clay fractions of <2µm were obtained by timed sedimentation, prepared as oriented mounts using the filter peel transfer technique and scanned from 2-45°2θ using Copper Kα radiation, in the air-dried state, after glycolation, and after heating to 300°C for one hour. Clay minerals identified were quantified using a mineral intensity factor approach based on calculated XRPD patterns. Dolomite includes Mg-dolomite and ankerite. Clays include illite, smectite-illite mixed layer, chlorite, and mica. Feldspars include K-feldspars and plagioclase. 'Others' may include pyrite, apatite, siderite, halite and/or anatase.

[c] Vitrinite reflectance (VR) value is the mean of multiple measurements in the same sample conducted by GeoMark Research Limited.

-- = not available.

APPENDIX 3.B

Helium porosimetry (HeP) and nuclear magnetic resonance (NMR) measurements

I used an in-house porosimeter built to conduct the helium porosimetry (HeP) measurements (Figure 3.B1A). I first draw a vacuum on the sample and reference chambers for 2 minutes. Immediately after, I shut Valve 2, and pressurize the reference chamber to approximately 200 psia with helium gas. I then close Valve 1 and open Valve 2. The helium pressure inside both the reference and sample chambers is recorded throughout the test, which is run for at least 48 hr. (black curve, Figure 3.B1B). The temperature of the experimental setup is actively controlled at 30.0 ± 0.5°C during the test (gray curve, Figure 3.B1B). Helium gas is virtually a non-adsorbable gas at room temperature (Lu et al., 1995). Therefore, I assumed that no helium gas was adsorbed on the sample during my HeP experiments and pressure change is due to diffusion of the gas into the connected pore volume.

I calculate the HeP porosity with a modified Boyle's Law. In Eq. 3.B1, I use the known volumes of the chambers (through calibration), the bulk volume of the sample (through geometrical measurement), and the pressures recorded during the experiments to calculate the porosity. The typical uncertainty of my porosity measurements is ± 1.0 porosity unit (p.u.).

$$\phi_{He} = \left(1 - \frac{[P_2(V_1+V_S)-P_1V_1-P_vV_S]/(P_2-P_v)}{V_b}\right) \text{ x } 100, \qquad \text{Eq. 3.B1}$$

where ϕ_{He} is the helium-derived porosity, P_1 is the initial reference chamber pressure (psia), P_2 is the final system pressure (psia), V_1 is the reference chamber volume (ml), V_s is the sample chamber volume (less the volume of the billets used, ml), P_v is the pressure after vacuuming out the system (psia), and V_b is the sample bulk volume of the core plug calculated by its geometry (diameter and length) (ml). The pressures P_1, P_2 and P_v are corrected pressures (P/Z) using corresponding compressibility factors Z_1, Z_2, and Z_v.

I conducted the NMR measurements using an Oxford Instruments GeoSpec2 2 MHz benchtop NMR system located at The University of Texas. I recorded the transverse relaxation time (T_2) in each sample until the signal to noise ratio (SNR) was approximately 100. The analysis was conducted at a room temperature of approximately 20°C. I inverted the T_2 data to estimate the volume of liquids contained in the sample using the Green Imaging Technologies (GIT) software. I calculate the NMR porosity using Eq. 3.B2.

$$\emptyset_{NMR} = \frac{V_L}{V_b}, \qquad \text{Eq. 3.B2}$$

where $Ø_{NMR}$ is the NMR-derived porosity; and V_L is the volume of liquids computed from the T_2-NMR signal.

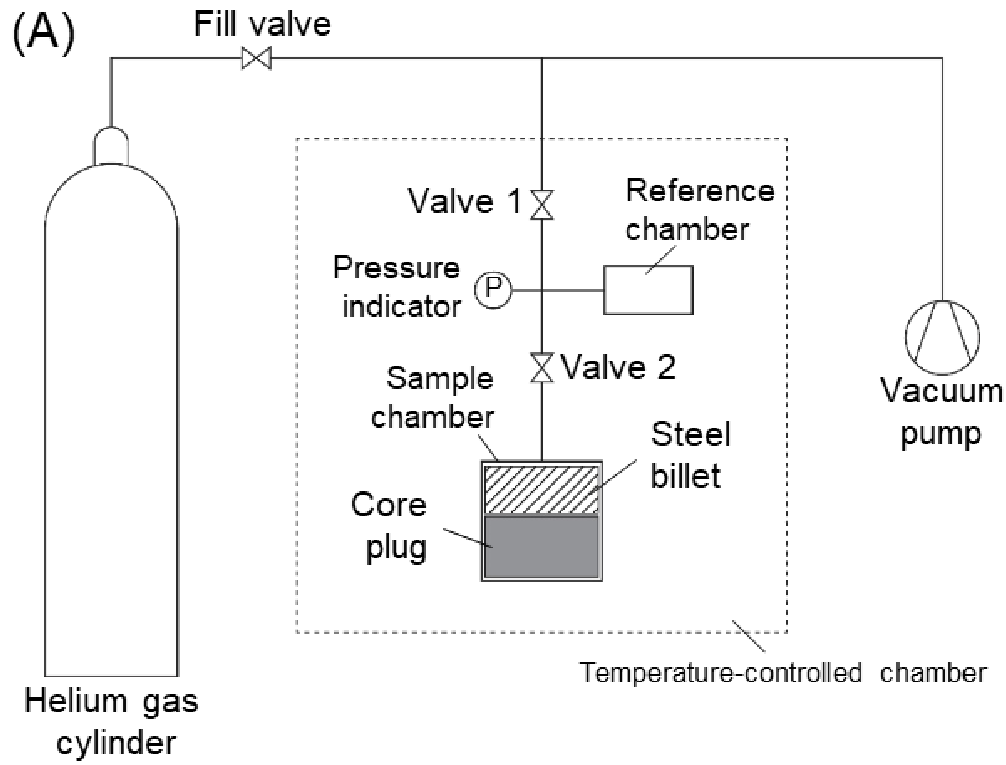

(A)
Fill valve
Valve 1
Reference chamber
Pressure indicator
P
Valve 2
Sample chamber
Steel billet
Core plug
Vacuum pump
Temperature-controlled chamber
Helium gas cylinder

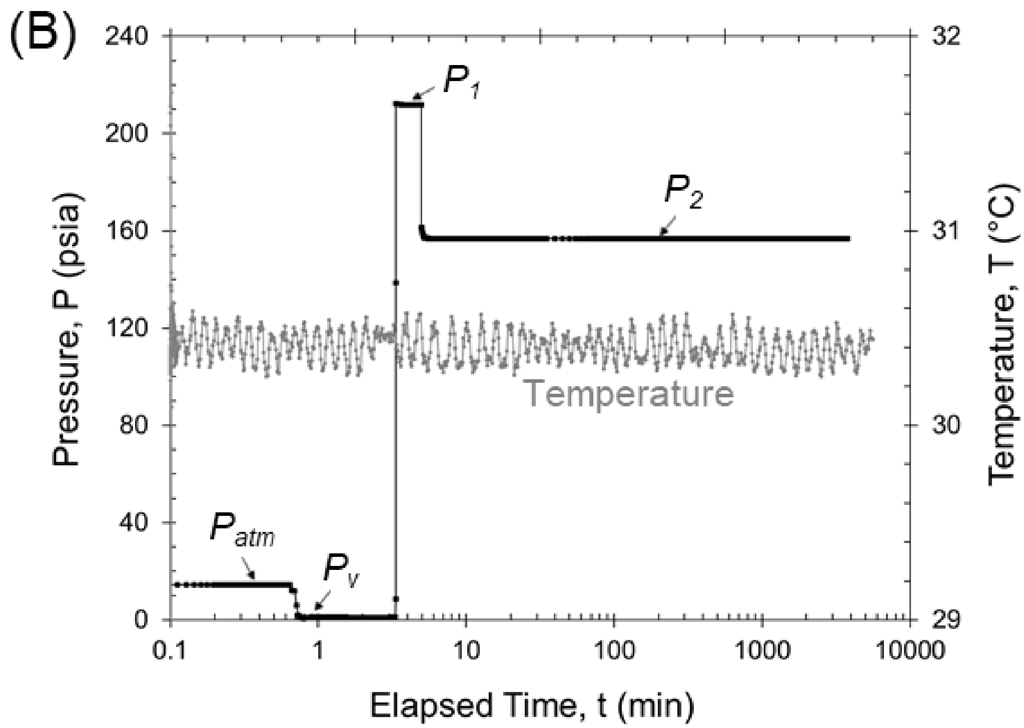

(B)
P_1
P_2
Temperature
P_{atm}
P_v
Pressure, P (psia)
Temperature, T (°C)
Elapsed Time, t (min)
0
40
80
120
160
200
240
29
30
31
32
0.1
1
10
100
1000
10000

Figure 3.B1. Helium porosimeter experimental setup and data recorded during experiment.

(A) Schematic of the helium porosimeter experimental setup. Reference chamber volume is ~13 ml, empty sample chamber volume is ~38 ml, steel billets are used in the sample chamber to minimize the dead volume. (B) Example of experimental data for helium porosity measurement in sample PN D-17. The atmospheric pressure (P_{atm}) is lowered to vacuum pressure (P_v) in the reference and in the core sample inside the sample chamber. The reference chamber is filled with helium gas to approximately 200 psi (P_1). The pressure in both the reference chamber and the sample chamber equilibrates (P_2) after Valve 2 is open. The pressure data is recorded over at least 48 hr.

Appendix 3.C

Permeability uncertainty calculation

I estimated the uncertainty of my permeability measurements with a 10,000 iteration Monte Carlo simulation for the propagation of errors. I assumed an uncertainty for q, μ, ΔP, L and A as shown in Table 3.C1. The uncertainty of my permeability measurements when $k < 20$ nD is primarily governed by the measured q due to the system leak, which manifests in the volume difference (dotted grey curve, Figure 3.5B) between the volume injected by the upstream pump (solid black, Figure 3.5B) and the volume withdrawn by the downstream pump (dashed black, Figure 3.5B). I find the uncertainty of the measured permeability is variable, ranging from ± 5 % to 30 % for $k < 20$ nD, and within ± 5% for $k > 20$ nD.

Table 3.C1. Typical uncertainties associated to each parameter in my permeability calculations.

Parameter	***Symbol***	***Uncertainty***
Flow rate	q	± 0.5 – 30 %
Dodecane viscosity	μ	± 2 %
Pressure differential	ΔP	± 2 %
Length of core plug	L	± < 0.25 %
Cross sectional area of core plug	A	± < 0.25 %

APPENDIX 3.D

Liquid imbibition

I calculated the volume of dodecane imbibed in each sample after 24 hr. of saturation inside the vacuum chamber based on the sample's weight difference before and after saturation. I assumed the dodecane density is 0.769 g/cm^3 for the volume calculations. Most samples imbibed a dodecane volume equivalent to the pore volume measured with the helium porosimeter (Figure 3.D1). Hence, samples were completely or almost completely saturated with liquids at the end of the saturation stage inside the vacuum chamber.

I also conducted the saturation of two twin samples from the dolomitic calcareous sandstone and organic-rich siliceous mudstone lithofacies using brine with a concentration of 30,000 ppm NaCl. I assumed the brine density is 1.000 g/cm^3 for the volume calculations. The results indicate that the organic-rich siliceous mudstone imbibed a volume of brine close to the pore volume measured with helium porosimetry (Figure 3.D2). However, the dolomitic calcareous sandstone imbibed a much lower volume of brine compared the pore volume measured with helium porosimetry. When compared with the volume of dodecane imbibed by their corresponding twin samples, the dolomitic calcareous sandstone is clearly oil-wet. In contrast, the mudstone seems to have a mixed-wettability based on the similar imbibed volumes of dodecane and brine.

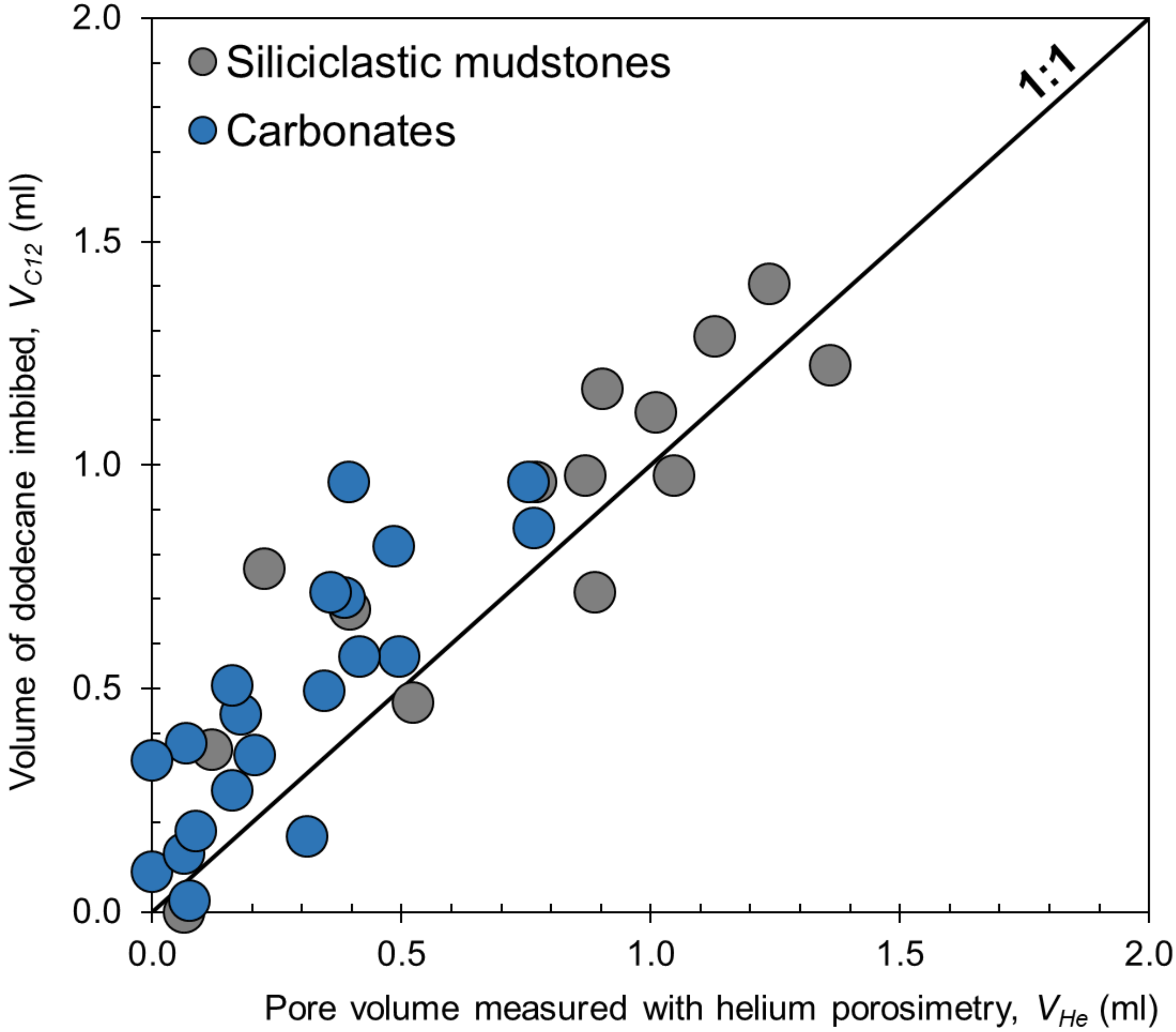

Figure 3.D1. Imbibed dodecane volume after 24 hr. of saturation inside vacuum chamber by sample.

Siliciclastic mudstone lithofacies are in grey, carbonate lithofacies are in blue.

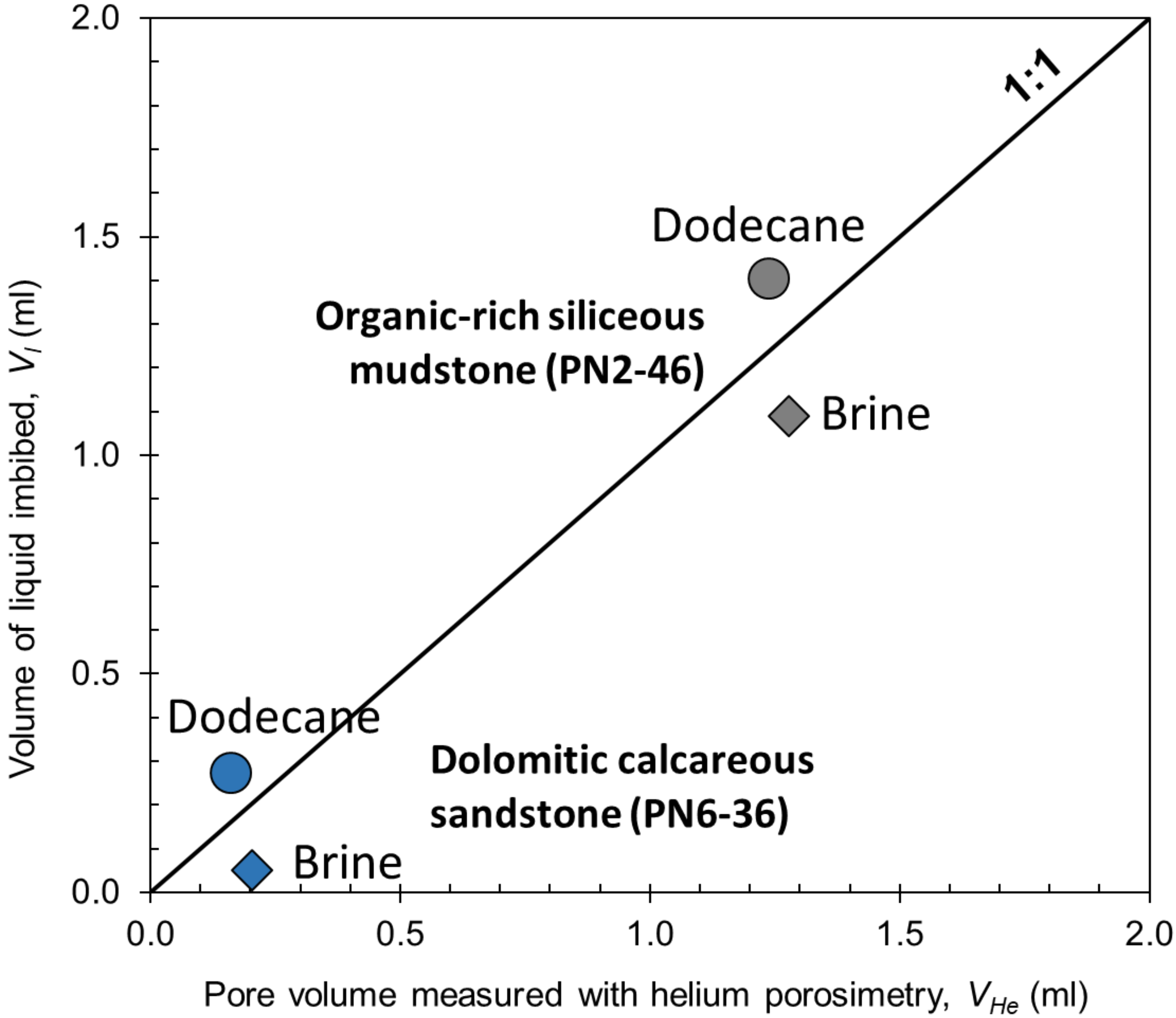

Figure 3.D2. Imbibed brine and dodecane volumes after 24 hr. of saturation inside vacuum chamber in twin samples from organic-rich siliceous mudstone and dolomitic calcareous sandstone lithofacies.

Organic-rich siliceous mudstone lithofacies in grey, dolomitic calcareous sandstone lithofacies in blue. Volume of brine imbibed represented by diamonds, volume of dodecane imbibed represented by circles.

REFERENCES

Bernard, S., B. Horsfield, H.-M. Schulz, R. Wirth, A. Schreiber, and N. Sherwood, 2012a, Geochemical evolution of organic-rich shales with increasing maturity: A STXM and TEM study of the Posidonia Shale (Lower Toarcian, northern Germany): Marine and Petroleum Geology, v. 31, p. 70-89.

Bernard, S., R. Wirth, A. Schreiber, H.-M. Schulz, and B. Horsfield, 2012b, Formation of nanoporous pyrobitumen residues during maturation of the Barnett Shale (Fort Worth Basin): International Journal of Coal Geology, v. 103, p. 3-11.

Bhandari, A. R., P. B. Flemings, R. Hofmann, and P. J. Polito, 2018, Stress-Dependent In Situ Gas Permeability in the Eagle Ford Shale: Transport in Porous Media, v. 123, p. 1-20.

Bhandari, A. R., P. B. Flemings, S. Ramiro-Ramirez, R. Hofmann, and P. J. Polito, 2019, Gas and liquid permeability measurements in Wolfcamp samples: Fuel, p. 1026–1036.

Bohacs, K. M., Q. R. Passey, M. D. Rudnicki, W. L. Esch, and O. R. Lazar, 2013, The spectrum of fine-grained reservoirs from 'shale sas' to 'shale oil'/ tight liquids: essential attributes, key controls, practical characterization, International Petroleum Technology Conference, Beijing, China, p. 16.

Camp, W. K., and B. Wawak, 2013, Enhancing SEM grayscale images through pseudocolor conversion: Examples from Eagle Ford, Haynesville, and Marcellus shales, *in* W. K. Camp, E. Diaz, and B. Wawak, eds., Electron microscopy of shale reservoirs, v. AAPG Memoir 102, AAPG, p. 15-26.

Chhatre, S. S., E. M. Braun, S. Sinha, M. D. Determan, Q. R. Passey, T. E. Zirkle, A. C. Wood, J. A. Boros, D. W. Berry, S. A. Leonardi, and R. A. Kudva, 2015, Steady-state stress-dependent permeability measurements of tight oil-bearing rocks: Petrophysics, v. 56, p. 116-124.

Curtis, M. E., R. J. Ambrose, C. H. Sondergeld, and C. S. Rai, 2010, Structural characterization of gas shales on the micro-and nano-scales, Canadian Unconventional Resources & International Petroleum Conference, Calgary, Alberta, Canada, p. 15.

Curtis, M. E., B. J. Cardott, C. H. Sondergeld, and C. S. Rai, 2012, Development of organic porosity in the Woodford Shale with increasing thermal maturity: International Journal of Coal Geology, v. 103, p. 26-31.

Defeu, C., G. G. Ferrer, E. Ejofodomi, D. Shan, and F. Alimahomed, 2018, Time Dependent Depletion of Parent Well and Impact on Well Spacing in the Wolfcamp Delaware Basin, SPE Liquids-Rich Basins Conference-North America, Midland, TX, USA, SPE, p. 13.

Dobber, A. W., and r. H. Goldstein, 2020, Diagenetic Controls on Reservoir Character of the Lower Permian Wolfcamp and Bone Spring Formations in the Delaware Basin, West Texas, URTeC, Austin, Texas, USA, p. 23.

Dutton, S. P., E. M. Kim, R. F. Broadhead, W. D. Raatz, C. L. Breton, S. C. Ruppel, and C. Kerans, 2005, Play analysis and leading-edge oil-reservoir development methods in the Permian basin: Increased recovery through advanced technologies: AAPG Bulletin, v. 89, p. 553-576.

EIA, 2022, Tight oil production estimates by play.

Euzen, T., N. Watson, M. Fowler, A. Mort, and T. F. Moslow, 2021, Petroleum distribution in the Montney hybrid play: Source, carrier bed, and structural controls: AAPG Bulletin, v. 105, p. 1867-1892.

Fraser, J. A., and P. K. Pedersen, 2021, Reservoir characterization of fairways in a tight light oil play of the Upper Cretaceous Cardium Formation, west Pembina, Alberta, Canada: AAPG Bulletin, v. 105, p. 1797-1820.

Fredd, C. N., and H. S. Fogler, 1998, Influence of transport and reaction on wormhole formation in porous media: AIChE Journal, v. 44, p. 1933-1949.

Fu, Q., R. W. Baumgardner, Jr, and H. S. Hamlin, 2020, Early Permian (Wolfcampian) succession in the Permian Basin: icehouse platform, slope carbonates, and basinal mudrocks, *in* S. C. Ruppel, ed., Anatomy of a Paleozoic basin: the Permian Basin, USA, v. 2, The University of Texas at Austin, Bureau of Economic Geology Report of Investigations 285; AAPG Memoir 118, p. 185-226.

Gale, J. F. W., S. J. Elliott, and S. E. Laubach, 2018, Hydraulic fractures in core from stimulated reservoirs: core fracture description of HFTS Slant Core, Midland Basin, West Texas, URTeC, Houston, Texas, USA, p. 18.

Gale, J. F. W., S. J. Elliott, B. G. Rysak, C. L. Ginn, N. Zhang, R. D. Myers, and S. E. Laubach, 2021, Fracture description of the HFTS-2 Slant Core, Delaware Basin, West Texas, URTeC, Houston, Texas, USA, p. 12.

Huang, J., T. Cavanaugh, and B. Nur, 2003, An introduction to SEM operational principles and geologic applications for shale hydrocarbon reservoirs, *in* W. K. Camp, E. Diaz, and B. Wawak, eds., Electron microscopy of shale hydrocarbon reservoirs, v. AAPG Memoir 102, AAPG, p. 1-6.

Hunt, D., and W. M. Fitchen, 1999, Compaction and the dynamics of carbonate-platform develoment: insights from the Permian Delaware and Midland basins, southeast New Mexico and west Texas, U.S.A., *in* P. M. Harris, A. H. Saller, and J. A. Simo, eds., Advances in carbonate sequence stratigraphy: application to reservoirs, outcrops and models, SEPM Special Publication No. 63, p. 75-106.

Jarvie, D. M., R. J. Hill, T. E. Ruble, and R. M. Pollastro, 2007, Unconventional shale-gas systems: The Mississippian Barnett Shale of north-central Texas as one model for thermogenic shale-gas assessment: AAPG Bulletin, v. 91, p. 475-499.

Katz, M. L., and M. R. Tek, 1961, A theoretical study of pressure distribution and fluid flux in bounded stratified porous systems with crossflow: Society of petroleum Engineers Journal, v. 2, p. 68-82.

King, H., M. Sansone, P. Kortunov, Y. Xu, N. Callen, S. Chhatre, H. Sahoo, and A. Buono, 2018, Microstructural Investigation of Stress-Dependent Permeability in Tight-Oil Rocks: Petrophysics, v. 59, p. 35-43.

Kosanke, T., and A. Warren, 2016, Geological controls on matrix permeability of the Eagle Ford Shale (Cretaceous), South Texas, U.S.A.: The Eagle Ford Shale: A renaisaance in U.S. oil production, v. AAPG Memoir 110.

Kuhl, E. J., 2003, Optimization of Recovery from Two-Layer Reservoirs with Crossflow: Master thesis, Pennsylvania State University, 95 p.

Kurtoglu, B., 2013, Integrated reservoir characterization and modeling in support of enhanced oil recovery for Bakken, Colorado School of Mines, 239 p.

Loucks, R. G., R. M. Reed, S. C. Ruppel, and D. M. Jarvie, 2009, Morphology, genesis, and distribution of nanometer-scale pores in siliceous mudstones of the Mississippian Barnett Shale: Journal of Sedimentary Research, v. 79, p. 848-861.

Lu, X.-C., F.-C. Li, and T. Watson, 1995, Adsorption measurements in Devonian shales: Fuel, v. 74, p. 599-603.

Male, F., B. Rysak, and R. Dommisse, 2021, Statistical analysis of fractures from the hydraulic fracture test site 1, URTeC, Houston, Texas, USA, p. 15.

Mastalerz, M., A. Drobniak, and A. B. Stankiewicz, 2018, Origin, properties, and implications of solid bitumen in source-rock reservoirs: A review: International Journal of Coal Geology, v. 195, p. 14-36.

Mathur, A., C. H. Sondergeld, and C. S. Rai, 2016, Comparison of Steady-State and Transient Methods for Measuring Shale Permeability, SPE Low Perm Symposium, Denver, Colorado, USA, p. 22.

Mavor, M., 2014, Reservoir fluid properties required for low-permeability oil reservoir analysis, Geoscience Technology Workshop, Hydrocarbon Charge Considerations in Liquid-Rich Unconventional Petroleum Systems, Vancouver, BC, Canada.

Mazzullo, J. M., 2000, Organogenic dolomitization in peritidal to deep-sea sediments: Journal of Sedimentary Research, v. 70, p. 10-23.

Milliken, K. L., L. T. Ko, M. Pommer, and K. M. Marsaglia, 2014, Sem Petrography of Eastern Mediterranean Sapropels: Analogue Data For Assessing Organic Matter In Oil and Gas Shales: Journal of Sedimentary Research, v. 84, p. 961-974.

Mohan, K., K. D. Scott, G. D. Monson, and P. A. Leonard, 2013, A systematic approach to understanding well performance in unconventional reservoirs: a Wolfcamp case study, URTeC, Denver, Colorado, USA, p. 10.

Park, H., 1989, Well test analysis of a multilayered reservoir with formation crossflow, Stanford University, 164 p.

Parsegov, S. G., K. Nandlal, D. S. Schechter, and R. Weijermars, 2018, Physics-driven optimization of drained rock volume for multistage fracturing: field example from the Wolfcamp formation, Midland Basin, URTeC, Houston, Texas, USA, p. 31.

Passey, Q. R., K. M. Bohacs, W. L. Esch, R. Klimentidis, and S. Sinha, 2010, From oil-prone source rock to gas-producing shale reservoir – geologic and petrophysical characterization of unconventional shale-gas reservoirs, CPS/SPE International Oil & Gas Conference and Exhibition, Beijing, China, p. 29.

Patzek, T. W., F. Male, and M. Marder, 2013, Gas production in the Barnett Shale obeys a simple scaling theory: Proceedings of the National Academy of Sciences, v. 110, p. 19731-19736.

Pendergrass, J. D., and V. J. Berry, 1962, Pressure transient performance of a multilayered reservoir with crossflow: Society of Petroleum Engineers Journal, v. 2, p. 347-354.

Phillips, O. M., 1991, Flow and reactions in permeable rocks: Cambridge, New York, Port Chester, Merlbourne, Sydney, Cambridge University Press, 285 p.

Rafatian, N., and J. Capsan, 2015, Petrophysical characterization of the pore space in Permian Wolfcamp rocks: Petrophysics, v. 56, p. 45-57.

Ramiro-Ramirez, S., P. B. Flemings, A. R. Bhandari, and O. S. Jimba, 2021, Steady-State liquid permeability measurements in samples from the Bakken Formation, Williston Basin, USA, SPE Annual Technical Conference and Exhibition, Dubai, UAE, p. 15.

Raterman, K. T., H. E. Farrell, O. S. Mora, A. L. Janssen, G. A. Gomez, S. Busetti, J. McEwen, K. Friehauf, J. Rutherford, R. Reid, G. Jin, B. Roy, and M. Warren, 2018, Sampling a stimulated rock volume: an Eagle Ford example: SPE Reservoir Evaluation & Engineering, v. 21, p. 15.

Romero-Sarmiento, M.-F., S. Ramiro-Ramirez, G. Berthe, M. Fleury, and R. Littke, 2017, Geochemical and petrophysical source rock characterization of the Vaca Muerta Formation, Argentina: Implications for unconventional petroleum resource estimations: International Journal of Coal Geology, v. 184, p. 27-41.

Russell, D. G., and M. Prats, 1962, The Practical Aspects of Interlayer Crossflow: Journal of Petroleum Technology, p. 6.

Rydzy, M. B., J. Patino, N. Elmetni, and M. Appel, 2016, Stressed permeability in shales: effects of matrix compressibility and fractures - a step towards measuring matrix permeability in fractured shale samples, International Symposium of the Society of Core Analysts, Snowmass, Colorado, USA, p. 12.

Sagasti, G., A. Ortiz, D. Hryb, M. Foster, and V. Lazzari, 2014, Understanding geological heterogeneity to customize field development: An example from the Vaca Muerta unconventional play, Argentina, URTeC, Denver, Colorado, USA, p. 20.

Salem, A. C., S. J. Naruk, and J. G. Solum, 2022, Impact of natural fractures on production from an unconventional shale: The Delaware Basin Wolfcamp shale: AAPG Bulletin, v. 106, p. 20.

Schieber, J., 2010, Common themes in the formation and preservation of intrinsic porosity in shales and mudstones – Illustrated with examples across the Phanerozoic, SPE Unconventional Gas Conference, Pittsburgh, Pennsylvania, USA, p. 10.

Sinclair, T. D., 2007, The generation and continued existence of overpressure in the Delaware Basin, Texas: Doctoral thesis, Durham University, 314 p.

Teklu, T. W., X. Li, Z. Zhou, and H. Abass, 2018, Experimental investigation on permeability and porosity hysteresis of tight formations: SPE Journal, v. 23, p. 672-690.

Thomeer, J. H. M., 1960, Introduction of a Pore Geometrical Factor Defined by the Capillary Pressure Curve: Journal of Petroleum Technology, v. 12, p. 73-77.

Thompson, M., P. Desjardins, J. Pickering, and B. Driskill, 2018, An integrated view of the petrology, sedimentology, and sequence stratigraphy of the Wolfcamp Formation, Delaware Basin, Texas, URTeC, Houston, Texas, p. 8.

Vermylen, J. P., 2011, Geomechanical Studies of the Barnett Shale, Texas, USA: Doctoral thesis, Stanford University, 143 p.

Weijermars, R., K. Nandlal, M. F. Tugan, W. Dusterhoft, and N. Stegent, 2020, Wolfcamp hydraulic fracture test site drained rock volume and recovery factors visualized by scaled complex analysis method (CAM): emulating multiple data sources (production rates, water cuts, pressure gauges, flow regime changes, and *b*-sigmoids), URTeC, Austin, TX, USA, p. 42.

Wilson, R. D., J. Chitale, K. Huffman, P. Montgomery, and S. J. Prochnow, 2020, Evaluating the depositional environment, lithofacies variation, and diagenetic processes of the Wolfcamp B and lower Spraberry intervals in the Midland Basin: Implications for reservoir quality and distribution: AAPG Bulletin, v. 104, p. 1287-1321.

Yu, W., and K. Sepehrnoori, 2018, Shale Gas and Tight Oil Reservoir Simulation, Gulf Professional Publishing, 432 p.

Zhan, L., P. S. Fair, R. J. Dombrowski, E. N. Quint, and R. Cao, 2018, Estimating ultralow permeability at multiple locations using simultaneous-impulse tests: A fit-for-purpose pressure-transient solution and its field application: Society of Petroleum Engineers Journal, v. 23, p. 1184-1200.

Zhang, T., Q. Fu, X. Sun, P. c. Hackley, L. T. Ko, and D. Shao, 2021, Meter-scale lithofacies cycle and controls on variations in oil saturation, Wolfcamp A, Delaware and Midland Basins: AAPG Bulletin, v. 105, p. 1821-1846.

Zoback, M. D., and A. H. Kohli, 2019, Unconventional Reservoir Geomechanics: New York, NY, Cambridge University Press, 484 p.

Chapter 4: Sensitivity analysis of a permeability heterogeneous two-layer reservoir model with cross-facies flow

4.1 Abstract

Single-phase flow simulations in a two-layered model with cross-facies flow indicate that the high-permeability layer's horizontal permeability (k_{h2}) and thickness (h_2) are the primary controls on the production rates and the upscaled permeabilities. In the model, the two layers have different thickness, porosity, and permeability. The fluid can flow across the left boundary while the other three boundaries are impermeable. The two layers can pressure-communicate via their common interface (i.e., cross-facies flow is allowed). The lower bound performance on production occurs when each layer produces independently (i.e., there is no cross-facies flow). The upper bound performance on production occurs when there is cross-facies flow and the high-permeability layer is infinitely conductive (e.g., k_{h2} = 10^9 nD). In the simulated reservoir performance, which represents the production rates using the permeabilities most representative of the in-situ reservoir conditions, there is cross-facies flow, and the high-permeability layer is not infinitely conductive (e.g., k_{h2} = 560 nD). Flow restriction occurs in the high permeability layer, and the reservoir performance lies between the lower and upper bounds. As the high-permeability layer's horizontal permeability (k_{h2}) or thickness (h_2) increase, flow restriction diminishes, and reservoir performance approaches the upper bound. The increase in production rates from cross-facies flow results in upscaled permeabilities multiple times higher than the permeabilities measured in the dominant lithofacies in low-permeability reservoirs. These results illuminate that cross-facies flow increases the production rates in permeability heterogeneous reservoirs hydraulically fractured vertically and produced with horizontal wells. I demonstrate that the elevated upscaled permeabilities required to history match production in low-permeability reservoir simulation models can be explained by the presence of cross-facies flow.

4.2 INTRODUCTION

The low-permeability formations often contain multiple lithofacies with drastically different matrix permeabilities (e.g., Kurtoglu, 2013; Kosanke and Warren, 2016; Ramiro-Ramirez et al., 2021). The cross-facies flow between lithofacies may be the key mechanism to explain the elevated high permeabilities required to history-match production in low-permeability reservoir simulation models. The impact of stratigraphic layer to layer permeability heterogeneity on flow performance has been widely studied in conventional (e.g., permeability in the order of millidarcies or more) stratified reservoir models (Katz and Tek, 1961; Pendergrass and Berry, 1962; Russell and Prats, 1962; Park, 1989; Phillips, 1991; Kuhl, 2003). In these reservoir models, the cross-facies flow occurs when the most permeable zones deplete rapidly and generate a vertical pressure gradient with the adjacent lithofacies. The fluids stored in the less permeable lithofacies are produced more efficiently (i.e., at faster rates) as they are drained by the high-permeability zones.

The reservoir simulation models (e.g., Patzek et al., 2013) often require upscaled permeabilities much higher than those measured independently in the laboratory on core plugs taken from the dominant lithofacies (e.g., mudstone) to history match production data. For example, in the Wolfcamp operational unit, published reservoir model results (e.g., Mohan et al., 2013; Defeu et al., 2018; Parsegov et al., 2018) show they require upscaled permeabilities between 350 nD and 10^6 nD to match production. However, I found that the permeability of the lithofacies that dominate the Wolfcamp (e.g., organic-rich siliceous mudstone lithofacies) is much smaller (k_{median} = 21 nD) (see Chapter 3). One explanation given for such high permeabilities is that pre-existing natural fractures in the reservoir reactivate and/or an enhanced permeability zone along the main hydraulic fracture is developed during stimulation (Mohan et al., 2013; Patzek et al., 2013). However, recent studies indicate that a significant fraction of the natural fractures may not reactivate during stimulation (Male et al., 2021), that their contribution to production is not significant (Salem et al., 2022), and also that a complex fracture network does not develop during stimulation (Gale et al., 2018; Raterman et al., 2018; Gale et al., 2021). Here, I show that cross-facies flow between Wolfcamp lithofacies that have drastically different permeabilities results in an increase of the upscaled permeabilities. I demonstrate this by running flow simulations in a permeability heterogeneous two-layer reservoir model informed with the petrophysical and geometrical properties (presented in Chapters 2 and 3).

The objectives of this chapter are to expand the simulation results of the two-layer model presented in Chapter 3 by running simulations using multiple variations of the reservoir parameters (e.g., different reservoir thickness, permeabilities) in the Wolfcamp A and Wolfcamp B models. This model illustrates that, during production, permeable layers drain fluids from the low-permeability strata through cross-facies flow and then laterally into the hydraulic fracture. The result is an increase of the upscaled permeability that is multiple times above the permeability of the low-permeability strata (e.g., mudstones and carbonates). I discuss the influence of these reservoir parameters on the cross-facies flow and how these results may impact field development plan strategies.

4.3 REVIEW OF PREVIOUS WORK

The flow behavior in stratified reservoirs with cross-facies flow has been the focus of many authors addressing the effect of geological heterogeneities (e.g., stratification) on reservoir performance. Katz and Tek (1961) derived analytical expressions to describe flow behavior during depletion of stratified systems involving cross-facies flow. The authors demonstrated that the performance in these systems lies between the upper and lower bounds. They defined the upper bound using a single-layer model with an arithmetic average of the petrophysical properties in the two layers. They defined the lower bound as the summation of the fluxes from each layer as treated individually. Russell and Prats (1962) showed that cross-facies flow can be identified in pressure and/or production decline data from layered reservoirs. When cross-facies flow occurs, the reservoir exhibits an exponential pressure decline; in contrast, layered reservoirs without cross-facies flow exhibit variable production decline rates in the pressure build-up curves. As the reservoir layers deplete, the decline curve changes. Based on these results, they showed that performance of a two-layer reservoir with cross-facies flow can be described by use of a single-layer reservoir with equivalent pore volume. Pendergrass and Berry (1962) further confirmed that a stratified reservoir with crossflow behaves substantially the same as a homogeneous reservoir. In summary, the performance in a two-layer reservoir with cross-facies flow can be matched with a single-layer reservoir model with equivalent pore volume. The upscaled permeability in this single-layer reservoir will lie between the permeabilities of the two layers involved.

4.4 Model description

I constructed a layered reservoir model which consists of two layers (Figure 4.1). The low-permeability layer represents the low-permeability strata (e.g., organic-rich siliceous mudstone, k = 20 nD), and the high-permeability layer represents the dolomitized carbonate deposits (e.g., k > 500 nD) in the upper Wolfcamp interval (Chapter 2 and 3). Because of symmetry of the problem, I perform calculations on one half of the space between high-permeability layers. Hence, the modelled height (h_n) of each layer is one-half their average bed thickness in the upper Wolfcamp stratigraphic section. The length of the model (L = 50 ft) is based on an assumed spacing between hydraulic fractures of 100 ft.

The flow behavior is described by Equation 4.1:

$$\frac{\partial P}{\partial t} = \frac{1}{\emptyset \mu c_f} \left(\frac{\partial}{\partial x}\left(k \frac{\partial P}{\partial x}\right) + \frac{\partial}{\partial y}\left(k \frac{\partial P}{\partial y}\right) \right), \qquad \text{Eq. 4.1}$$

where P = fluid pressure, t = time, k = matrix permeability, $\emptyset$ = rock porosity, μ = fluid viscosity, and c_f = fluid compressibility.

At initial conditions (IC), the domain is assumed to be at constant pressure (P) of 6000 psi (Table 4.1):

IC: $P(L, h, t = 0) = 6000\, psi$

The boundary conditions (BC) are no flow at the top, bottom, and right boundaries; the left boundary simulates the interface between the hydraulic fracture and the reservoir, and its pressure is constant at P_f = 3000 psi (Table 4.1):

BC: $P(L = 0, h, t) = 3000\, psi$ (left boundary)

$\frac{\partial P}{\partial y}\ (L,\ 0,\ t) = 0$ (bottom boundary)

$\frac{\partial P}{\partial y}\ (L,\ h = h_1 + h_2,\ t) = 0$ (top boundary)

$\frac{\partial P}{\partial x}\ (L = 50\, ft,\ h,\ t) = 0$ (right boundary)

I assume 1) single-phase flow; 2) negligible gravity effects; 3) the bulk rock is incompressible, and all flow is driven by fluid expansion; 4) fluid properties (Table 4.1) are constant and characteristic of Wolfcamp crude oil; 5) permeability is homogenous throughout each layer; 6) each layer has permeability anisotropy: the horizontal permeability is greater than the vertical permeability.

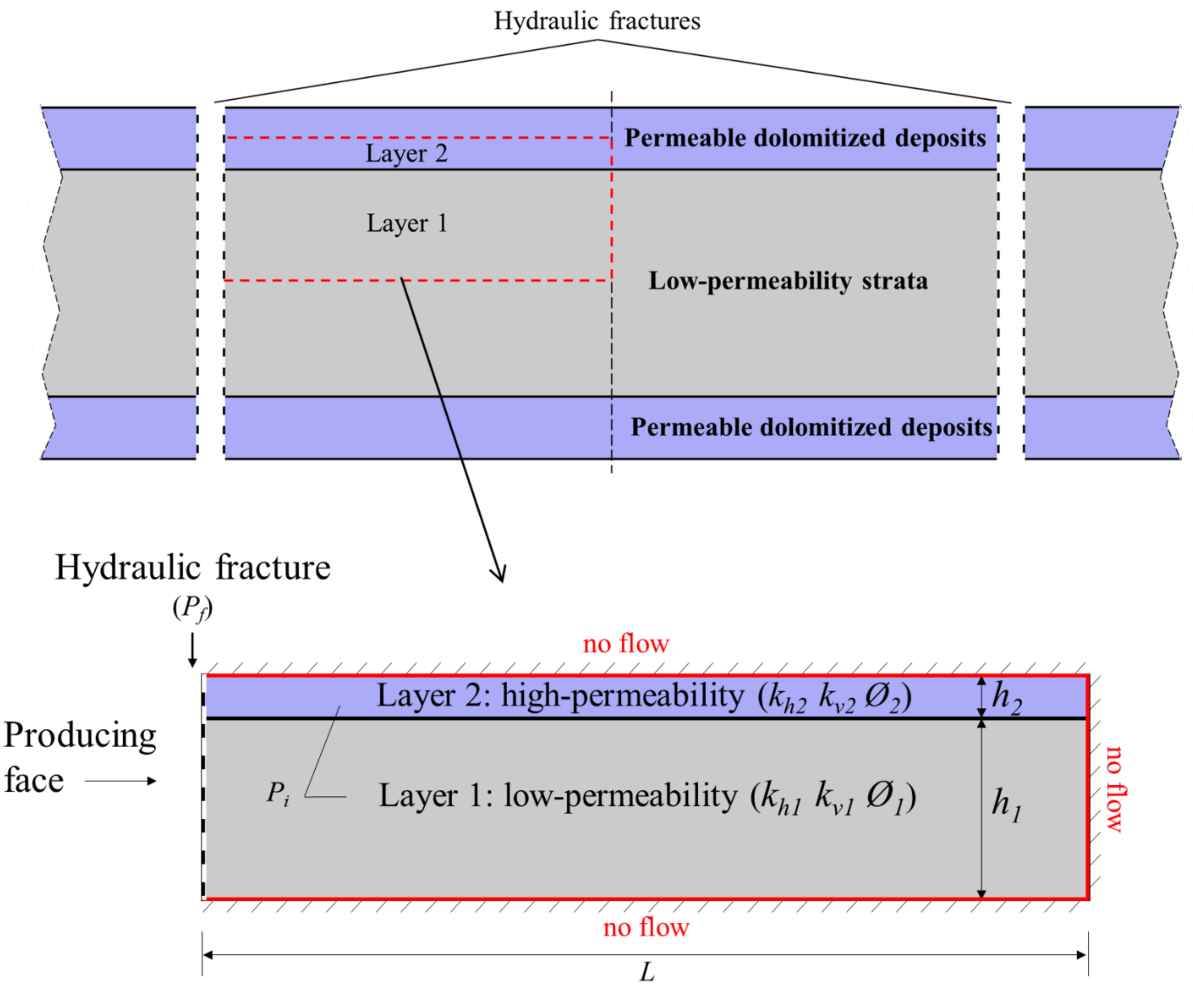

Figure 4.1: Schematic of layered model.

Schematic of layered model composed of a high-permeability layer (blue) and low-permeability strata (gray). Table 4.1 summarizes the model parameters.

Table 4.1. Model parameters.

Parameter		Wolfcamp A	Wolfcamp B
Model length	L	50 ft	
Layer 1 thickness	h_1	6.7 ft	11.0 ft
Layer 2 thickness	h_2	1.4 ft	0.6 ft
Layer 1 horizontal permeability	k_{h1}	20 nD	
Layer 1 vertical permeability	k_{v1}	0.1 k_{h1}	
Layer 2 horizontal permeability	k_{h2}	560 nD	
Layer 2 vertical permeability	k_{v2}	0.1 k_{h2}	
Layer 1 porosity	$Ø_1$	0.12	
Layer 2 porosity	$Ø_2$	0.05	
Initial reservoir pressure	P_i	6,000 psi	
Pressure at the fracture	P_f	3,000 psi	
Fluid density[1]	ρ_f	725 kg/m^3	
Fluid viscosity[1]	μ	6.6 e-4 Pa.s	
Fluid compressibility[1]	c_f	1.55 e-9 1/Pa	

[1]Wolfcamp crude oil properties at 4500 psi (Mavor, 2014).

4.5 SIMULATION CASES

I conducted multiple flow simulations using varying reservoir parameters (Table 4.2) to investigate how they affect the pressure distribution within each layer's domain and the fluxes at the producing face in the Wolfcamp A and Wolfcamp B models. The Wolfcamp A has a high permeability layer that is h_2 = 1.4 ft thick, and a low permeability layer that is h_1 = 6.7 ft thick. The Wolfcamp B has a high permeability layer that is h_2 = 0.6 ft thick, and a low permeability layer that is h_1 = 11.0 ft thick. The high permeability layer's thickness (h_2) represents one-half the average thickness of the dolomitic calcareous mudstone and dolomitic calcareous sandstone lithofacies in each Wolfcamp unit; the low-permeability layer's thickness (h_1) represents one-half the average distance between permeable layers in each Wolfcamp unit that is occupied by low-permeability lithofacies. These thicknesses are maintained constant in all simulation cases, except indicated otherwise (e.g., in Case 4 and Case 5, Table 4.2).

Table 4.2. Specific model parameters used in each case.

		h_1 (ft)	h_2 (ft)	k_{v1} (nD)	k_{h1} (nD)	k_{v2} (nD)	k_{h2} (nD)
Case 1: Lower Bound	Wolfcamp A	6.7	1.4	0	20	0	560
	Wolfcamp B	11.0	0.6	0	20	0	560
Case 2: Upper Bound	Wolfcamp A	6.7	1.4	2	20	10^8	10^9
	Wolfcamp B	11.0	0.6	2	20	10^8	10^9
Case 3: Simulated production	Wolfcamp A	6.7	1.4	2	20	56	560
	Wolfcamp B	11.0	0.6	2	20	56	560
Case 4: Increasing thickness of low-permeability layer (h_1)	Wolfcamp A	6.7 to 134.0	1.4	2	20	56	560
	Wolfcamp B	11.0 to 220.0 ft	0.6	2	20	56	560
Case 5: Increasing thickness of high-permeability layer (h_2)	Wolfcamp A	6.7	1.4 to 27.0	2	20	56	560
	Wolfcamp B	11.0	0.6 to 16.5	2	20	56	560
Case 6: Increasing horizontal permeability of high-permeability layer (k_{h2})	Wolfcamp A	6.7	1.4	2	20	0.1 k_{h2}	10^2 to 10^4
	Wolfcamp B	11.0	0.6	2	20	0.1 k_{h2}	10^2 to 10^4
Case 7: Increasing vertical permeability of low-permeability layer (k_{v1})	Wolfcamp A	6.7	1.4	0.5 to 10^6	20	56	560
	Wolfcamp B	11.0	0.6	0.5 to 10^6	20	56	560

4.5.1 Case 1: No cross-facies flow (Lower bound performance)

In Case 1 (Table 4.2), I assume that there is no cross-facies flow (due to impermeable interface), and therefore there is only horizontal flow towards the fracture within each layer's domain. Hence, I impose the following boundary condition in my simulations:

$$\frac{\partial P}{\partial y}\ (L,\ h1,\ t) = 0 \qquad \text{(impermeable interface)}$$

I represent cumulative flux as a function of the 'Recovery Factor' (*RF*). The *RF* represents the cumulative produced pore volume over the maximum producible pore volume for the given model parameters (Table 4.1). I set the horizontal permeability of the low-permeability layer (k_{h1}) to 20 nD, which is the median permeability of the organic-rich siliceous mudstone. I set the porosity of this layer ($Ø_1$) to 12%, which is the average porosity of the organic-rich siliceous mudstone. I set the horizontal permeability of the high-permeability layer (k_{h2}) to 560 nD and I assume its porosity ($Ø_2$) to be 5 %; these are the values found for the dolomitic calcareous mudstone and dolomitic calcareous sandstone lithofacies.

4.5.2 Case 2: Cross-facies flow (Upper bound performance)

In Case 2 (Table 4.2), I determine the upper bound on model performance, which represents the highest production rates for the assumed model parameters. In this case, there is communication across the interface between both layers (i.e., there is cross-facies flow). Hence, there is two-dimensional flow. I set the high-permeability layer's horizontal permeability to $k_{h2} = 10^9$ nD. I set the low-permeability layer's horizontal permeability (k_{h1}) and each layer's porosity ($Ø_1$, $Ø_2$) the same as those in Case 1. I assume the vertical permeability (k_{v1}, k_{v2}) in each layer is 10 times less than their horizontal permeability. This permeability anisotropy is based on vertical and horizontal permeability measurements in two contiguous vertical and horizontal core plugs from the organic-rich siliceous mudstone lithofacies in the Wolfcamp.

4.5.3 Case 3: Cross-facies flow (Simulated production performance)

In Case 3 (Table 4.2), I simulate the performance of the model using the parameters that are most representative of the in-situ reservoir conditions. I inform this model with the porosities ($Ø_1$, $Ø_2$) and horizontal permeabilities (k_{h1}, k_{h2}) used in Case 1, and the vertical permeabilities (k_{v1}, k_{v2}) used in Case 2. I use the same layer thicknesses (h_1, h_2) as those used in Case 1 and Case 2.

4.5.4 Case 4: Cross-facies flow with increasing thickness of low-permeability layer (h_1)

In Case 4 (Table 4.2), I determine the effect of increasing the low-permeability layer's thickness (h_1) on the model performance. I increase the low-permeability layer's thickness (h_1) while leaving fixed the thickness of the high-permeability layer (h_2). I use the same porosities ($Ø_1$, $Ø_2$), horizontal permeabilities (k_{h1}, k_{h2}), and vertical permeabilities (k_{v1}, k_{v2}) as those used in Case 3.

4.5.5 Case 5: Cross-facies flow with increasing thickness of high-permeability layer (h_2)

In Case 5 (Table 4.2), I determine the effect of increasing the high-permeability layer's thickness (h_2) on the model performance. I increase the high-permeability layer's thickness (h_2) while leaving fixed the thickness of the low-permeability layer (h_1). I use the same porosities ($Ø_1$, $Ø_2$), horizontal permeabilities (k_{h1}, k_{h2}), and vertical permeabilities (k_{v1}, k_{v2}) as those used in Case 3.

4.5.6 Case 6: Cross-facies flow with increasing horizontal permeability of high-permeability layer (k_{h2})

In Case 6 (Table 4.2), I determine the effect of increasing the high-permeability layer's horizontal permeability (k_{h2}) on the model performance. I increase the high-permeability layer's horizontal permeability (k_{h2}) while leaving fixed the low-permeability layer's horizontal and vertical permeabilities (k_{h1}, k_{v1}). I use the same porosities ($Ø_1$, $Ø_2$), layer thicknesses (h_1, h_2), and low-permeability layer's horizontal and vertical permeabilities (k_{h1}, k_{v1}) as those used in Case 3.

4.5.7 Case 7: Cross-facies flow with increasing vertical permeability of low-permeability layer (k_{v1})

In Case 7 (Table 4.2), I determine the effect of increasing the low-permeability layer's vertical permeability (k_{v1}) on the model performance. I increase the low-permeability layer's vertical permeability (k_{v1}) while leaving fixed the low-permeability layer's horizontal permeability (k_{h1}) and the high-permeability layer's horizontal and vertical permeabilities (k_{h2}, k_{v2}). I use the same porosities ($Ø_1$, $Ø_2$), layer thicknesses (h_1, h_2), low-permeability layer's horizontal permeabilities (k_{h1}), and high-permeability layer's horizontal and vertical permeabilities (k_{h2}, k_{v2}) as those used in Case 3.

4.6 Simulation Results

4.6.1 Case 1: No cross-facies flow (Lower bound performance)

In Case 1, the pressure in each layer dissipates independently as the fluids contained in their pore volume are produced across their left boundary (Figure 4.2). The pressure in the high-permeability layer equilibrates with the pressure in the fracture (i.e., P_f = 3000 psi) at earlier times (t < 1 year) than the low-permeability layer. This is because the high-permeability layer's horizontal permeability is much higher (k_{h2} = 560 nD) than the low-permeability layer's horizontal permeability (k_{h1} = 20 nD). Once the high-permeability layer is fully depleted, its pressure equilibrates with the pressure in the fracture (P_f), and production continues only from the low-permeability layer. At infinite times, the pressure in the entire reservoir domain equilibrates with P_f.

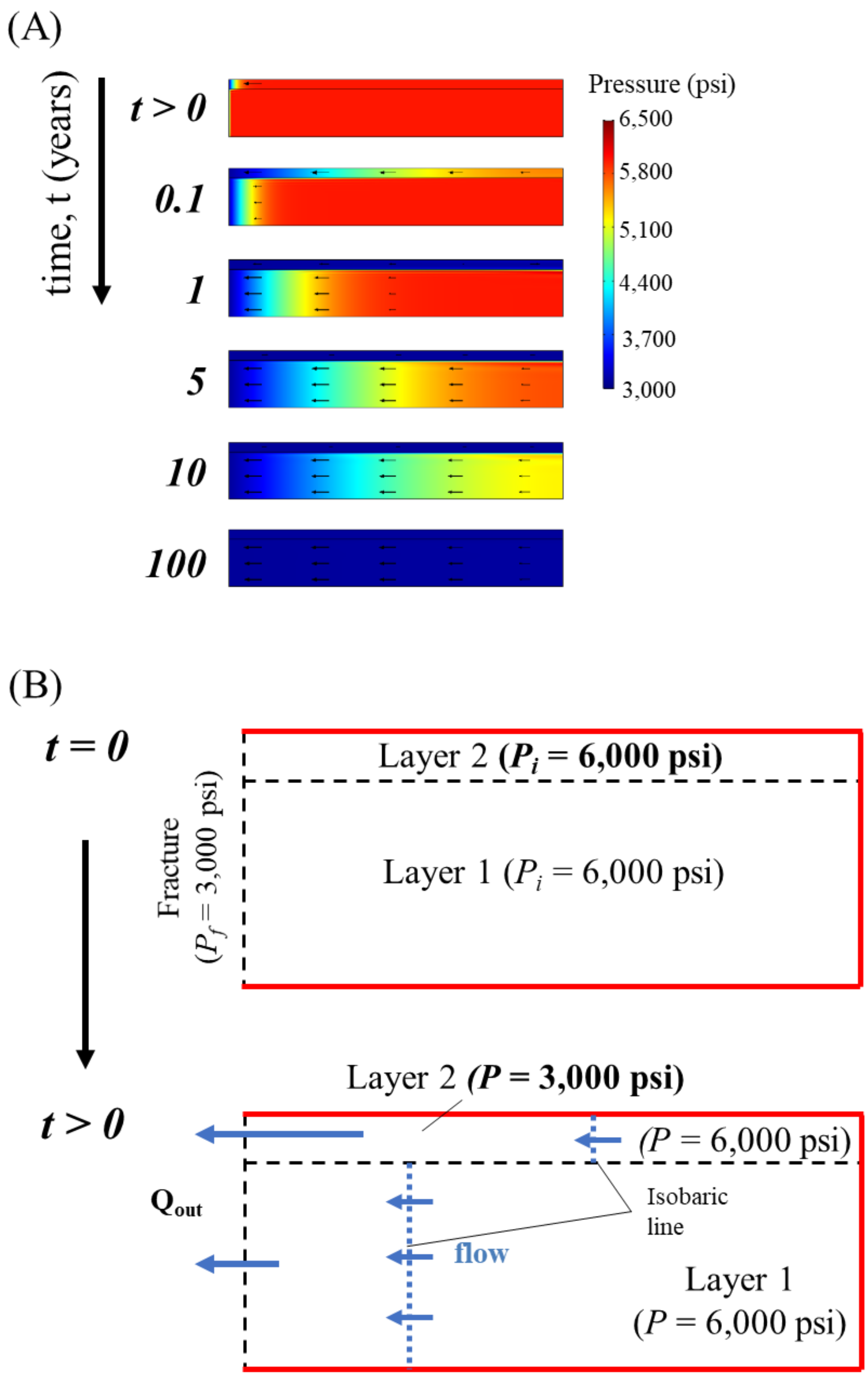

Figure 4.2. Pressure dissipation in the lower bound performance model.

(A) Examples of pressure distribution within each layer's domain over time in the Wolfcamp A model. Arrows indicate flow direction and magnitude in logarithmic scale. (B) Schematics showing the interpretation of isobaric lines and flow direction at initial conditions (t = 0) and at early times (t > 0).

Figure 4.3 shows the numerical solution for the lower bound performance on the Wolfcamp A (orange, dashed curve) and Wolfcamp B (black, solid curve) models. The results represent the production profile in the low-permeability layer only. In both models, approximately 85% of the producible pore volume (i.e., *RF*) was produced at the end of t = 30 years. The numerical solutions in the Wolfcamp A and Wolfcamp B are identical because the production scales with the reservoir length (L), which is the same in both models. Production scales with L because all flow is 1D horizontal towards the fracture (i.e., the producing face on at the left boundary).

To demonstrate that production rate scales with L in this model, I use the consolidation model (see Flemings, 2021) as an analog to solve this 1D problem analytically. The overpressure ($\Delta P = P_i - P_f$) dissipation over time due to fluid expansion is given by:

$$\Delta P = \sum_{m=0}^{m=\infty} \frac{2P_i}{M} \left(\sin\frac{Mx}{L}\right) exp(-M^2 T_v), \qquad \text{Eq. 4.2}$$

where

$$M = \frac{\pi}{2}(2m+1), \qquad \text{Eq. 4.3}$$

and

$$T_v = \frac{c_v t}{L^2}, \qquad \text{Eq. 4.4}$$

where

$$C_v = \frac{k}{\mu c_f \emptyset} \qquad \text{Eq. 4.5}$$

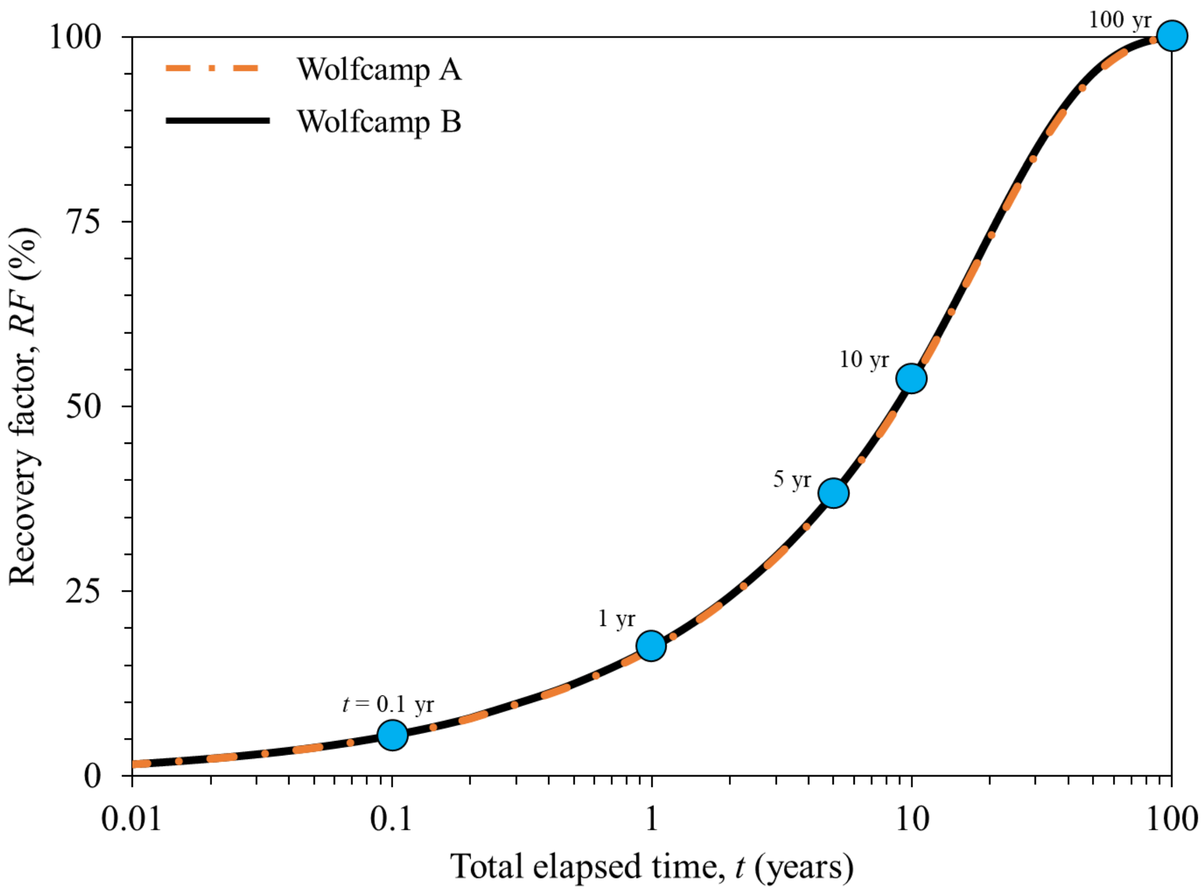

Figure 4.3. Numerical solution for the lower bound performance on the Wolfcamp A (orange, dashed curve) and Wolfcamp B (black, solid curve) models.

Blue dots represent time slices shown in Figure 4.2. The *RF* represents the cumulative produced pore volume over the maximum producible pore volume for the given model parameters (Table 4.1, Table 4.2).

Figure 4.4 shows that the analytical and numerical solutions for the overpressure dissipation at different time factors (T_v) converge.

The next step is to calculate the recovery factor (*RF*), which is given by:

$$RF = 1 - \sum_{m=0}^{m=\infty} \frac{2}{M} exp(-M^2 T_v) \qquad \text{Eq. 4.6}$$

The *RF* results are shown in Figure 4.5. When Tv = 1.0, the recovery factor is approximately 95% and the overpressure is ~95%. Figure 4.6 shows that the analytical and numerical solutions for the *RF* converge, demonstrating that production rates scale with the reservoir length *L* when only 1D horizontal flow exists within each layer's domain.

Next, I analyze the production decline rates. In my reservoir model (Figure 4.1), the right boundary represents the mid-point between hydraulic fractures. During production, I showed that the fluid pressure in the layers diffuses towards the hydraulic fractures until they both equilibrate (Figure 4.2). This fluid pressure diffusion occurs at a rate proportional to the inverse of the square root of time on production until the pressure at the right boundary drops below the initial pressure (i.e., interference time) (Patzek et al., 2013). Beyond this point in time, fluid production slows down and follows an exponential decline (Patzek et al., 2013). From Figure 4.4, I know that the interference time occurs at *Tv* = 0.05 (*t* = 2.3 years). From Figure 4.5, I know that the *RF* is 25.5% at *Tv* = 0.05. These two values (*t* = 2.3, *RF* = 25.5%) define the coordinates of the point in the production curve beyond which production declines exponentially (Figure 4.7). Hence, the production rate decline is proportional to $1/\sqrt{t}$ from $t = 0$ to $t = 2.3$ years. At $t > 2.3$ years, the production rates start to decline exponentially.

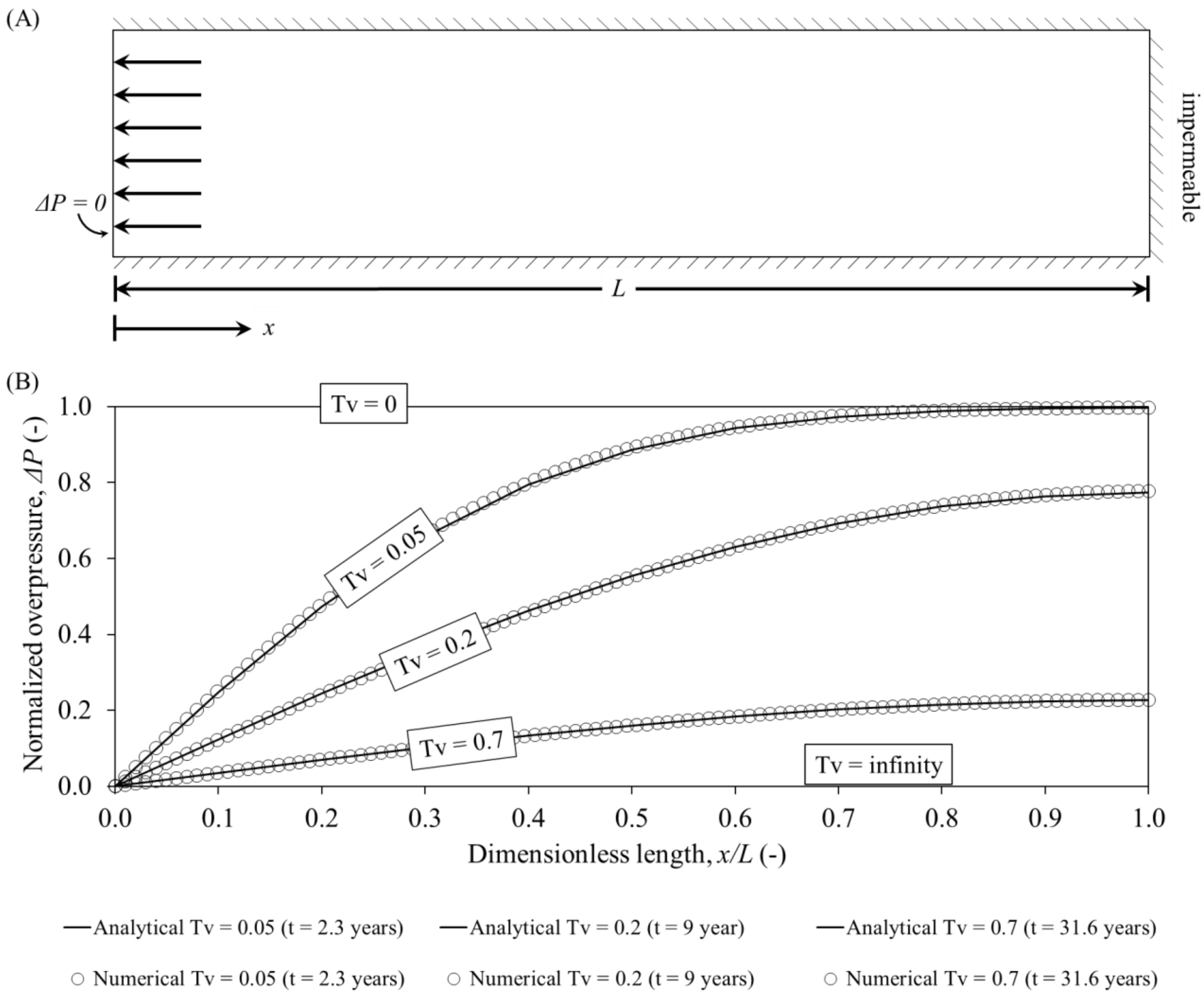

Figure 4.4. Overpressure dissipation during fluid expansion.

(A) Fluid expansion starts instantaneously inside the reservoir layer of length L. The right boundary is impermeable. (B) Overpressure profile over length from *Tv* = 0 to *Tv* = infinite. The overpressure dissipates nonuniformly along the layer from *Tv* = 0 to *Tv* = infinite. The analytical solution is represented by solid lines and the numerical solution is represented by circles.

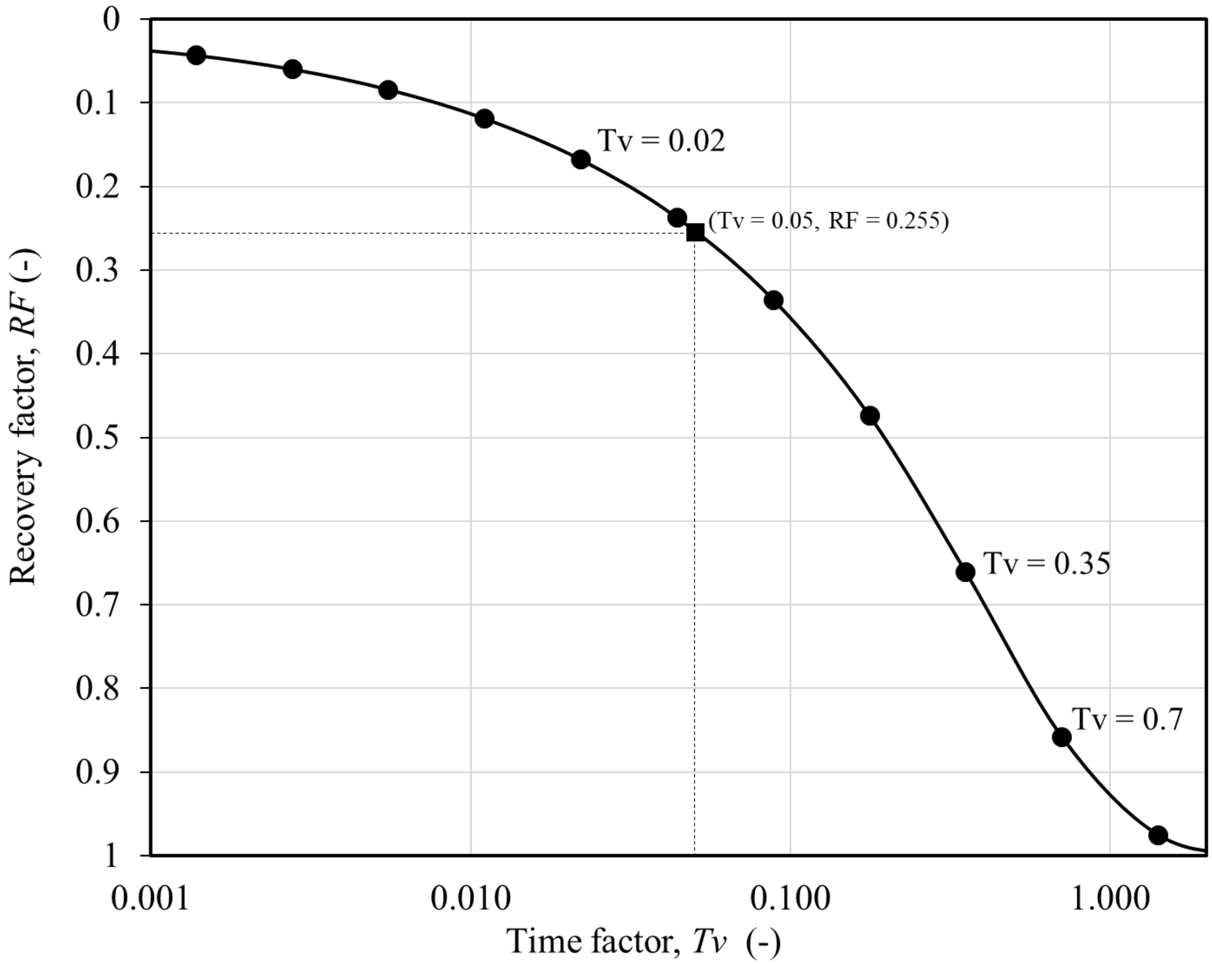

Figure 4.5. Recovery factor is equivalent to the average overpressure, during one-dimensional fluid expansion.

The recovery factor (*RF*) is the cumulative produced pore volume over the maximum producible pore volume for the given model parameters.

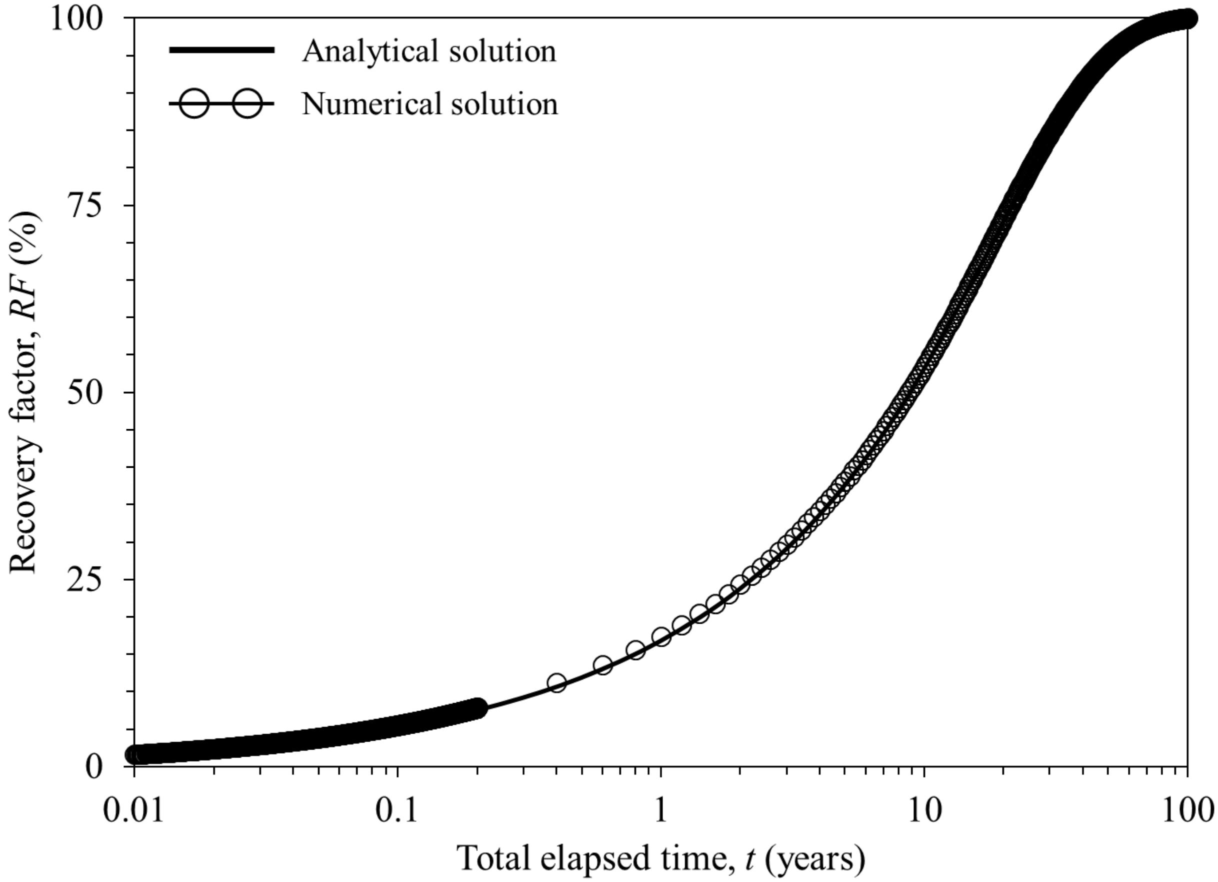

Figure 4.6. Analytical solution (black, solid curve) and numerical solution (black, circles) for the lower production bound performance on the Wolfcamp A and Wolfcamp B models.

The recovery factor (*RF*) is the cumulative produced pore volume over the maximum producible pore volume for the given model parameters.

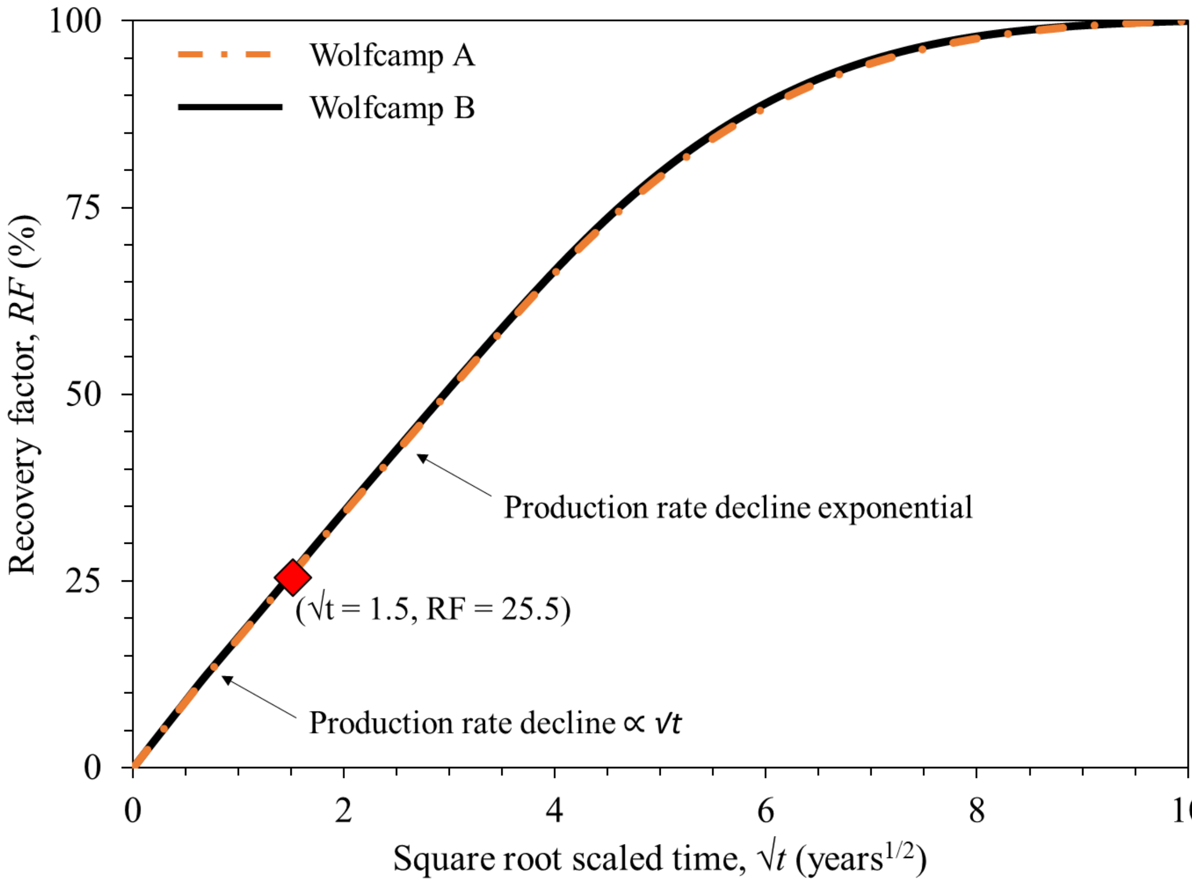

Figure 4.7. Scaled production in the Wolfcamp A (orange, dashed curve) and Wolfcamp B (black, solid curve).

From $t = 0$ years to $t = 2.3$ years ($\sqrt{t} = 1.5$) (red diamond), the production rate decline is proportional to $1/\sqrt{t}$. At $t > 2.3$ years ($\sqrt{t} = 1.5$), production rate decline becomes exponential. The recovery factor (*RF*) is the cumulative produced pore volume over the maximum producible pore volume for the given model parameters.

4.6.2 Case 2: Cross-facies flow (Upper bound performance)

In Case 2, the pressure in the low permeability layer dissipates as the fluids contained in it are produced across its left boundary and across the interface with the high-permeability layer (Figure 4.8A). Hence, there is two-dimensional flow in this model. The high-permeability layer's pressure equilibrates with the pressure in the fracture (i.e., P_f = 3000 psi) almost instantly ($t>0$) because its horizontal permeability is extremely high (k_{h2} = 10^9 nD) (Table 4.2). Once depleted, the high-permeability layer acts as a constant pressure boundary. It continues draining fluids form the low-permeability layer through cross-facies flow. These fluids are then transported horizontally towards the fracture. The isobaric lines in the low-permeability layer show that pressure dissipates in both the x- and y- directions (Figure 4.8) because there are two constant pressure boundaries: one at the fracture (i.e., left boundary), and another one at the interface with the high-permeability layer. At infinite times, the pressure in the entire reservoir domain equilibrates with P_f.

Figure 4.9 shows the numerical solution for the lower bound performance on the Wolfcamp A (dashed curve) and the Wolfcamp B (solid curve) models. The results represent the sum of the cumulative fluxes occurring across the left boundary of the low-permeability layer and across the interface between both layers. The production rates are higher in the Wolfcamp A. At the end of 4 years, the *RF* is ~85% in the Wolfcamp A model. In contrast, the Wolfcamp B model required almost 9 years to reach the same *RF* (~85%).

Production rates are different in the Wolfcamp A and Wolfcamp B models because the thickness of their low-permeability layer (h_1) is not the same. The Wolfcamp B model has a thicker low-permeability layer (h_1 = 11 ft) than the Wolfcamp A model (h_1 = 6.8 ft). There is no effect of the high-permeability layer's thickness on production rates because flow in this layer is unrestricted almost instantaneously after production. Therefore, the production rates in the upper bound production bound model are strongly dependent on the low-permeability layer's thickness because there is two-dimensional flow; the thinner the low-permeability layer, the faster the production rates.

The production rate decline is more difficult to analyze in the upper bound production model because there is two-dimensional flow. However, we can observe that the upper bound production curves exhibit steeper slopes than the lower bound model (Figure 4.10). The early production decline seems to be proportional to $1/\sqrt{t}$, and then it reaches an exponential decline at later times when the pressure at the base of the low-permeability layer (i.e., bottom boundary) drops below 6000 psi.

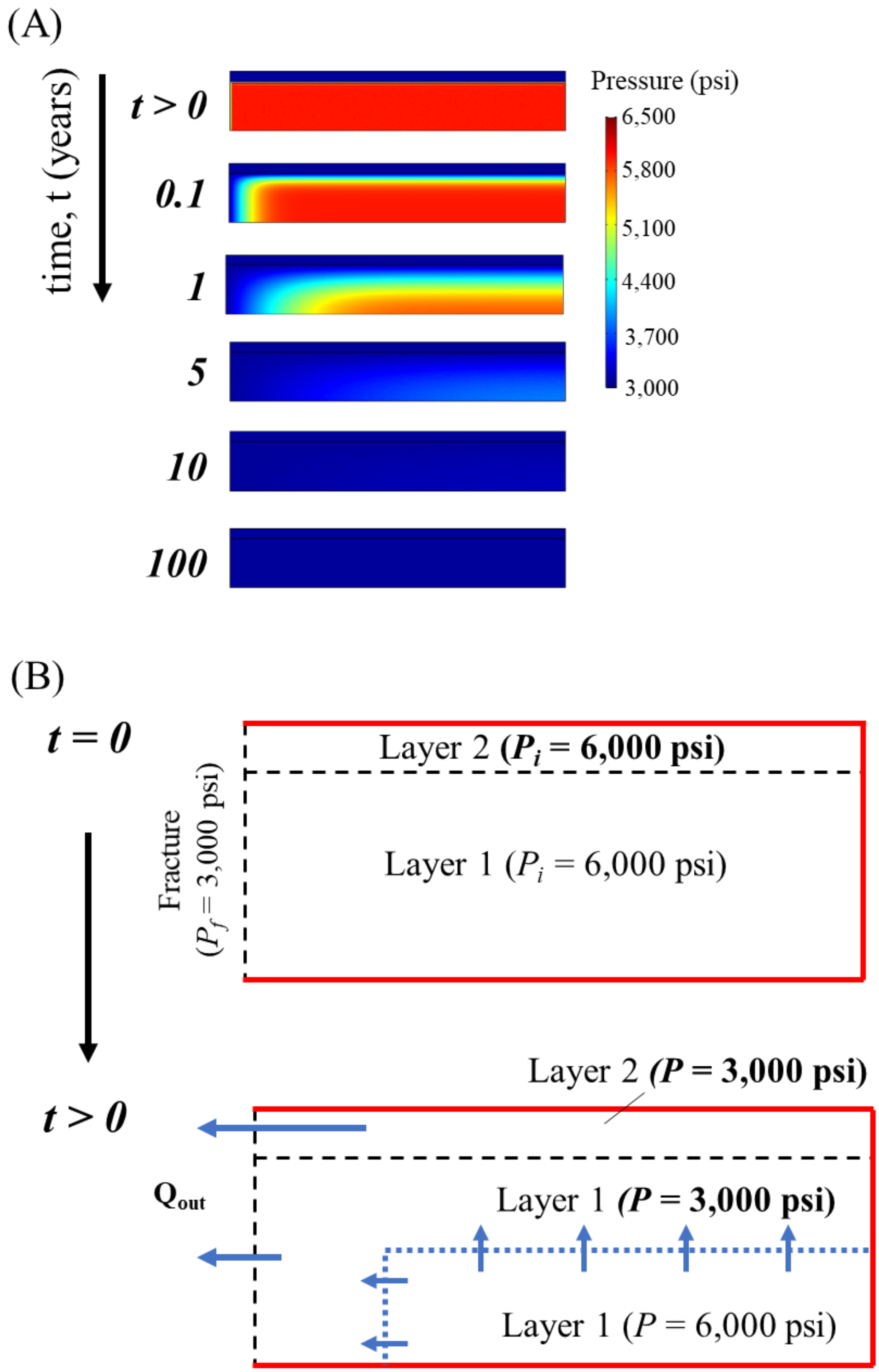

Figure 4.8. Pressure dissipation in the upper bound performance model.

(A) Examples of pressure distribution within each layer's domain over time in the Wolfcamp A model. (B) Schematics showing the interpretation of isobaric lines and flow direction at initial conditions (t = 0) and at early times (t > 0).

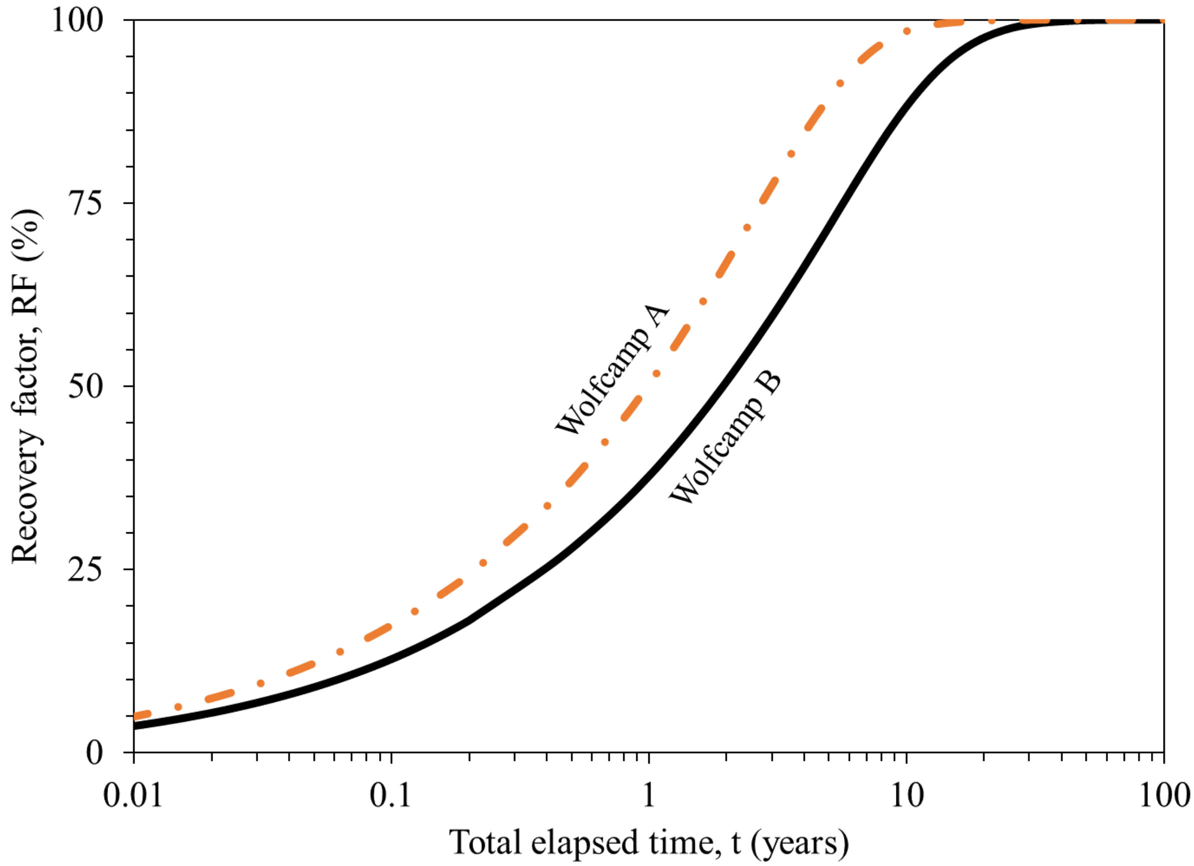

Figure 4.9. Numerical solution for the upper bound performance on the Wolfcamp A (orange, dashed curve) and Wolfcamp B (black, solid curve) models.

The *RF* represents the cumulative produced pore volume over the maximum producible pore volume for the given model parameters (Table 4.1, Table 4.2).

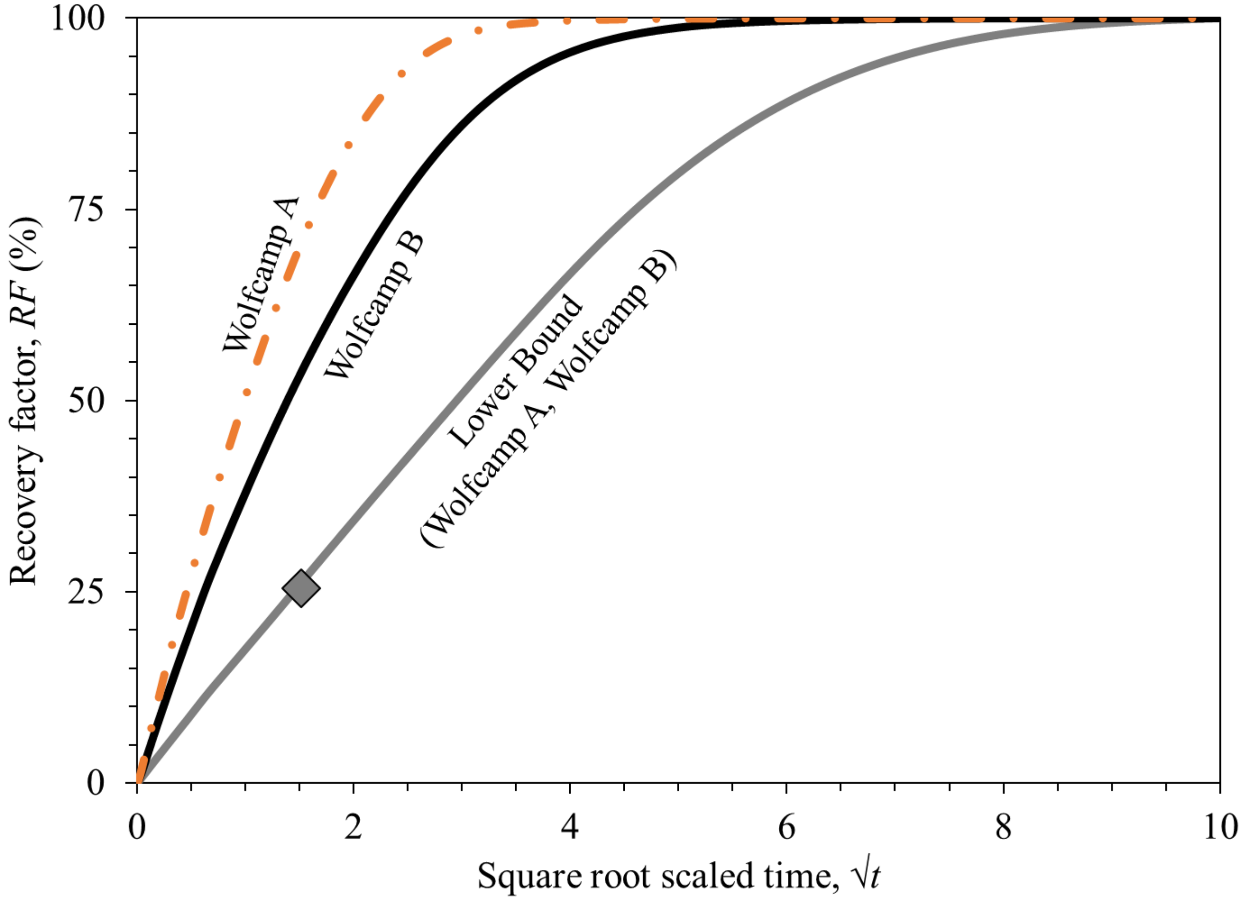

Figure 4.10. Scaled production for the upper bound performance on the Wolfcamp A (orange, dashed curve) and Wolfcamp B (black, solid curve) models.

The lower bound performance (black, solid curve) is the numerical solution (Case 1). The upper bound performance (dark gray, solid curve) is the numerical solution (Case 2). The *RF* represents the cumulative produced pore volume over the maximum producible pore volume for the given model parameters (Table 4.1, Table 4.2).

4.6.3 Case 3: Cross-facies flow (Simulated production performance)

In Case 3, the high-permeability layer exhibits a horizontal pressure gradient at early times (Figure 4.11). This pressure gradient indicates that the high-permeability layer's horizontal permeability (k_{h2}) is not large enough to avoid horizontal flow restriction at the beginning of the simulations. In other words, the high permeability layer cannot carry all the fluids supplied from the low-permeability layer (through cross-facies flow) during early production time. As production continues, the high-permeability layer eventually depletes and then it acts as a constant pressure boundary.

Figure 4.12 shows the numerical solution for the simulated production performance on the Wolfcamp A and Wolfcamp B models. The results represent the sum of the cumulative fluxes occurring across the left boundary of the low-permeability layer and across the interface between both layers. The simulated production curve lies between the upper (gray, solid curve) and lower (black, solid curve) bound solutions. Early simulated production performs similar to the lower bound solution (i.e., no-cross facies flow), whereas late production is closes to the upper bound solution (i.e., maximum production rates with cross-facies flow) in both the Wolfcamp A and Wolfcamp B models. This performance behavior of the simulated production is similar to that observed by Katz and Tek (1961).

The numerical solution for the simulated production also indicates that the production rates in the Wolfcamp A model (Figure 4.12) are higher than those in the Wolfcamp B model (Figure 4.12). For example, the Wolfcamp A model reaches $RF = 50\ \%$ at the end of two years, whereas the Wolfcamp B model requires four years of production time (Table 4.3). The reason for that is two-fold: a) the Wolfcamp A model has a thinner low-permeability layer (h_1), and b) the Wolfcamp A model has a thicker high-permeability layer (h_2), which increases its flow capacity and flow in this layer is unrestricted at earlier times.

The higher production rates in the Wolfcamp A model can be seen more clearly when the numerical solution is represented as a function of the square root of time (Figure 4.13). In the Wolfcamp A model (Figure 4.13A), the slope of the numerical solution curve (dashed line) during early time is approximately two-times higher than the slope of the numerical simulation in the Wolfcamp B model (Figure 4.13B).

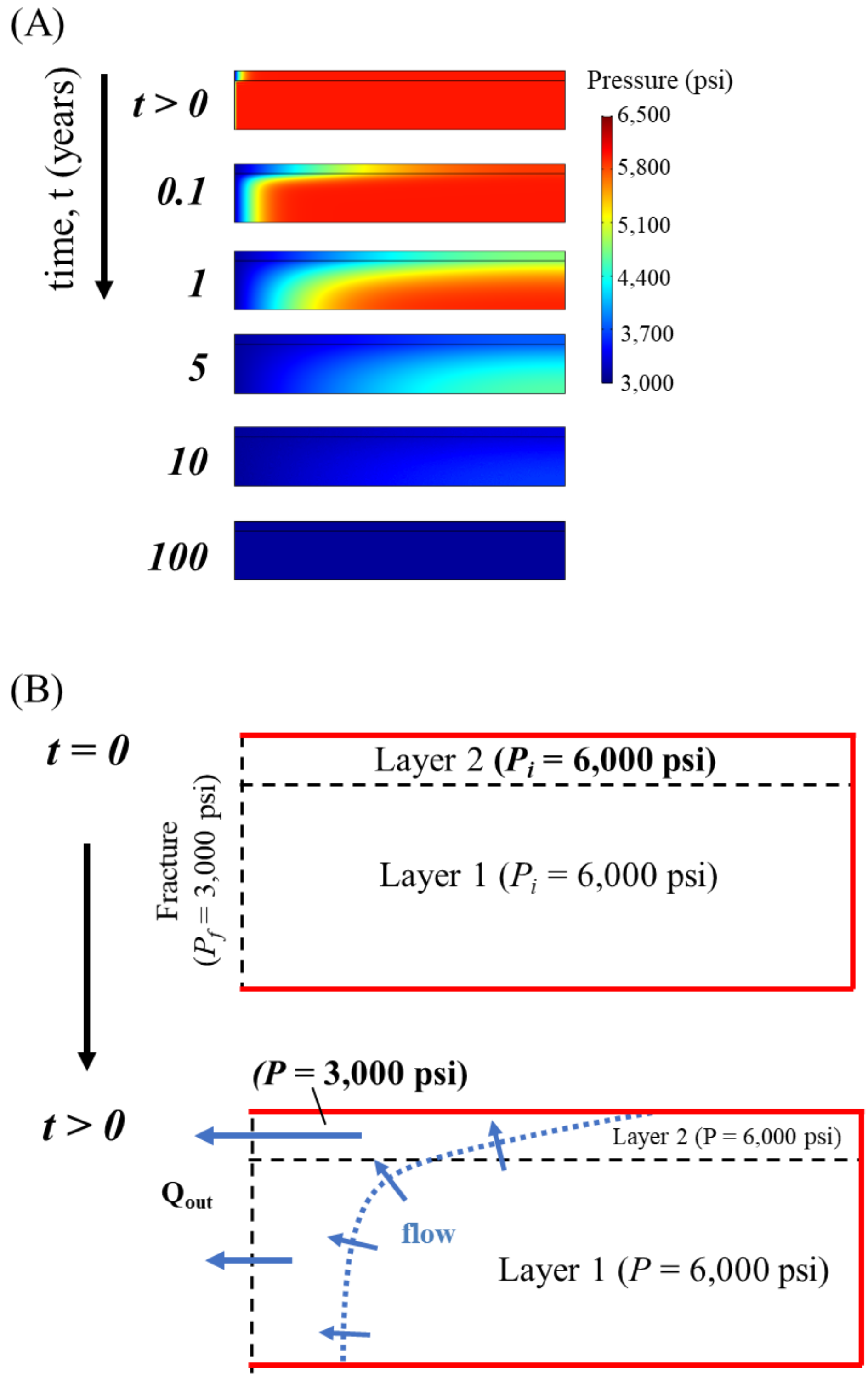

Figure 4.11. Pressure dissipation in the simulated production performance model.

(A) Examples of pressure distribution within each layer's domain over time in the Wolfcamp A model. (B) Schematics showing the interpretation of isobaric lines and flow direction at initial conditions (t = 0) and at early times (t > 0).

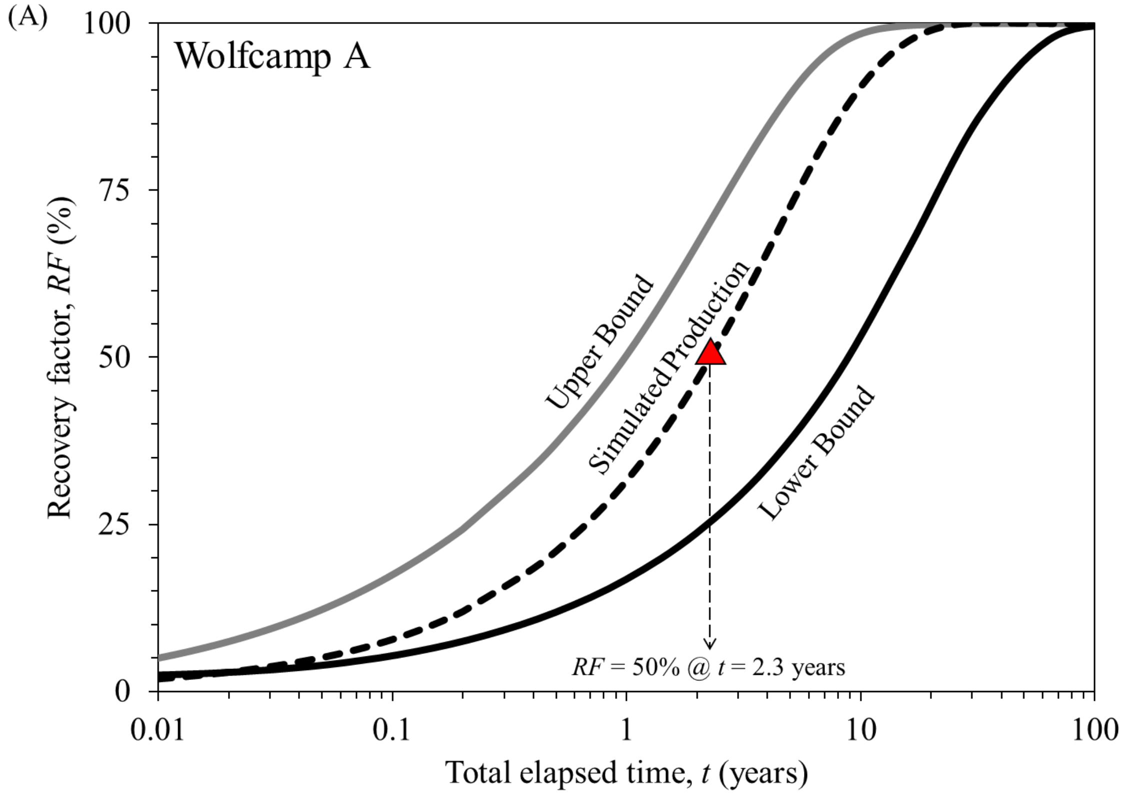
(A)
Wolfcamp A
Upper Bound
Simulated Production
Lower Bound
RF = 50% @ t = 2.3 years
Recovery factor, RF (%)
Total elapsed time, t (years)
0
25
50
75
100
0.01
0.1
1
10
100

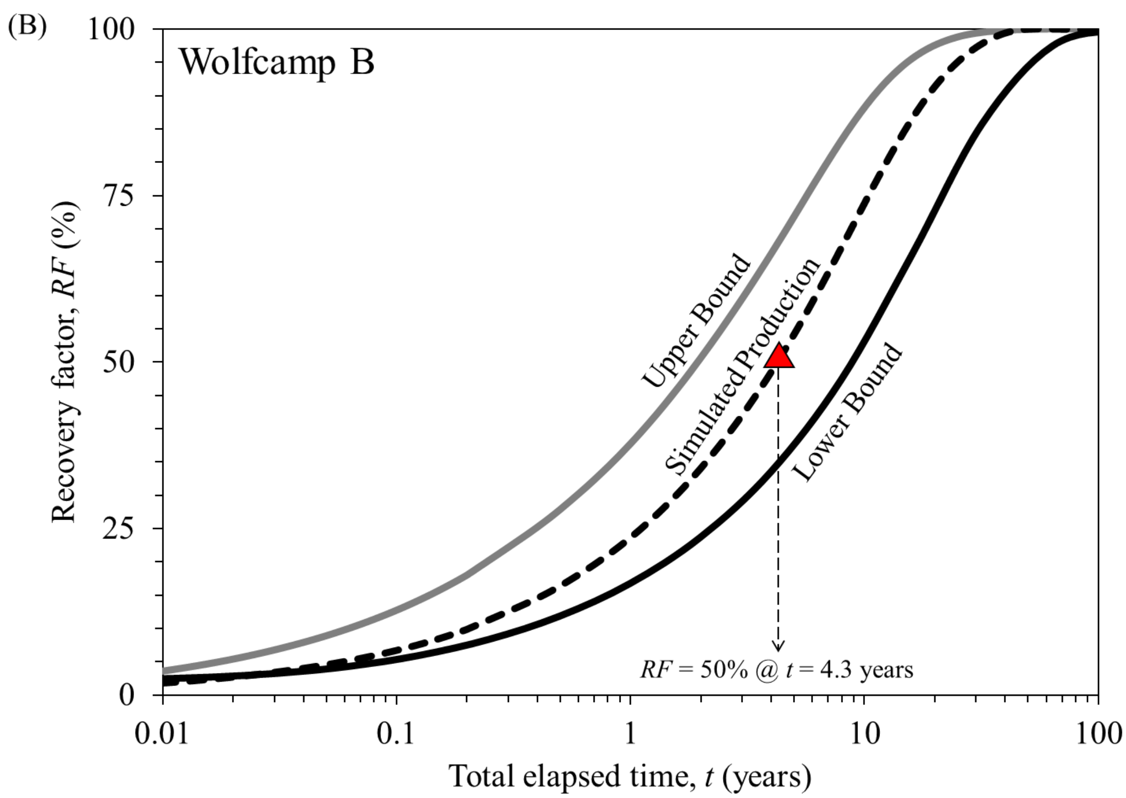
(B)
Wolfcamp B
Upper Bound
Simulated Production
Lower Bound
RF = 50% @ t = 4.3 years
Recovery factor, RF (%)
Total elapsed time, t (years)
0
25
50
75
100
0.01
0.1
1
10
100

Figure 4.12. Numerical solution for the simulated production performance (black, dashed curve) on the (A) Wolfcamp A and (B) Wolfcamp B models.

The red triangle represents the pint in time in the simulated production performance solution at which the recovery factor (*RF*) is 50%. The lower bound performance (black, solid curve) is the analytical solution (Case 1). The upper bound performance (dark gray, solid curve) is the numerical solution (Case 2). The *RF* represents the cumulative produced pore volume over the maximum producible pore volume for the given model parameters (Table 4.1, Table 4.2).

Table 4.3. Production time (*t*) required to achieve recovery factors from 5% to 100% in the low-permeability layer of Wolfcamp A and Wolfcamp B models.

The recovery factor (*RF*) is the cumulative produced pore volume over the maximum producible pore volume for the given model parameters.

RF (%)	Wolfcamp A *t* (years)	Wolfcamp B *t* (years)
5	0.05	0.06
25	0.70	1.10
50	2.30	4.30
75	5.50	10.40
95	13.10	24.90
100	28.00	48.00

(A)

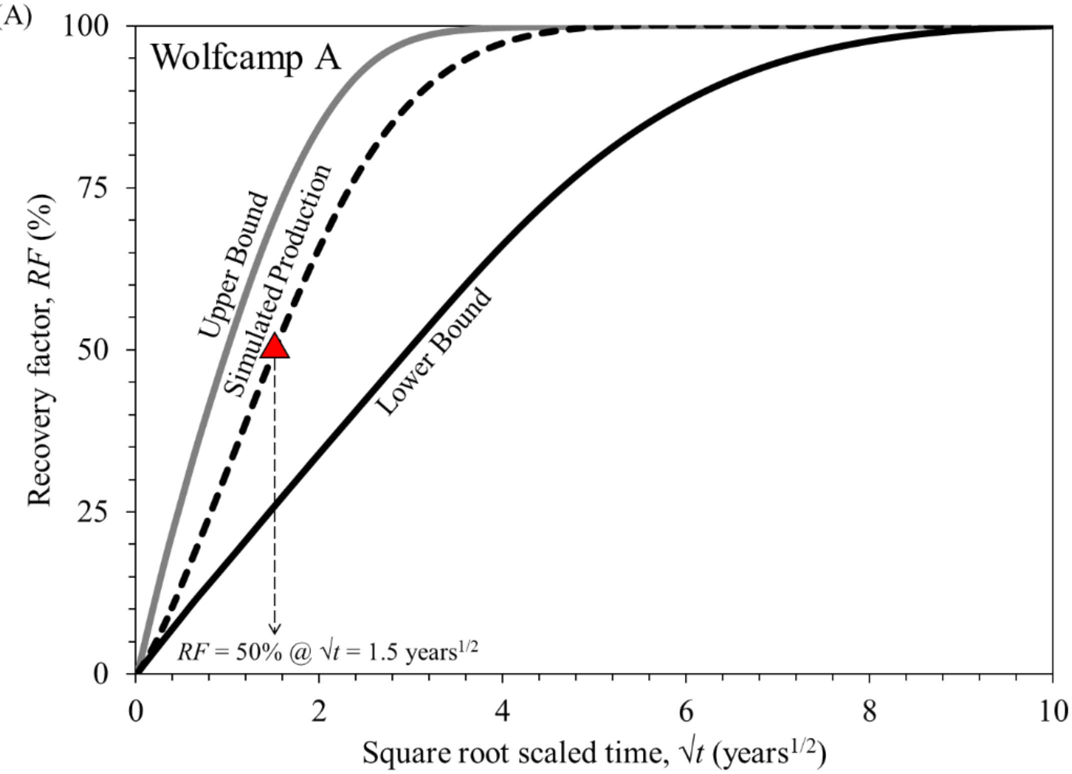
Wolfcamp A
Upper Bound
Simulated Production
Lower Bound
RF = 50% @ √t = 1.5 years1/2
Recovery factor, RF (%)
Square root scaled time, √t (years1/2)
100
75
50
25
0
0
2
4
6
8
10

(B)

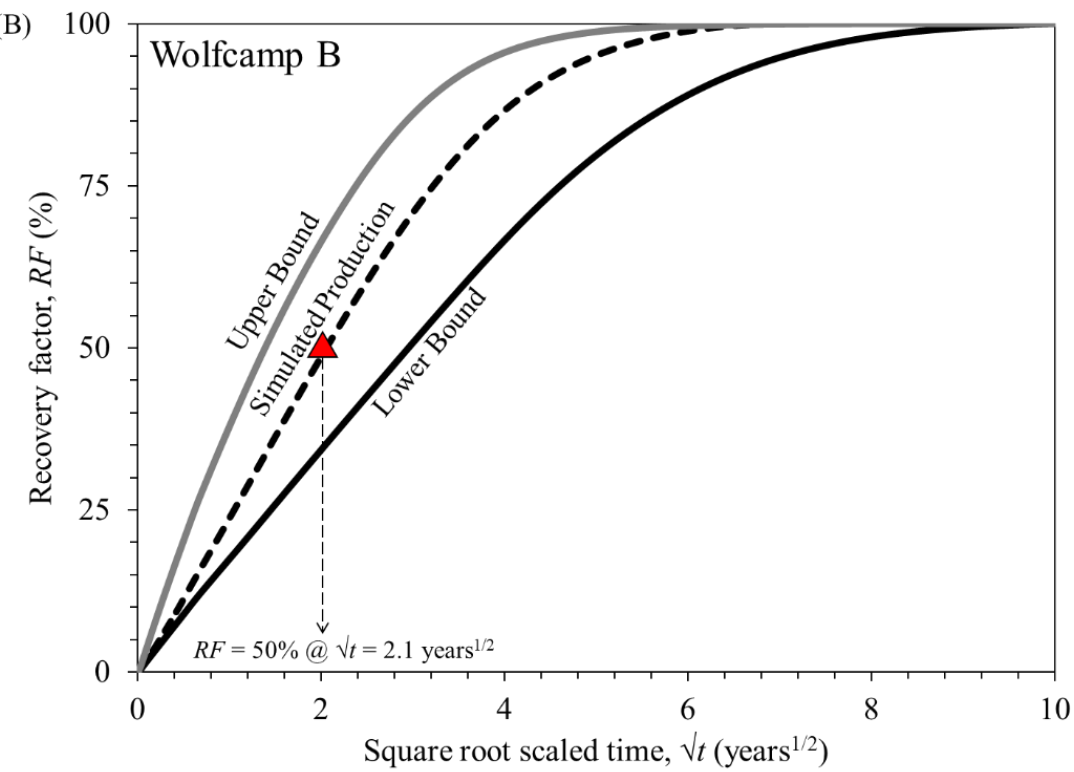
Wolfcamp B
Upper Bound
Simulated Production
Lower Bound
RF = 50% @ √t = 2.1 years1/2
Recovery factor, RF (%)
Square root scaled time, √t (years1/2)
100
75
50
25
0
0
2
4
6
8
10

Figure 4.13. Scaled production for the simulated production performance (black, dashed curve) on the (A) Wolfcamp A and (B) Wolfcamp B models.

The red triangle represents the pint in time in the simulated production performance solution at which the recovery factor (*RF*) is 50%. The lower bound performance (black, solid curve) is the numerical solution (Case 1). The upper bound performance (dark gray, solid curve) is the numerical solution (Case 2). The recovery factor (*RF*) is the cumulative produced pore volume over the maximum producible pore volume for the given model parameters.

4.6.4 Case 4: Cross-facies flow with increasing thickness of low-permeability layer (h_1)

In Case 4, the pressure in the low-permeability layer requires longer times to dissipate when its thickness (h_1) increases (Figure 4.14). However, the pressure dissipation in the high-permeability layer is not affected by the different low-permeability layer's thicknesses (h_1).

Figure 4.15 shows the numerical solution for the simulated production performance at increasing low-permeability layer's thickness (h_1) on the Wolfcamp A and Wolfcamp B models. The results represent the sum of the cumulative fluxes occurring across the left boundary of the low-permeability layer and across the interface between both layers. We can observe that, as I increase the low-permeability layer's thickness from h_1 (black, dashed curve) to 20*h_1 (black, dotted curves), the production rates decrease, and the solution approaches the lower bound performance (black, solid curve).

Figure 4.16 shows more clearly that the slope of the production curves decreases as the low permeability layer's thickness increases from h_1 (black, dashed curve) to 20* h_1 (black, dotted curves) on the Wolfcamp A and Wolfcamp B models.

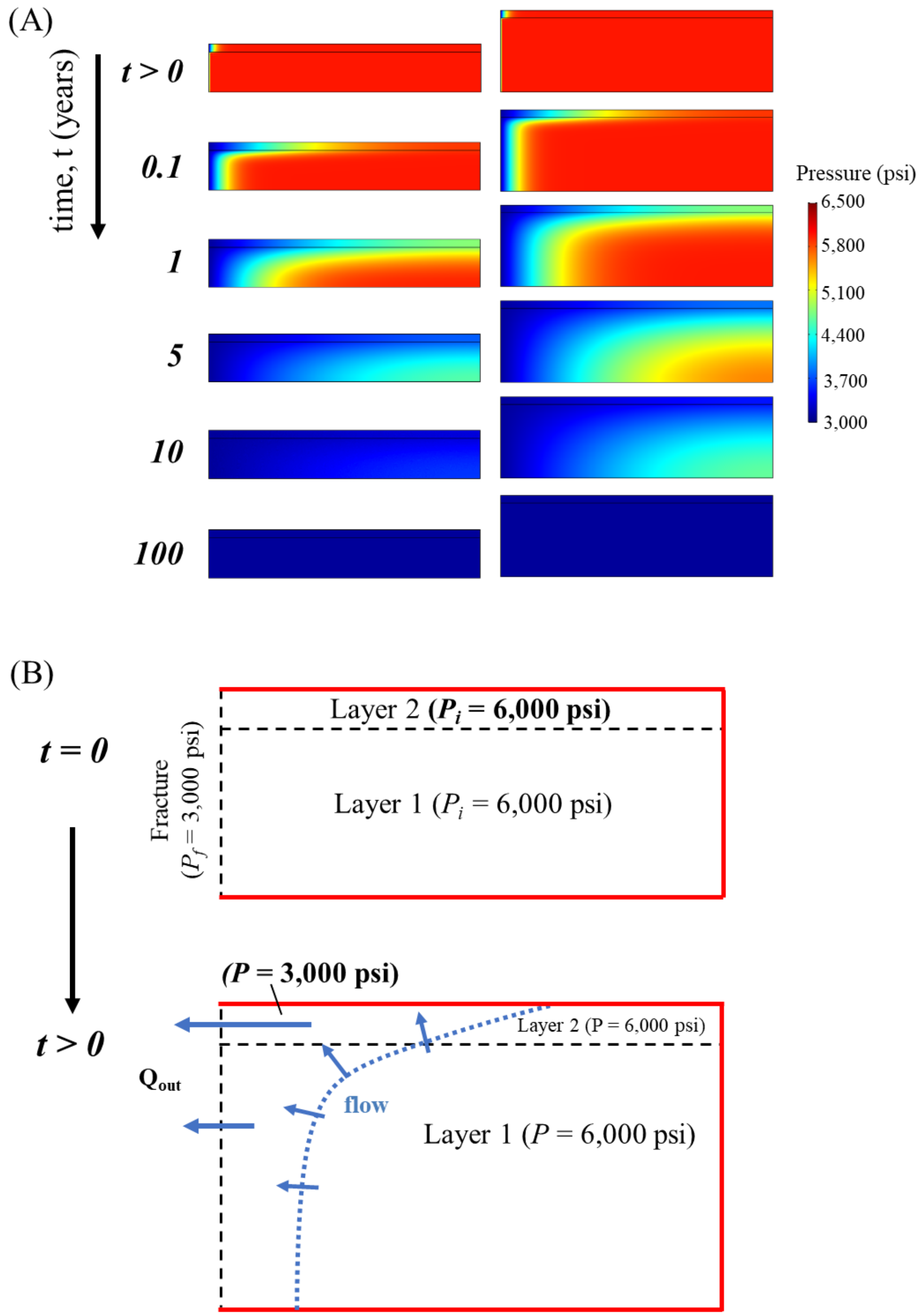

Figure 4.14. Pressure dissipation in the simulated production performance model at increasing low-permeability layer's thickness (h_1).

(A) Examples of pressure distribution within each layer's domain over time in the Wolfcamp A model. (B) Schematics showing the interpretation of isobaric lines and flow direction at initial conditions (t = 0) and at early times (t > 0).

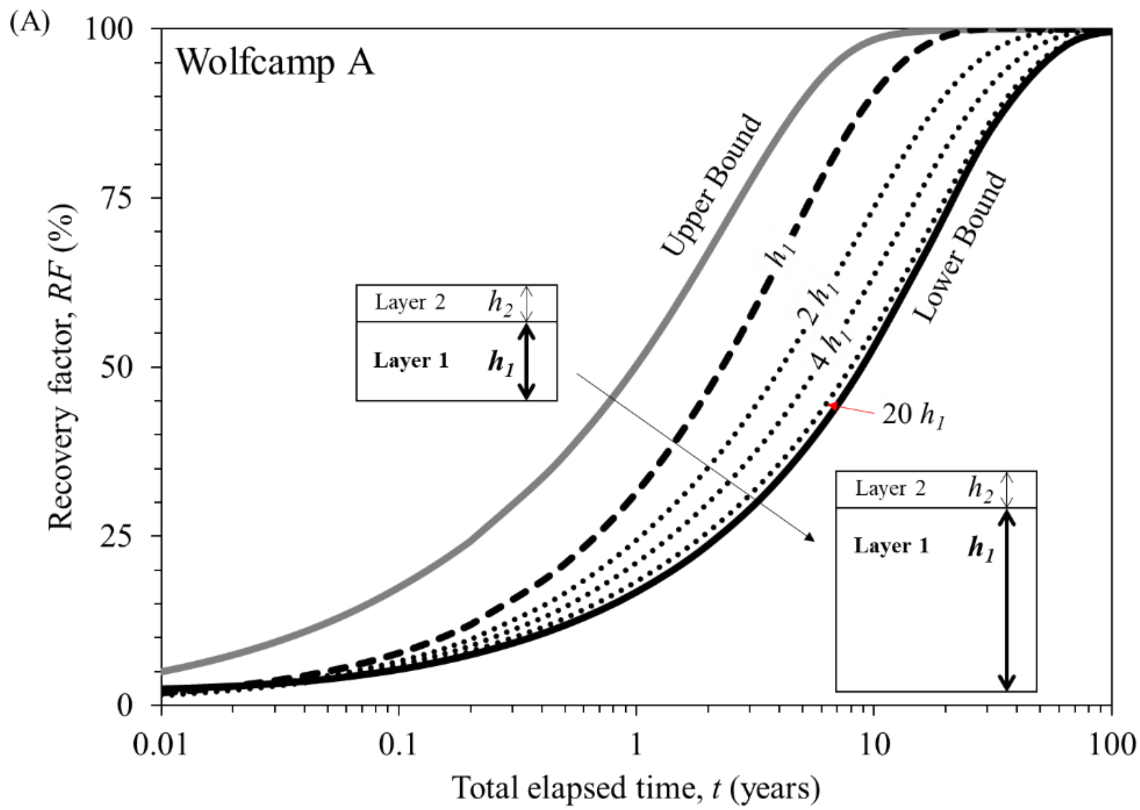
(A)
Wolfcamp A
Upper Bound
h_1
$2\ h_1$
$4\ h_1$
Lower Bound
$20\ h_1$
Layer 2
h_2
Layer 1
h_1
Layer 2
h_2
Layer 1
h_1
Recovery factor, RF (%)
Total elapsed time, t (years)

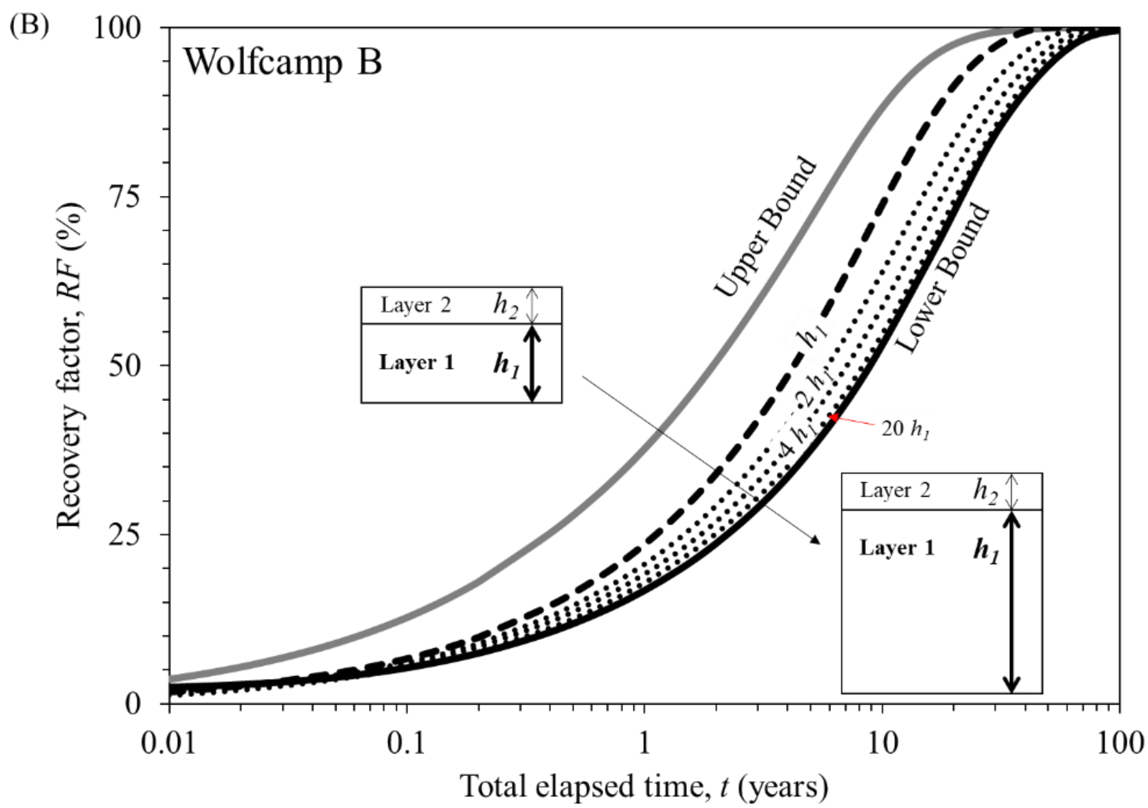
(B)
Wolfcamp B
Upper Bound
h_1
$2\ h_1$
$4\ h_1$
Lower Bound
$20\ h_1$
Layer 2
h_2
Layer 1
h_1
Layer 2
h_2
Layer 1
h_1
Recovery factor, RF (%)
Total elapsed time, t (years)

Figure 4.15. Numerical solutions for the simulated production performance at increasing low-permeability layer's thickness (h_1) (black, dotted curves) on the (A) Wolfcamp A and (B) Wolfcamp B models.

The low-permeability layer's thickness (h_1) is increased while leaving the high-permeability layer's thickness (h_2) fixed. The black, dashed curve is the simulated production performance using h_1 (Case 3). The lower bound performance (black, solid curve) is the analytical solution (Case 1). The upper bound performance (dark gray, solid curve) is the numerical solution (Case 2). The *RF* represents the cumulative produced pore volume over the maximum producible pore volume for the given model parameters (Table 4.1, Table 4.2).

(A)

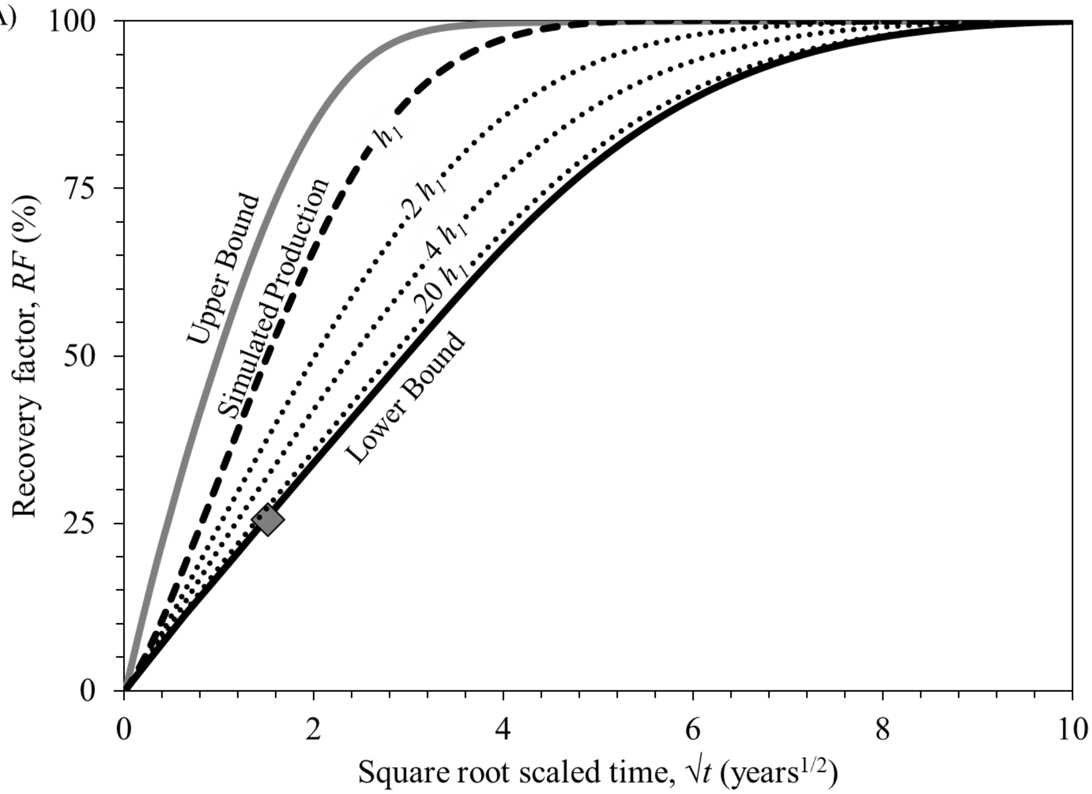
100
75
50
25
0
0
2
4
6
8
10
Recovery factor, RF (%)
Square root scaled time, √t (years^1/2)
Upper Bound
Simulated Production
h1
2 h1
4 h1
20 h1
Lower Bound

(B)

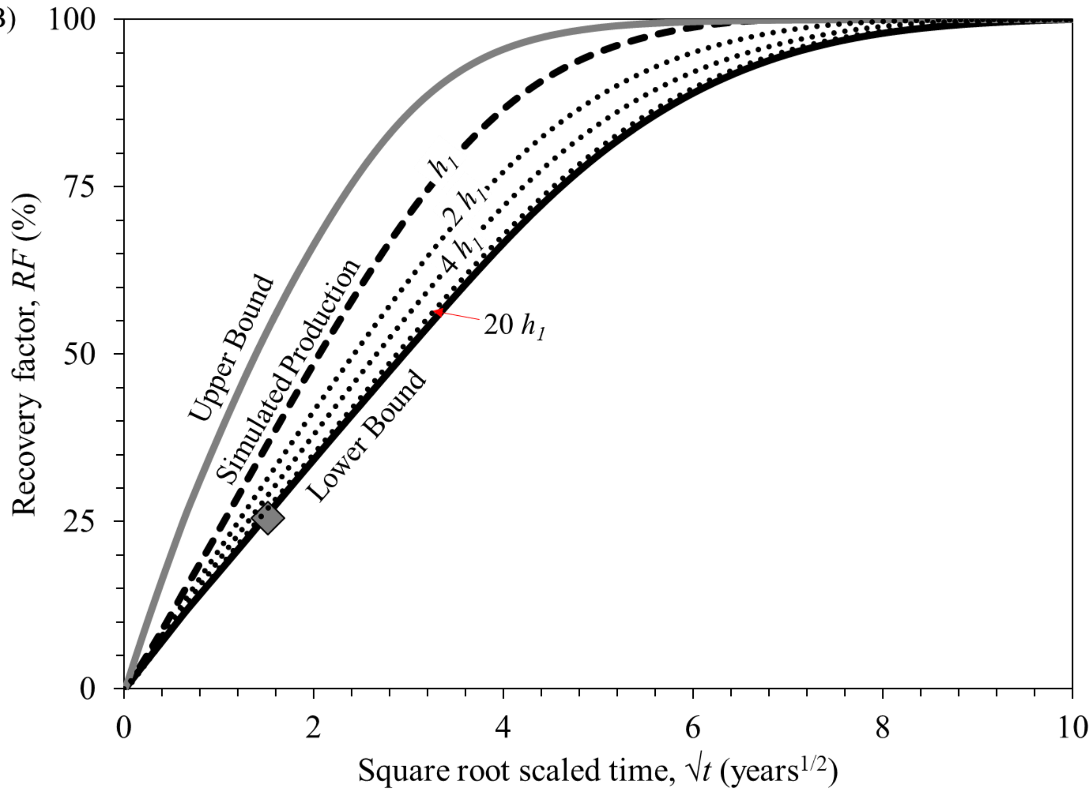
100
75
50
25
0
0
2
4
6
8
10
Recovery factor, RF (%)
Square root scaled time, √t (years^1/2)
Upper Bound
Simulated Production
h1
2 h1
4 h1
20 h1
Lower Bound

Figure 4.16. Scaled production for the simulated production performance at increasing thickness of the low-permeability layer (h_1) (black, dotted curves) on the (A) Wolfcamp A and (B) Wolfcamp B models.

The low-permeability layer's thickness (h_1) is increased while leaving the high-permeability layer's thickness (h_2) fixed. The black, dashed curve is the simulated production performance using h_1 (Case 3). The lower bound performance (black, solid curve) is the numerical solution (Case 1). The upper bound performance (dark gray, solid curve) is the numerical solution (Case 2). The recovery factor (RF) is the cumulative produced pore volume over the maximum producible pore volume for the given model parameters.

4.6.5 Case 5: Cross-facies flow with increasing thickness of high-permeability layer (h_2)

In Case 5, the pressure in the high-permeability layer dissipates faster when its thickness (h_2) increases. This is because a thicker high-permeability layer increases its flow capacity and the flow restriction is reduced. For example, Figure 4.17 shows that at t = 1 year the pressure has almost completely dissipated in the model high thicker h_2, compared to the model with thinner h_2.

Figure 4.18 shows the numerical solution for the simulated production performance at increasing high-permeability layer's thickness (h_2) on the Wolfcamp A and Wolfcamp B models. The results represent the sum of the cumulative fluxes occurring across the left boundary of the low-permeability layer and across the interface between both layers. We can observe that, as I increase the high-permeability layer's thickness (h_2), the production rates increase, and the solution approaches upper bound (black, solid curve). However, the early production rates are remarkably similar regardless of the thickness of the high-permeability layer. This is because flow is restricted in the high-permeability layer at early times. As production continues, the high-permeability layer depletes, flow restriction is reduced, and the solution approaches the upper bound performance.

Figure 4.19 shows the numerical solution for the simulated production performance at increasing high-permeability layer's thickness (h_2) as a function of the square root of time ($\sqrt{t}$) on the Wolfcamp A and Wolfcamp B models. The slope of the production curves is steeper as the high-permeability layer's thickness increases. However, there is a thickness beyond which there is no significant increase in production rates. For example, in the Wolfcamp A model (Figure 4.19A), production rates at $7*h_2$ are practically the same than those at $19*h_2$.

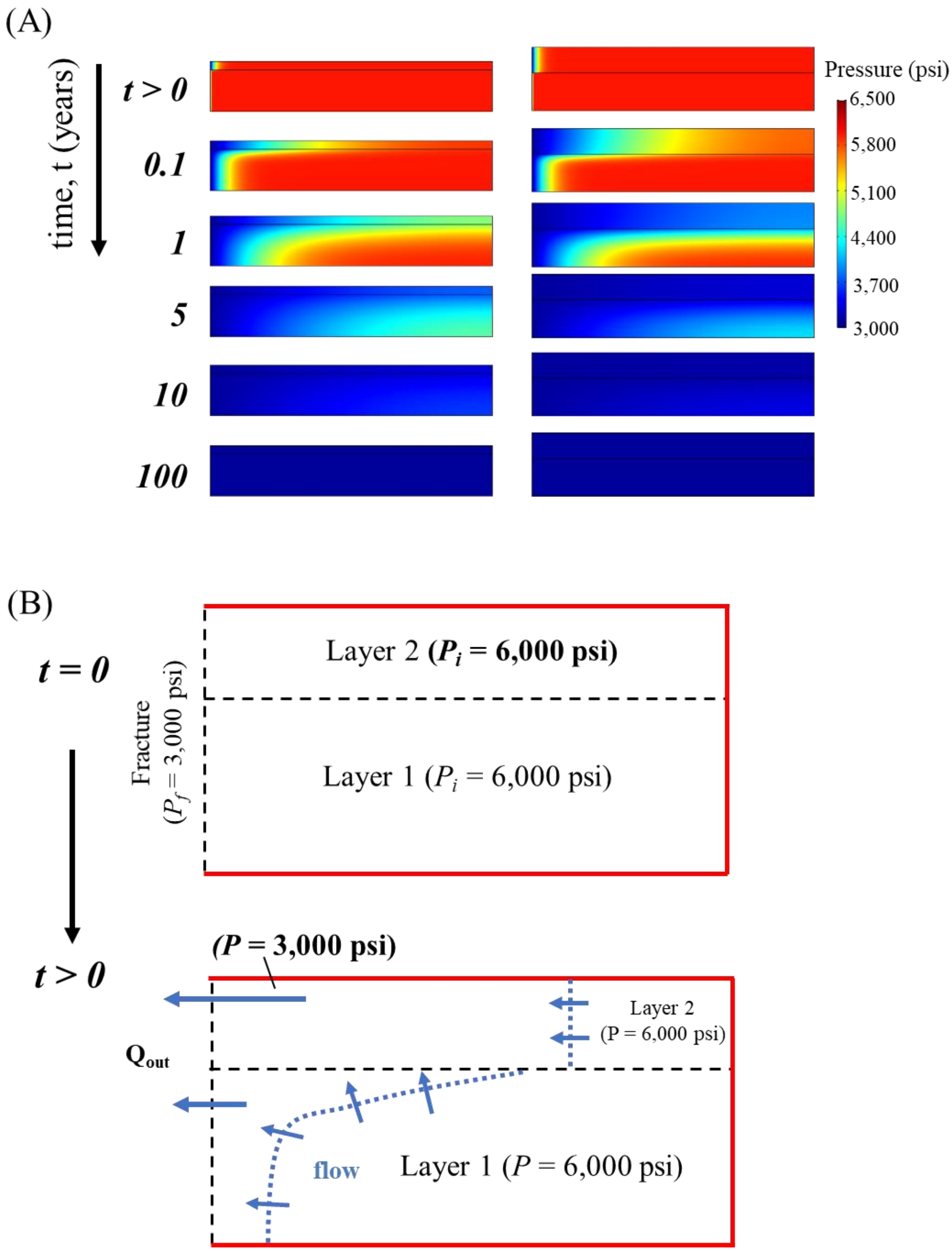

Figure 4.17. Pressure dissipation in the simulated production performance model at increasing high-permeability layer's thickness (h_2).

(A) Examples of pressure distribution within each layer's domain over time in the Wolfcamp A model. (B) Schematics showing the interpretation of isobaric lines and flow direction at initial conditions (t = 0) and at early times (t > 0).

(A)

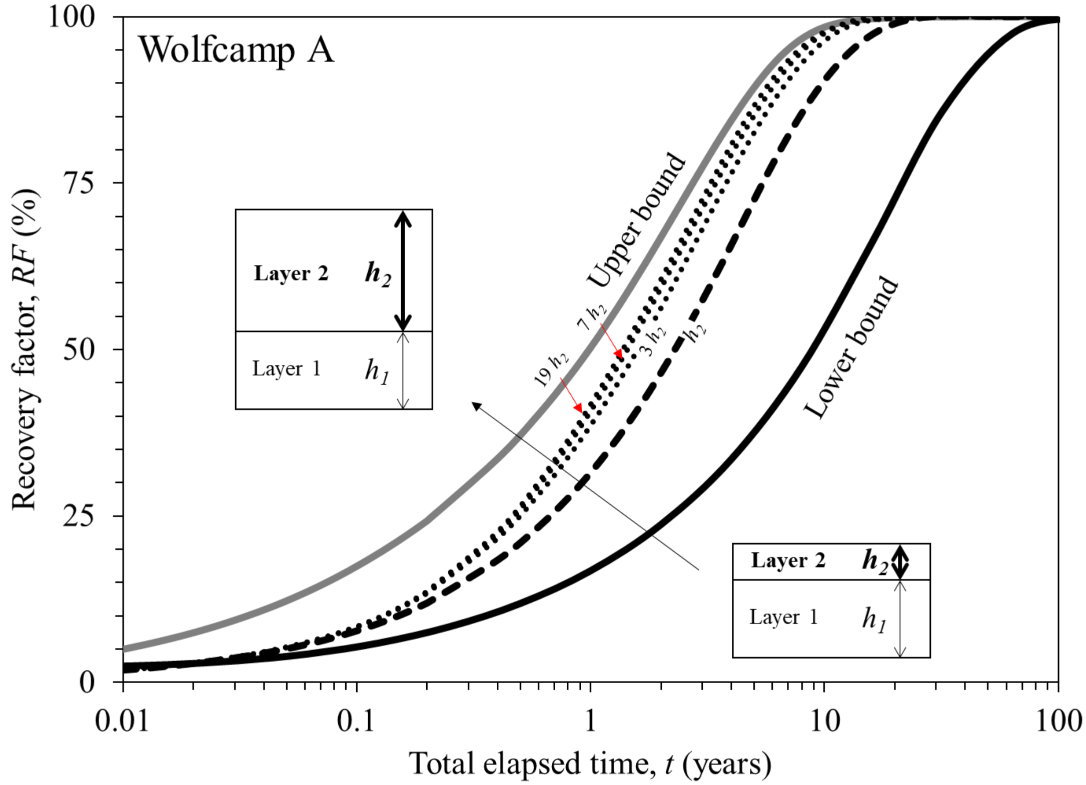

100
75
50
25
0
Wolfcamp A
Recovery factor, RF (%)
Upper bound
Lower bound
19 h2
7 h2
3 h2
h2
Layer 2
h2
Layer 1
h1
Layer 2
h2
Layer 1
h1
0.01
0.1
1
10
100
Total elapsed time, t (years)

(B)

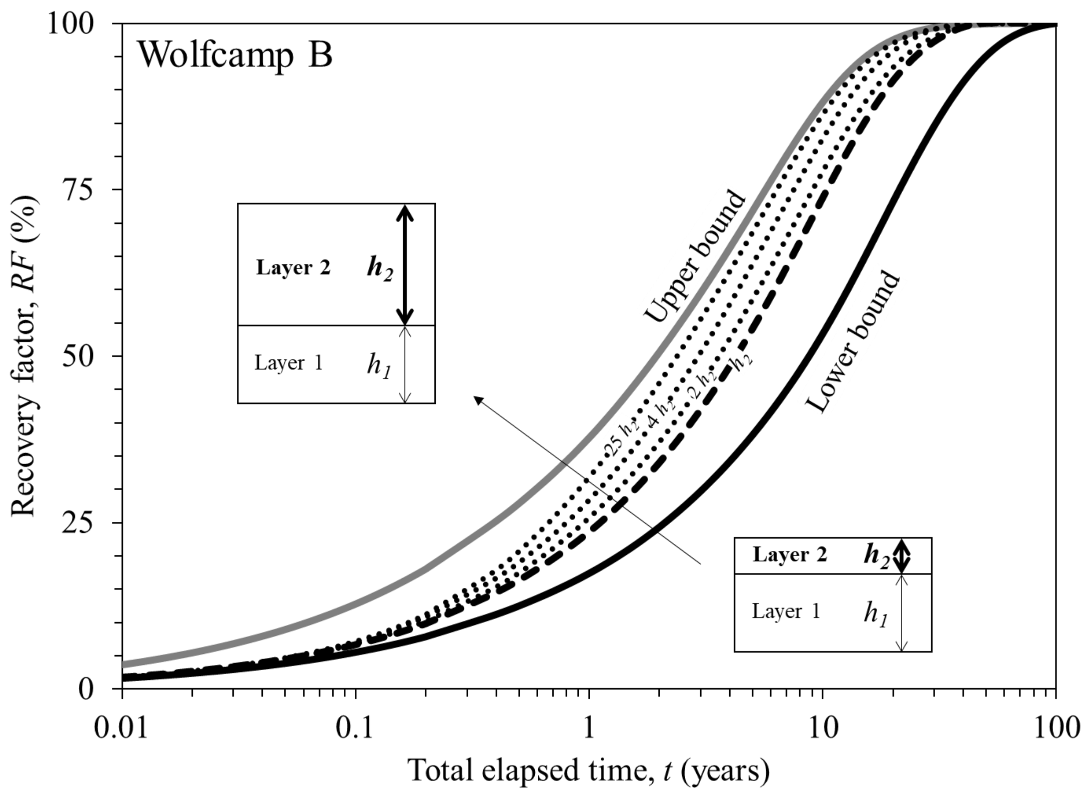

100
75
50
25
0
Wolfcamp B
Recovery factor, RF (%)
Upper bound
Lower bound
25 h2
4 h2
2 h2
h2
Layer 2
h2
Layer 1
h1
Layer 2
h2
Layer 1
h1
0.01
0.1
1
10
100
Total elapsed time, t (years)

Figure 4.18. Numerical solutions for the simulated production performance at increasing high-permeability layer's thickness (h_2) (black, dotted curves) on the (A) Wolfcamp A and (B) Wolfcamp B models.

The high-permeability layer's thickness (h_2) is increased while leaving the low-permeability layer's thickness (h_1) fixed. The black, dashed curve is the simulated production performance using h_2 (Case 3). The lower bound performance (black, solid curve) is the analytical solution (Case 1). The upper bound performance (dark gray, solid curve) is the numerical solution (Case 2). The *RF* represents the cumulative produced pore volume over the maximum producible pore volume for the given model parameters (Table 4.1, Table 4.2).

(A)

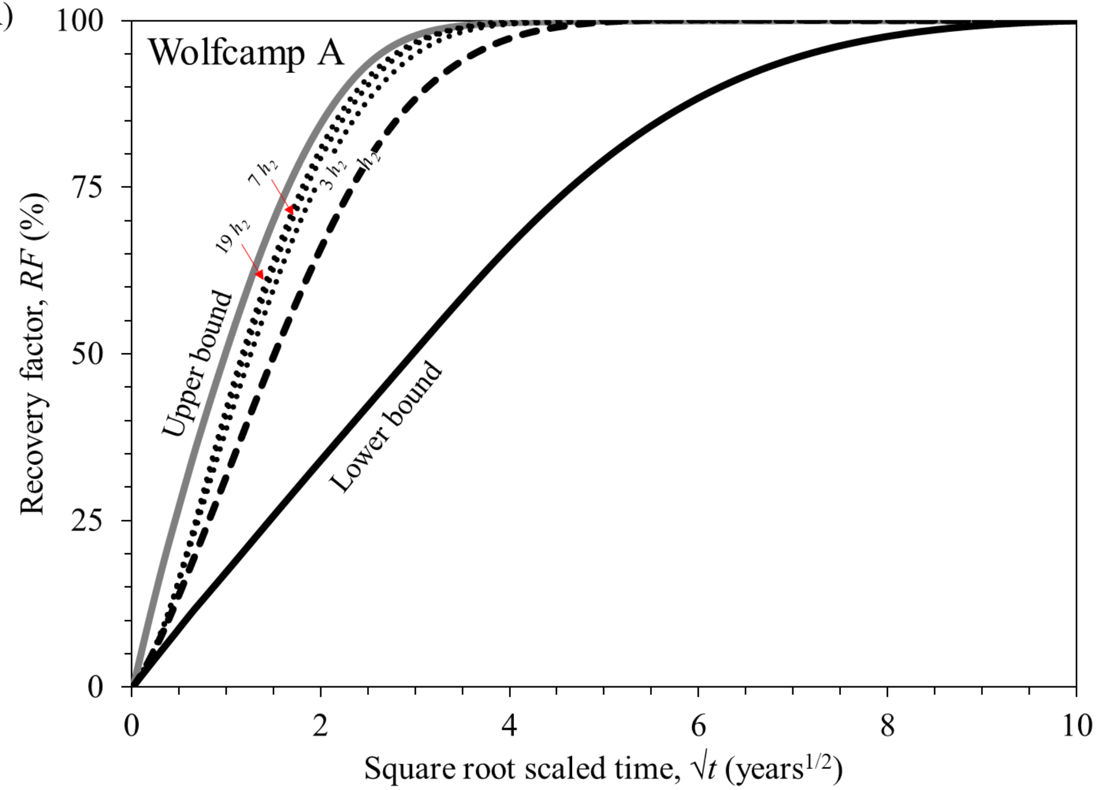
Wolfcamp A
Recovery factor, RF (%)
Square root scaled time, √t (years1/2)
Upper bound
Lower bound
19 h2
7 h2
3 h2
h2
0
25
50
75
100
0
2
4
6
8
10

(B)

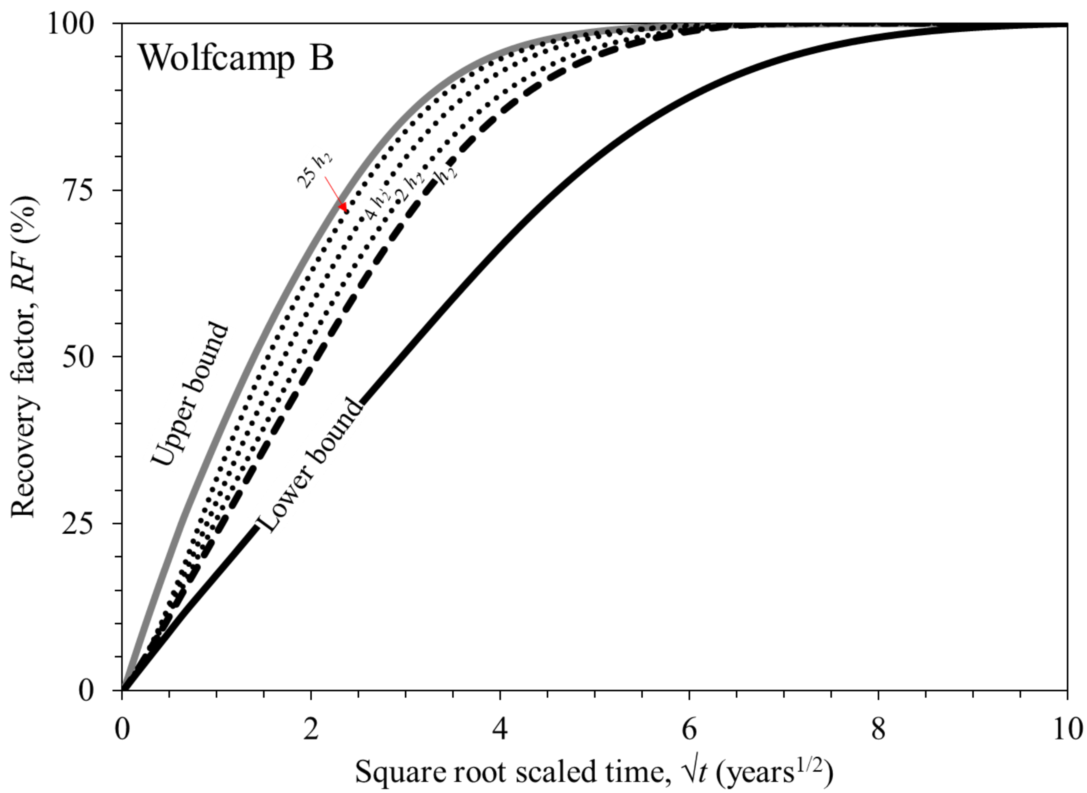
Wolfcamp B
Recovery factor, RF (%)
Square root scaled time, √t (years1/2)
Upper bound
Lower bound
25 h2
4 h2
2 h2
h2
0
25
50
75
100
0
2
4
6
8
10

Figure 4.19. Scaled production for the simulated production performance at increasing thickness of the high-permeability layer (h_2) (black, dotted curves) on the (A) Wolfcamp A and (B) Wolfcamp B models.

The high-permeability layer's thickness (h_2) is increased while leaving the low-permeability layer's thickness (h_1) fixed. The black, dashed curve is the simulated production performance using h_2 (Case 3). The lower bound performance (black, solid curve) is the numerical solution (Case 1). The upper bound performance (dark gray, solid curve) is the numerical solution (Case 2). The *RF* represents the cumulative produced pore volume over the maximum producible pore volume for the given model parameters (Table 4.1, Table 4.2).

4.6.6 Case 6: Cross-facies flow with increasing horizontal permeability of high-permeability layer (k_{h2})

In Case 6, the pressure in the high-permeability layer dissipates faster as its horizontal permeability (k_{h2}) increases. This is because the high-permeability layer increases its flow capacity and the flow restriction is reduced. For example, Figure 4.20 shows that, at t = 1 year, the pressure has almost completely dissipated in the model high higher k_{h2}, compared to the model with lower k_{h2}.

Figure 4.21 shows the numerical solution for the simulated production performance at increasing high-permeability layer's horizontal permeability (k_{h2}) on the Wolfcamp A and Wolfcamp B models. The results represent the sum of the cumulative fluxes occurring across the left boundary of the low-permeability layer and across the interface between both layers. The production curves approach the upper bound solution as the horizontal permeability increases from $k_{h2} = 10^2$ nD to $k_{h2} = 10^6$ nD. This behavior clearly indicates that the flow capacity of the high permeability layer increases with increasing its horizontal permeability (k_{h2}), and therefore production rates are higher.

Figure 4.22 shows the numerical solution for the simulated production performance at increasing high-permeability layer's horizontal permeability (k_{h2}) as a function of the square root of time ($\sqrt{t}$) on the Wolfcamp A and Wolfcamp B models. The slope of the numerical solutions becomes steeper as the high-permeability layer's horizontal permeability (k_{h2}) increases. It is important to note that even with a k_{h2} = 100 nD, the there is a significant effect on the production rates. Also, at $k_{h2} = 10^4$ nD (10 µD), the production rates are almost identical to the upper bound case, in which $k_{h2} = 10^9$ nD (1 Darcy).

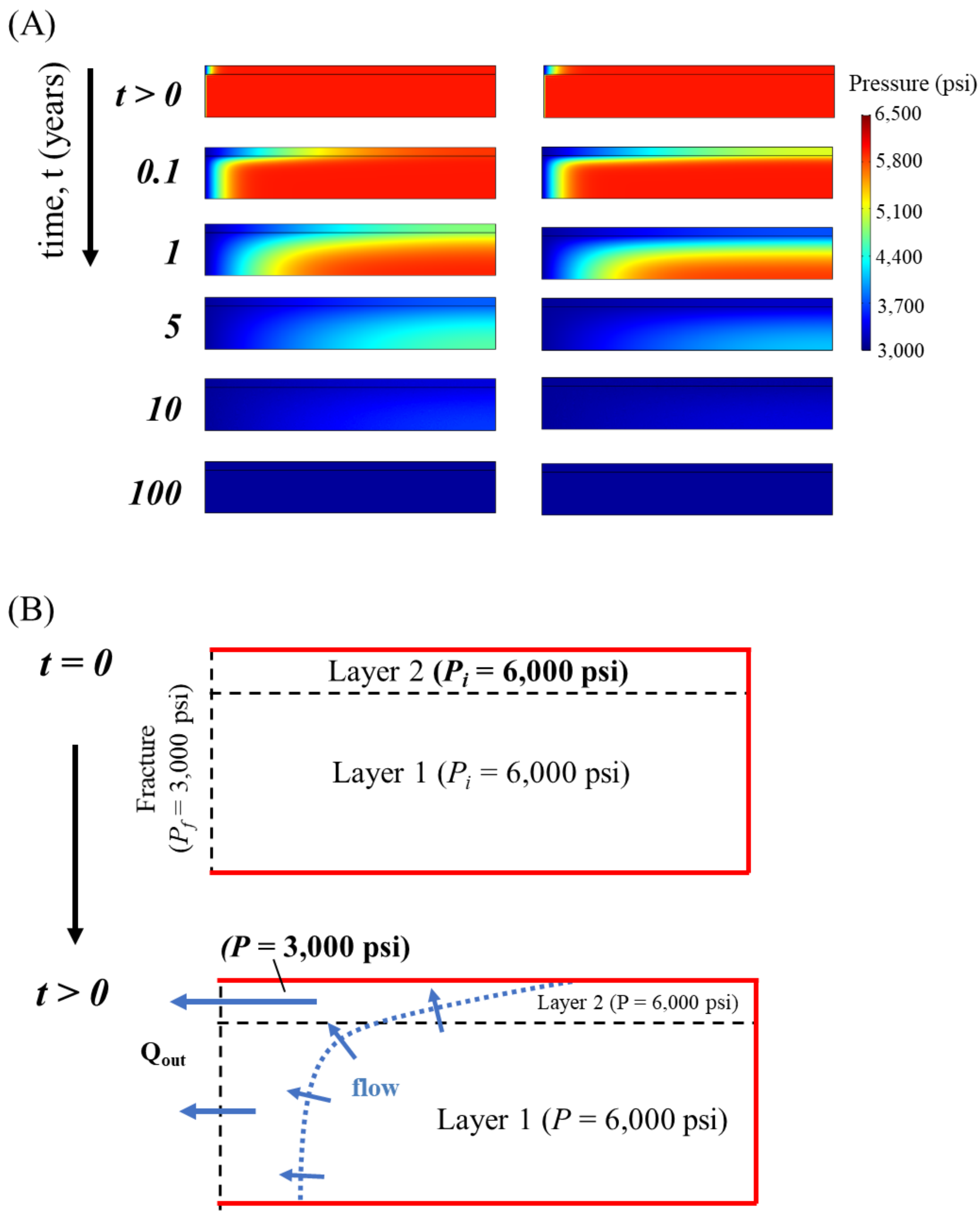

Figure 4.20. Pressure dissipation in the simulated production performance model at increasing high-permeability layer's horizontal permeability (k_{h2}).

(A) Examples of pressure distribution within each layer's domain over time in the Wolfcamp A model. (B) Schematics showing the interpretation of isobaric lines and flow direction at initial conditions (t = 0) and at early times (t > 0).

(A)

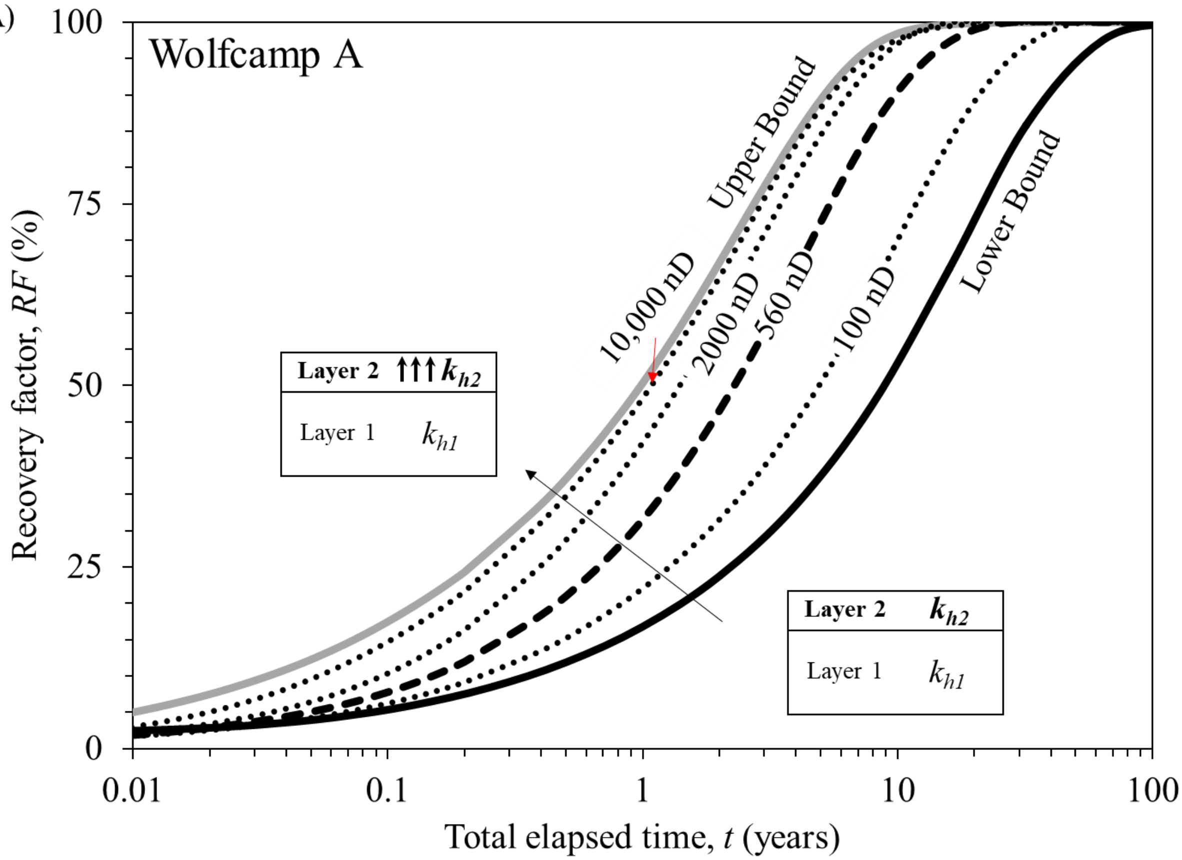
Wolfcamp A
Upper Bound
Lower Bound
10,000 nD
2000 nD
560 nD
100 nD
Layer 2 ↑↑↑ k_{h2}
Layer 1 k_{h1}
Layer 2 k_{h2}
Layer 1 k_{h1}
Recovery factor, RF (%)
Total elapsed time, t (years)
0
25
50
75
100
0.01
0.1
1
10
100

(B)

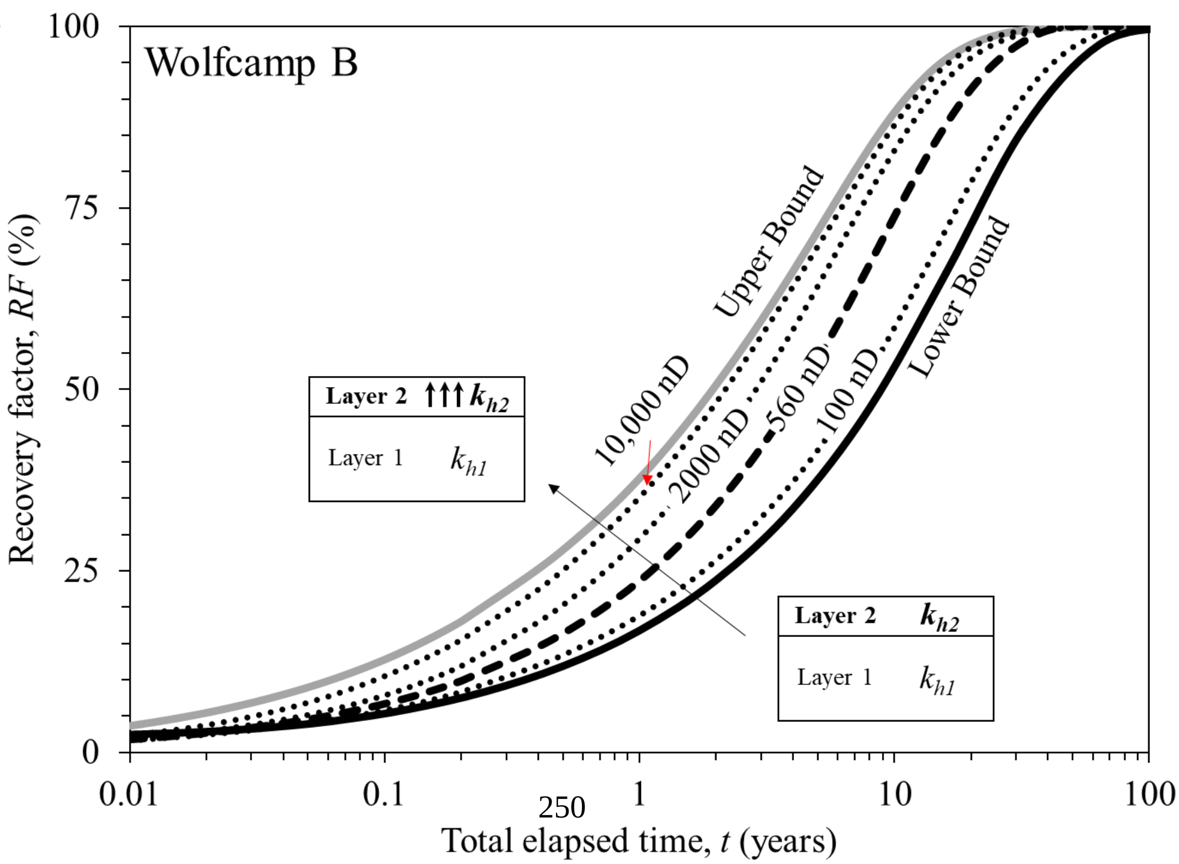
Wolfcamp B
Upper Bound
Lower Bound
10,000 nD
2000 nD
560 nD
100 nD
Layer 2 ↑↑↑ k_{h2}
Layer 1 k_{h1}
Layer 2 k_{h2}
Layer 1 k_{h1}
Recovery factor, RF (%)
Total elapsed time, t (years)
0
25
50
75
100
0.01
0.1
1
10
100

Figure 4.21. Numerical solutions for simulated production performance at increasing horizontal permeability in the high-permeability layer (k_{h2}) (black, dotted curves) on the (A) Wolfcamp A and (B) Wolfcamp B models.

The high-permeability layer's horizontal permeability (k_{h2}) is increased while leaving the low-permeability layer's horizontal permeability (k_{h1}) and both layers' vertical permeabilities (k_{v1}, k_{v2}) fixed. The black, dashed curve is the simulated production performance using k_{h2} = 560 nD (Case 3). The lower bound performance (black, solid curve) is the analytical solution (Case 1). The upper bound performance (dark gray, solid curve) is the numerical solution (Case 2). The *RF* represents the cumulative produced pore volume over the maximum producible pore volume for the given model parameters (Table 4.1, Table 4.2).

(A)

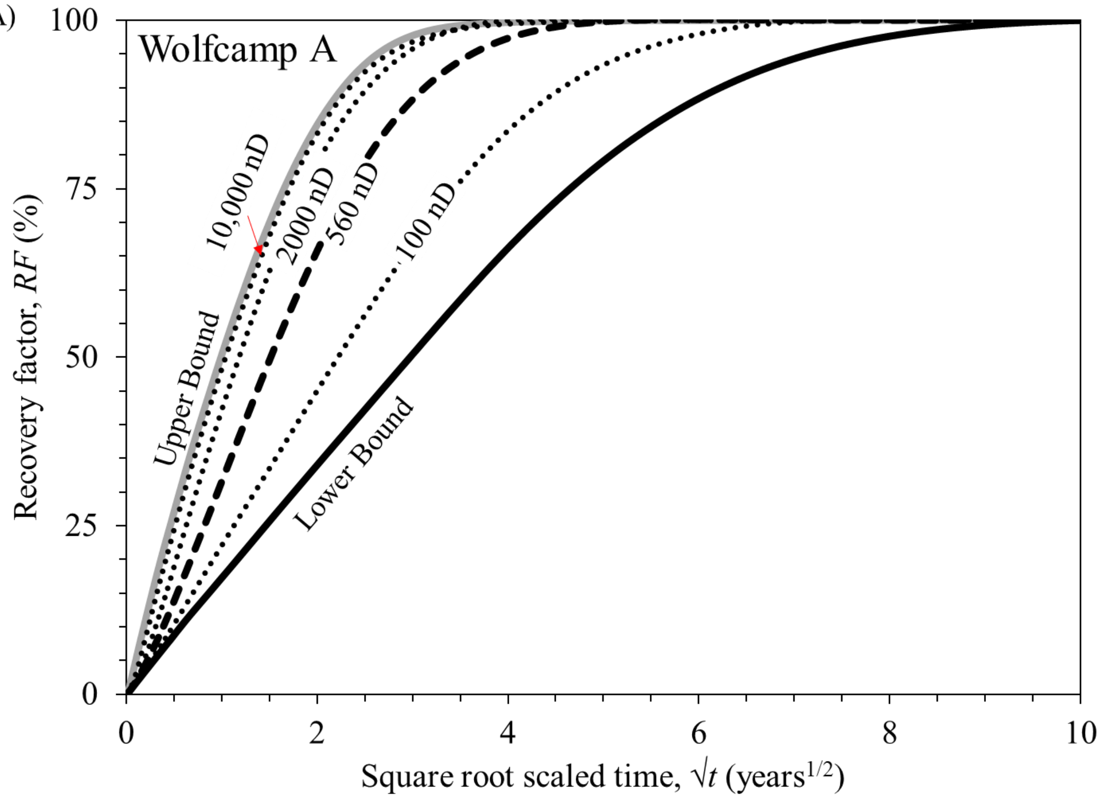

Wolfcamp A
10,000 nD
2000 nD
560 nD
100 nD
Upper Bound
Lower Bound
Recovery factor, RF (%)
Square root scaled time, √t (years^1/2)
0
25
50
75
100
0
2
4
6
8
10

(B)

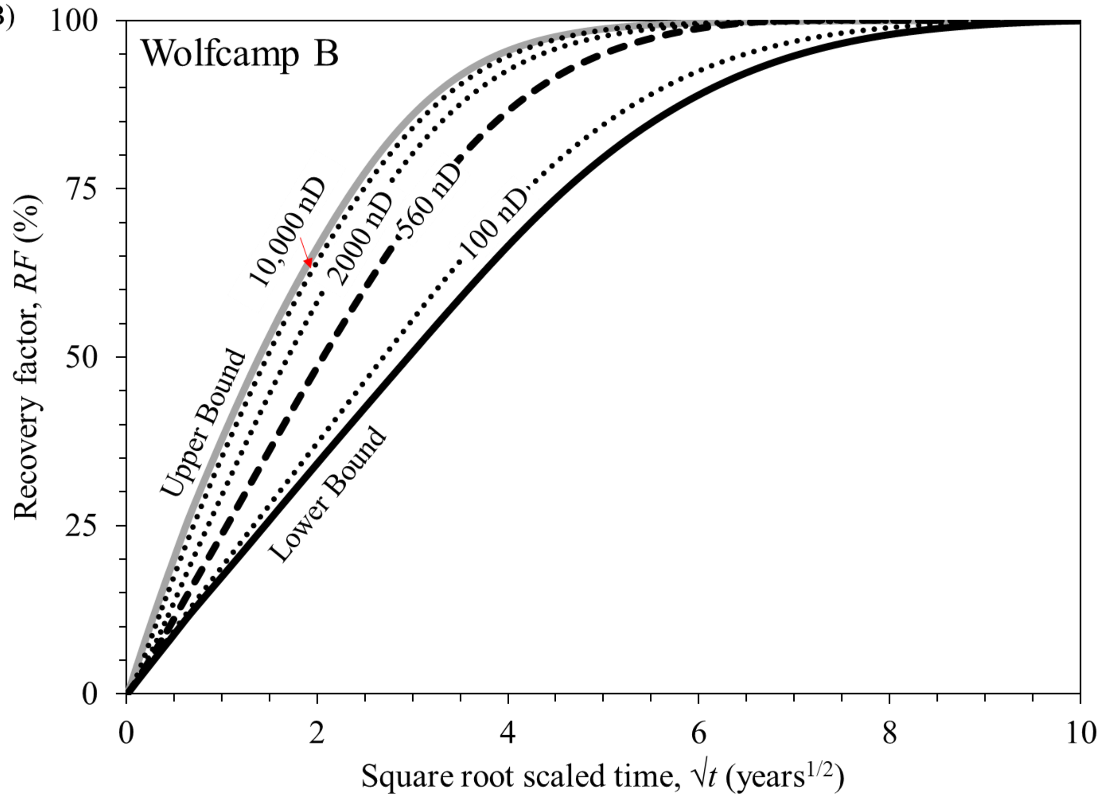

Wolfcamp B
10,000 nD
2000 nD
560 nD
100 nD
Upper Bound
Lower Bound
Recovery factor, RF (%)
Square root scaled time, √t (years^1/2)
0
25
50
75
100
0
2
4
6
8
10

Figure 4.22. Scaled production for the simulated production performance at increasing horizontal permeability in the high-permeability layer (k_{h2}) (black, dotted curves) on the (A) Wolfcamp A and (B) Wolfcamp B models.

The high-permeability layer's horizontal permeability (k_{h2}) is increased while leaving the low-permeability layer's horizontal permeability (k_{h1}) and both layers' vertical permeabilities (k_{v1}, k_{v2}) fixed. The black, dashed curve is the simulated production performance using k_{h2} = 560 nD (Case 3). The lower bound performance (black, solid curve) is the numerical solution (Case 1). The upper bound performance (dark gray, solid curve) is the numerical solution (Case 2). The recovery factor (*RF*) is the cumulative produced pore volume over the maximum producible pore volume for the given model parameters.

4.6.7 Case 7: Cross-facies flow with increasing vertical permeability of low-permeability layer (k_{v1})

In Case 7, the pressure in the low-permeability layer dissipates faster across the interface between both layers at increasing vertical permeabilities (k_{v1}). Hence, the flux at the interface between both layers increases with increasing the low-permeability layer's vertical permeability (k_{v1}). As a result, the isobaric lines become vertical (Figure 4.23).

Figure 4.24 shows the numerical solution for the simulated production performance at increasing low-permeability layer's vertical permeability (k_{v1}) on the Wolfcamp A and Wolfcamp B models. The results represent the sum of the cumulative fluxes occurring across the left boundary of the low-permeability layer and across the interface between both layers. We can observe that the production rates increase as the low-permeability layer's vertical permeability (k_{v1}) increases. However, there is a vertical permeability beyond which there is no significant increase in the production rates. This is because production rates are limited by the flow in high-permeability layer.

Figure 4.25 shows the numerical solution for the simulated production performance at increasing low-permeability layer's vertical permeability (k_{v1}) as a function of the square root of time ($\sqrt{t}$) on the Wolfcamp A and Wolfcamp B models. The slope of the production curve increases as the low-permeability layer's vertical permeability (k_{v1}) increases. However, it is important to note that the increase in production rates at vertical permeabilities beyond k_{v1} = 2 nD do not increase drastically. This is because the flow restriction in the high-permeability layer is a limiting factor for production rates. Also, it is remarkable that even a small vertical permeability of k_{v1} = 0.5 nD results in a significant increase in production rates when compared to the lower bound performance.

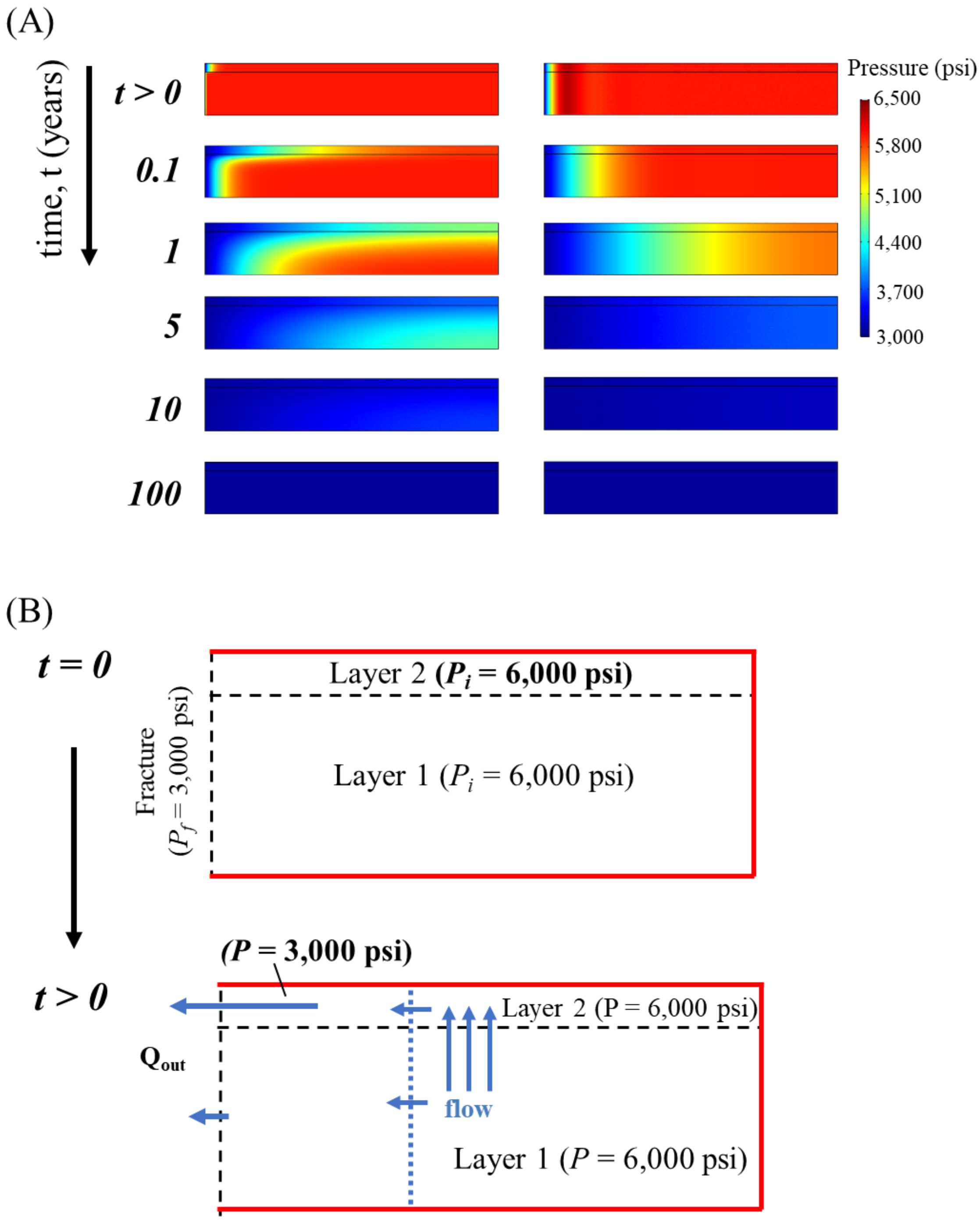

Figure 4.23. Pressure dissipation in the simulated production performance model at increasing low-permeability layer's vertical permeability (k_{v1}).

(A) Examples of pressure distribution within each layer's domain over time in the Wolfcamp A model. (B) Schematics showing the interpretation of isobaric lines and flow direction at initial conditions (t = 0) and at early times (t > 0).

(A)

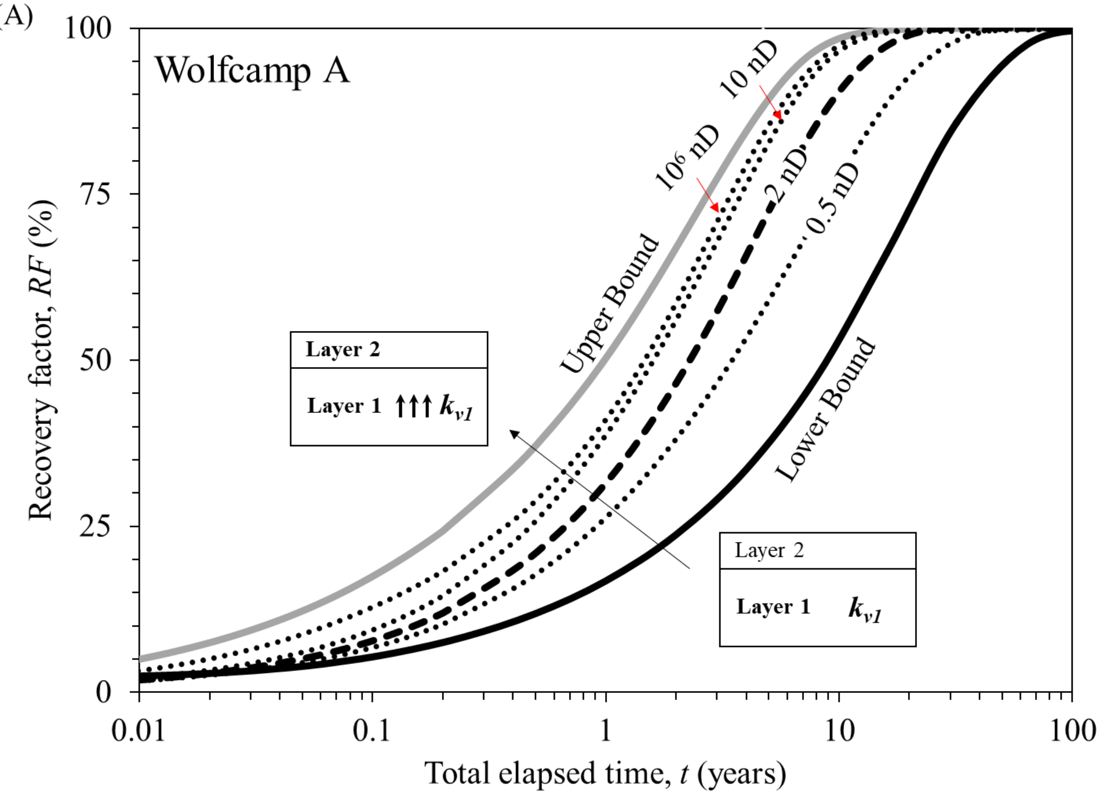

Wolfcamp A
100
75
50
25
0
Recovery factor, RF (%)
0.01
0.1
1
10
100
Total elapsed time, t (years)
Upper Bound
Lower Bound
10 nD
10^6 nD
2 nD
0.5 nD
Layer 2
Layer 1 ↑↑↑ k_v1
Layer 2
Layer 1 k_v1

(B)

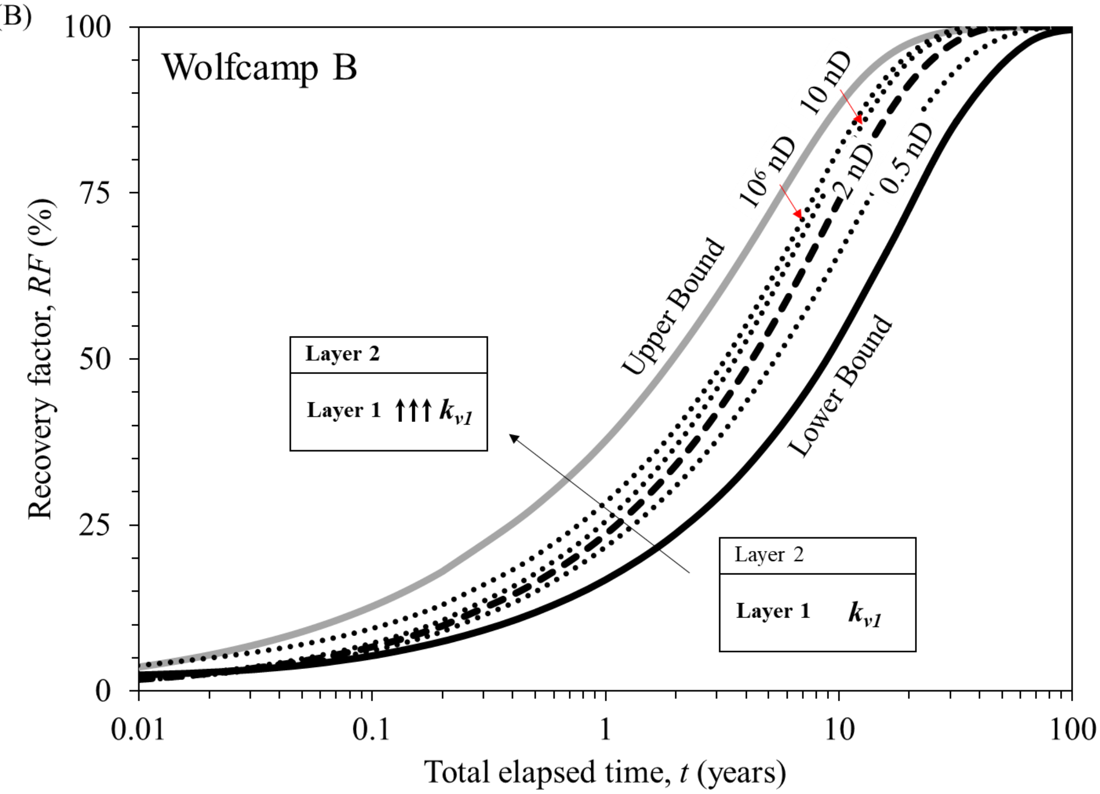

Wolfcamp B
100
75
50
25
0
Recovery factor, RF (%)
0.01
0.1
1
10
100
Total elapsed time, t (years)
Upper Bound
Lower Bound
10 nD
10^6 nD
2 nD
0.5 nD
Layer 2
Layer 1 ↑↑↑ k_v1
Layer 2
Layer 1 k_v1

Figure 4.24. Numerical solutions for simulated production performance at increasing vertical permeabilities in the low-permeability layer (k_{v1}) (black, dotted curves) on the (A) Wolfcamp A and (B) Wolfcamp B models.

The low-permeability layer's vertical permeability (k_{v1}) is increased while leaving the horizontal permeabilities in both layers (k_{h1}, k_{h2}) fixed. The black, dashed curve is the simulated production performance using k_{v1} = 20 nD (Case 3). The lower bound performance (black, solid curve) is the analytical solution (Case 1). The upper bound performance (dark gray, solid curve) is the numerical solution (Case 2). The *RF* represents the cumulative produced pore volume over the maximum producible pore volume for the given model parameters (Table 4.1, Table 4.2).

(A)

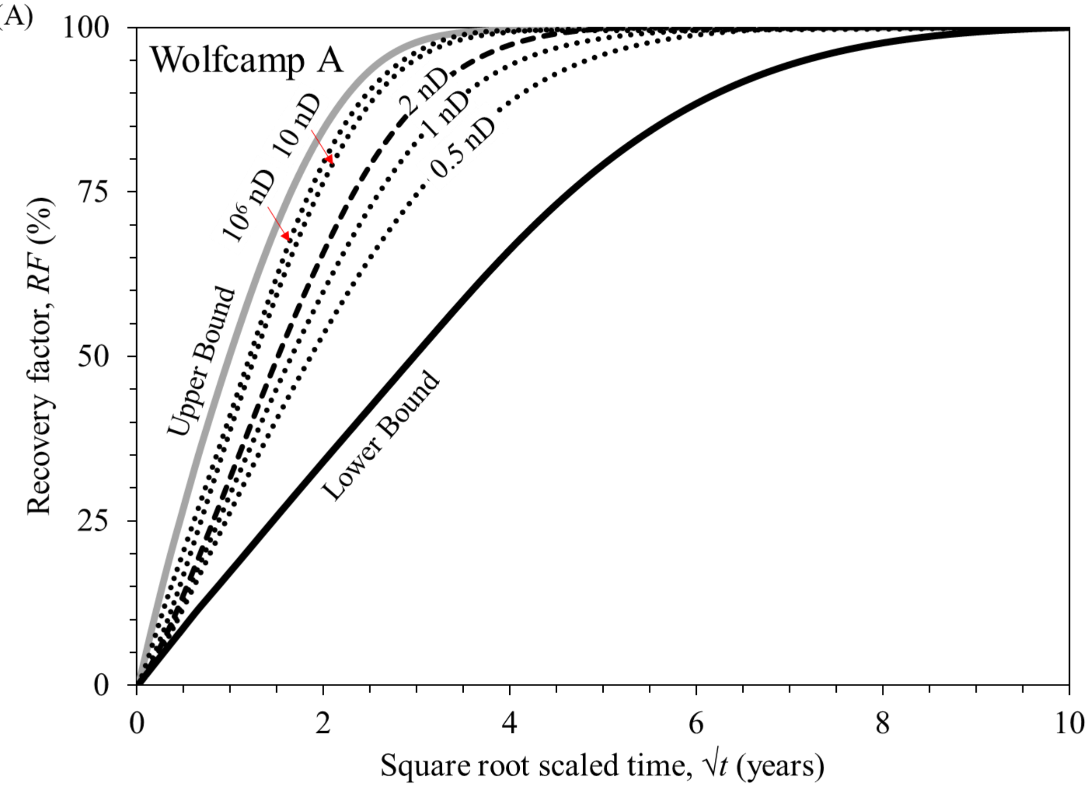

Wolfcamp A
100
75
50
25
0
Recovery factor, RF (%)
0
2
4
6
8
10
Square root scaled time, √t (years)
Upper Bound
10⁶ nD
10 nD
2 nD
1 nD
0.5 nD
Lower Bound

(B)

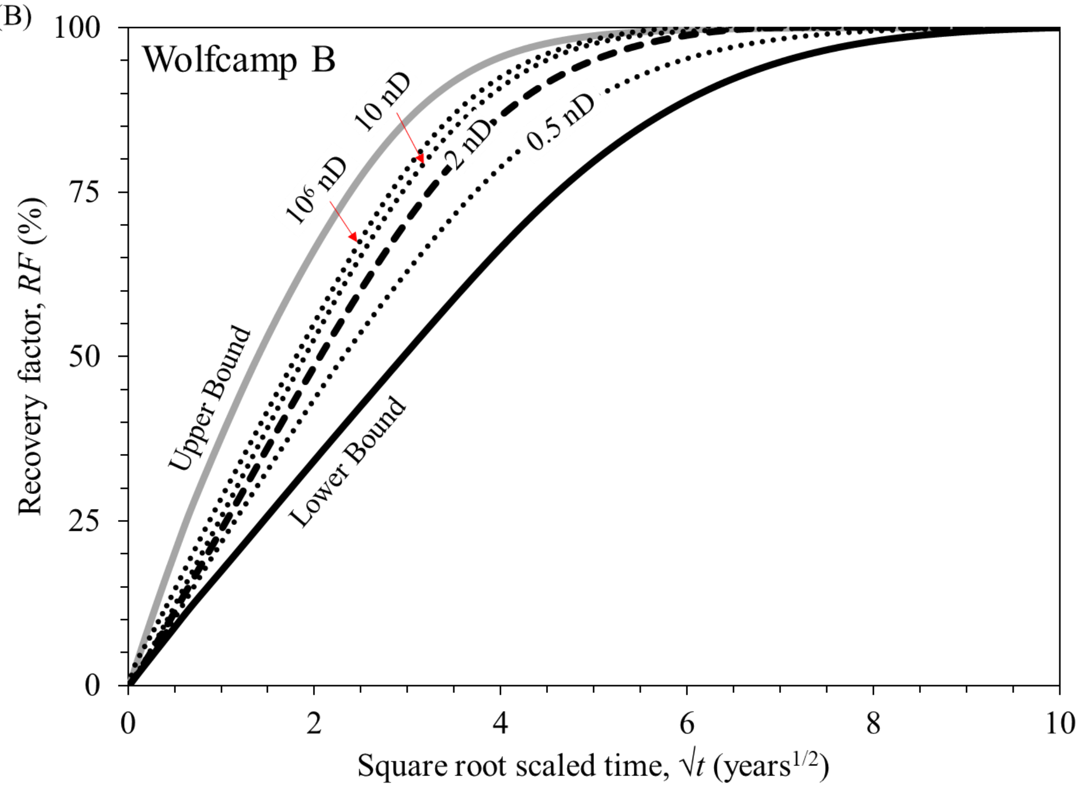

Wolfcamp B
100
75
50
25
0
Recovery factor, RF (%)
0
2
4
6
8
10
Square root scaled time, √t (years^1/2)
Upper Bound
10⁶ nD
10 nD
2 nD
0.5 nD
Lower Bound

Figure 4.25. Scaled production for the simulated production performance at increasing vertical permeabilities in the low-permeability layer (k_{v1}) (black, dotted curves) on the (A) Wolfcamp A and (B) Wolfcamp B models.

The low-permeability layer's vertical permeability (k_{v1}) is increased while leaving the horizontal permeabilities in both layers (k_{h1}, k_{h2}) fixed. The black, dashed curve is the simulated production performance using k_{v1} = 20 nD (Case 3). The lower bound performance (black, solid curve) is the numerical solution (Case 1). The upper bound performance (dark gray, solid curve) is the numerical solution (Case 2). The recovery factor (*RF*) is the cumulative produced pore volume over the maximum producible pore volume for the given model parameters.

4.7 UPSCALED PERMEABILITIES

I built a single layer model equivalent to the two-layer model to estimate the required upscaled permeabilities (k_{ups}) to match the production behavior of the two-layer model. This single layer model has the same length (L) and total thickness ($h_1 + h_2$), and equivalent pore volume (porosity is weight averaged) to the two-layer model (Figure 4.26). In the previous section, I focused my analysis on the fluxes occurring at the top and left boundaries of the low-permeability layer only. Here, I match the sum of the fluxes occurring across the producing face (left boundary) in each layer.

Figure 4.27 shows the pressure dissipation in the single layer model at various times. The isobaric lines are vertical because the porosities and permeabilities are the same in both layers, and there is only 1D horizontal flow towards the fracture (i.e., left boundary). Because there is only horizontal flow, I can use the 1D analytical solution presented in Case 1 to match production behavior in this single-layer model. I use the analytical solution because it is computationally less expensive than the numerical simulation. Figure 4.28 demonstrates that the analytical and numerical solutions for the single-layer model in both the Wolfcamp A and Wolfcamp B are practically identical.

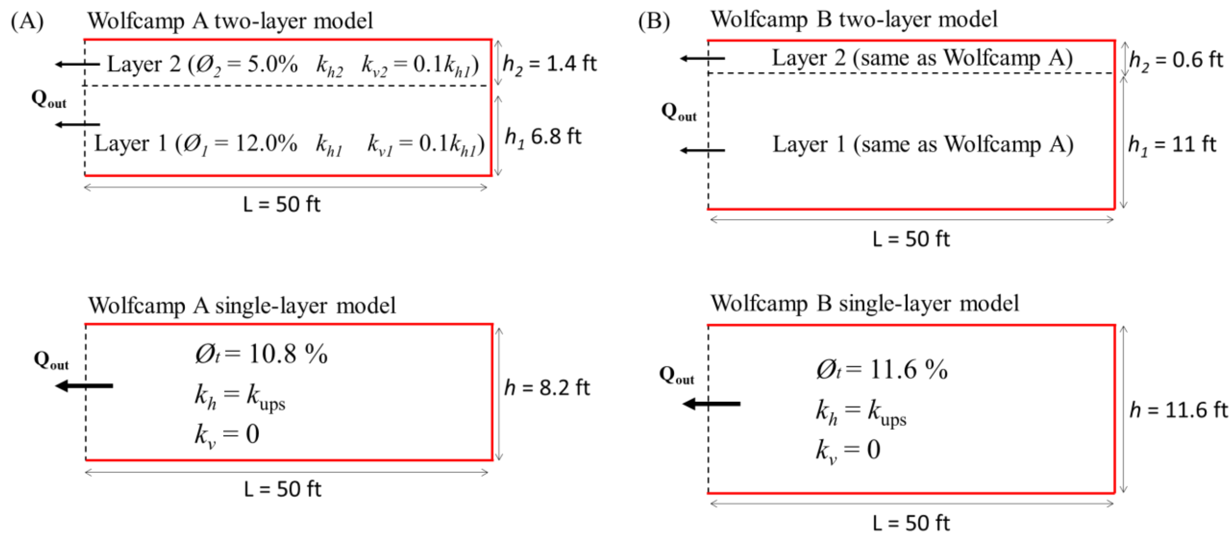

Figure 4.26. Schematic of single layer model equivalent to two-layer model in (A) Wolfcamp A and (B) Wolfcamp B models.

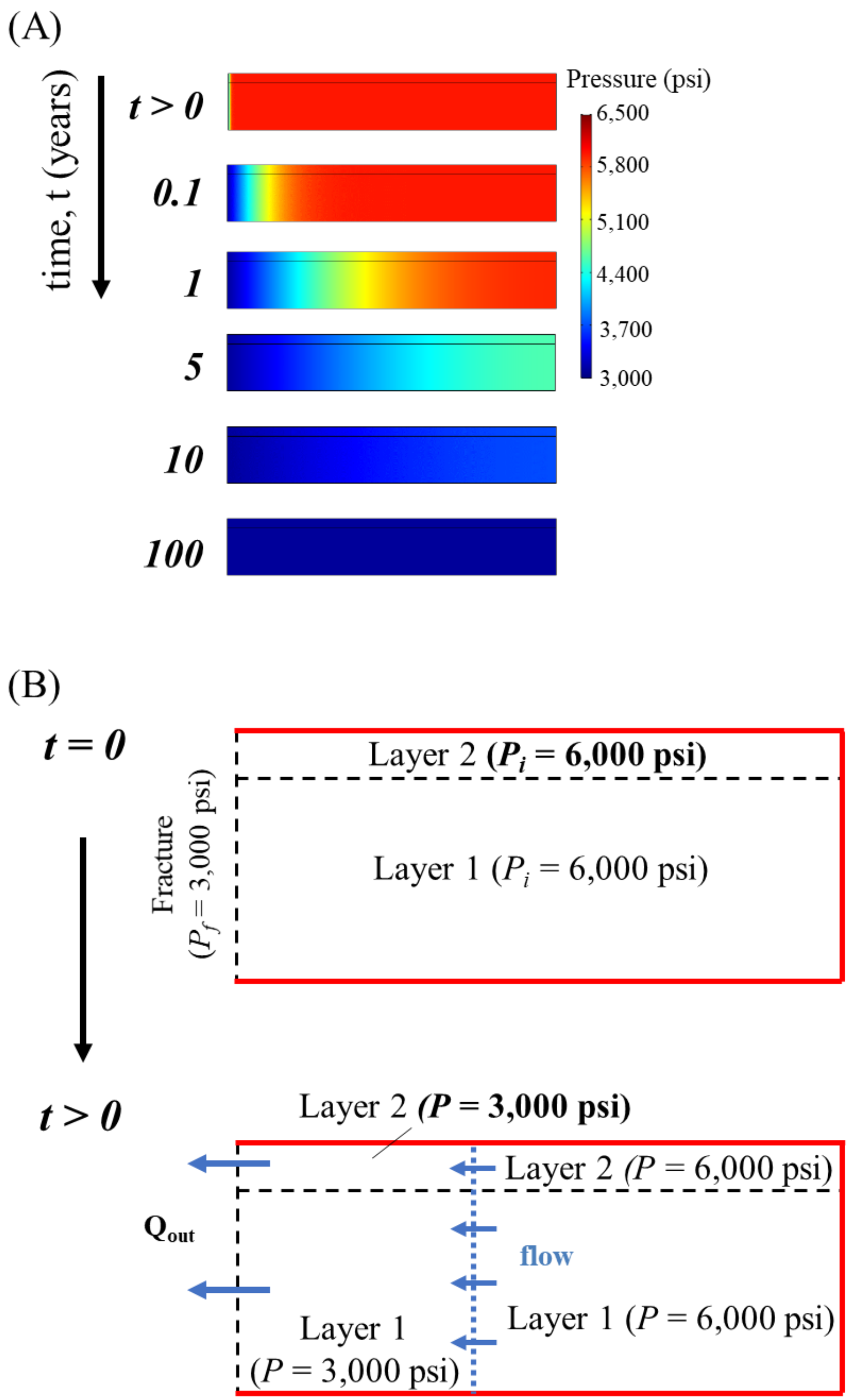

Figure 4.27. Pressure dissipation in single-layer (homogeneous) model.

(A) Examples of pressure distribution within each layer's domain over time in the Wolfcamp A model. (B) Schematics showing the interpretation of isobaric lines and flow direction at initial conditions (t = 0) and at early times (t > 0).

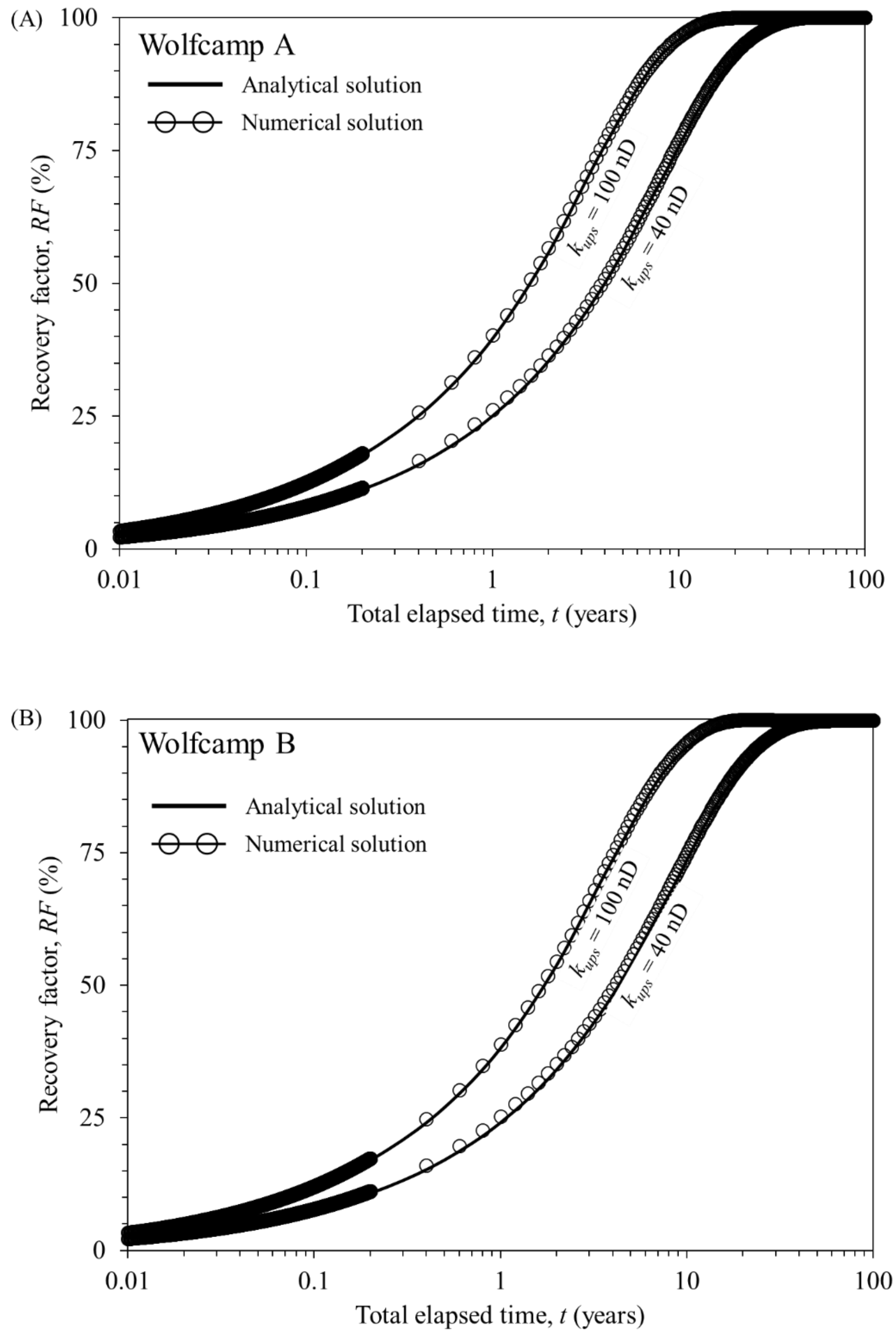

Figure 4.28. Analytical (black, solid curve) and numerical (black, circles) solutions for the single layer model using upscaled permeabilities (k_{ups}) of 40 nD and 100 nD in the (A) Wolfcamp A and (B) Wolfcamp B models.

The *RF* represents the cumulative produced pore volume over the maximum producible pore volume for the given model parameters (Table 4.1, Table 4.2).

4.7.1 Upscaled permeability in Case 1: no cross-facies flow (Lower bound performance)

The required upscaled permeability to match the lower bound performance in the Wolfcamp A model (Figure 4.29A) is k_{ups} = 45 nD during early production time, and k_{ups} = 20 nD at later production times. In the Wolfcamp B model (Figure 4.29B), the required upscaled permeability to match the lower bound performance is k_{ups} = 30 nD during early production time, and k_{ups} = 20 nD to at later production times.

The upscaled permeabilities (k_{ups}) required to match early production are higher due to the contribution of the high-permeability layer to the total flux. Once the high-permeability layer depletes, production is from the low permeability layer only. The upscaled permeability (k_{ups}) required to match late-time production is actually the horizontal permeability of the low-permeability layer (i.e., k_{h1} = 20 nD) because it is the only layer producing fluids. The time at which the high-permeability layer is mostly depleted can be identified by the early-time slope change in the numerical solution for the lower bound (black solid curve, Figure 4.30).

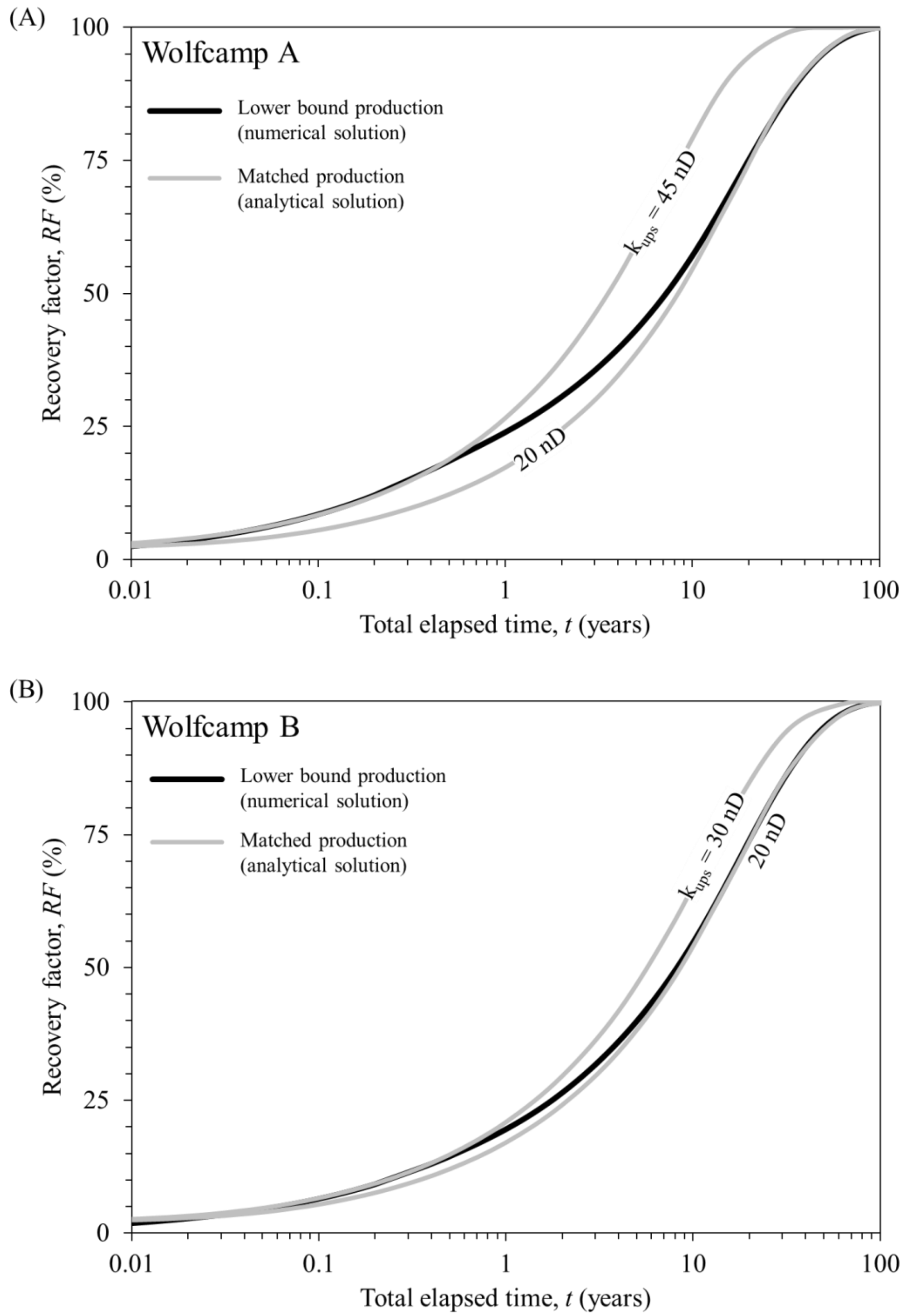

Figure 4.29. Analytical solutions (light grey, solid curves) matching production behavior of the lower bound performance on the (A) Wolfcamp A and (B) Wolfcamp B models.

The lower bound performance (black, solid curve) is the numerical solution (Case 1). The *RF* represents the cumulative produced pore volume over the maximum producible pore volume for the given model parameters (Table 4.1, Table 4.2).

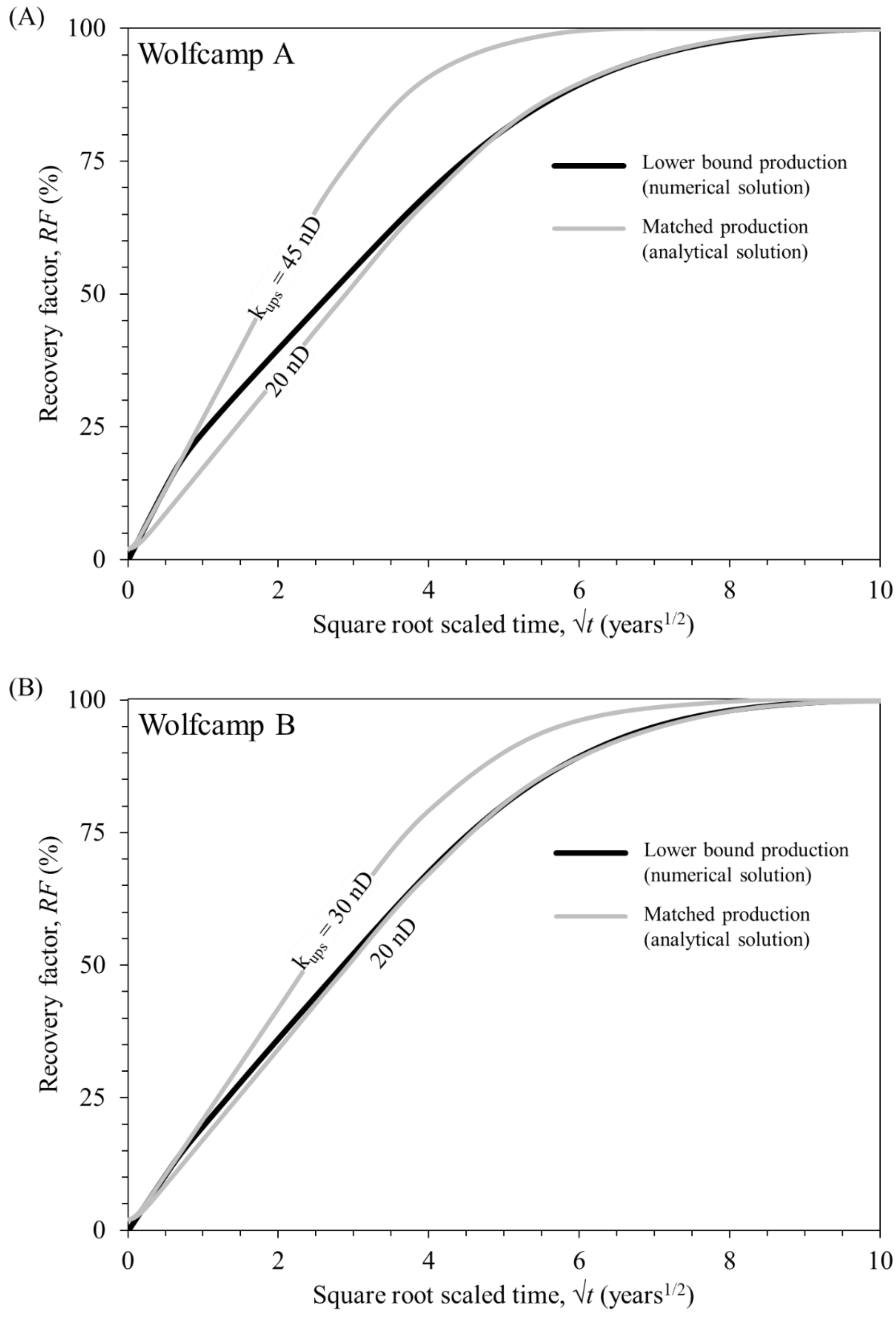

Figure 4.30. Scaled analytical solutions (light grey, solid curves) matching production of the lower bound performance on the (A) Wolfcamp A and (B) Wolfcamp B models.

The black, solid curve represents the lower bound production (Case 1). The *RF* represents the cumulative produced pore volume over the maximum producible pore volume for the given model parameters (Table 4.1, Table 4.2).

4.7.2 Upscaled permeability in Case 2: cross-facies flow (Upper bound performance)

The required upscaled permeability to match the upper bound performance is k_{ups} = 190 nD at early times, and k_{ups} = 130 nD at later times in the Wolfcamp A model (Figure 4.31A, Figure 4.32A). In the Wolfcamp B model (Figure 4.31B, Figure 4.32B), the required upscaled permeability to match early production in the upper bound is k_{ups} = 110 nD, and k_{ups} = 63 nD to match late production.

In the upper bound model (Case 2), I showed that the high-permeability layer depletes almost instantly when production starts (Figure 4.8). Therefore, the reason for requiring two different permeabilities at early- and late-production times is related to the production behavior in the low-permeability layer. The production rates occur at faster rates until the pressure at the base of the low-permeability layer drops below the initial pressure (Pi = 6000 psi). Then, production occurs at slower rates. Hence, early production requires higher upscaled permeability, whereas late production requires lower upscaled permeabilities.

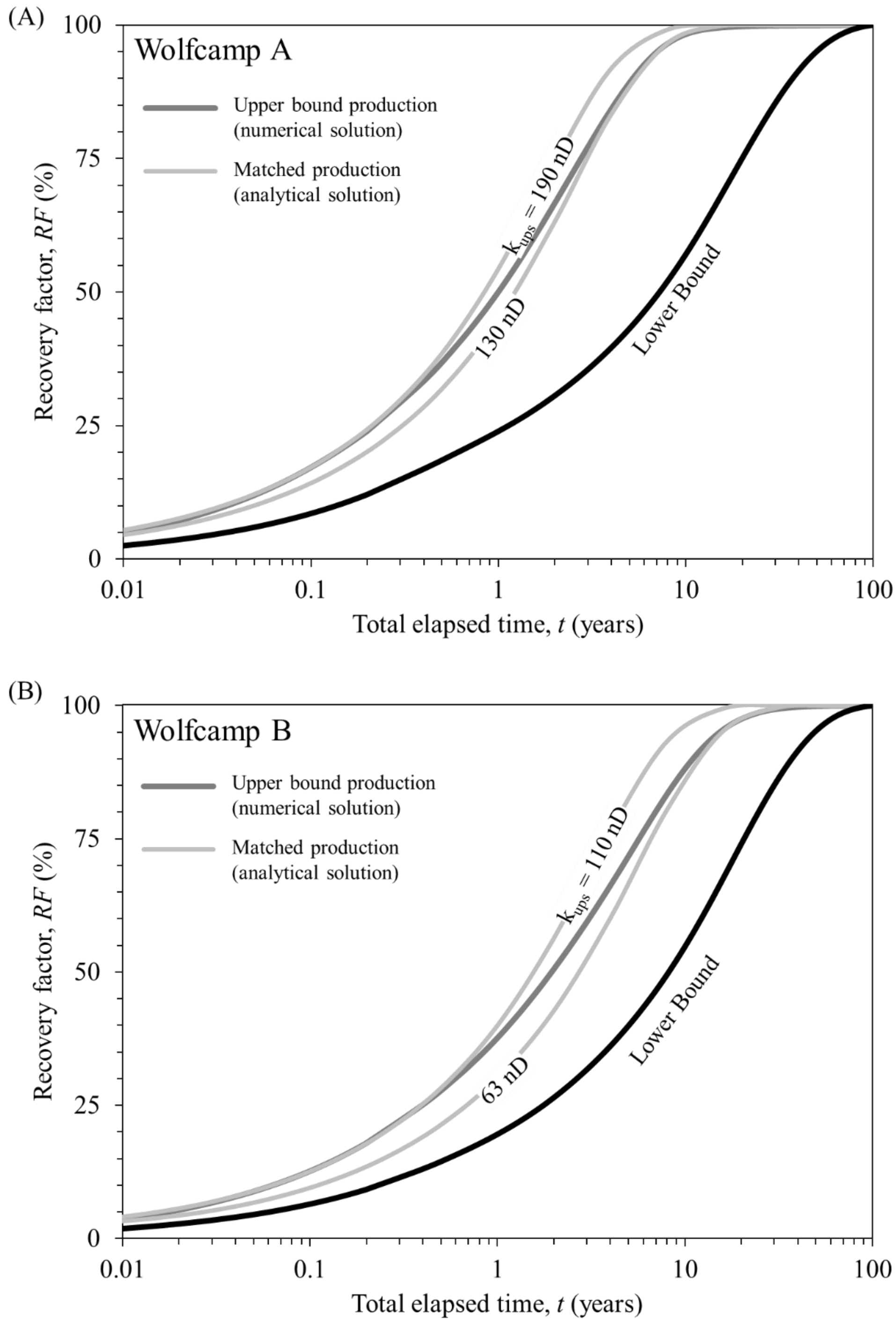

Figure 4.31. Analytical solutions (light grey, solid curves) matching production of the upper bound performance on the (A) Wolfcamp A and (B) Wolfcamp B models.

The lower bound performance (black, solid curve) is the numerical solution (Case 1). The upper bound performance (dark gray, solid curve) is the numerical solution (Case 2). The *RF* represents the cumulative produced pore volume over the maximum producible pore volume for the given model parameters (Table 4.1, Table 4.2).

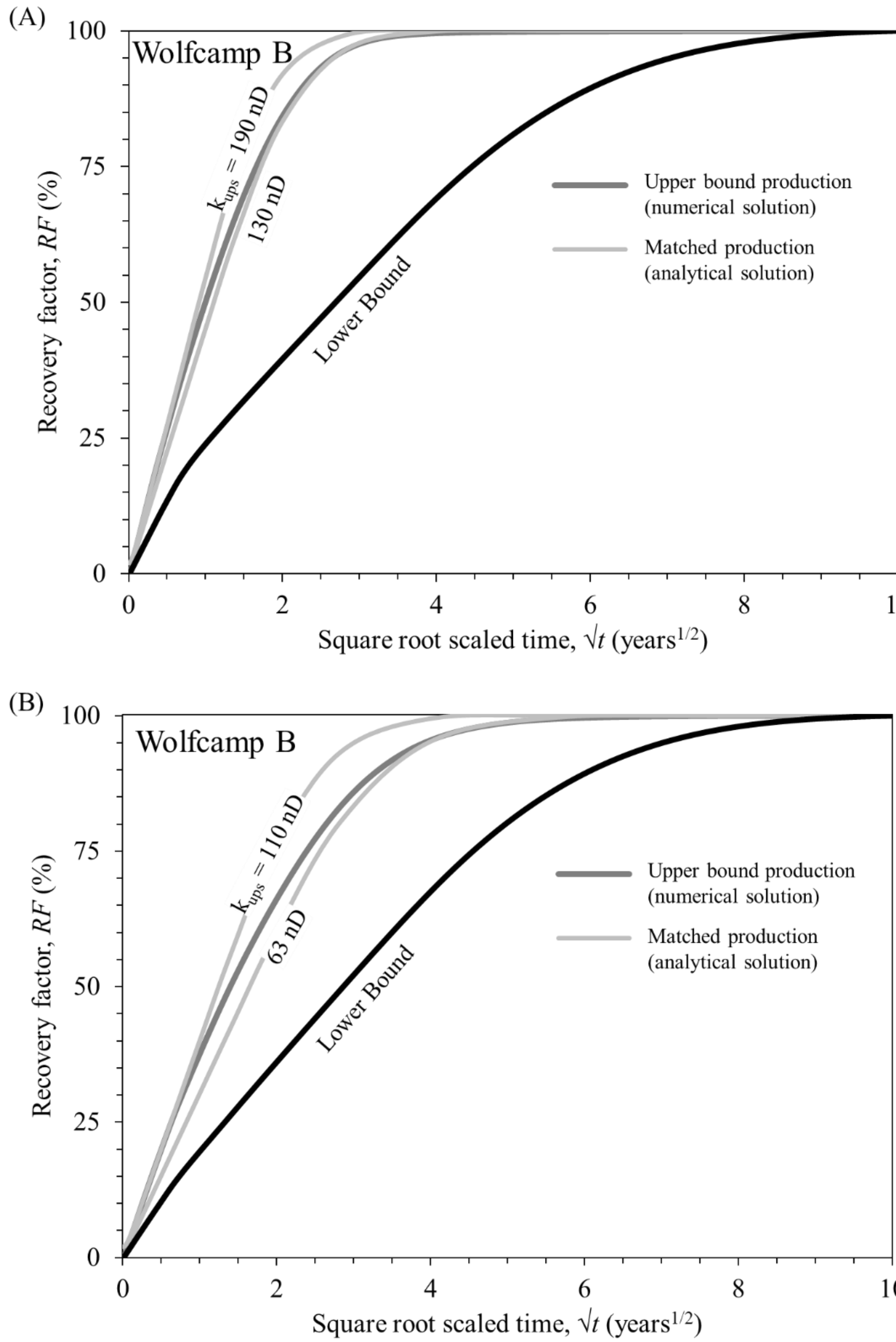

Figure 4.32. Scaled analytical solutions (light grey, solid curves) matching production of the upper bound performance on the (A) Wolfcamp A and (B) Wolfcamp B models.

The lower bound performance (black, solid curve) is the numerical solution (Case 1). The upper bound performance (dark gray, solid curve) is the numerical solution (Case 2). The *RF* represents the cumulative produced pore volume over the maximum producible pore volume for the given model parameters (Table 4.1, Table 4.2).

4.7.3 Upscaled permeability in Case 3: cross-facies flow (Simulated production performance)

In the Wolfcamp A model, the required upscaled permeability (k_{ups}) to match the simulated production performance is k_{ups} = 55 nD at early times, and k_{ups} = 74 nD at later times in the (Figure 4.33A). In the Wolfcamp B model, the required upscaled permeability to match the simulated production performance is k_{ups} = 30 nD at early times, and k_{ups} = 40 nD at later times (Figure 4.33B).

Figure 4.34 shows more clearly that the simulated production performance can practically be matched in its entirety with a single upscaled permeability in the Wolfcamp A (k_{ups} = 74 nD) and Wolfcamp B (k_{ups} = 40 nD) models. In the Wolfcamp A model, the reason for its higher production rates and upscaled permeabilities compared to the Wolfcamp B is primarily due to the high-permeability layer's thickness (h_2). The high-permeability layer in the Wolfcamp A model is over two-times (h_2 = 1.4 ft) thicker than that in the Wolfcamp B model (h_2 = 0.6 ft). The thicker high-permeability layer in the Wolfcamp A diminishes its flow restriction and production rates increase. For example, a recovery factor of RF = 50% is reached at the end of 2.2 years of production, whereas the Wolfcamp B required 4.2 years (Table 4.4).

The Table 4.4 summarizes the required production times to reach a recovery factor RF = 50% and the upscaled permeabilities required to match production in the lower bound, simulated production, and upper bound performance on the Wolfcamp A and Wolfcamp B models. We can clearly see that cross-facies flow increases the production rates and the upscaled permeabilities by at least two times compared with a model without cross-facies flow.

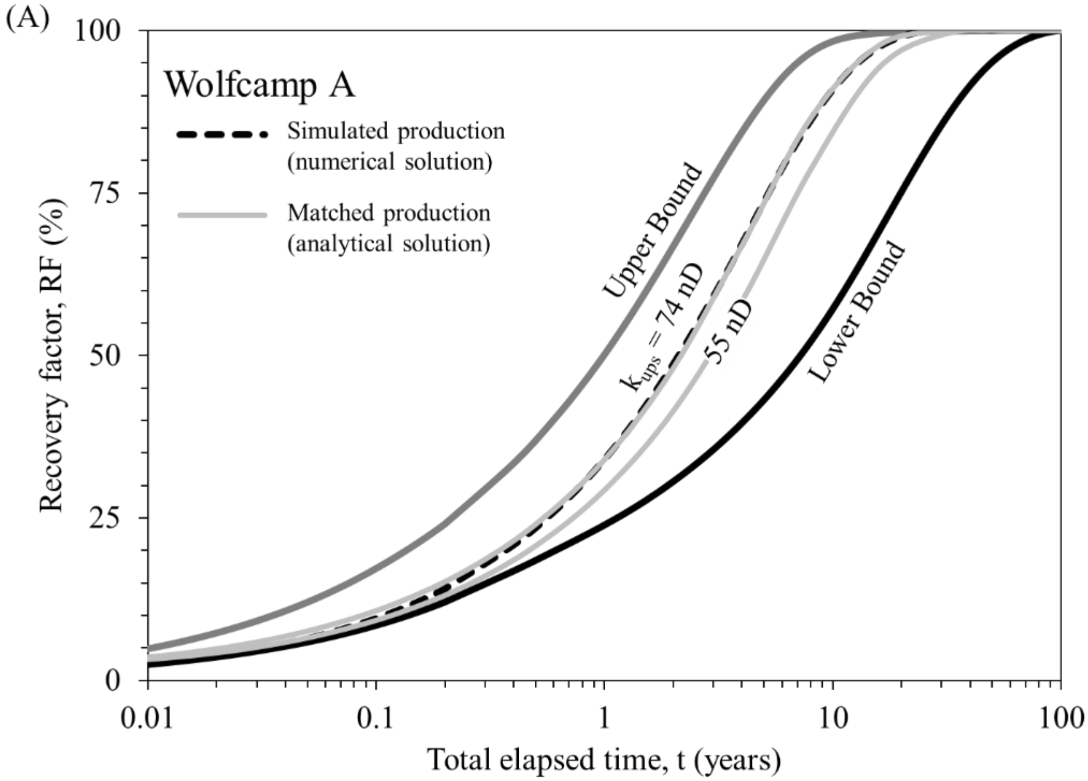
(A)
Wolfcamp A
Simulated production
(numerical solution)
Matched production
(analytical solution)
Upper Bound
k_{ups} = 74 nD
55 nD
Lower Bound
Recovery factor, RF (%)
Total elapsed time, t (years)
0
25
50
75
100
0.01
0.1
1
10
100

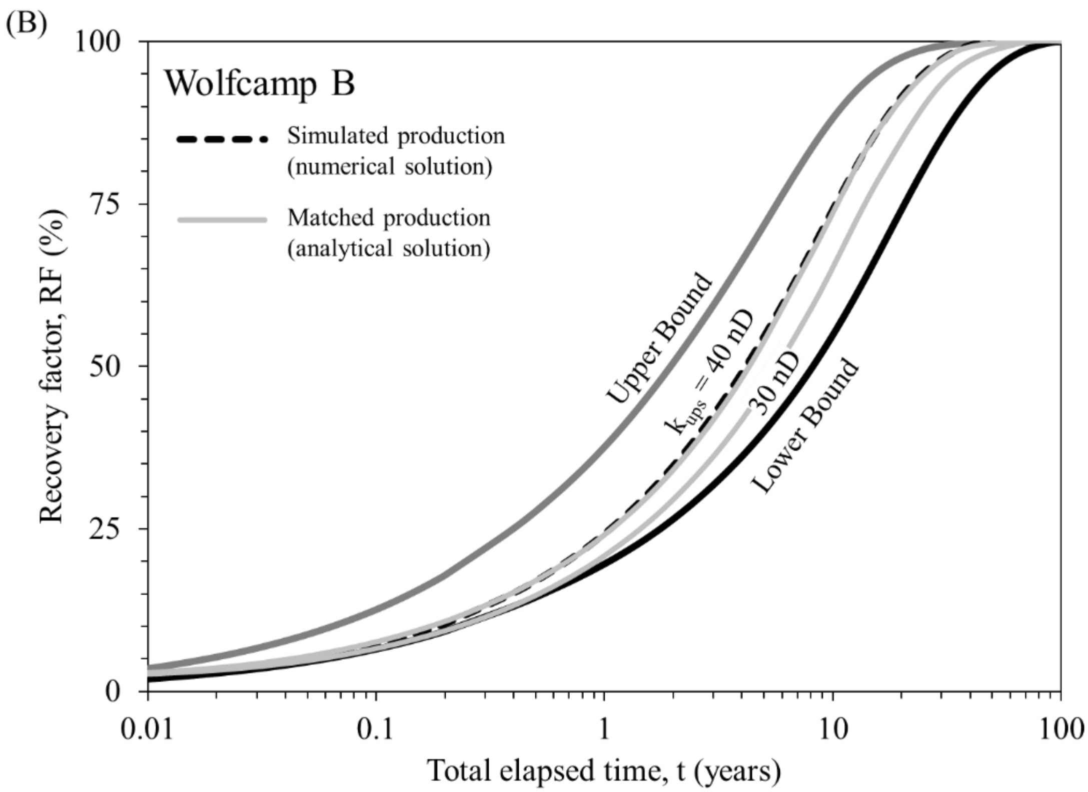
(B)
Wolfcamp B
Simulated production
(numerical solution)
Matched production
(analytical solution)
Upper Bound
k_{ups} = 40 nD
30 nD
Lower Bound
Recovery factor, RF (%)
Total elapsed time, t (years)
0
25
50
75
100
0.01
0.1
1
10
100

Figure 4.33. Analytical solutions (light grey, solid curves) matching production of the simulated production performance on the (A) Wolfcamp A and (B) Wolfcamp B models.

The black, dashed curve is the simulated production performance using k_{h2} = 560 nD (Case 3). The lower bound performance (black, solid curve) is the numerical solution (Case 1). The upper bound performance (dark gray, solid curve) is the numerical solution (Case 2). The *RF* represents the cumulative produced pore volume over the maximum producible pore volume for the given model parameters (Table 4.1, Table 4.2).

(A)

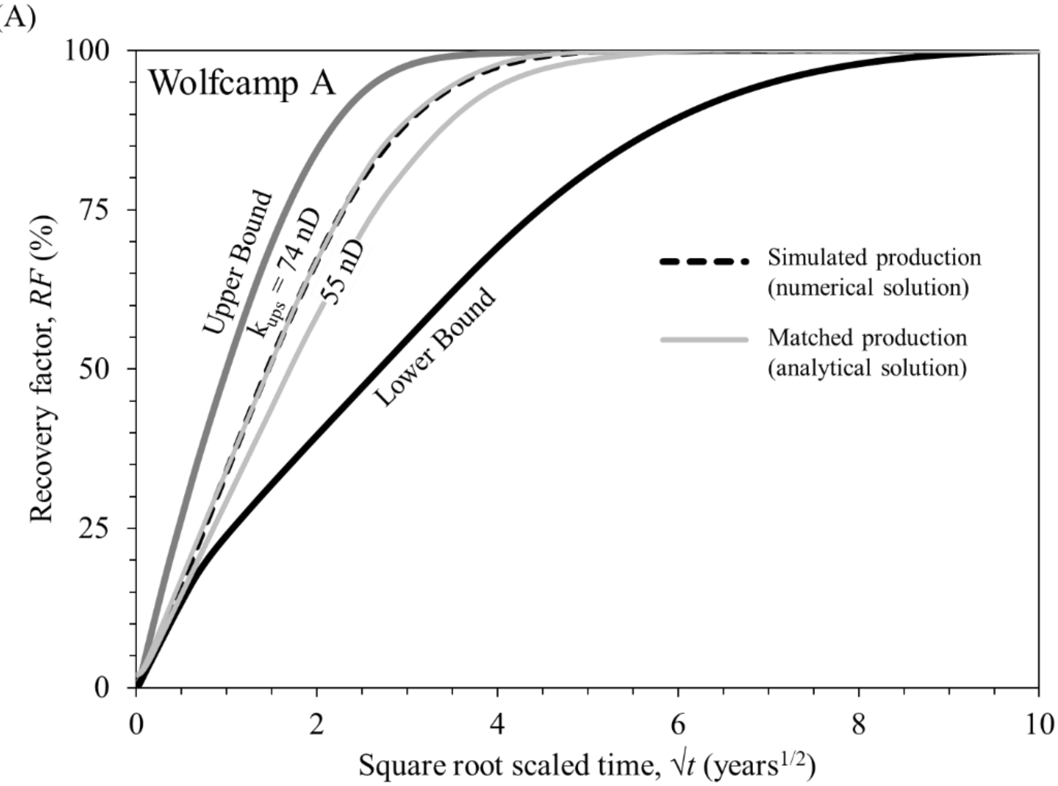

Wolfcamp A
100
75
50
25
0
Recovery factor, RF (%)
Upper Bound
k_ups = 74 nD
55 nD
Lower Bound
Simulated production
(numerical solution)
Matched production
(analytical solution)
0
2
4
6
8
10
Square root scaled time, √t (years^1/2)

(B)

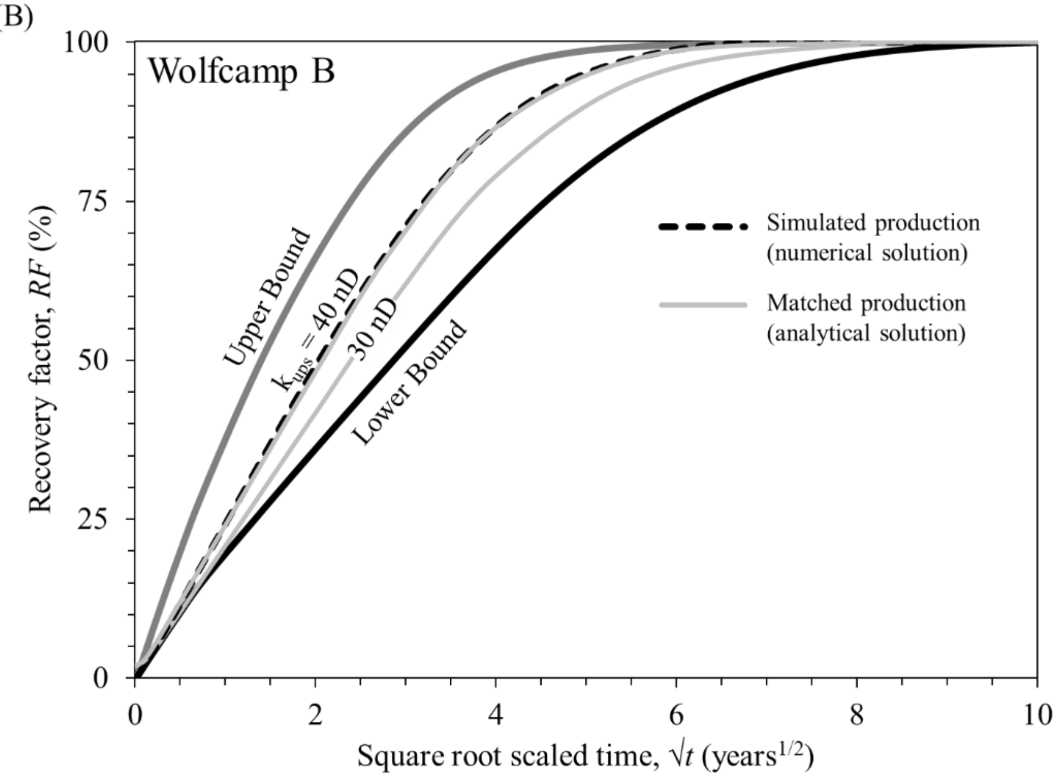

Wolfcamp B
100
75
50
25
0
Recovery factor, RF (%)
Upper Bound
k_ups = 40 nD
30 nD
Lower Bound
Simulated production
(numerical solution)
Matched production
(analytical solution)
0
2
4
6
8
10
Square root scaled time, √t (years^1/2)

Figure 4.34. Scaled analytical solutions (light grey, solid curves) matching production of the simulated production performance on the (A) Wolfcamp A and (B) Wolfcamp B models.

The black, dashed curve is the simulated production performance using k_{h2} = 560 nD (Case 3). The lower bound performance (black, solid curve) is the numerical solution (Case 1). The upper bound performance (dark gray, solid curve) is the numerical solution (Case 2). The *RF* represents the cumulative produced pore volume over the maximum producible pore volume for the given model parameters (Table 4.1, Table 4.2).

Table 4.4. Production time (t) required to achieve a recovery factor of RF = 50 %, and upscaled permeabilities (k_{ups}) required to match production in the lower bound, simulated production, and upper bound performance on the Wolfcamp A and Wolfcamp B models.

The recovery factor (RF) is the cumulative produced pore volume over the maximum producible pore volume for the given model parameters.

	Wolfcamp A		Wolfcamp B	
	t (years)	k_{ups} (nD)	t (years)	k_{ups} (nD)
No cross-facies flow (Lower bound)	7.3	20 to 45	8.2	20 to 30
Cross-facies flow (Simulated production)	2.2	55 to 74	4.2	30 to 40
Cross-facies flow (Upper bound)	1.0	130 to 190	2.0	63 to 110

4.8 Cross-facies flow implications on hydraulic fracture spacing

The faster reservoir drainage occurring when high-permeability layers are intersected by hydraulic fractures has important implications for well completion designs. Figure 4.35 represents the recovery factors (*RF*) and cumulative production (*Q*) for different reservoir lengths (*L*) at the end of 5 years in the Wolfcamp A and Wolfcamp B models. When there is cross-facies flow (Figure 4.35A, C), recovery factors are very high at short reservoir lengths. As reservoir length increases, recovery factors decline sharply, and then they plateau at lengths beyond ~100 ft. In contrast, the cumulative production increases rapidly at increasing reservoir lengths, but they plateau at reservoir lengths beyond ~75 ft. This indicates that, although recovery factors are very high at shorter lengths, the cumulative production is small. Also, at reservoir lengths beyond ~75 ft, there is no significant increase in cumulative production and recovery factors. Considering that the reservoir length in my model is half the distance between two consecutive hydraulic fractures, the optimal spacing between hydraulic fractures in this example to maximize recovery factors and cumulative production at the end of 5 years would be ~ 150 ft (i.e., 2*L*).

If the Wolfcamp A and Wolfcamp B reservoirs were entirely composed of low-permeability mudstones (e.g., k = 20 nD), the recovery factors would decline more sharply and the cumulative production would plateau at much shorter reservoir lengths (e.g., L ~ 25 ft) (Figure 4.35B, D) compared to reservoirs with cross-facies flow between low- and high-permeability layers (Figure 4.35A, C). Therefore, completions in reservoirs consisting of only low-permeability strata require shorter spacing between hydraulic fractures to maximize recovery factors and cumulative production.

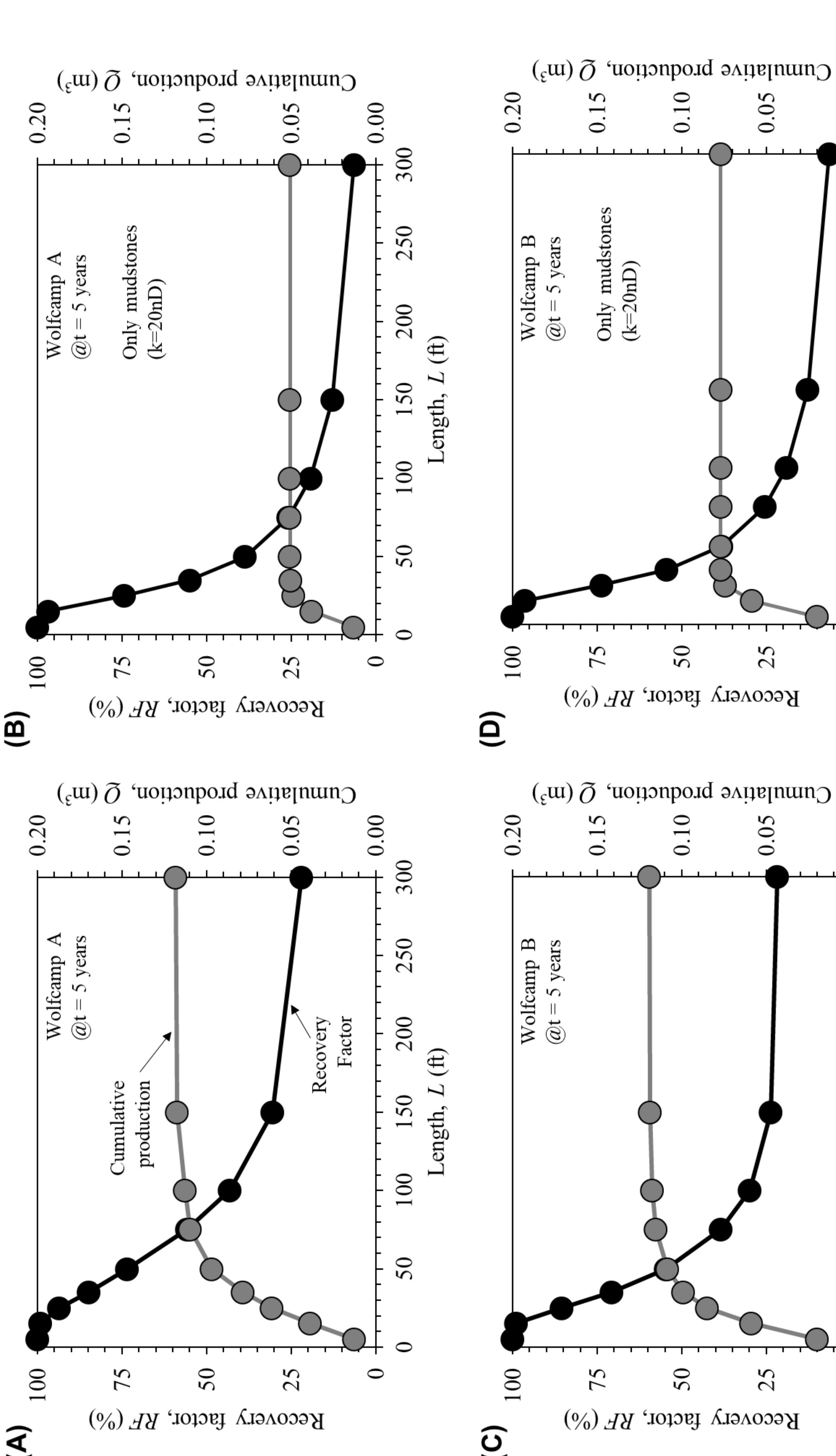

(A)
Wolfcamp A
@t = 5 years
Cumulative production
Recovery Factor
(B)
Wolfcamp A
@t = 5 years
Only mudstones
(k=20nD)
(C)
Wolfcamp B
@t = 5 years
(D)
Wolfcamp B
@t = 5 years
Only mudstones
(k=20nD)
Recovery factor, RF (%)
Cumulative production, Q (m3)
Length, L (ft)

Figure 4.35. Recovery factor (black) and cumulative production (grey) for varying reservoir lengths in the Wolfcamp A and Wolfcamp B models at the end of 5 years of production.

(A) Wolfcamp A model with cross-facies flow between low- and high-permeability layers. (B) Wolfcamp A model consisting of low-permeability strata with k = 20 nD. (C) Wolfcamp B model with cross-facies flow between low- and high-permeability layers. (D) Wolfcamp B model consisting of low-permeability strata with k = 20 nD.

4.9 DISCUSSION

The simulated production performance indicates that production rates in the Wolfcamp A and Wolfcamp B models are faster when cross-facies flow occurs, compared to their performance when each layer is produced independently (i.e., no cross-facies flow, lower bound performance). Therefore, cross-facies flow is a production drainage mechanism that increases the upscaled permeabilities in stratified low-permeability reservoirs.

The Wolfcamp A and Wolfcamp B models have the same porosities and permeabilities, and yet they exhibit different production rates. The Wolfcamp A model shows faster production rates because its high-permeability layer is thicker ($h_{2,\,WCA}$ = 1.4 ft) than that in the Wolfcamp B model ($h_{2,\,WCB}$ = 0.6 ft). This thickness increase diminishes flow restriction, and the Wolfcamp A's high-permeability layer can produce the fluids drained from the low permeability layer at faster rates (e.g., RF = 50% at t = 2.2 years) than the high-permeability layer in the Wolfcamp B (e.g., RF = 50% at t = 4.2 years). Accordingly, the upscaled permeability in the Wolfcamp A is higher ($k_{ups,\,WCA}$ = 74 nD) than that in the Wolfcamp B ($k_{ups,\,WCB}$ = 40 nD).

The insights earned from these simulations may be used to inform drilling and completion strategies in the upper Wolfcamp. Horizontal wells may increase production rates when they are landed and completed in depth intervals containing a high frequency of high-permeability layers, or by intersecting fewer but thicker high-permeability layers. In other words, intervals exhibiting a high net to gross ratio of the high-permeability layers to the low permeability strata may be targeted to maximize production rates. Alternatively, fewer and thinner permeable layers but with much higher horizontal permeabilities (e.g., k_{h2} > 2,000 nD) can be targeted as they may also increase production rates. It is important to note that a significant volume of low-permeability organic-rich siliceous mudstones must exist between the permeable layers because they store most hydrocarbons in the upper Wolfcamp. Otherwise, the cumulative production would be low despite the fast production rates, and more wells per section would be needed. However, if the thickness of the organic-rich siliceous mudstone strata between permeable layers is exceedingly large, production rates may slow down too much. Hence, finding the right balance between production rates and cumulative production is key to design efficient field development plans in the upper Wolfcamp.

Lastly, well completions in reservoirs containing high-permeability layers may increase the spacing between hydraulic fractures (e.g., $2L \sim 150$ ft) compared to well completions in reservoirs composed only of low-permeability strata (e.g., $2L \sim 50$ ft). A longer spacing between hydraulic fractures may require less hydraulic fracture treatments, which would lower production costs.

4.10 CONCLUSIONS

Based on the results presented in this paper, the following conclusions can be made:

1. The cross-facies flow in stratified low-permeability reservoirs with permeability heterogeneity increase multiple times the well production rates and upscaled permeabilities compared to the production in a reservoir without cross-facies flow.
2. Cross-facies flow is controlled primarily by the high-permeability layer's horizontal permeability (k_{h2}) and thickness (h_2). When either of these two reservoir parameters increases, flow restriction in the high-permeability layer diminishes and production rates increase. The low-permeability layer's vertical permeability (k_{v2}) is important, but its effect on cross-facies flow is limited by the high-permeability layer's horizontal permeability (k_{h2}) and thickness (h_2).
3. Production rates are higher in the Wolfcamp A model because its high-permeability layer is ~2 times thicker ($h_{2\_Wolfcamp\ A}$ = 1.4 ft) than that the low permeability layer in the

Wolfcamp B model ($h_{2\_Wolfcamp\ B}$ = 0.6 ft). A recovery factor (RF) of 50% in the Wolfcamp A is reached after ~2 years, whereas the Wolfcamp B model requires ~4 years. Subsequently, the upscaled permeability (k_{ups}) in the Wolfcamp A model is higher (k_{ups} = 74nD) than that in the Wolfcamp B model (k_{ups} = 40 nD).

4. Hydraulic fracture spacing may be increased in reservoirs containing high-permeability layers, compared to reservoirs composed of only low-permeability strata.

References

Defeu, C., G. G. Ferrer, E. Ejofodomi, D. Shan, and F. Alimahomed, 2018, Time Dependent Depletion of Parent Well and Impact on Well Spacing in the Wolfcamp Delaware Basin, SPE Liquids-Rich Basins Conference-North America, Midland, TX, USA, SPE, p. 13.

Flemings, P. B., 2021, A Concise Guide to Geopressure: Origin, Prediction, and Applications, Cambridge Press.

Gale, J. F. W., S. J. Elliott, and S. E. Laubach, 2018, Hydraulic fractures in core from stimulated reservoirs: core fracture description of HFTS Slant Core, Midland Basin, West Texas, URTeC, Houston, Texas, USA, p. 18.

Gale, J. F. W., S. J. Elliott, B. G. Rysak, C. L. Ginn, N. Zhang, R. D. Myers, and S. E. Laubach, 2021, Fracture description of the HFTS-2 Slant Core, Delaware Basin, West Texas, URTeC, Houston, Texas, USA, p. 12.

Katz, M. L., and M. R. Tek, 1961, A theoretical study of pressure distribution and fluid flux in bounded stratified porous systems with crossflow: Society of petroleum Engineers Journal, v. 2, p. 68-82.

Kosanke, T., and A. Warren, 2016, Geological controls on matrix permeability of the Eagle Ford Shale (Cretaceous), South Texas, U.S.A.: The Eagle Ford Shale: A renaisaance in U.S. oil production, v. AAPG Memoir 110.

Kuhl, E. J., 2003, Optimization of Recovery from Two-Layer Reservoirs with Crossflow: Master thesis, Pennsylvania State University, 95 p.

Kurtoglu, B., 2013, Integrated reservoir characterization and modeling in support of enhanced oil recovery for Bakken, Colorado School of Mines, 239 p.

Male, F., B. Rysak, and R. Dommisse, 2021, Statistical analysis of fractures from the hydraulic fracture test site 1, URTeC, Houston, Texas, USA, p. 15.

Mavor, M., 2014, Reservoir fluid properties required for low-permeability oil reservoir analysis, Geoscience Technology Workshop, Hydrocarbon Charge Considerations in Liquid-Rich Unconventional Petroleum Systems, Vancouver, BC, Canada.

Mohan, K., K. D. Scott, G. D. Monson, and P. A. Leonard, 2013, A systematic approach to understanding well performance in unconventional reservoirs: a Wolfcamp case study, URTeC, Denver, Colorado, USA, p. 10.

Park, H., 1989, Well test analysis of a multilayered reservoir with formation crossflow, Stanford University, 164 p.

Parsegov, S. G., K. Nandlal, D. S. Schechter, and R. Weijermars, 2018, Physics-driven optimization of drained rock volume for multistage fracturing: field example from the Wolfcamp formation, Midland Basin, URTeC, Houston, Texas, USA, p. 31.

Patzek, T. W., F. Male, and M. Marder, 2013, Gas production in the Barnett Shale obeys a simple scaling theory: Proceedings of the National Academy of Sciences, v. 110, p. 19731-19736.

Pendergrass, J. D., and V. J. Berry, 1962, Pressure transient performance of a multilayered reservoir with crossflow: Society of Petroleum Engineers Journal, v. 2, p. 347-354.

Phillips, O. M., 1991, Flow and reactions in permeable rocks: Cambridge, New York, Port Chester, Merlbourne, Sydney, Cambridge University Press, 285 p.

Ramiro-Ramirez, S., P. B. Flemings, A. R. Bhandari, and O. S. Jimba, 2021, Steady-State liquid permeability measurements in samples from the Bakken Formation, Williston Basin, USA, SPE Annual Technical Conference and Exhibition, Dubai, UAE, p. 15.

Raterman, K. T., H. E. Farrell, O. S. Mora, A. L. Janssen, G. A. Gomez, S. Busetti, J. McEwen, K. Friehauf, J. Rutherford, R. Reid, G. Jin, B. Roy, and M. Warren, 2018, Sampling a stimulated rock volume: an Eagle Ford example: SPE Reservoir Evaluation & Engineering, v. 21, p. 15.

Russell, D. G., and M. Prats, 1962, The Practical Aspects of Interlayer Crossflow: Journal of Petroleum Technology, p. 6.

Salem, A. C., S. J. Naruk, and J. G. Solum, 2022, Impact of natural fractures on production from an unconventional shale: The Delaware Basin Wolfcamp shale: AAPG Bulletin, v. 106, p. 20.

Appendices

APPENDIX A: PERMEABILITY RESULTS

In this appendix, I provide the permeability vs. effective stress plots and tables summarizing the permeabilities measured in each sample. I present the results by lithofacies.

A.1 Lithofacies 1: Organic-rich siliceous mudstone

See Figure A.1 and Table A.1.

A.2 Lithofacies 2: Argillaceous mudstone

See Figure A.2 and Table A.2.

A.3 Lithofacies 3a: Calcareous mudstone

See Figure A.3 and Table A.3.

A.4 Lithofacies 3b: Dolomitic calcareous mudstone

See Figure A.4 and Table A.4.

A.5 Lithofacies 4a: Calcareous sandstone

See Figure A.5 and Table A.5.

A.6 Lithofacies 4b: Dolomitic calcareous sandstone

See Figure A.6 and Table A.6.

A.7 Lithofacies 5: Matrix-supported conglomerate

See Figure A.7 and Table A.7.

A.8 Lithofacies 6: Dolomudstone

See Figure A.8 and Table A.8.

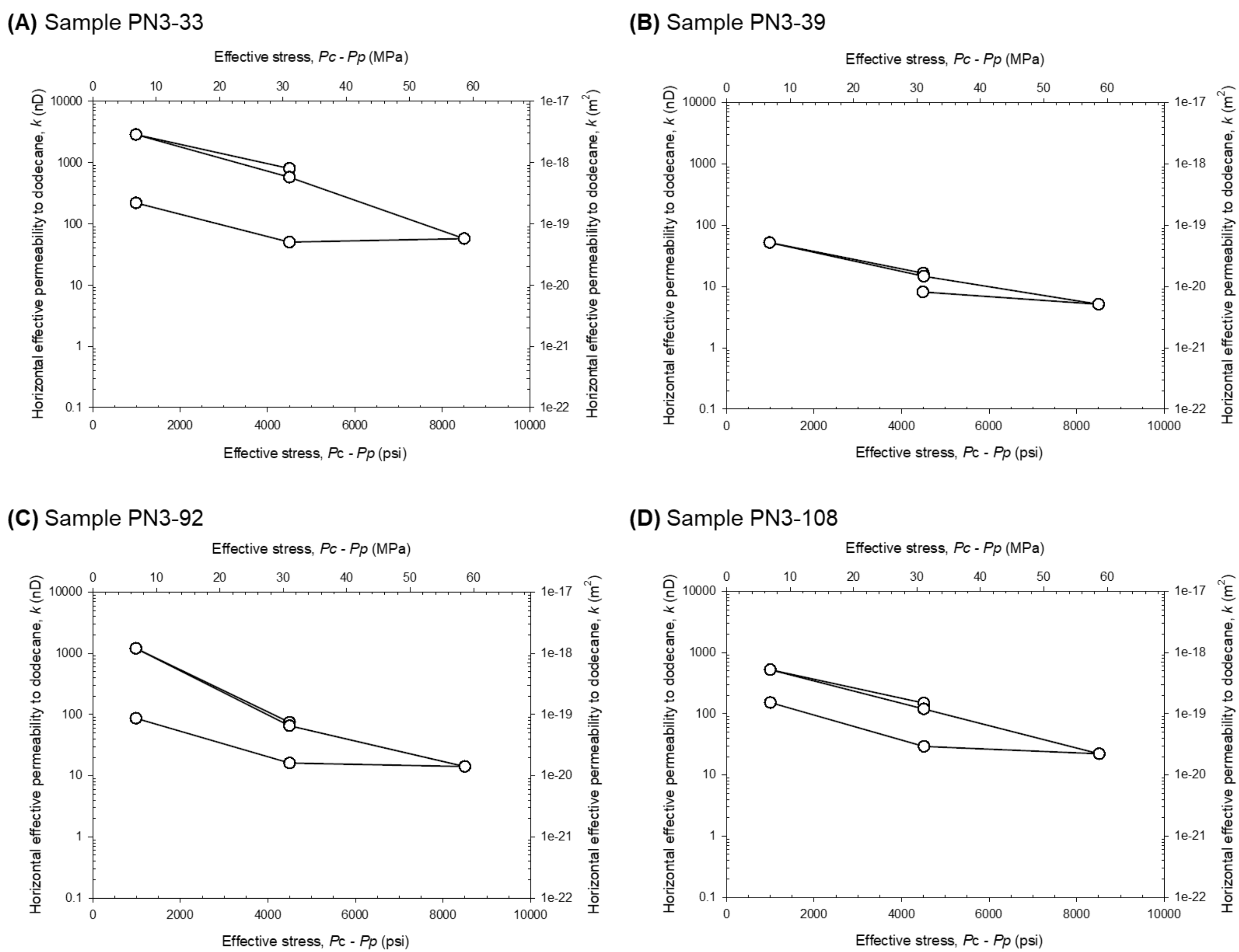
(A) Sample PN3-33
(B) Sample PN3-39
(C) Sample PN3-92
(D) Sample PN3-108
Effective stress, Pc - Pp (MPa)
Effective stress, Pc - Pp (psi)
Horizontal effective permeability to dodecane, k (nD)
Horizontal effective permeability to dodecane, k (m2)

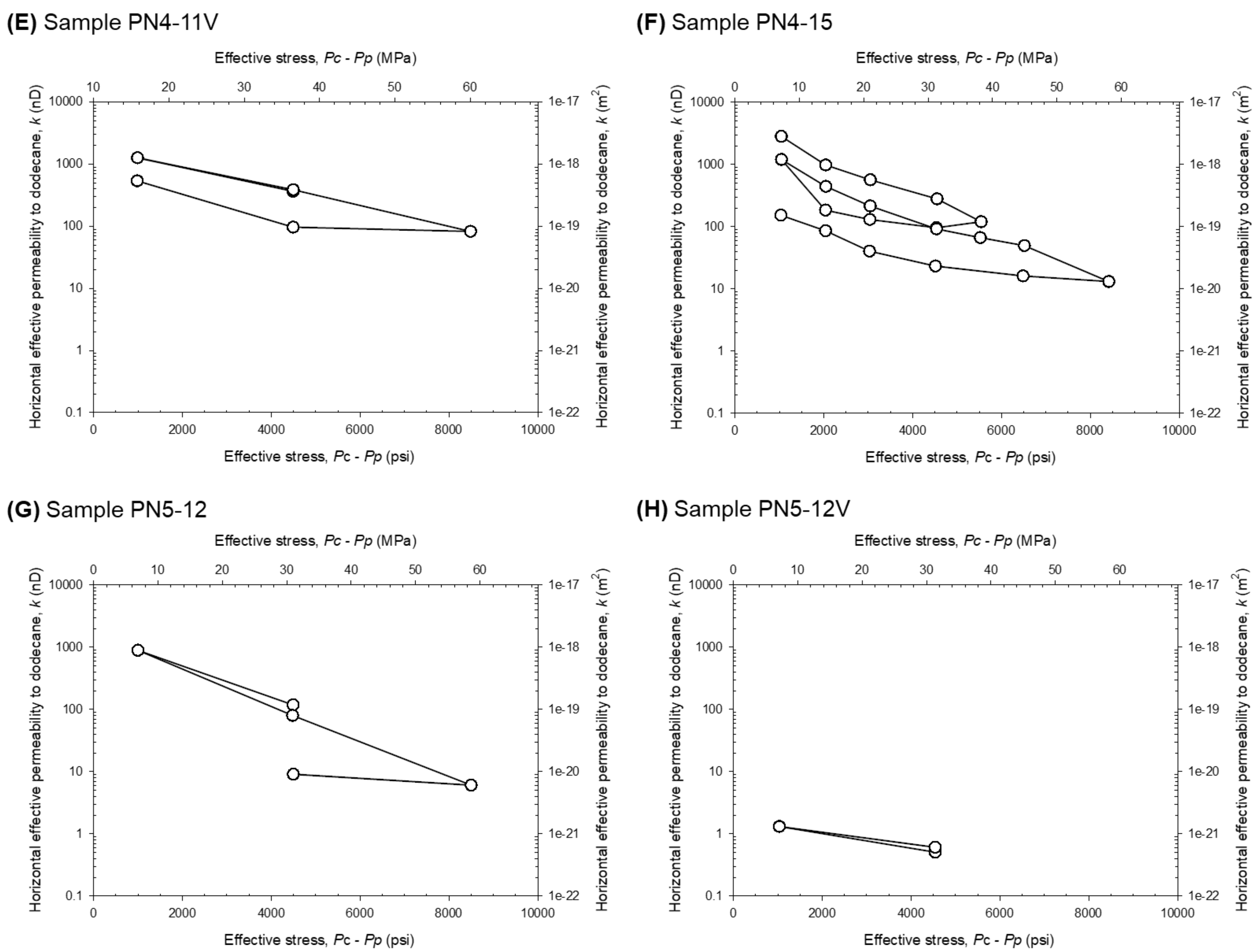
(E) Sample PN4-11V
(F) Sample PN4-15
(G) Sample PN5-12
(H) Sample PN5-12V
Effective stress, Pc - Pp (MPa)
Effective stress, Pc - Pp (psi)
Horizontal effective permeability to dodecane, k (nD)
Horizontal effective permeability to dodecane, k (m²)

(I) Sample PN5-50

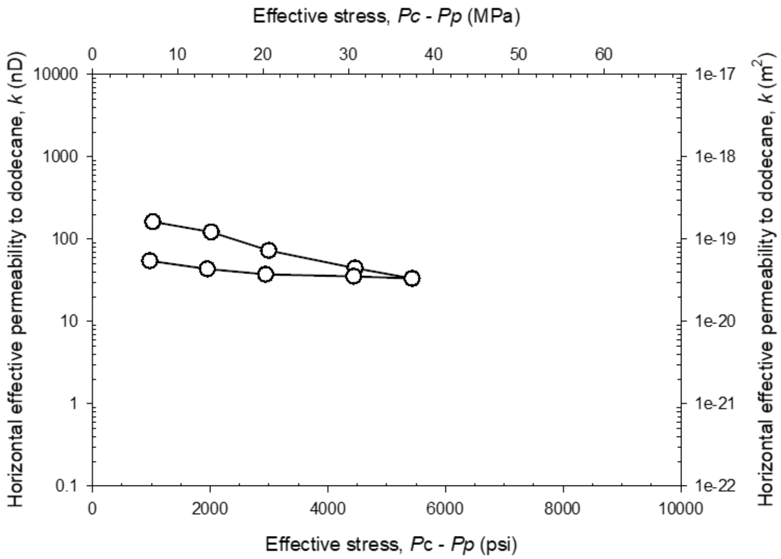

(J) Sample PN6-75

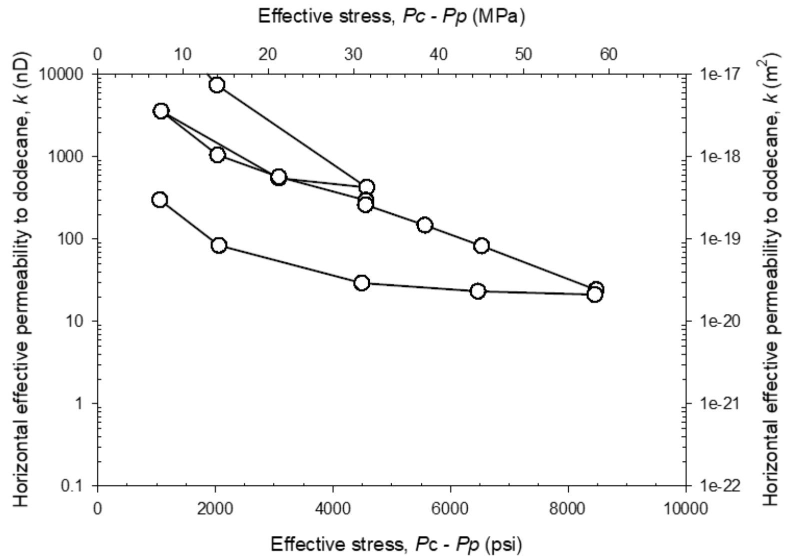

(K) Sample PN6-75V

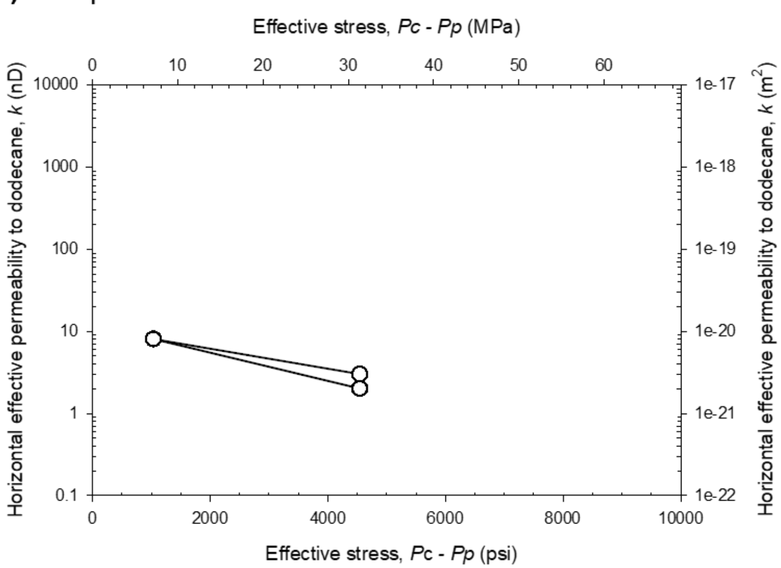

Figure A.1. Permeability vs. effective stress plots in samples from Lithofacies 1: Organic-rich siliceous mudstone.

(A) Sample PN3-33. (B) Sample PN3-39. (C) Sample PN3-92. (D) Sample PN3-108. (E) Sample PN4-11V. (F) Sample PN4-15. (G) Sample PN5-12. (H) Sample PN5-12V. (I) Sample PN5-50. (J) Sample PN6-75. (K) Sample PN6-75V.

Table A.1. Summary of stress conditions and measured permeability in Lithofacies 1: Organic-rich siliceous mudstone.

Sample	*Pc*		*Pp*		*Pc-Pp*		*k*	
	psia	MPa	psia	MPa	psi	MPa	nD	m^2
PN3-33	5500	37.92	1015	7.00	4485	30.92	794	7.8E-19
	2000	13.79	1015	7.00	985	6.79	2832	2.8E-18
	5500	37.92	1014	6.99	4486	30.93	570	5.6E-19
	9500	65.50	1029	7.10	8471	58.40	57	5.7E-20
	5500	37.92	1015	7.00	4485	30.92	50	4.9E-20
	2000	13.79	1012	6.98	988	6.81	218	2.1E-19
PN3-39	5500	37.92	1015	7.00	4485	30.93	16	1.6E-20
	2000	13.79	1016	7.00	984	6.79	52	5.1E-20
	5500	37.92	1004	6.92	4497	31.00	15	1.4E-20
	9500	65.50	1017	7.01	8483	58.49	5	5.0E-21
	5500	37.92	1022	7.05	4478	30.87	8	8.0E-21
PN3-92	5500	37.92	1015	7.00	4485	30.93	74	7.3E-20
	2000	13.79	1016	7.01	984	6.78	1196	1.2E-18
	5500	37.92	1018	7.02	4482	30.90	65	6.4E-20
	9500	65.50	1017	7.01	8483	58.49	14	1.4E-20
	5500	37.92	1013	6.98	4487	30.94	16	1.6E-20
	2000	13.79	1014	6.99	986	6.80	86	8.5E-20
PN3-108	5515	38.02	1016	7.01	4498	31.02	148	1.5E-19
	2015	13.89	1015	7.00	1000	6.89	521	5.1E-19
	5515	38.02	1016	7.00	4499	31.02	119	1.2E-19
	9515	65.60	1016	7.01	8498	58.60	22	2.2E-20
	5515	38.02	1012	6.98	4502	31.04	29	2.9E-20
	2015	13.89	1014	6.99	1001	6.90	151	1.5E-19
PN4-11V	5500	37.92	1015	7.00	4485	30.92	363	3.6E-19
	2000	13.79	1012	6.97	988	6.81	1258	1.2E-18
	5500	37.92	1014	6.99	4486	30.93	385	3.8E-19
	9500	65.50	1029	7.10	8471	58.40	82	8.1E-20
	5500	37.92	1016	7.00	4484	30.92	96	9.5E-20
	2000	13.79	1016	7.00	984	6.78	534	5.3E-19
PN4-15	2000	13.79	955	6.58	1045	7.2	2799	2.8E-18
	3000	20.68	958	6.61	2042	14.1	969	9.6E-19
	4000	27.58	958	6.61	3042	21.0	559	5.5E-19
	5500	37.92	958	6.61	4542	31.3	277	2.7E-19
	6500	44.82	968	6.67	5532	38.1	119	1.2E-19
	5500	37.92	973	6.71	4527	31.2	95.1	9.4E-20
	4000	27.58	967	6.67	3033	20.9	129	1.3E-19
	3000	20.68	962	6.63	2038	14.1	182	1.8E-19
	2000	13.79	952	6.56	1048	7.2	1190	1.2E-18

	3000	20.68	955	6.58	2045	14.1	439	4.3E-19
	4000	27.58	960	6.62	3040	21.0	213	2.1E-19
	5500	37.92	970	6.69	4530	31.2	91	9.0E-20
	6500	44.82	985	6.79	5515	38.0	66	6.5E-20
	7500	51.71	995	6.86	6505	44.9	49	4.8E-20
	9500	65.50	1100	7.58	8400	57.9	13	1.3E-20
	7500	51.71	1025	7.07	6475	44.6	16	1.6E-20
	5500	37.92	995	6.86	4505	31.1	23	2.3E-20
	4000	27.58	975	6.72	3025	20.9	40	3.9E-20
	3000	20.68	963	6.64	2037	14.0	85	8.4E-20
	2000	13.79	965	6.65	1035	7.1	151	1.5E-19
	5500	37.92	1017	7.01	4482	30.91	117	1.2E-19
	2000	13.79	1000	6.90	999	6.89	882	8.7E-19
	5500	37.92	1026	7.08	4474	30.84	79	7.8E-20
	9500	65.50	1016	7.00	8484	58.50	6	5.9E-21
	5500	37.92	1011	6.97	4489	30.95	9	9.2E-21
	5500	37.92	965	6.65	4535	31.27	0.5	5.0E-22
	5500	37.92	965	6.65	4535	31.27	0.5	5.3E-22
	2000	13.79	965	6.65	1035	7.14	1.3	1.3E-21
	2000	13.79	965	6.65	1035	7.14	1.3	1.3E-21
PN5-12	5500	37.92	965	6.65	4535	31.27	0.6	6.3E-22
	2000	13.79	975	6.72	1025	7.07	161	1.6E-19
	3000	20.68	985	6.79	2015	13.89	121	1.2E-19
	4000	27.58	1008	6.95	2992	20.63	72	7.1E-20
	5500	37.92	1045	7.21	4455	30.72	44	4.3E-20
	6500	44.82	1075	7.41	5425	37.40	33	3.3E-20
	5500	37.92	1067	7.36	4433	30.56	35	3.5E-20
	4000	27.58	1060	7.31	2940	20.27	37	3.7E-20
	3000	20.68	1050	7.24	1950	13.44	43	4.2E-20
	2000	13.79	1026	7.07	974	6.72	54	5.3E-20
	2000	13.79	924	6.37	1076	7.42	44316	4.4E-17
	3000	20.68	974	6.71	2026	13.97	7350	7.3E-18
	5500	37.92	932	6.42	4568	31.50	420	4.1E-19
	4000	27.58	926	6.38	3074	21.20	545	5.4E-19
	2000	13.79	920	6.34	1080	7.44	3555	3.5E-18
	3000	20.68	965	6.66	2035	14.03	1041	1.0E-18
PN6-75	4000	27.58	925	6.38	3075	21.20	566	5.6E-19
	5500	37.92	953	6.57	4547	31.35	258	2.5E-19
	6500	44.82	945	6.52	5555	38.30	146	1.4E-19
	7500	51.71	981	6.76	6519	44.95	82	8.1E-20
	9500	65.50	1062	7.32	8438	58.18	21	2.0E-20
	7500	51.71	1046	7.21	6454	44.50	23	2.3E-20
	5500	37.92	1014	6.99	4486	30.93	29	2.9E-20

	3000	20.68	940	6.48	2060	14.21	83	8.2E-20
	2000	13.79	945	6.52	1055	7.27	297	2.9E-19
PN6-75V	5500	37.92	965	6.65	4535	31.27	3	3.0E-21
	5500	37.92	965	6.65	4535	31.27	3	2.6E-21
	2000	13.79	965	6.65	1035	7.14	8	7.8E-21
	2000	13.79	965	6.65	1035	7.14	8	8.1E-21
	5500	37.92	965	6.65	4535	31.27	2	2.5E-21

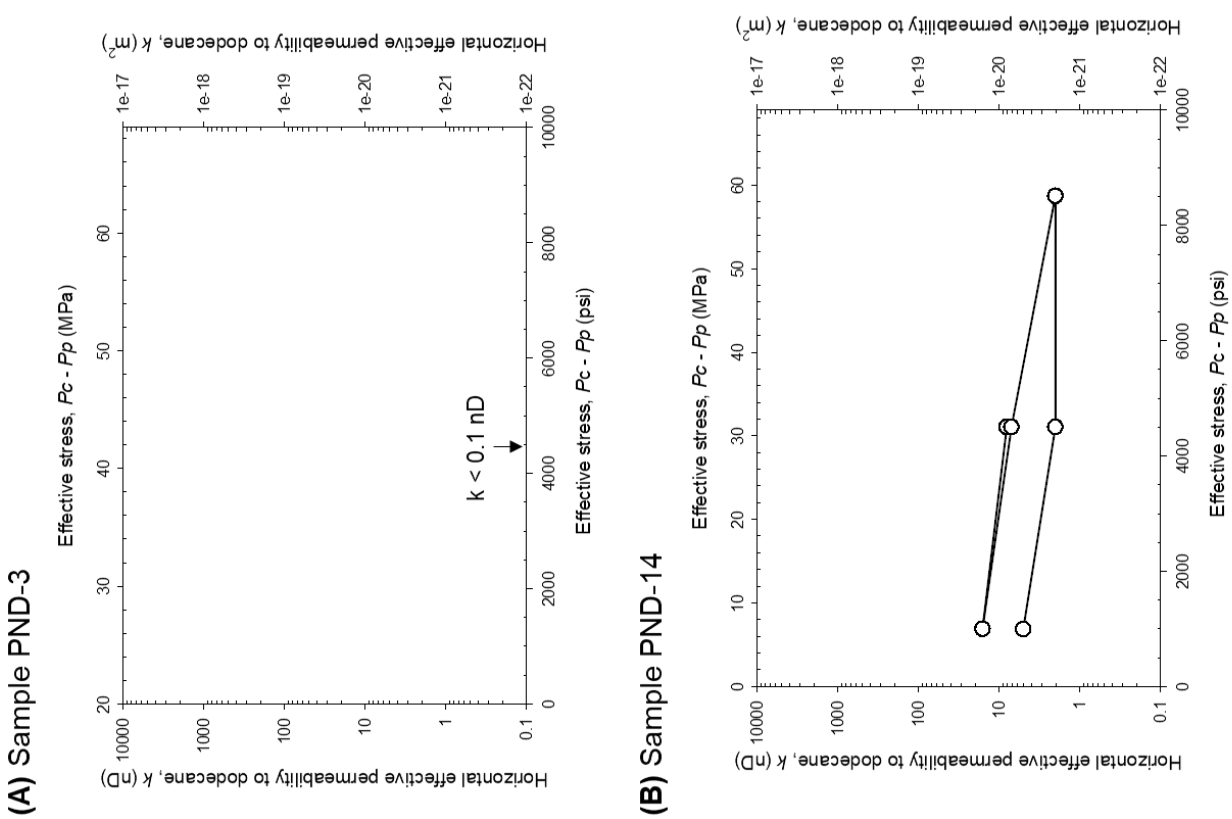

Figure A.2. Permeability vs. effective stress plots in samples from Lithofacies 2: Argillaceous mudstone.

(A) Sample PND-3. (B) Sample PND-14.

Table A.2. Summary of stress conditions and measured permeability in Lithofacies 2: Argillaceous mudstone.

Sample	***Pc***		***Pp***		***Pc-Pp***		***k***	
	psia	**MPa**	**psia**	**MPa**	**psi**	**MPa**	**nD**	**m^2**
PND-3	5515	38.02	1015	7.00	4500	31.03	0.03	3.4E-23
PND-14	5515	38.02	1015	7.00	4500	31.03	8	7.4E-21
	2015	13.89	1010	6.97	1004	6.92	16	1.5E-20
	5515	38.02	1015	7.00	4500	31.03	7	6.9E-21
	9515	65.60	1015	7.00	8500	58.60	2	1.8E-21
	5515	38.02	1015	7.00	4500	31.03	2	1.7E-21
	2015	13.89	1015	7.00	1000	6.89	5	4.7E-21

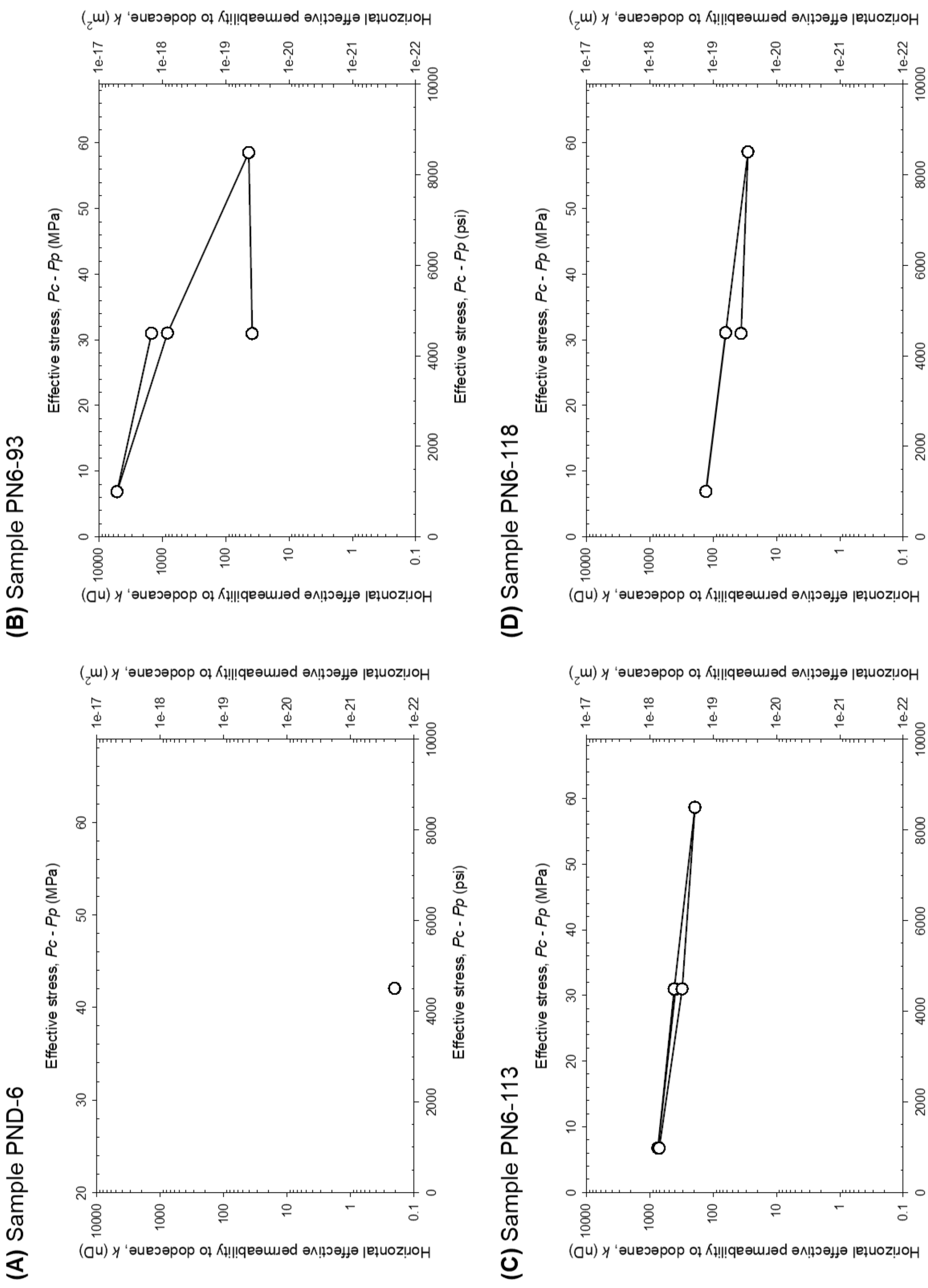

(A) Sample PND-6
(B) Sample PN6-93
(C) Sample PN6-113
(D) Sample PN6-118
Effective stress, Pc - Pp (MPa)
Effective stress, Pc - Pp (psi)
Horizontal effective permeability to dodecane, k (nD)
Horizontal effective permeability to dodecane, k (m2)

Figure A.3. Permeability vs. effective stress plots in samples from Lithofacies 3a: Calcareous mudstone.

(A) Sample PND-6. (B) Sample PN6-93. (C) Sample PN6-113. (D) Sample PN6-118.

Table A.3. Summary of stress conditions and measured permeability in Lithofacies 3a: Calcareous mudstone.

Sample	***Pc***		***Pp***		***Pc-Pp***		***k***	
	psia	**MPa**	**psia**	**MPa**	**psi**	**MPa**	**nD**	**m^2**
PND-6	5515	38.02	1015	7.00	4500	31.03	0.2	2.4E-22
PN6-93	5500	6.95	1008	0.01	4492	30.97	1471	1.5E-18
	2000	6.90	1001	0.04	998	6.88	5176	5.1E-18
	5500	6.92	1004	0.01	4496	31.00	826	8.1E-19
	9500	7.06	1023	0.00	8477	58.44	43	4.2E-20
	5500	7.01	1016	0.00	4484	30.91	38	3.7E-20
PN6-113	5500	37.92	1016	7.01	4484	30.91	388	3.8E-19
	2000	13.79	1014	6.99	986	6.80	740	7.3E-19
	5500	37.92	1015	7.00	4485	30.92	409	4.0E-19
	9500	65.50	1015	7.00	8484	58.50	193	1.9E-19
	5500	37.92	1013	6.99	4487	30.93	306	3.0E-19
	2000	13.79	1015	7.00	984	6.79	706	7.0E-19
PN6-118	5500	37.92	998	6.88	4502	31.04	63	6.2E-20
	2000	13.79	997	6.88	1003	6.91	129	1.3E-19
	5500	37.92	997	6.87	4503	31.05	63	6.2E-20
	9500	65.50	1009	6.95	8491	58.55	28	2.8E-20
	5500	37.92	1015	7.00	4485	30.92	36	3.5E-20

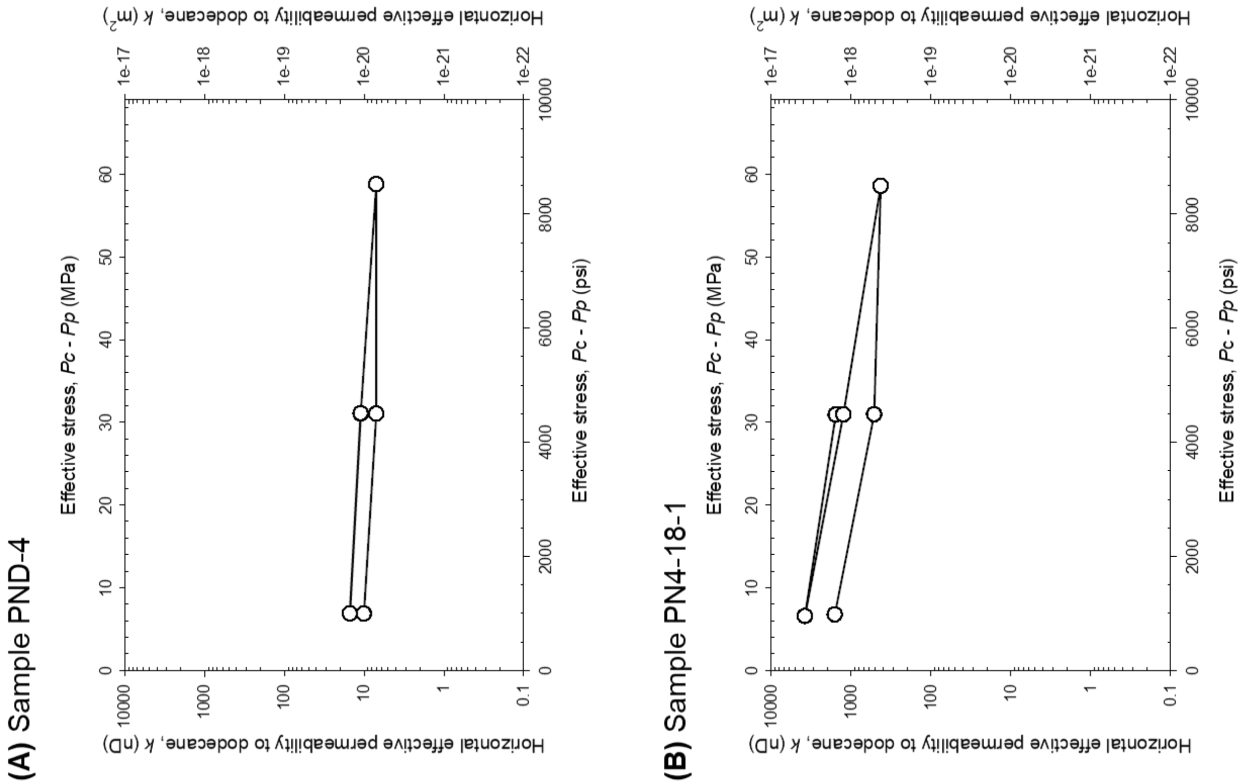

Figure A.4. Permeability vs. effective stress plots in samples from Lithofacies 3b: Dolomitic calcareous mudstone.

(A) Sample PND-4. (B) Sample PN4-18-1.

Table A.4. Summary of stress conditions and measured permeability in Lithofacies 3b: Dolomitic calcareous mudstone.

Sample	***Pc***		***Pp***		***Pc-Pp***		***k***	
	psia	**MPa**	**psia**	**MPa**	**psi**	**MPa**	**nD**	**m^2**
PND-4	5515	38.02	1017	7.01	4498	31.01	11	1.1E-20
	2015	13.89	1012	6.98	1003	6.91	15	1.5E-20
	5515	38.02	1012	6.97	4503	31.05	11	1.0E-20
	9515	65.60	1006	6.94	8508	58.66	7	6.6E-21
	5515	38.02	1019	7.02	4496	31.00	7	6.9E-21
	2015	13.89	1015	7.00	1000	6.89	10	9.8E-21
PN4-18-1	5500	37.92	1022	7.04	4478	30.88	1543	1.5E-18
	2000	13.79	1042	7.19	957	6.60	3747	3.7E-18
	5500	37.92	1017	7.01	4482	30.91	1238	1.2E-18
	9500	65.50	1019	7.03	8480	58.47	422	4.2E-19
	5500	37.92	1016	7.00	4484	30.92	508	5.0E-19
	2000	13.79	1015	7.00	985	6.79	1582	1.6E-18

(A) Sample PN2-2

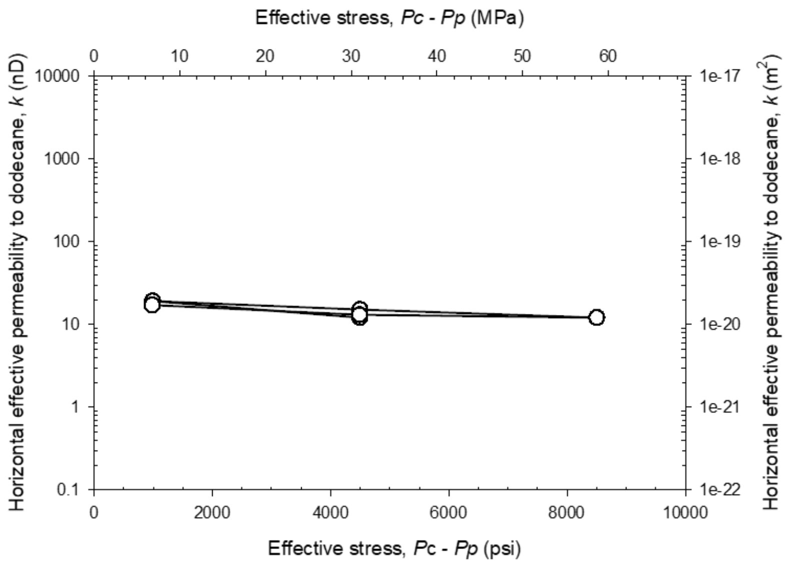

(B) Sample PN2-51

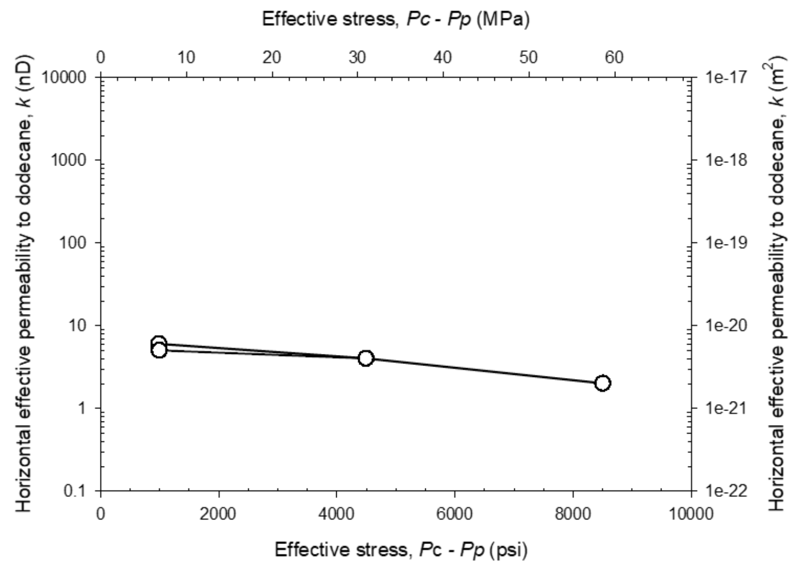

(C) Sample PN6-69

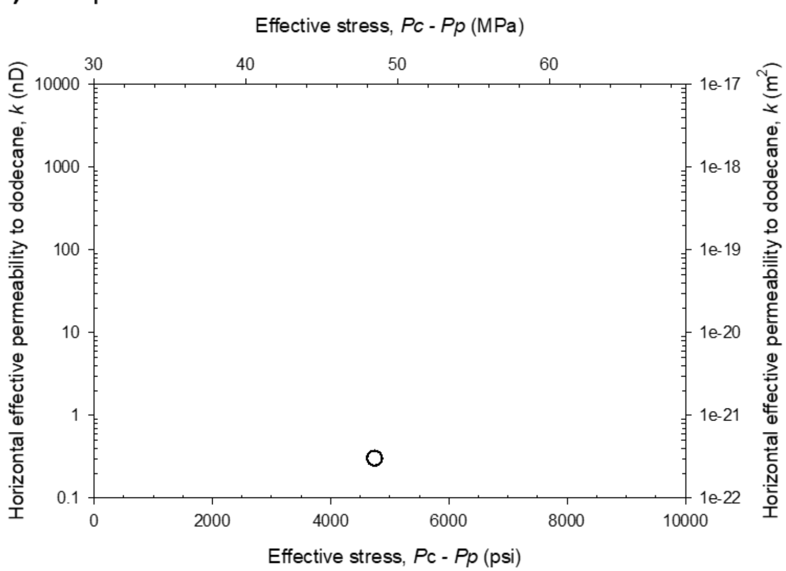

(D) Sample PN6-78

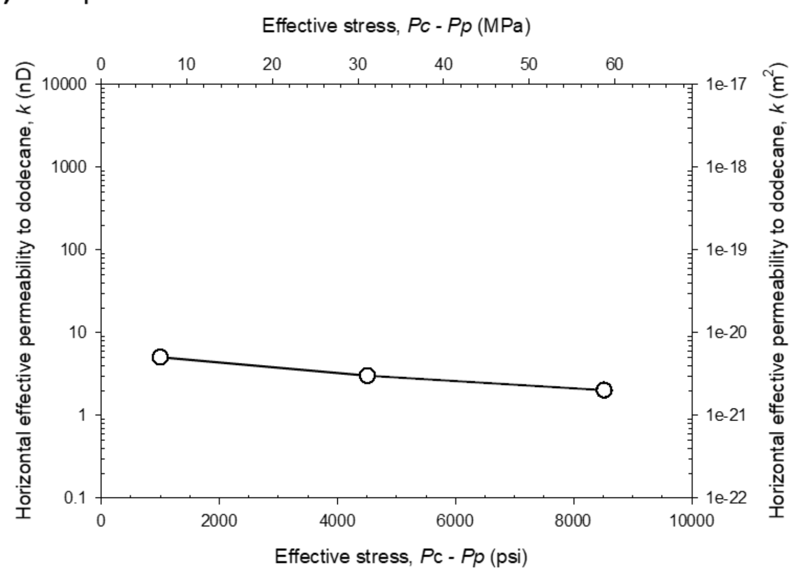

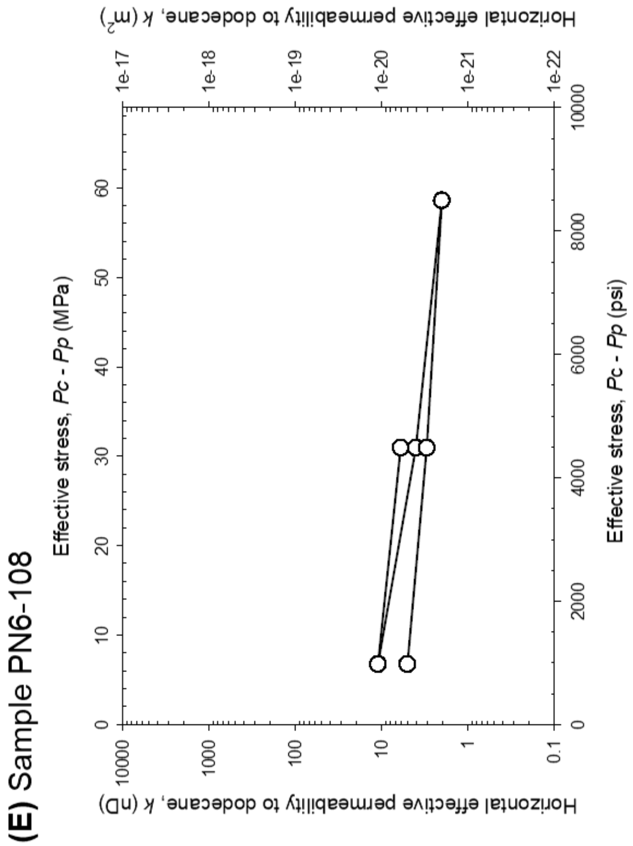

Figure A.5. Permeability vs. effective stress plots in samples from Lithofacies 4a: Calcareous sandstone.

(A) Sample PN2-2. (B) Sample PN2-51. (C) Sample PN6-69. (D) Sample PN6-78. (E) Sample PN6-108.

Table A.5. Summary of stress conditions and measured permeability in Lithofacies 4a: Calcareous sandstone.

Sample	***Pc***		***Pp***		***Pc-Pp***		***k***	
	psia	**MPa**	**psia**	**MPa**	**psi**	**MPa**	**nD**	**m^2**
PN2-2	5500	37.92	1015	7.00	4485	30.92	12	1.2E-20
	2000	13.79	1011	6.97	988	6.82	19	1.9E-20
	5500	37.92	1013	6.98	4487	30.94	15	1.5E-20
	9500	65.50	1016	7.00	8484	58.49	12	1.2E-20
	5500	37.92	1019	7.02	4481	30.90	13	1.3E-20
	2000	13.79	1016	7.01	984	6.78	17	1.7E-20
PN2-51	5500	37.92	1015	7.00	4485	30.92	4	4.2E-21
	2000	13.79	1014	6.99	985	6.79	6	6.3E-21
	5500	37.92	1014	6.99	4486	30.93	4	4.2E-21
	9500	65.50	1015	7.00	8485	58.50	2	2.0E-21
	5500	37.92	1018	7.02	4482	30.90	4	3.9E-21
	2000	13.79	1009	6.96	991	6.83	5	4.9E-21
PN6-69	5499	37.92	765	5.27	4735	32.65	0.3	3.0E-22
PN6-78	5515	38.02	1015	7.00	4500	31.03	3	3.0E-21
	2015	13.89	1015	7.00	1000	6.89	5	4.8E-21
	5515	38.02	1015	7.00	4500	31.03	3	2.7E-21
	9515	65.60	1015	7.00	8500	58.60	2	1.6E-21
PN6-108	5500	37.92	1015	7.00	4485	30.92	6	5.8E-21
	2000	13.79	1015	7.00	985	6.79	11	1.0E-20
	5500	37.92	1017	7.01	4483	30.91	4	3.9E-21
	9500	65.50	1015	7.00	8485	58.50	2	1.7E-21
	5500	37.92	1017	7.01	4483	30.91	3	2.7E-21
	2000	13.79	1014	6.99	985	6.79	5	5.4E-21

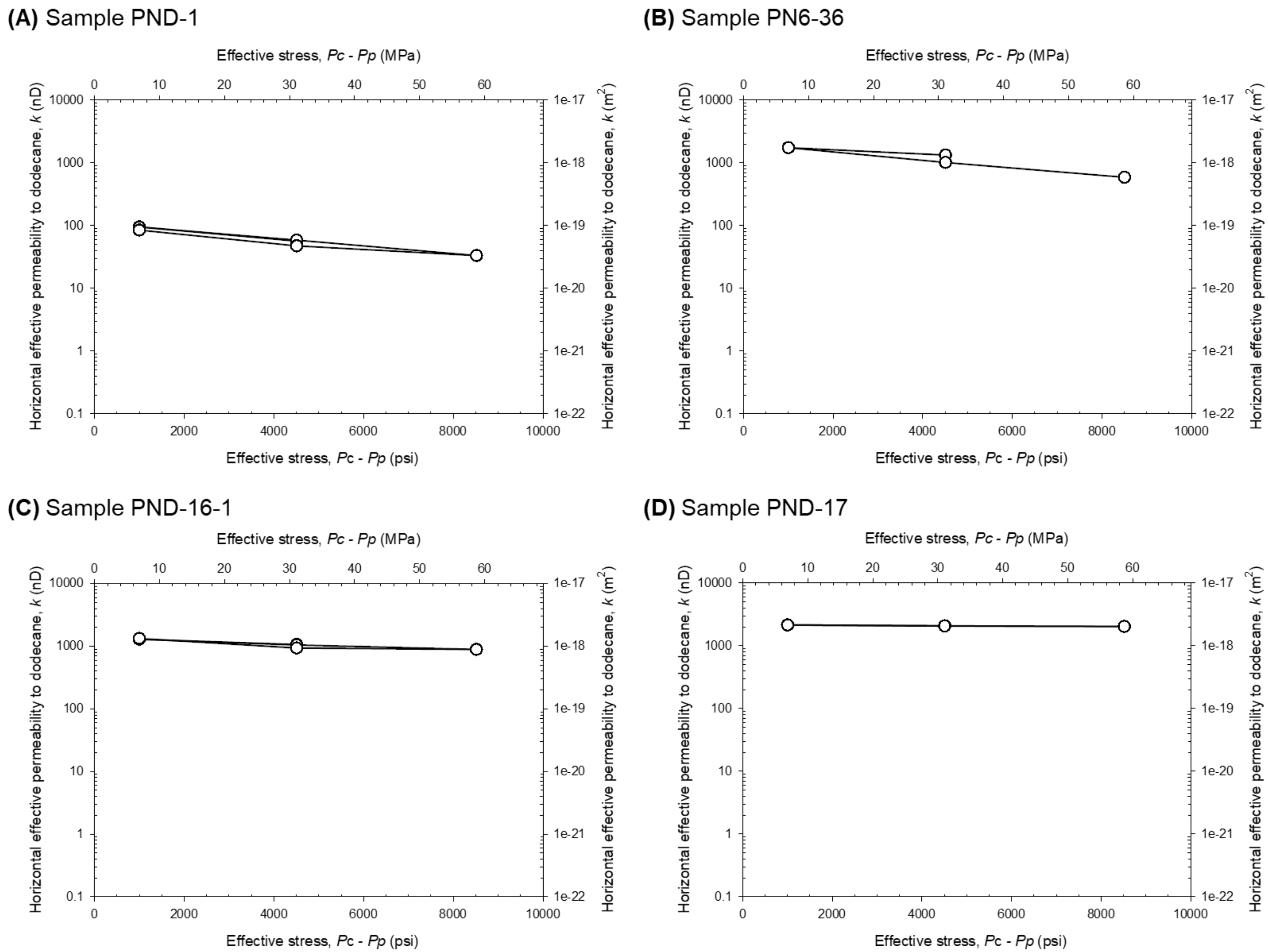
(A) Sample PND-1
(B) Sample PN6-36
(C) Sample PND-16-1
(D) Sample PND-17
Effective stress, Pc - Pp (MPa)
0 10 20 30 40 50 60
Effective stress, Pc - Pp (psi)
0 2000 4000 6000 8000 10000
Horizontal effective permeability to dodecane, k (nD)
10000 1000 100 10 1 0.1
Horizontal effective permeability to dodecane, k (m2)
1e-17 1e-18 1e-19 1e-20 1e-21 1e-22

Figure A.6. Permeability vs. effective stress plots in samples from Lithofacies 4b: Dolomitic calcareous sandstone.

(A) Sample PND-1. (B) Sample PN6-36. (C) Sample PND16-1. (D) Sample PND-17.

Table A.6. Summary of stress conditions and measured permeability in Lithofacies 4b: Dolomitic calcareous sandstone.

Sample	*Pc*		*Pp*		*Pc-Pp*		*k*	
	psia	**MPa**	**psia**	**MPa**	**psi**	**MPa**	**nD**	**m²**
PND-1	5515	38.02	1015	7.00	4500	31.02	56	5.5E-20
	2015	13.89	1014	6.99	1000	6.90	94	9.3E-20
	5515	38.02	1014	6.99	4500	31.03	58	5.7E-20
	9515	65.60	1014	6.99	8501	58.61	33	3.2E-20
	5515	38.02	1014	6.99	4501	31.03	47	4.6E-20
	2015	13.89	1015	7.00	1000	6.89	84	8.3E-20
PN6-36	5500	37.92	1000	6.90	4500	31.02	1318	1.3E-18
	2000	13.79	999	6.89	1001	6.90	1726	1.7E-18
	5500	37.92	1001	6.90	4499	31.02	1003	9.9E-19
	9500	65.50	1014	6.99	8486	58.51	583	5.8E-19
PND-16-1	5515	38.02	1016	7.00	4499	31.02	1055	1.0E-18
	2015	13.89	1015	7.00	999	6.89	1281	1.3E-18
	5515	38.02	1016	7.00	4499	31.02	1039	1.0E-18
	9515	65.60	1016	7.01	8498	58.59	880	8.7E-19
	5515	38.02	1016	7.00	4499	31.02	928	9.2E-19
	2015	13.89	1015	7.00	1000	6.89	1320	1.3E-18
PND-17	5515	38.02	1013	6.98	4502	31.04	2054	2.0E-18
	2015	13.89	1015	7.00	999	6.89	2121	2.1E-18
	5515	38.02	1015	7.00	4499	31.02	2050	2.0E-18
	9515	65.60	1015	7.00	8500	58.60	2004	2.0E-18
	5515	38.02	1015	7.00	4500	31.02	2039	2.0E-18
	2015	13.89	1014	7.00	1001	6.89	2116	2.1E-18

(A) Sample PN2-30

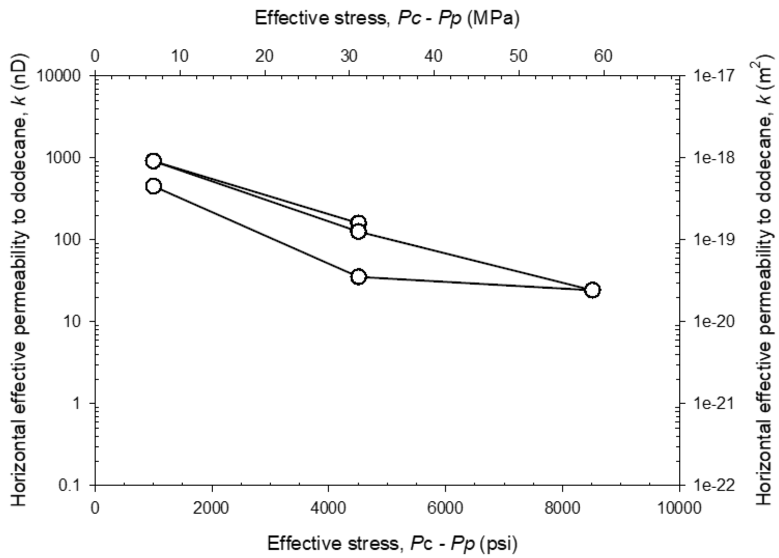

(B) Sample PN3-54

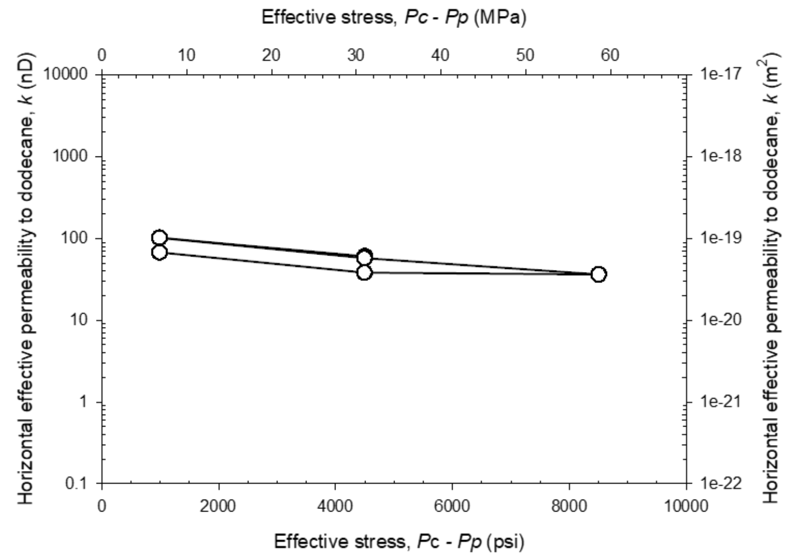

(C) Sample PN3-90

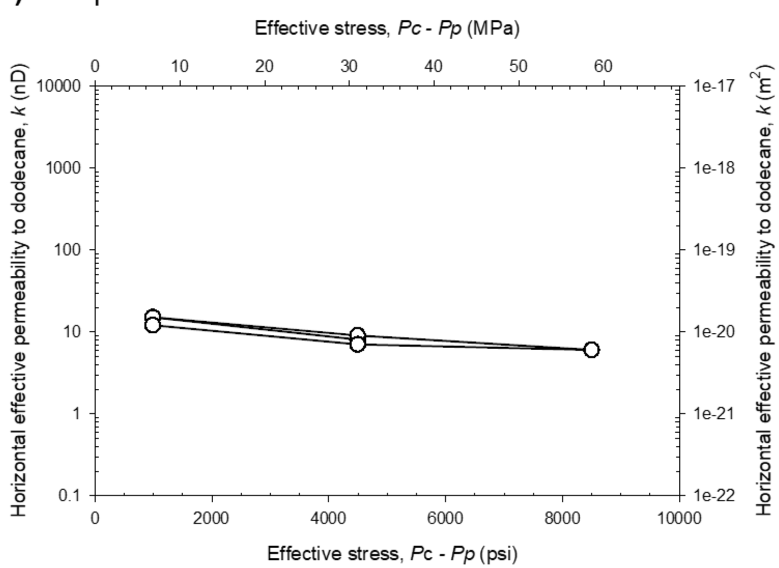

Figure A.7. Permeability vs. effective stress plots in samples from Lithofacies 5: Matrix-supported conglomerate.

(A) Sample PN2-30. (B) Sample PN6-36. (C) Sample PND3-54. (D) Sample PN3-90.

Table A.7. Summary of stress conditions and measured permeability in Lithofacies 5: Matrix-supported conglomerate.

Sample	***Pc***		***Pp***		***Pc-Pp***		***k***	
	psia	**MPa**	**psia**	**MPa**	**psi**	**MPa**	**nD**	**m^2**
PN2-30	5515	38.02	1016	7.00	4499	31.02	158	1.6E-19
	2015	13.89	1015	7.00	1000	6.89	904	8.9E-19
	5515	38.02	1015	7.00	4499	31.02	125	1.2E-19
	9515	65.60	1018	7.02	8496	58.58	24	2.4E-20
	5515	38.02	1013	6.99	4501	31.04	35	3.5E-20
	2015	13.89	1015	7.00	999	6.89	447	4.4E-19
PN3-54	5500	37.92	1009	6.96	4491	30.96	60	5.9E-20
	2000	13.79	1015	7.00	984	6.79	101	1.0E-19
	5500	37.92	1016	7.00	4484	30.92	57	5.6E-20
	9500	65.50	1015	7.00	8485	58.50	36	3.6E-20
	5500	37.92	1016	7.01	4484	30.92	38	3.8E-20
	2000	13.79	1013	6.99	987	6.80	67	6.6E-20
PN3-90	5500	37.92	1016	7.01	4484	30.91	8	8.4E-21
	2000	13.79	1013	6.99	986	6.80	15	1.5E-20
	5500	37.92	1016	7.01	4484	30.91	9	8.9E-21
	9500	65.50	1019	7.02	8481	58.47	6	5.9E-21
	5500	37.92	1015	7.00	4485	30.92	7	6.9E-21
	2000	13.79	1013	7.00	986	6.79	12	1.2E-20

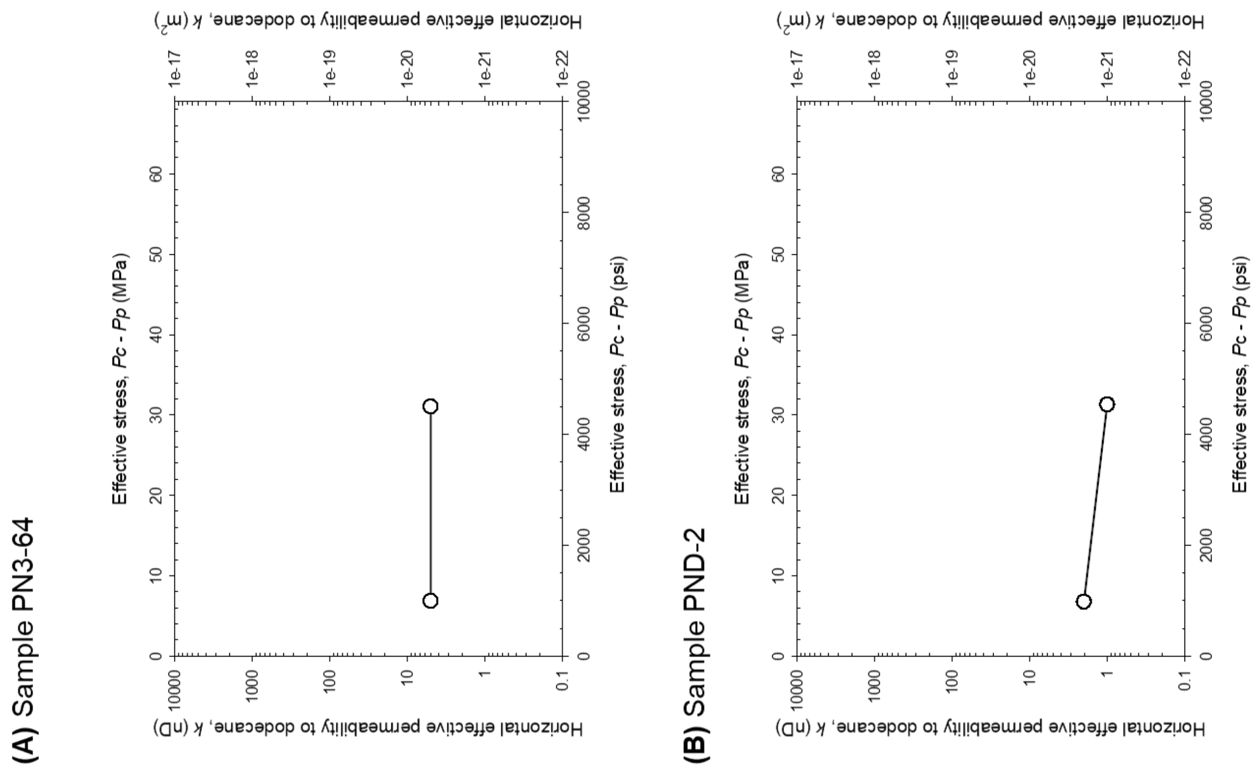

Figure A.8. Permeability vs. effective stress plots in samples from Lithofacies 6: Dolomudstone. (A) Sample PN3-64. (B) Sample PND-2.

Table A.8. Summary of stress conditions and measured permeability in Lithofacies 6: Dolomudstone.

Sample	*Pc*		*Pp*		*Pc-Pp*		*k*	
	psia	**MPa**	**psia**	**MPa**	**psi**	**MPa**	**nD**	**m^2**
PN3-64	5500	37.92	965	6.65	4535	31.27	1	8.9E-22
	2000	13.79	1015	7.00	984	6.79	2	1.5E-21
PND-2	5515	38.02	1016	7.00	4499	31.02	5	4.7E-21
	2015	13.89	1015	7.00	1000	6.89	5	5.1E-21

APPENDIX B: MEAN EFFECTIVE STRESS IN WOLFCAMP AT DELAWARE BASIN

The in situ mean effective stress (σ'_m) in Wolfcamp samples was estimated with Eq. B.1:

$$\sigma'_m = \frac{(\sigma_v - P_p) + 2(\sigma_h - P_p)}{3}, \qquad \text{Eq. B.1}$$

where σ_v is the overburden stress, and σ_{hmin} is the least principal stress, and P_p is the pore pressure. Eq. B.1 assumes that one of the principal stresses is vertical and that the two horizontal stresses are equal. The average overburden gradient is 1.075 psi/ft and was determined from integration of density log data. The least principal stress was calculated from regional studies of the fracture gradient and it lies at an average gradient of 0.86 psi/ft and 0.95 psi/ft, depending on the depth of the samples. The average overpressure gradient ranges from 0.79 psi/ft to 0.90 psi/ft. The mean stresses are 10526 psi and 11743 psi for the shallowest sample (PN2-2, Table 3.A1) and deepest sample (PN6-118, Table 3.A1). This is an estimate of the present-day effective stress but the sample may have been loaded to much higher stresses in the past because significant erosion has occurred in the Permian Basin (Sinclair, 2007).

Table B.1. Upper and lower bounds of mean effective stress (σ'_m) in the studied upper Wolfcamp cored interval.

σ_v is the overburden stress, P_p is the pore pressure, σ_{hmin} is the least principal stress, σ'_m is the mean effective stress calculated using Eq. B.1.

Sample	Depth (ft)	σ_v (psi)	P_p (psi)	σ_{hmin} (psi)	σ_m (psi)	σ'_m (psi)
(upper bound) PN2-22	11274.2	12120	8862	9730	10526	1665
PN3-108	11386.6	12241	9371	10191	10874	1503
PND-17	11819.5	12706	10626	11181	11689	1064
(lower bound) PN6-118	11841.5	12730	10705	11249	11743	1038

References

Sinclair, T. D., 2007, The generation and continued existence of overpressure in the Delaware Basin, Texas: Doctoral thesis, Durham University, 314 p.

APPENDIX C: CORE PLUG EXTRACTION PROTOCOL AND PREPARATION FOR EXPERIMENTAL ANALYSES

C.1 Core sampling selection strategy

1. Define lithofacies in the core.

2. With the aid of core photographs, evaluate and document the quality of the core at the inch-scale. Use a traffic light system to discriminate between 'high' (green), 'medium' (orange), and 'low' (red) core quality:

   a. High quality (green): the core is intact (no fractures, no major heterogeneities). Extraction of core plugs is feasible.

   b. Medium quality (orange): the core shows no fractures, but it has major heterogeneities (e.g., burrowing). Extraction of core plugs may or may not be feasible. Further visual inspection of the actual core is necessary to decide.

   c. Low quality (red): the core is fractured. Extraction of core plugs is not feasible.

3. Select 'high quality' intervals (green) sampling locations for each lithofacies. If no 'high quality' intervals exist for certain(s) lithofacies, select 'medium quality' (orange) intervals as potential sampling locations.

4. For each lithofacies, group the sampling locations into three tiers:

   a. Tier 1 includes the first preference for sampling locations.

   b. Tier 2 includes alternative sampling locations in case coring from Tier 1 locations fails.

   c. Tier 3 includes alternative sampling locations in case coring from Tier 2 locations fails.

C.2 Core plug extraction protocol and preservation

1. Drill the core plugs using humidified nitrogen gas as drill bit cooling fluid to prevent fluid interaction with the rock components (e.g., clay swelling if cooling fluid is water).
2. Carefully remove the core plug from the drill bit and mark the top and bottom of the core plug, and the direction of the bedding plane.
3. Take a picture of the core plug and document key features such as quality of the core plug, presence of fractures and heterogeneities, etc.
4. Tightly wrap the core plug immediately after extraction in plastic film, and then in aluminum foil.
5. Place the wrapped core plug in a plastic container, and tightly seal with tape the joint between the container and its lid.
6. Store the samples in a temperature-controlled environment to minimize fluid loss.

C.3 Sample quality assessment after extraction

C.3.1 Selection of core plugs and micro-CT acquisition

1. Review the observations documented during the core plug extraction. For each lithofacies, select a number (e.g., three) of non-fractured core plugs. Unwrapped them, and carefully evaluate their integrity. Document the presence of microfractures if visible to the naked eye.
2. Conduct micro-CT scans in the core plugs that have no visible microfractures in an NSI scanner at The University of Texas High-Resolution X-ray Computed Tomography Facility (UTCT). In this project, the following parameters were typically used:

- Voxel size = 24.7 μm.
- Fein Focus High Power source.

- 180 kV.
- 160.0 mA.
- aluminum filter.
- Perkin Elmer detector.
- 0.25 pF gain.
- 1-2 fps.
- 1x1 binning.
- no flip.
- source to object 200 mm.
- source to detector 1316 mm.
- helical continuous CT scan.
- no frames averaged.
- 0 skip frames.
- 3600-11000 projections.
- 5-6 gain calibrations.
- 5 mm calibration phantom.
- beam-hardening correction = 0.2.
- Post-reconstruction ring correction applied using parameters:
    - oversample = 2.
    - radial bin width = 21.
    - sectors = 32.
    - minimum arc length = 1.
    - angular bin width = 9.

- angular screening factor = 4.

C.3.2 Visualization of micro-CT scans acquired in core plugs

1. Download ImageJ (https://imagej.nih.gov/ij/).
2. Open ImageJ and select: File → Import → Image sequence.
3. Select folder where the CT scans are stored → select the first image file of the sequence to be imported → click ‘Ok’.
4. In ‘Sequence Options’ window, leave default settings and click ‘Ok’. The progress bar in the bottom right corner indicates the progress of the compilation, and the bottom left corner indicates the number of images that have been processed.
5. Once import is completed, go to: Image → Adjust → Brightness/Contrast. Adjust brightness and contrast by scrolling to the left/right the four bars (i.e., Minimum, Maximum, Brightness, Contrast).
6. Once brightness/contrast are adjusted to desired levels, click ‘Apply’, and select ‘Yes’ when asked if you want to ‘apply to all X slices in the stack. Once completed, close the window.
7. If desired, apply rotation to the compiled image sequence so that the bedding in the sample is parallel to the horizontal direction. Go to: Image → Transform → Rotate.
8. Type in the Angle (degrees) that you want to apply to the rotation and click ‘Ok. You can repeat this process as many times as desired to meet the desired orientation of the image sequence.
9. Obtain orthogonal views of the compiled image sequence to visualize the geometry and extent of the fractures (if any) across the sample. Go to: Image → Stacks → Orthogonal Views.

10. Three images will be shown on the screen, each of them representing a different cross-sectional view. To remove the yellow overlay, go to: Image → Overlay → Hide Overlay.

11. To save an image of the orthogonal view, first you need to create a copy of it. Click on the desired orthogonal view, then go to the main ImageJ window, and go to: Image → Duplicate → Ok.

12. To save the image, go to: File → Save as → (select the desired format for the image file).

13. To save the image sequence as a video, select the window containing the image sequence, and then select the main ImageJ window and go to: File → Save As → AVI → Ok → (select folder where AVI file will be saved) → Save.

    Important: make sure you do not close ImageJ until the Image sequence is completely saved as an AVI file. The progress bar at the bottom right corner will indicate when the process is complete.

C.4 Sample preparation for porosity and permeability measurements

C.4.1 Tools

a. Sandpapers (Grit: P100, P320, P800).

b. Caliper.

c. Scale (0.01 g resolution).

C.4.2 Sample preparation procedure

1. Measure the length of the core plug.

2. Correlate the core plug length with the length of the video containing the compiled CT image sequence.

3. Mark in the core plug the interval length that exhibits the best quality for permeability measurements (e.g., interval with no microfractures). The length of the prepared core plug

is typically between 14-18 mm.

Note: it is recommended to prioritize the innermost part of the core plug (with respect to the main core) to minimize the risk of having drilling fluid invasion into the sample.

4. Secure core plug in the arm of the dry cut saw.
5. Activate the saw, and then lower the arm slowly until the saw touches the core plug. Control the pressure applied on the core plug manually until the saw has cut ~5 mm.
6. Leave the saw running without applying any pressure manually. The pressure applied on the core plug by the arm's own weight is sufficient to complete the cut.
7. Once cut, unload the core plug. Measure its length at different points and evaluate what parts of the core are thicker than others.
8. Using sandpaper, make both sides of the core plug parallel. The length difference between multiple locations in the core plug should be no larger than ~0.05 mm. Continue sanding one or both sides of the core plug accordingly.
9. When sample preparation is complete, wrap the sample tightly in plastic film and then in aluminum foil. Place the wrapped core plug in a plastic cup, close it and put some tape in the joint between the cup and the lid.

APPENDIX D: POROSITY MEASUREMENTS

D.1 Helium porosimetry (HeP)

D.1.1 Equipment

a. Schematic of helium porosimeters (Figure D.1).

b. Environment chamber (cooler) (Figure D.2A).

c. DAQ Computer (Figure D.2B).

d. Temperature control electronics (Figure D.2B).

e. Helium bottle and pressure regulator (Figure D.2C).

f. Vacuum pump (Figure D.2D).

g. Helium port (Figure D.3A).

h. Vacuum port (Figure D.3A).

i. Air safety valve (Figure D.3B).

j. Swagelok valves (Figure D.3C).

k. Sensor temperature probe (Figure D.3D).

l. Pressure transducers (Figure D.3C, D).

m. Light bulb (Figure D.3E).

n. Fan (Figure D.3E).

o. Sample chambers for 1.0 in. and 1.5 in. sample diameters (Figure D.4A).

p. Steel billets for 1.0 in. (Figure D.4B) and 1.5 in. (Figure D.4C) sample chambers.

q. O-rings.

r. Nuts and bolts.

s. Tubing.

t. Vacuum tubing.

u. 7/16” Wrenches (2).

v. Vacuum grease.

w. Power supply.

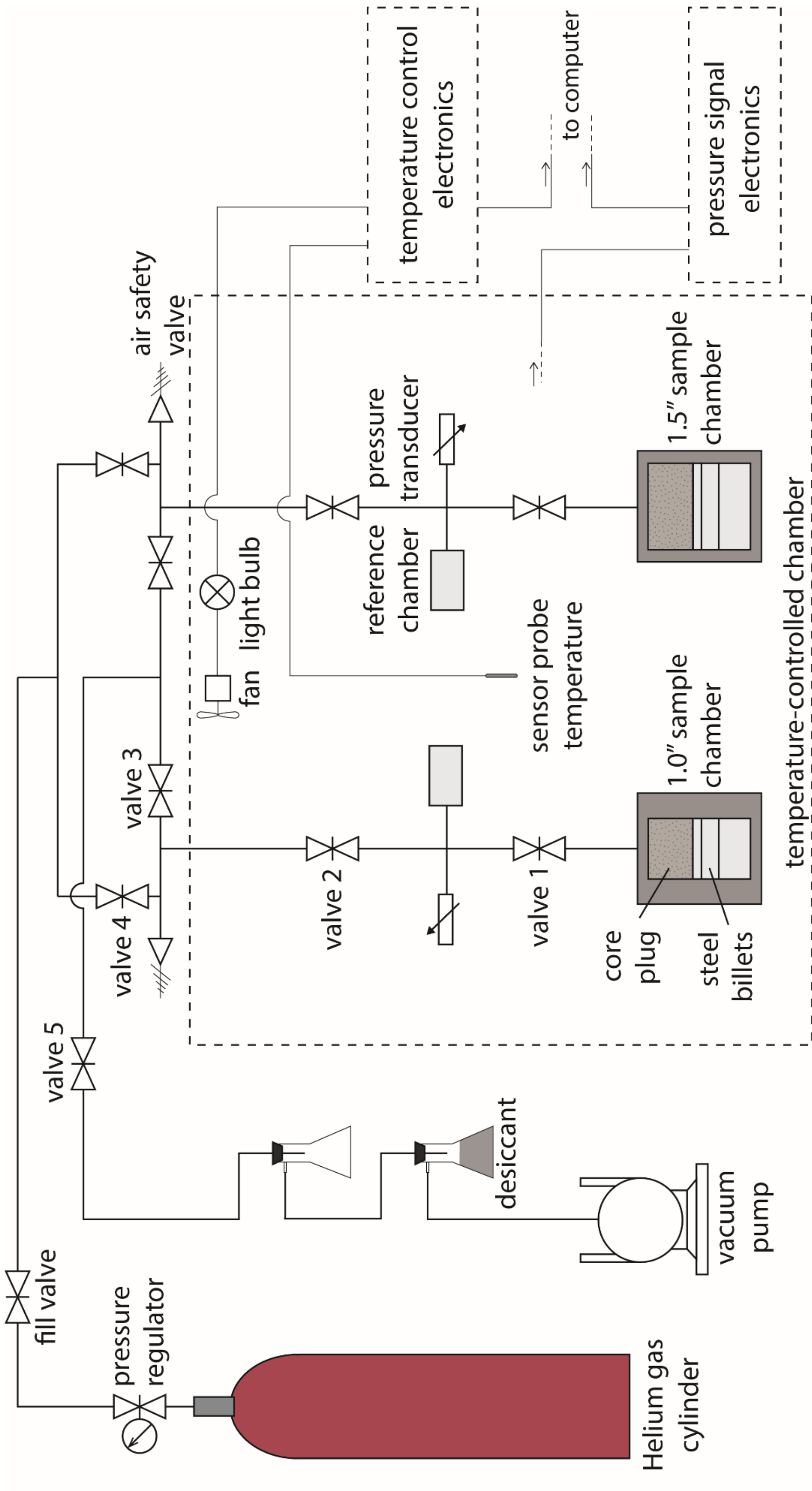

Figure D.1. Schematic of helium porosimeters.

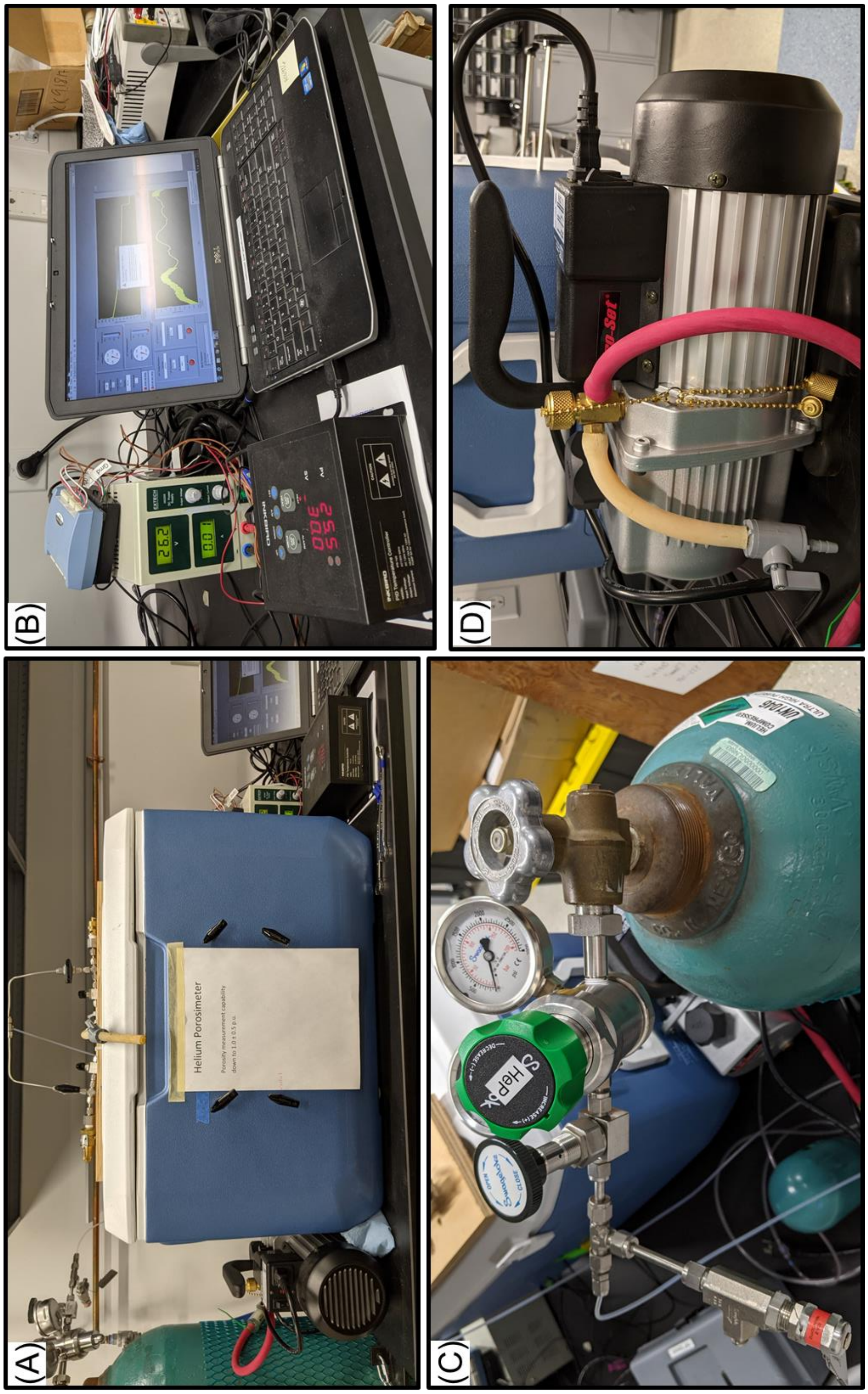

Figure D.2. Photographs of HeP components.

Photograph of (A) helium porosimeter at UT Geomechanics Laboratory, (B) Temperature control system and computer, (C) Helium gas cylinder and pressure regulator, and (D) Vacuum pump.

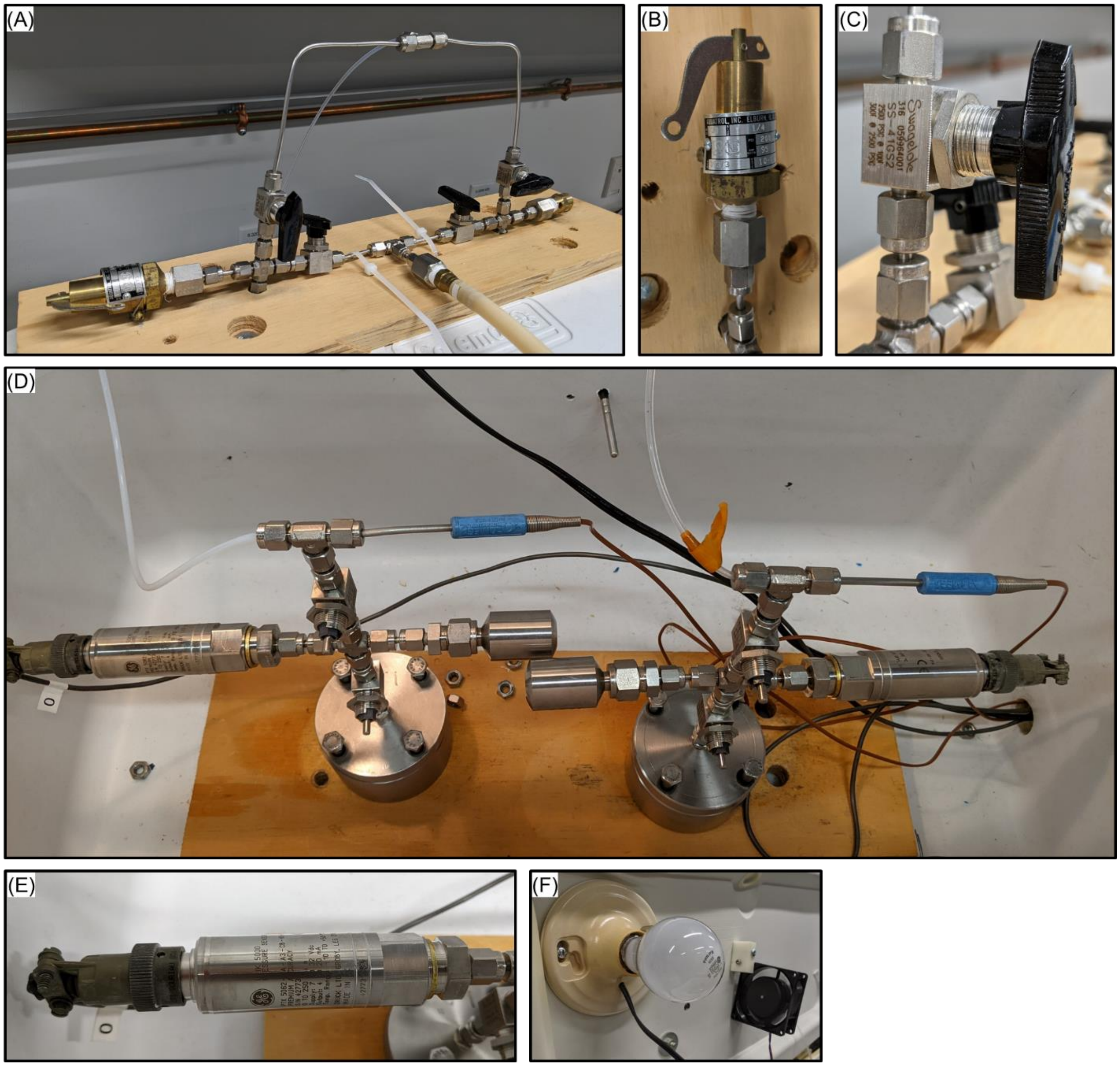

Figure D.3. Photographs of HeP pressure and temperature components.

Photographs of (A) Helium port and vacuum port, (B) Air safety valve, (C) Valve, (D) Interior of cell showing main components of helium porosimeter, (E) Pressure transducer, and (F) Light bulb and fan.

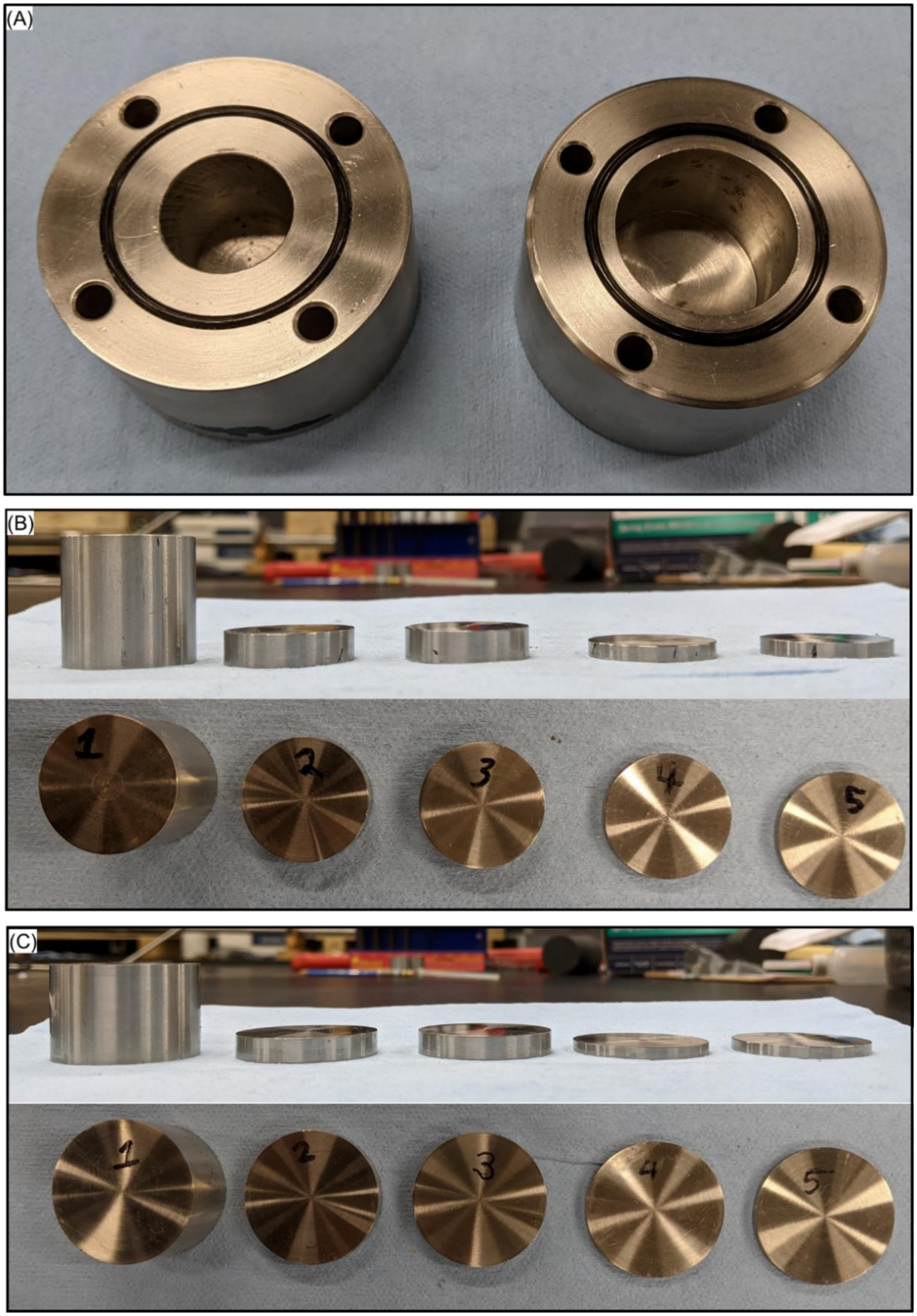

Figure D.4. Photographs of HeP sample chamber and steel billets.

Photographs of (A) Sample chamber, 1.0 in. sample diameter (left) and 1.5 in. sample diameter (right), (B) 1.0 in. diameter steel billets, and (C) 1.5 in. diameter steel billets.

D.1.2 Experiment execution procedures

1. Measure and record the diameter and length of the core plug sample at six different positions to get a good estimate of what the nominal diameter and length are.
2. Measure the mass of the sample.
3. Select the necessary billets to place under the sample so that the combined sample and billet height is as close to 1.25 in. (3.175 cm.) without going over. Record the billets used.
4. Place the billets in the sample chamber.
5. Place the sample into the sample chamber. The sample should not extend past the surface of the lower portion of the chamber.
6. Apply a small amount of vacuum grease to the O-ring of the sample chamber.
7. Seal the chamber using two 7/16" wrenches.
8. Place chamber in the HeP chamber such that the four protruding screws fit snugly in the wood plank.
9. Attach the two valve stems and make sure they are tightened in the handlebars.
10. If the temperature control program is not already running, open up and start the LabView VI, setting the temperature to 30° C. Ensure you have not left anything you need in the temperature chamber (opening it during or after temperature equilibration may cause a substantial delay).
11. Allow the system with the sample inside to equilibrate for ~5 hr. before starting with the test
12. After ~5 hr., open the Helium delivery tube valve (valve 4) to either the left (1.0") or right (1.5") port, depending on which chamber is in use.
13. Connect the vacuum pump tube to the vacuum inlet (valve 5) and plug in the vacuum pump.
14. If not already open, open the data acquisition (LabView VI).

15. Manually enter the correct values into the following fields: Sample Rate (Hz) (default= 1), Moving Average (default= 1), Test Title, Sample Name, and Operator (Put your surname).
16. Begin data collection by clicking the right-pointing arrow at the top.
17. Click Yes/No 1.0” and 1.5” data to file.
18. When prompted, enter the file name (typically HePXXXX).
19. Once data collection has begun, ensure the chamber lower valve (valve 1), the reference middle valve (valve 2), valve on the vacuum port (valve 5) and the valve next to the Helium delivery port (valve 3) are all open, turn on the vacuum pump.
20. After two minutes, close the chamber lower valve (valve 1) and the valve next to the Helium delivery port valve (valve 3).
21. Open the main valve on the helium cylinder and then open the Swagelok valve (fill valve). After a five second count, close the reference chamber valve (valve 2).
22. Close the main valve on the helium cylinder and then close the Swagelok valve (fill valve) next to it.
23. Turn the pump off.
24. Two minutes after closing the reference chamber valve (valve 2), open the sample chamber valve (valve 1).
25. Leave the data acquisition recording one datapoint per second for 2-5 minutes. Then change the sampling rate to 1 datapoint per minute (60 seconds) for 2 hours. Lastly, change the sampling rate to 1 datapoint every five minutes (360 seconds) for the remaining of the test.
26. Run the test for ~48 hours.

27. After the test is complete, hit the STOP M/C red button and open slowly the chamber reference valve (valve 2) and if not already open, the vacuum/helium interface (upper) valve.

28. Bleed off the pressure in 3 to 4 small steps over 2-3 hrs. to avoid sudden depressurization of the sample (During this process, display the pressure on the screen by running the program by clicking the right-pointing arrow at the top; set the Moving average to 1; and do not record the data to file).

29. Open the environmental chamber, detach the two valve stems, remove the four nuts sealing the chamber and remove the sample.

30. Record the mass of the sample.

D.2 Nuclear magnetic resonance (NMR)

D.2.1 Equipment

a. Oxford Instruments GeoSpec2 2 MHz benchtop NMR system at UT Petroleum and Geosystems Engineering.

b. Chiller.

c. Sample glass tube.

d. Plastic cylinder with reference mark.

e. Computer.

D.2.2 Experiment procedures

1. Record the weight of the sample.

2. To avoid fluid loss during the experiment, wrap the core plug in thin plastic film (Saran Wrap or Glad Cling Wrap).

3. Carefully place the core plug inside the NMR sample glass tube.

4. Place the glass tube with the sample inside into the plastic cylinder with the reference mark, and make sure that the top of the sample is below the reference mark. If not, adjust up or down the NMR sample glass tube collar accordingly.
5. Place the NMR sample glass tube with the sample inside into the NMR system.
6. Start the Green Imaging Technology software on the computer.
7. Acquire T_2 NMR using the following parameters:
   - Signal-to-noise-ratio (SNR) = 100
   - T2 max = 300
   - Tau = 0.054
8. Once acquisition is complete, remove the NMR sample glass tube and collect the core plug.
9. Record the weight of the tested core plug again.

APPENDIX E: DETAILED METHODOLOGY OF STEADY-STATE LIQUID PERMEABILITY EXPERIMENTS

E.1 Equipment

E.1.1 Permeability test cell

a. Picture of permeability chamber (Figure E.1).

b. Schematic of Permeability test cell (Figure E.2).

c. Housing/cell structure.

d. Insulation panels.

e. Temperature control electronics.

f. Data acquisition electronics.

g. Heat radiator (Figure E.1).

h. Fan (Figure E.1).

i. Sensor probe temperature.

j. Handles to operate valves from exterior.

k. Power supply.

l. Computer and monitor.

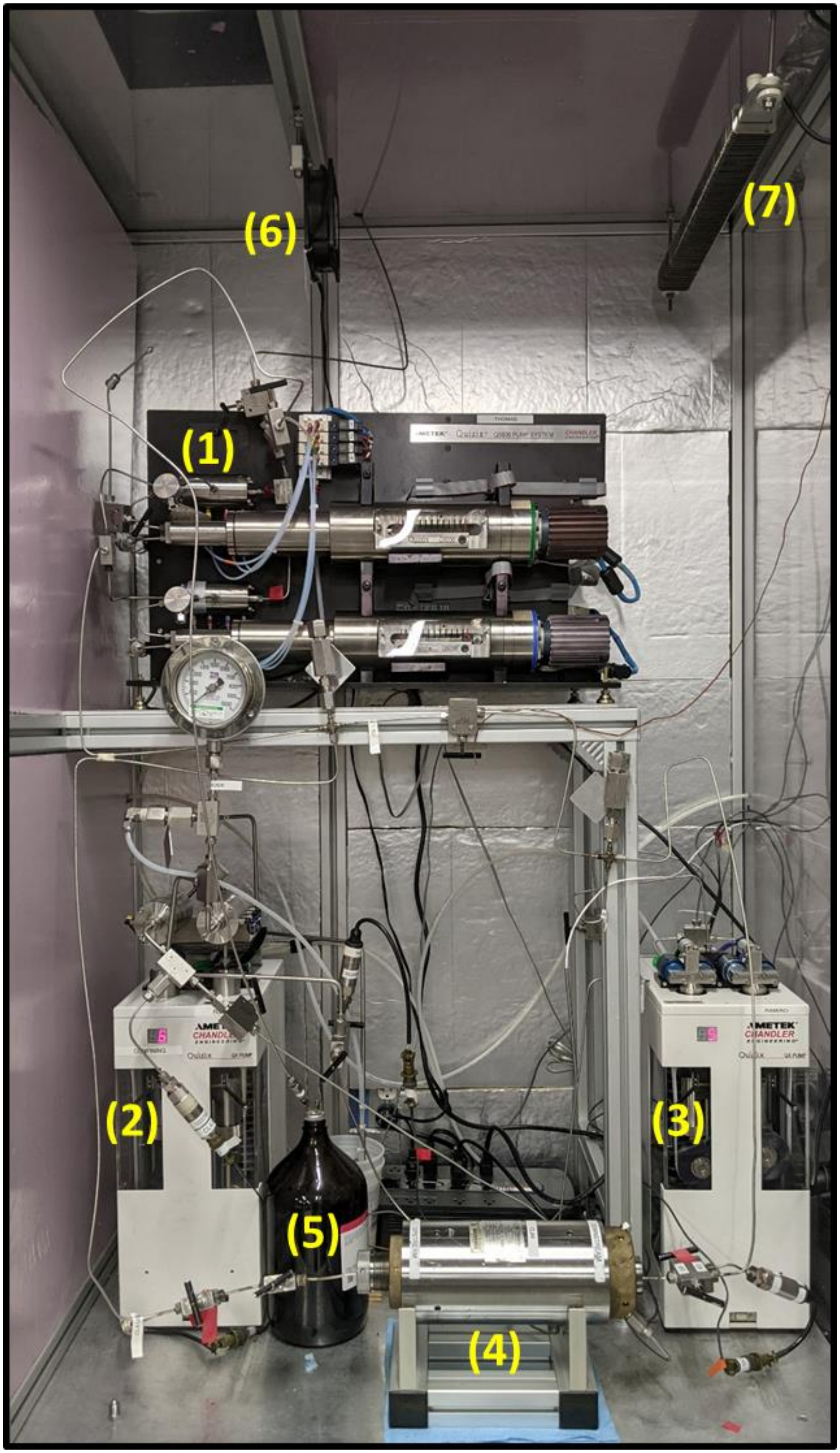
(1)
(2)
(3)
(4)
(5)
(6)
(7)

Figure E.1. Photograph of permeability test cell.

Picture of one of permeability experimental setups at the UT Geomechanics Laboratory (Jackson School of Geosciences). (1) Upstream pumps, (2) Downstream pump, (3) Confining pressure pump, (4) Core holder, (5) Dodecane bottle, (6) Fan, and (7) Radiator.

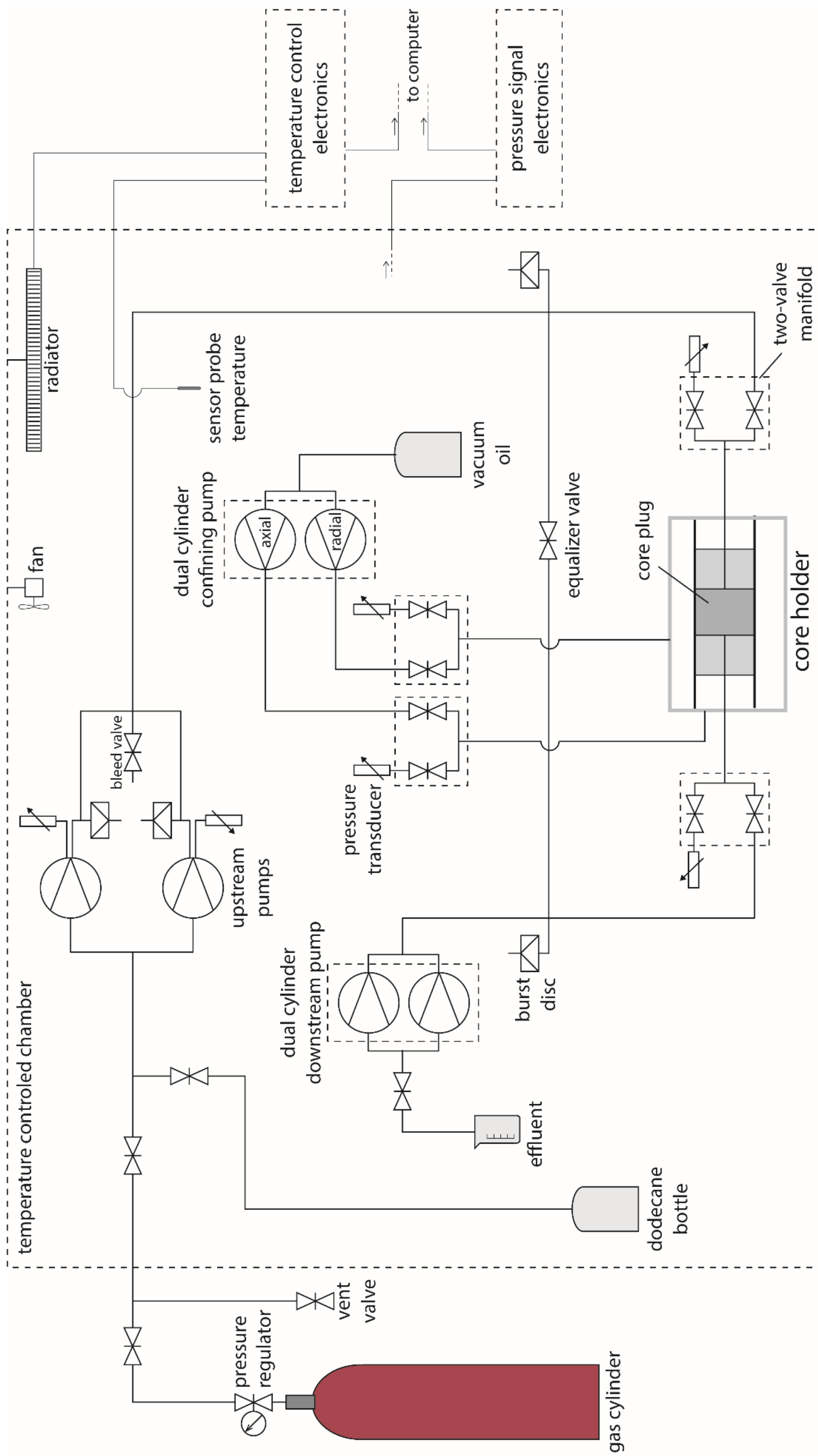

Figure E.2. Schematic of permeability experimental setup.

E.1.2 Core holder components

a. Assembled core holder (Figure E.1).

b. Schematic of core holder (Figure E.3).

c. Body and support structure.

d. Downstream core holder components.

    i. End cap.

    ii. Axial piston.

    iii. Ferrule.

e. Upstream core holder components.

    i. Screw retainer.

    ii. Endcap.

    iii. Ferrule.

f. Pore fluid tubing and pistons.

    i. 1.0-inch diameter piston (Figure E.4A).

    ii. 1.5-inch diameter piston (Figure E.4B).

g. Viton sample sleeve (Figure E.5).

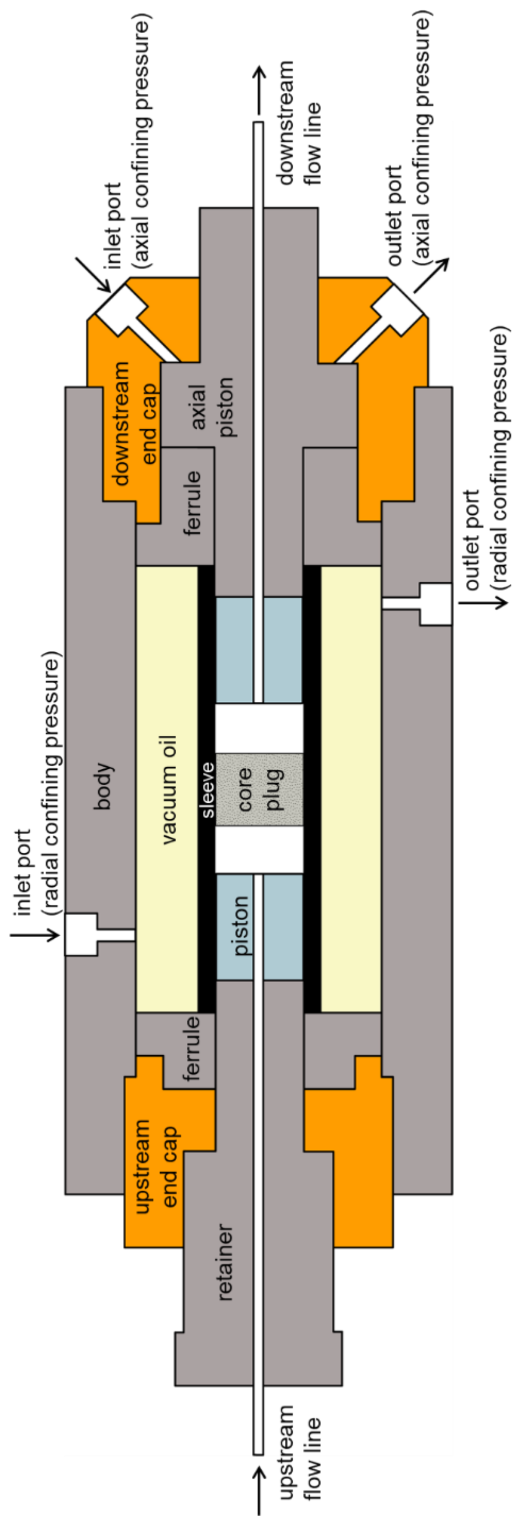

Figure E.3. Schematic of the core holder.

Schematic of core holder manufactured by Core Labs. Model RCHT-1.5&1.0. Maximum working pressure is 15,750 psi.

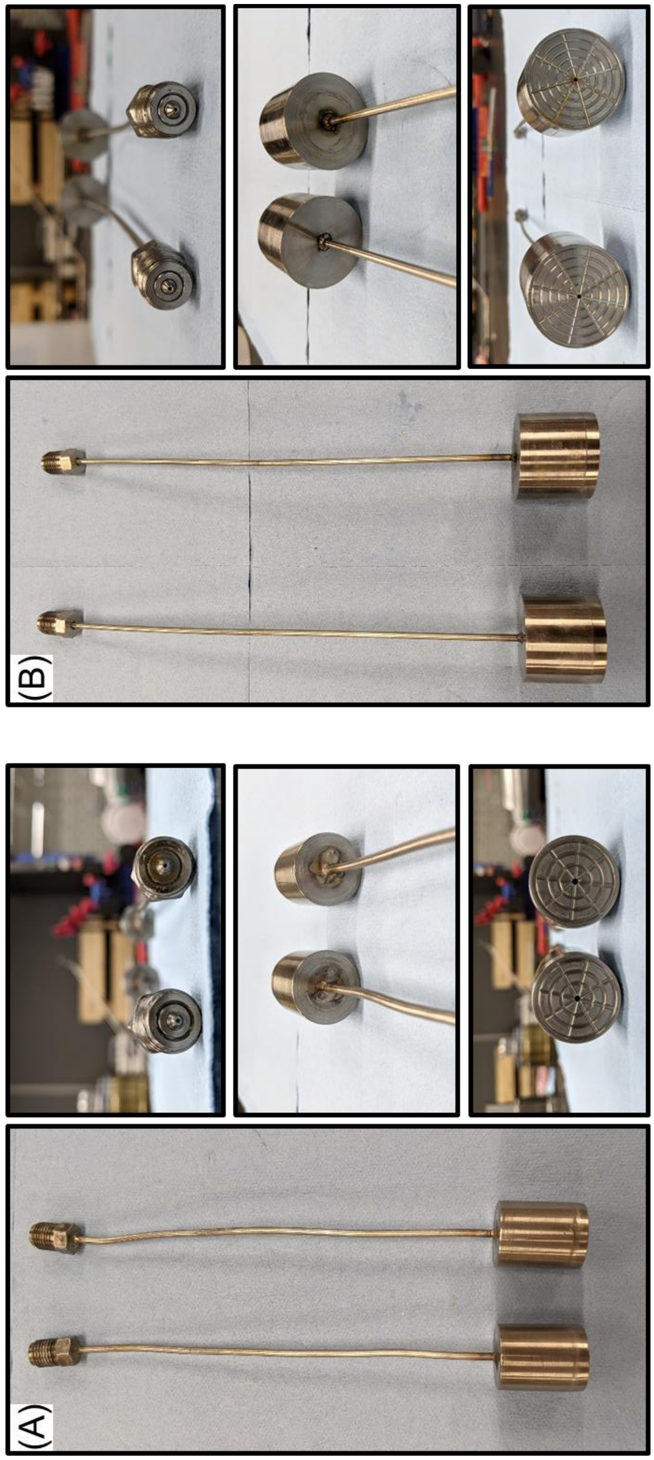

Figure E.4. Photographs of pistons.

Photographs of (A) 1.0-inch diameter pistons and (B) 1.5-inch diameter pistons. Flow distribution channels are manufactured in the face of the piston that is in contact with the core plug.

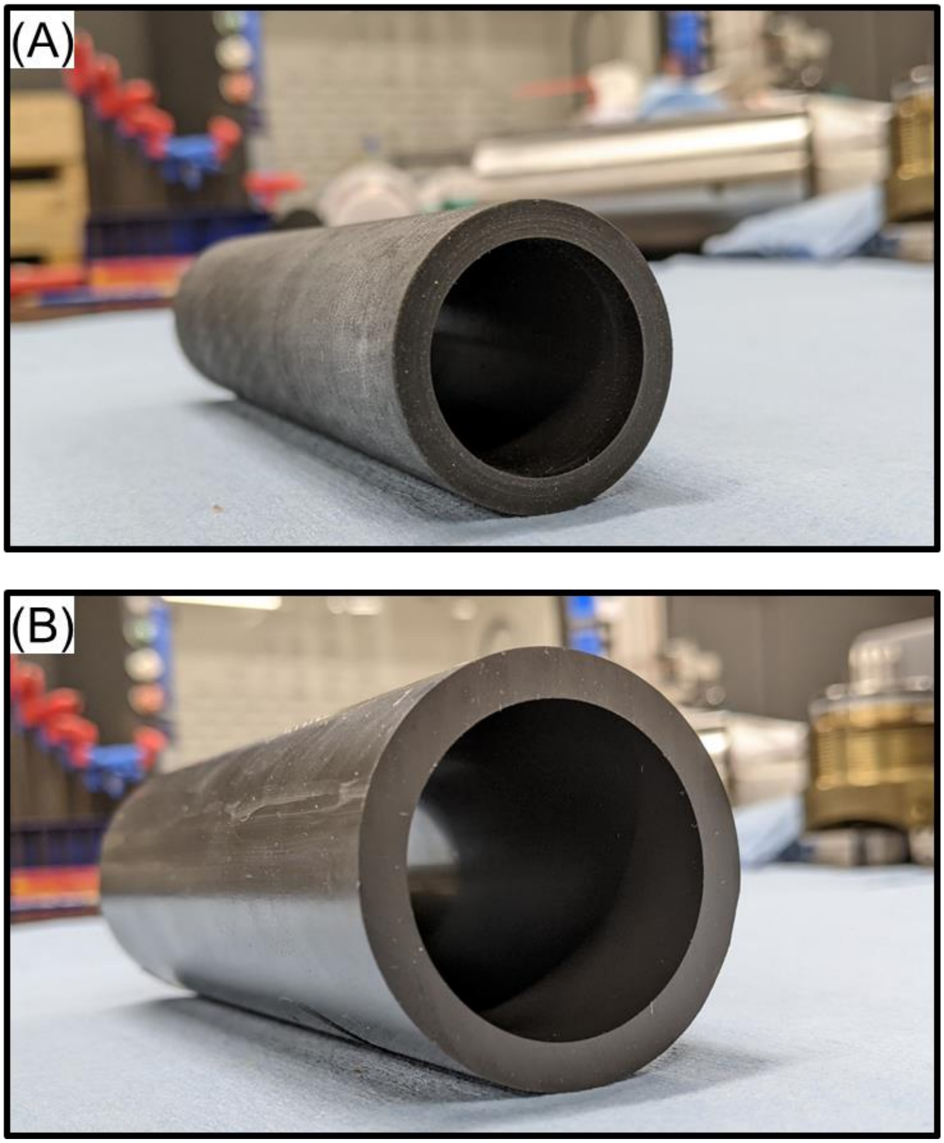

Figure E.5. Photographs showing cross-sectional views of Viton sleeves.

Cross-sectional view of (A) 1.0 in. inner diameter 70 Durometer Viton sleeve (0.2 in. thick) and (B) 1.5 in. inner diameter 70 Durometer Viton sleeve (0.2 in. thick). The Viton sleeve isolates the core plug from the fluid (vacuum pump oil) that fills the annular space between the core holder and the sleeve. When the confining pressure is applied, the fluid in the annular space transmits the pressure to the Viton sleeve, creating a seal between the sleeve and the sample. Hence, there is no flow bypass of the pore pressure fluid between the sample and the sleeve. The seal between the sleeve and the sample is confirmed by tests conducted in blank billets, where no fluid flow was detected.

E.1.3 Pressurization components

a. Quizix® Q5000 pump (Figure E.1).

b. Quizix® QX-10K pump (Figure E.1).

E.1.4 Fluid system equipment

a. Pressure transducer and gasket.

b. Valves.

c. Fluid tubing.

d. Nuts and ferrules.

e. Safety burst discs and assembly.

E.1.5 Other equipment

a. Tube cutter (Figure E.6A).

b. Analytical balance (Figure E.6B).

c. Tube bender (Figure E.6C).

d. Fluxed silver solder.

e. Propane gas torch.

f. SWAK® anaerobic pipe thread sealant (Figure E.6D).

g. Vacuum grease (Figure E.6E)

h. Confining oil (Figure E.6F).

i. Dodecane bottle (Figure E.6G).

j. Leak detection fluid (Figure E.6H).

k. Spanner wrenches.

l. Compressed air source and tubing.

Figure E.6. Photographs of additional components used to build the permeability cells and to conduct the liquid permeability measurements.

Photographs of (A) Tubing cutter, (B) analytical balance, (C) tube bender, (D) Swak® sealant, (E) vacuum grease, (F) vacuum pump oil, (G) dodecane bottle, and (H) leak detector.

E.1.6 Sample saturation equipment

a. Schematic of saturation system (Figure E.7).

b. Fume hood (Figure E.8A).

c. Vacuum chamber with valve (Figure E.8B).

d. Two-valve manifold (Figure E.8C).

e. Empty beaker.

f. Vacuum pump.

g. Tubing.

h. Empty vacuum flask.

i. Vacuum flask with desiccant.

j. Power supply.

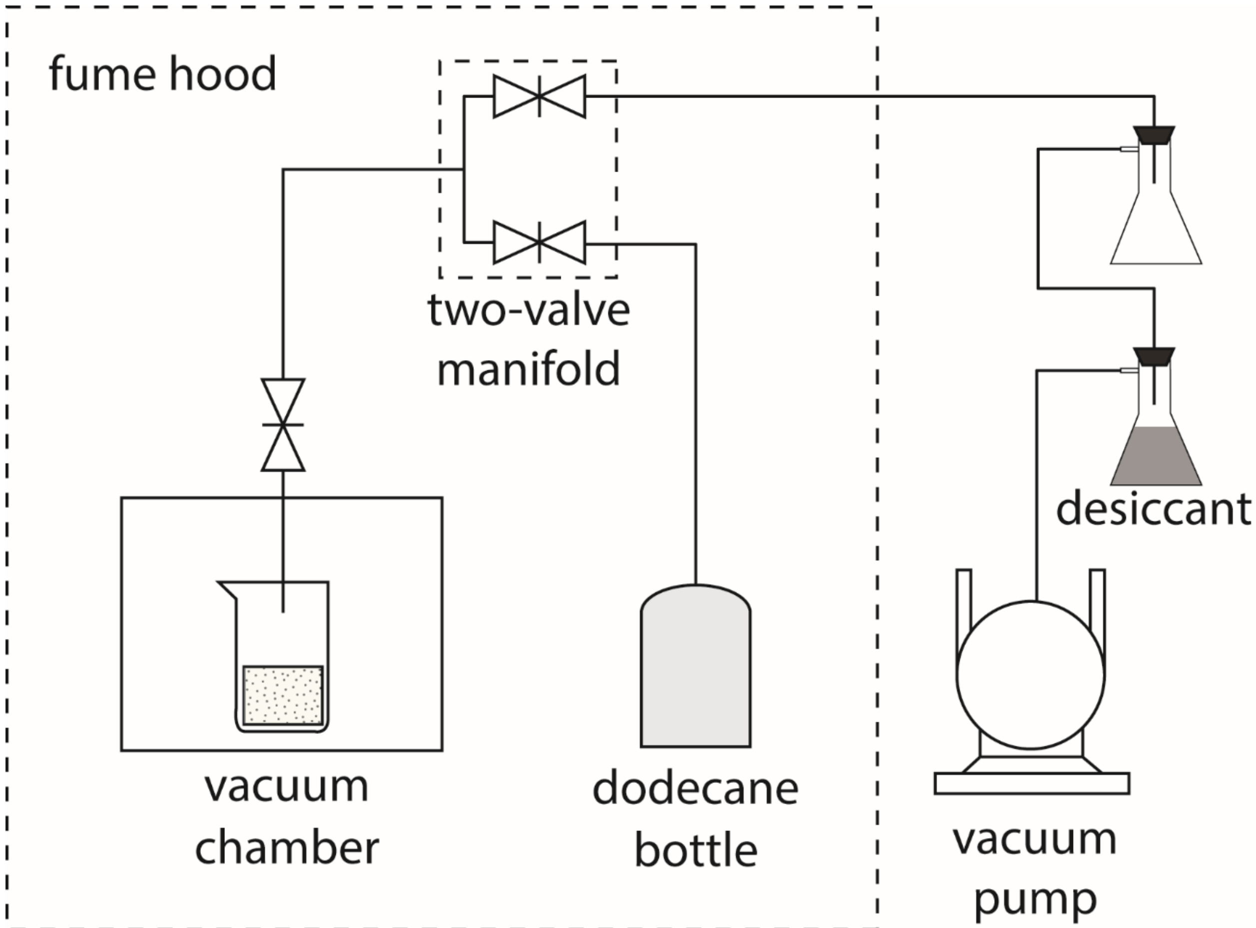

Figure E.7. Schematic of saturation cell.

Schematic of saturation cell consisting of a vacuum chamber with a flask inside hosting the sample, a dodecane bottle, a two-valve manifold that isolates the vacuum line from the dodecane feeding line, and a vacuum pump connected to a desiccant and an empty bottle to trap fluids that could enter the pump during vacuum. The vacuum chamber is inside the fume hood.

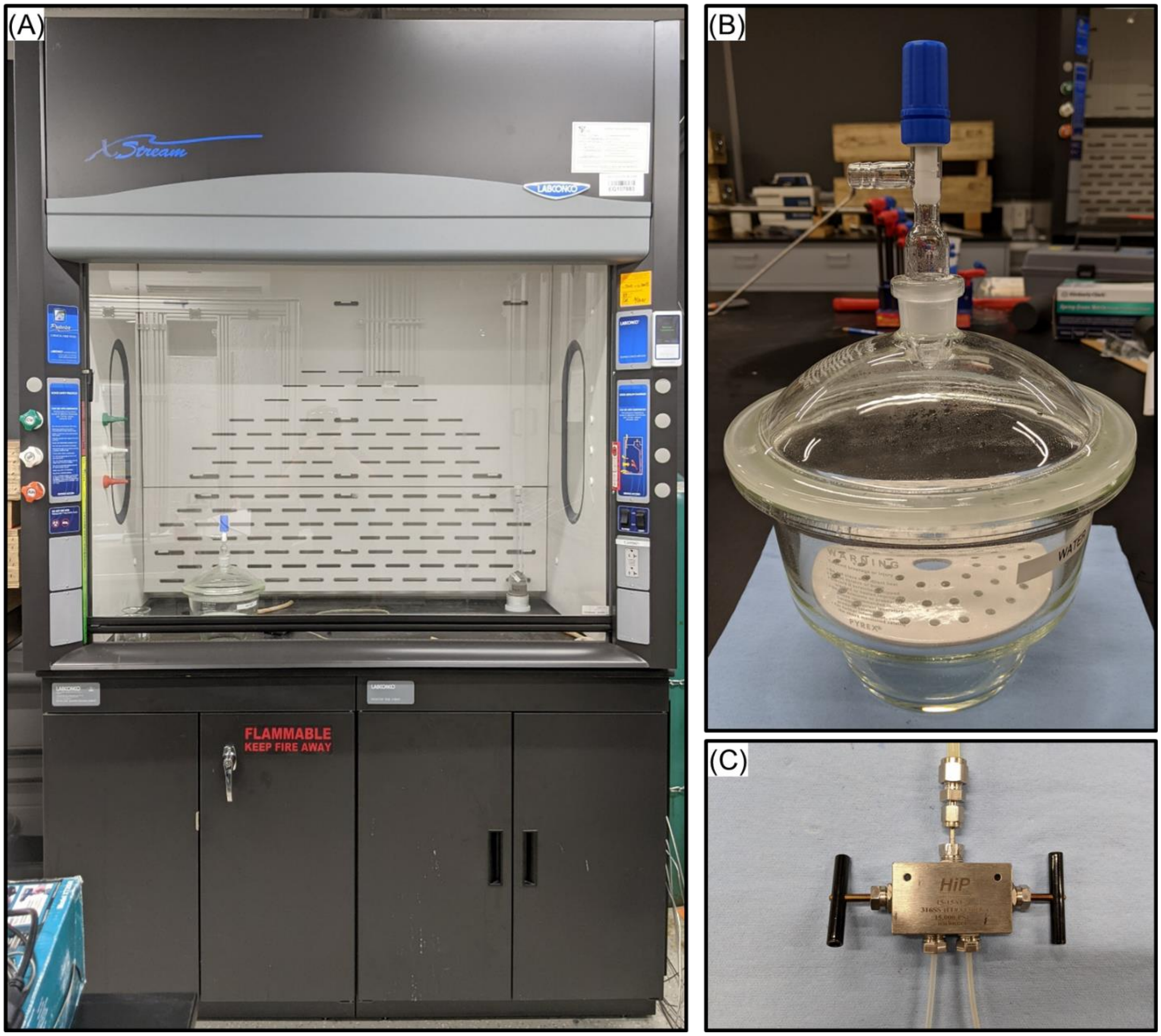

Figure E.8. Photographs of saturation cell components.

Photographs of (A) Fume hood. (B) Vacuum chamber with valve on lid. (C) Two-valve manifold.

E.2 Core holder assembly

1. Install the O-rings and backup seals in the downstream endcap, axial piston, and downstream and upstream ferrules. Once installed, apply a small amount of vacuum grease to them.
2. Insert the axial piston in the core holder endcap. Hit the axial piston with a dead blow hammer to fully insert it into the endcap. Place a piece of wood on top of the axial piston to not damage the part when hitting it with the hammer.
3. Insert the ferrules in the inner part of the endcaps. Carefully tighten the headless screws (aka. blind screws) all the way in until touching the ferrule, and then unscrew them one whole turn. The ferrule should rotate freely while locked in the endcap.
4. Place the downstream endcap vertically and insert the Viton sleeve into the ferrule.
5. Screw the endcap with the installed Viton sleeve into the core holder. Screw it first manually, and then with the aid of two spanner wrenches until they touch.
6. Insert the plastic tube inside the Viton sleeve from the upstream side of the core holder.
7. Screw the upstream endcap into the core holder. Screw it first manually, and then with the aid of two spanner wrenches until they touch. The round stick will help guide the upstream endcap's ferrule into the Viton sleeve.
8. Insert the downstream piston and push it all the way in with the aid of the plastic tube to avoid damaging the flow inlet in the piston.
9. Insert a sample inside the Viton sleeve.
10. Insert the upstream piston and then the retainer.

E.3 Pressurization of radial and axial confining

1. Connect the confining pressure flow lines to the lower ports located in the downstream endcap (axial confining) and in the core holder (radial confining). Leave the ports in the upper side of the endcap and core holder unplugged.
2. Fill the axial reservoir and the annulus volume between the walls of the core holder and the Viton sleeve with vacuum oil by setting both the axial and radial confining pressure pumps to 'Independent constant rate cycle' mode.
3. Continue injecting oil until it overflows from the upper ports, then stop the corresponding confining pressure pump and plug the upper port in the core holder.

E.4 System leak testing

IMPORTANT: Wear safety glasses when the permeability cell is open, and the system is pressurized.

1. Refer to Figure E.2 for the valves and tubing connections that are potential leaking points.
2. Load a blank billet inside the core holder.
3. Set the confining pressure to 5000 psi.
4. Open all pore fluid line valves.
5. Close the delivery valves of the downstream pore fluid pump. Leave these valves closed for the remaining of the leak test.
6. Open the delivery and fill valves in the upstream pore fluid pumps.
7. Connect the vacuum pump to the vent valve and run vacuum for 2 minutes to remove the air in the system.
8. Close the vent valve.
9. Close the fill and delivery valves in the upstream pore fluid pumps.

10. Make sure the helium gas regulator is set to 0 psi, and then open the helium gas cylinder valve.
11. Set the helium gas regulator to 2000 psi.
12. Open the fill valves of the upstream pore fluid pumps. Monitor the pressure inside the upstream pump cylinders in PumpWorks; the pressure inside the cylinders must be the same as the outlet pressure set in the helium gas regulator (i.e., 2000 psi).
13. Close the fill valves of the upstream pore fluid pumps.
14. Set the upstream pumps to 'Independent constant pressure' mode and set the pressure to 2000 psi.
15. Open the delivery valve in the upstream pump and search for leaks. If the leak is large, you will hear a sound of gas leaking from the tubing connection.
16. Mark with tape the leaking points, depressurize the system and tighten the leaky connections with the required tools. If the leak occurs in a soldered connection, removal of the connection and re-soldering outside the cell will be required.
17. Repeat steps 12 to 16 until no leaks are noticed by ear.
18. Pressurize the helium to 2000 psi in the upstream pump.
19. Leave the upstream pump delivery valve open and stop the pump. Monitor the pressure inside the pump cylinder in PumpWorks. If pressure does not drop, all leaks are fixed. If pressure drops, leaks exist in the system, and you must continue with step 20.
20. Pressurize the helium to 2000 psi in the upstream pump and open the delivery valve.
21. With the aid of a brush, cover each tubing connection with leak detection fluid and check for air bubbles.

22. Mark each leaky connection in the system with tape, depressurize the system and tighten the connections.

23. Repeat steps 18 to 21 until no leaks are observed visually.

24. Close the cabinet and let the temperature equilibrate for at least 4 hours.

25. Pressurize the system to 2000 psi, leave the pump operating in ‘constant pressure mode’, and record the volume change inside the operating pump cylinder with PumpWorks for at least 12 hr.

26. Process the recorded data and assess leaks in the system based on the volume change of the pump cylinder. If the leak rate is lower than the expected flow rate across the sample, leak testing is finished. If the leak rate is equal or larger than the expected flow rate across the sample, then go to step 27.

27. Repeat steps 23 to 25 in sequentially isolated segments to identify where the leak is. Start by closing the valve next to the core holder, record the data, and assess the leak. If the leak is still significant, close the next valve in the system and record the data again. Repeat this step until you find the segment where the leak is.

E.5 Sample liquid saturation outside core holder

IMPORTANT: Sample saturation must always be conducted inside the fume hood.

Wear safety glasses when operating the vacuum pump.

1. Unwrap the sample and record its weight.

2. Put the sample inside an empty beaker.

3. Place the beaker inside the vacuum chamber and open the valve located at the top of the vacuum chamber cover (blue & white colored valve).

4. Close the liquid delivery valve and open the vacuum pump valve.

5. Start the vacuum pump and leave the vacuum running for 2 minutes.
6. Close the valve located at the top of the vacuum chamber cover (blue & white colored valve) and then close the vacuum pump valve.
7. Stop the vacuum pump.

   Note: make sure that you leave the purge valve open in the vacuum pump once finished.
8. Open the liquid delivery valve.
9. Open the valve located at the top of the vacuum chamber cover (blue & white colored valve). The saturating liquid will start filling the beaker with the sample.
10. Continue injecting liquid until a layer of ~3-5 mm of liquid covers the sample.
11. Close valve located at the top of the vacuum chamber cover (blue & white colored valve).
12. Close the liquid delivery valve.
13. Leave the sample under saturation for 24 hr.
14. Before removing the sample from the vacuum chamber, slightly damp a paper towel with the saturating fluid.
15. Remove the sample from the vacuum chamber and place it on top of the damp towel. Rotate/roll the sample to remove any excess saturating liquids from its surface.
16. Document the weight of the sample immediately after and place it back into the baker containing the saturating fluid until you load the sample into the core holder.

E.6 Sample loading into core holder

1. Check the pressure readings in the pressure transducers (in LabView, PumpWorks) and in the manometer that is connected to the confining pressure. Make sure all readings are below ~20 psi before opening any valves.
2. Open all the valves in the system.

3. Close the valves next to the core holder.

4. Remove the top plug in the core holder (the one that connects the annular space of the core holder to the atmospheric pressure).

5. Remove the piston and retainer from the core holder. Unscrew the retainer very slowly. If you find that it does not rotate freely, DO NOT FORCE IT. Leave it as is and contact your lab manager.

6. Inspect the Viton sleeve located inside the core holder using a flashlight. Make sure the sleeve is in good condition. If the sleeve is punctured or shows wearing signs, replace it. Contact your lab manager if you do not know how to replace the Viton sleeve.

7. Clean the threads of the end cap in the core holder and retainer with a paper towel. Re-inspect to make sure that no detritus is left in the threads or inside the Viton sleeve.

8. Open the valve next to the core holder on the upstream side.

9. Start the upstream pump using the constant pressure cycling paired mode at a pore pressure of P_p = 10 psia. Leave the pump running until no air is flowing out of the piston.

10. Close the upstream valve next to the core holder, and then stop the pump.

11. Repeat steps 6 through 8 for the downstream side by opening and closing the valve next to the core holder in the downstream side. You can operate the same pump that you used for the upstream side.

12. Once air in the system is purged, place the core plug inside the core holder. Do not dry the core plug with a paper towel.

13. Start the upstream pump using the same pump settings and pressure specified in Step 9, and then open the upstream valve next to the core holder.

14. Place the retainer and upstream piston back into the core holder. You MUST ALWAYS manually screw the retainer SLOWLY back into the core holder. This is a very delicate part of the loading process. If there is any resistance to screw the retainer in, unscrew and try to screw it in again. If there is still some resistance, stop the pump and call the Lab Manager for help. NEVER force-screw the retainer.
15. When the upstream piston touches the core plug, unscrew the retainer ~2-3 threads.
16. With the upstream pump still running, close the upstream valve next to the core holder, and open the downstream valve next to the core holder immediately after.
17. Leave the pump running flow through the downstream piston for 5-10 seconds.
18. Move to the System Pressurization section below.

Note: it is normal to see liquid flowing out of the core holder through the hole in the retainer during the final steps of the process. Make sure you place paper towels underneath the retainer to trap the overflowing liquids.

E.7 System pressurization and sample saturation inside core holder

1. Set the confining axial pump to constant pressure cycling paired mode at P_c = 100 psi.
2. Once pressure is reached, set it to P_c = 200 psi. Watch very closely the pressure reading. The pressure will build up very quickly once the piston touches the sample. Stop the pump when that occurs.
3. Try to unscrew the retainer. If it does not rotate, the piston is effectively touching the sample and you can continue to the next step. Contact your lab manager otherwise.
4. Start the axial confining pressure pump again with the pressure set to P_c = 200 psi and leave it running at that pressure. Make sure the pressure is stable at P_c ~ 200 psi before moving to the next step.

5. Set the radial confining pressure pump to independent constant pressure cycling paired mode at P_c = 50 psi. Leave it running until the confining fluid (e.g., oil) flows out of the upper unplugged hole in the core holder. When overflow starts, stop the radial confining pressure pump, and screw the plug in.
6. Start the radial confining pressure pump again using the same settings specified in Step 5.
7. When P_c = 50 psi pressure is reached, increase it to 100 psi, 150 psi and 200 psi sequentially. Watch very closely that the radial confining pressure does not go over the pressure set in PumpWorks. If that occurs, stop the pump, and start it again until the pressure stabilizes.
8. Once both the radial and axial confining pressures are at P_c = 200 psi, leave them running. Make sure the pressure is stable and does not go over 200 psi. It is ok if the pressure goes over by 1-5 psi (e.g., 205 psi).
9. Set the upstream pressure to constant pressure cycling paired mode at P_p = 25 psi.
10. Set the confining and pore pressures to P_c = 250 psi and P_p = 50, respectively.
11. Bleed the pore pressure lines by opening the pore pressure bleeding valve. Close the bleeding valve once no air comes out of the line.
12. Let the system to go back to P_p = 50 psi.
13. Ramp P_c = 250 psi $\rightarrow$ 500 psi, and P_p = 50 psi $\rightarrow$ 250 psi, at 25 psi/min.
14. Ramp P_c = 500 psi $\rightarrow$ 750 psi, and P_p = 250 psi $\rightarrow$ 500 psi, at 25 psi/min.
15. Ramp P_c = 750 psi $\rightarrow$ 1000 psi, and P_p = 500 psi $\rightarrow$ 750 psi, at 25 psi/min.
16. To conduct saturation of the sample under pressure, leave the system at P_c = 1000 psi and P_p = 750 psi for 5 days.
17. After 5 days, ramp P_c = 1000 psi $\rightarrow$ 2000 psi, and P_p = 750 $\rightarrow$ 950 psi, at 25 psi/min.

18. Continue with the next step in the test program.

E.8 Experiment execution procedures

IMPORTANT: When pressurized, make sure you wear safety glasses before opening the permeability cabinet.

1. Open the cabinet, close the equalizer valve, and make sure that both the upstream and downstream valves next to the core holder are open.
2. Close the permeability cabinet and set the upstream pore pressure pump to constant pressure cycling paired mode to $P_{p,\ up}$ = 950 psi. Make sure that the downstream pore pressure pump is also set to constant pore pressure cycling paired mode at $P_{p,\ down}$ = 950 psi.
3. Let the cabinet to equilibrate the inside temperature for ~20 minutes before moving to the next step.
4. Start recording data in PumpWorks at 60 seconds interval.
5. Start recording data in LabView at 60 seconds interval. Use the same file name for both PumpWorks and LabView.
6. Ramp upstream pore pressure $P_{p,\ up} = 950 \rightarrow 1050$ psi at 25 psi/min.
7. Record data for 24 hr.
8. After 24 hr., do not stop the pumps, process the datafile and compute for permeability. Write down the calculated flow rate upstream (q_{up}).
9. Stop recording data in PumpWorks and in LabView.
10. Stop the upstream pore pressure pump and set it to constant flow rate paired mode at q_{up} = X ml/min (your calculated flow rate from previous step).
11. Start the pump and record data into a new datafile in both PumpWorks and LabView.

12. Leave recording for at least 24 hr., or until steady-state conditions are reached. You can monitor this in real-time using LabView.
13. Process the datafile and compute for permeability.
14. Stop the upstream pump, open the permeability cabinet, and open the equalizer valve.
15. Ramp the axial and confining pressure pumps to the next pressure step in the test program and wait for 24 hr. until you start a new permeability test.

E.9 System depressurization and sample unloading

IMPORTANT: When pressurized, make sure you wear safety glasses before opening the permeability cabinet.

1. Stop the upstream pore pressure pump, leave the downstream pore pressure pump on, and open the equalizer valve.
2. Open the upstream pore pressure pump delivery valve in PumpWorks.
3. Ramp the confining pressure and pore pressure down to P_c = 200 and P_p = 10 psi, respectively, over 24 hr.
4. Once the set pressures are reached, stop the pore pressure pump, and open all the fill and delivery valves of the pore pressure pumps in PumpWorks.
5. Ramp the radial confining pressure from P_c = 200 psi $\rightarrow$ 20 psi.
6. Ramp the axial confining pressure from P_c = 200 $\rightarrow$ 20 psi.
7. Open the fill and delivery valves of the axial confining pressure pump in Pump Works®.
8. Open the fill and delivery valves of the radial confining pressure pump in Pump Works®.
9. Close the pore pressure valves next to the core holder.
10. Remove the confining fluid plug on top of the core holder.
11. Slightly damp a paper towel with the saturating fluid.

12. Unscrew retainer and extract both the retainer and piston out of the core holder.

13. Extract core plug from core holder and remove excess liquids from its surfaces using the damped towel.

14. Document the weight of the sample immediately after.

E.10 Core holder disassembly

1. Remove the confining fluid plug on top of the core holder.

2. Manually operate the radial confining pressure pump to remove oil out of the core holder using the 'Independent constant pressure' mode in PumpWorks. First, close the fill valve and open the delivery valve, set the cylinder to 'retract' and start the pump. Once the cylinder is full of oil, close the delivery valve and open the fill valve, set the cylinder to 'expand' and start the pump.

3. Repeat Step 2 until most oil in the radial annulus space is removed.

4. Stop the pump and unscrew the pistons from the valves.

5. Move the core holder to a bench or table.

6. In reverse order, follow the steps indicated in E.2 Core holder assembly.

APPENDIX F: DARCY'S LAW VALIDATION IN STEADY-STATE LIQUID PERMEABILITY MEASUREMENTS

I calculated the permeability of the core plugs using the steady-state method. This method consists of injecting the test fluid (e.g., dodecane) through the core plug at a constant rate at the upstream end while maintaining a constant pressure at the downstream end to generate a pressure differential between the upstream and downstream ends of the core plug (Figure F.1). When the flow rate is constant across the sample (i.e., steady-state condition), I calculate the permeability (k) of the core plug using Darcy's Law (Eq. F.1).

$$k = -\frac{q\mu}{A}\frac{L}{\Delta P}, \qquad \text{Eq. F.1}$$

where μ is the viscosity of the fluid at the pore pressure and temperature at which the experiments are conducted.

This law is only valid under the following assumptions:

- The flow across the sample is at a steady-state condition (i.e., it is not time-dependent).
- The temperature of the fluid is constant, so that fluid viscosity is constant.
- The fluid flow through the sample is in the laminar flow regime (i.e., fluid flow is dominated by viscous forces, Reynolds number < 2300).
- The porous media is uniform and there is single-phase flow only (100% saturated with the flowing fluid).
- The fluid is incompressible.

- There is no interaction between the rock and the pore fluid.
- The cross-sectional area of the core plug is constant.

Eq. F.1 indicates that the pressure differential between the downstream and upstream sides (*ΔP*) of the core plug increases linearly with the flow rate (*q*). Hence, the permeability of the core plug remains constant at increasing flow rates. To validate this behavior, I conducted four steady-state liquid (dodecane) permeability measurements at increasing *q* while maintaining a constant average pore pressure of ~1000 psi [6.89 MPa] in an organic-rich siliceous mudstone core plug (Sample PN3-108) (Table F.1). I maintained the confining pressure constant at 5500 psi [37.92 MPa] in these tests.

Figure F.2 shows that the regression line obtained for these four measurements is linear and it intercepts the origin. These results validate Darcy's law in my permeability experiments. The permeability corresponds to the slope of the trend line $\left(m = \frac{q}{\Delta P}\right)$ multiplied by $\left(\frac{\mu L}{A}\right)$. In this example (Figure F.2), the regression line equation is:

$$q\left[\frac{ml}{min}\right] = 1.2e^{-4}\Delta P\ [MPa], \text{ or } q\left[\frac{cm^3}{sec}\right] = 2e^{-7}\Delta P\ [atm]. \qquad \text{Eq. F.2}$$

Therefore,

$$k = 2e^{-7}\left(\frac{\mu[cP]L[cm]}{A[cm^2]}\right) = 2e^{-7}\left(\frac{1.333\ x\ 1.681}{11.40}\right) = 40e^{-9}Darcy = 40\ nanoDarcy$$

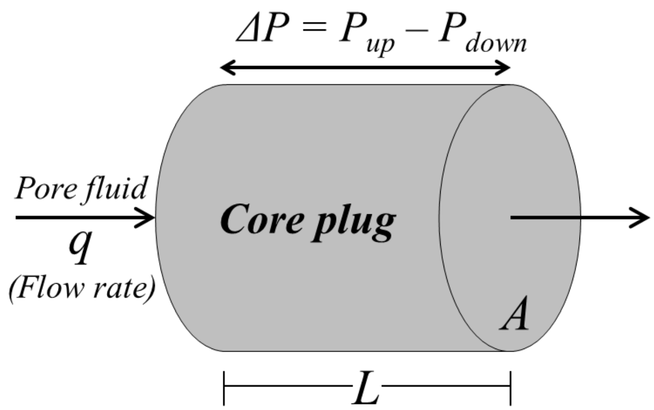

Figure F.1. Schematic of core plug during the permeability experiments.

Schematic of core plug showing the direction of injected test fluid at a flow rate (q), pressure differential (ΔP), length of the core plug (L), and cross-sectional area of the core plug (A).

Table F.1. Flow rate and pressure conditions during permeability tests to assess Darcy's law validation.

Upstream flow rate (q) and downstream pressures used in each steady-state liquid permeability test to assess validity of Darcy's law in my experiments. The precision of the pumps' flow rate and pressure are 5E-6 ml/min and 0.1 psi [6.9E-4 MPa], respectively.

Test #	**Flow rate (upstream), q**	**Pore pressure (upstream), P_{up}**		**Pore pressure (downstream), P_{down}**		**Pressure differential, ΔP**	
	(ml/min)	(MPa)	(psi)	(MPa)	(psi)	(MPa)	(psi)
1	0.70E-04	7.2	1049.8	6.6	952.4	0.6	96.4
2	1.60E-04	7.6	1099.1	6.2	901.9	1.3	197.2
3	2.40E-04	8.0	1155.0	5.9	851.6	2.0	303.4
4	3.30E-04	8.3	1210.9	5.5	801.7	2.8	409.2

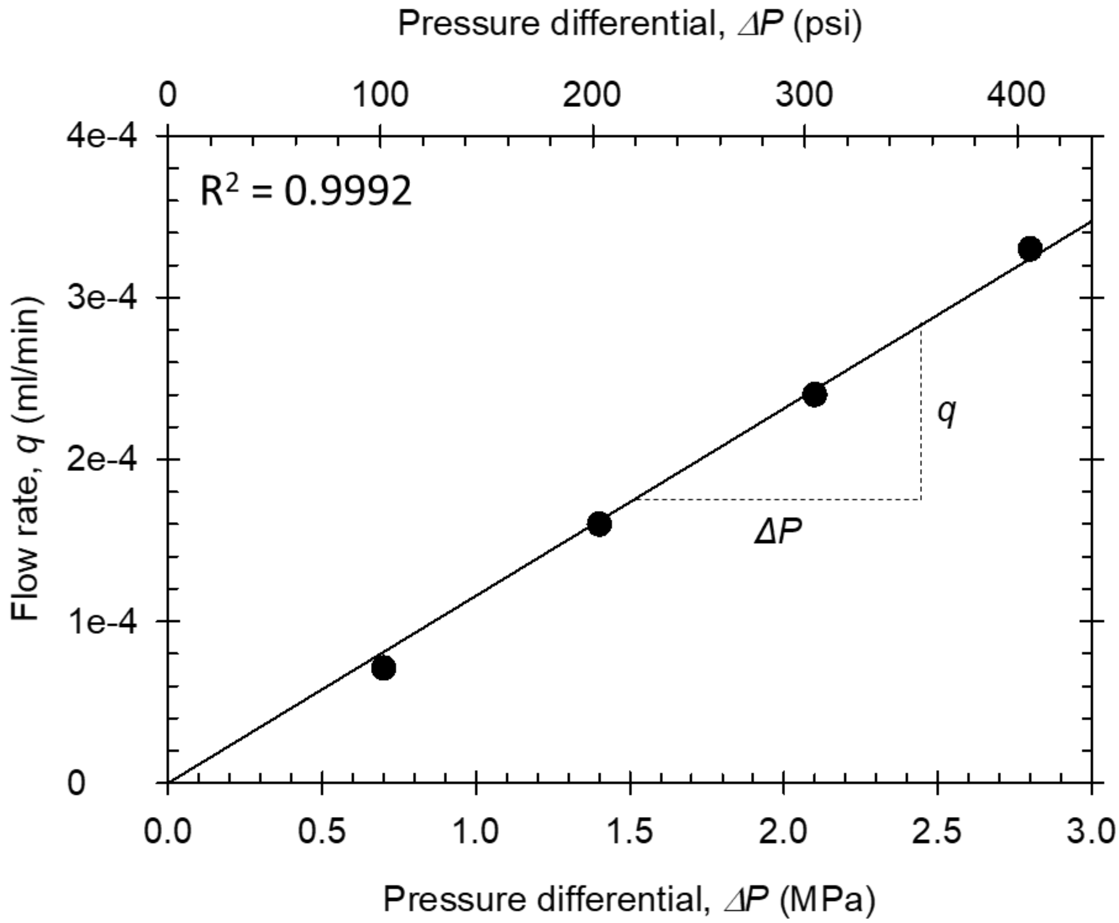

Figure F.2. Experimental data showing Darcy's law validation.

Experimental data demonstrates linear correlation between flow rate (q) and pressure differential (ΔP) in Sample PN3-108.

APPENDIX G: STEADY-STATE LIQUID PERMEABILITY MEASUREMENTS IN SAMPLES FROM THE BAKKEN FORMATION, WILLISTON BASIN, USA[3]

G.1 Abstract

I measured steady-state liquid (dodecane) permeability in four horizontal core plugs from the middle member of the Bakken Formation at multiple effective stress conditions to investigate how permeability evolves with confining stress and to infer the matrix permeability. Three of the four tested samples behaved almost perfectly elastically as the hysteresis effect was negligible. In contrast, the fourth sample showed a permeability decrease of ~40% at the end of the test program. My interpretation is that the closure of open artificial micro-fractures initially present in the sample (based on micro-CT imaging) caused that permeability hysteresis. The matrix permeability to dodecane (oil) of the tested samples is between ~50 nD and ~520 nD at the confining pressure of 9500 psi. The 520 nD sample exhibited the lowest porosity, the highest calcite content, and the largest dominant pore throat radii. In contrast, the 50 nD sample was more porous, and exhibited the highest dolomite content and the smallest dominant pore throat radii. This study shows that my multi-stress testing protocol allows the study of the permeability hysteresis effect to interpret the matrix permeability. I also document the presence of middle Bakken

[3]The full content of this appendix was published as a proceedings paper of the *SPE Annual Technical Conference and Exhibition.* The citation of that publication is:

Ramiro-Ramirez, S., P. B., Flemings, A. R., Bhandari, and O. S., Jimba, 2021, Steady-State Liquid Permeability Measurements in Samples from the Bakken Formation, Williston Basin, USA, SPE ATCE, Dubai, UAE, p. 15.

I designed and performed the experiments presented in that study and prepared the manuscript for publication. My co-authors are listed in order of contribution and provided support for the conceptual development of the project, experimental design and execution, and manuscript preparation.

lithologies with permeabilities up to one order of magnitude greater than others. These permeable lithologies may have a significant contribution to well production rates.

G.2 Introduction

The Devonian-Mississippian Bakken Formation of the Williston Basin in North Dakota and Montana (Figure G.1) is the second-largest tight oil-producing onshore interval in the United States (EIA, 2021). It is composed of four members (from the bottom to the top): the Pronghorn, the lower Bakken Shale, the middle Bakken, and the upper Bakken Shale (Figure G.2). The lower and upper Bakken Shales are rich in organic matter (e.g., TOC > 10 wt.%) and are considered the source rocks for the oil produced in the Bakken and the underlying Three Forks Formation (Schmoker and Hester, 1986; Sonnenberg, 2020). The middle Bakken member is composed of siltstones and sandstones with varying abundances in calcite and dolomite; it is one of the main producing units in the Williston Basin because it stores a significant fraction of the oil migrated from the shales (Kurtoglu, 2013; Sonnenberg, 2020).

Production behavior in the middle Bakken is strongly dependent on its matrix permeability (Sonnenberg and Pramudito, 2009; Tran et al., 2011; Kurtoglu, 2013). Field development plans, including primary production and enhanced oil recovery methods, largely depend on this rock property (Tran et al., 2011; Kurtoglu, 2013; Yu et al., 2014; Li et al., 2015; Assady et al., 2019). Several laboratory studies have measured the permeability in middle Bakken core plugs using transient (e.g., oscillating-pulse, pulse-decay) and steady-state methods (e.g., He and Ling, 2016; Teklu et al., 2018; Assady et al., 2019). They reported permeability values ranging from 10 nD to over 8000 nD. However, those measurements were conducted using either gas (e.g., nitrogen, CO_2) or water as the pore fluid. Since the Bakken is primarily an oil-producing formation, experimental measurements using a liquid hydrocarbon (e.g., dodecane) as the pore fluid would be more representative of the reservoir. Kurtoglu (2013) conducted a steady-state permeability test using kerosene (liquid hydrocarbon) as the pore fluid in one middle Bakken sample and reported a permeability of 27 nD. However, the author only measured the permeability at one effective stress condition. Previous researchers (e.g., Chhatre et al., 2015; Mathur et al., 2016; King et al., 2018; Bhandari et al., 2019; Ramiro-Ramirez et al., 2020) have shown that permeability should be measured at varying stress conditions to interpret the matrix permeability more accurately in low permeability rocks.

The objectives of this paper are to: a) conduct steady-state liquid permeability measurements in four horizontal core plugs from the middle Bakken; b) interpret the matrix permeability of the samples based on the permeability behavior with stress; and c) characterize the fabric and pore system of the tested samples to explain differences in the measured permeabilities between lithologies. My work demonstrates that permeability varies by more than one order of magnitude over an interval of only 10 feet in the middle Bakken. This permeability heterogeneity may play a critical role in well production rates.

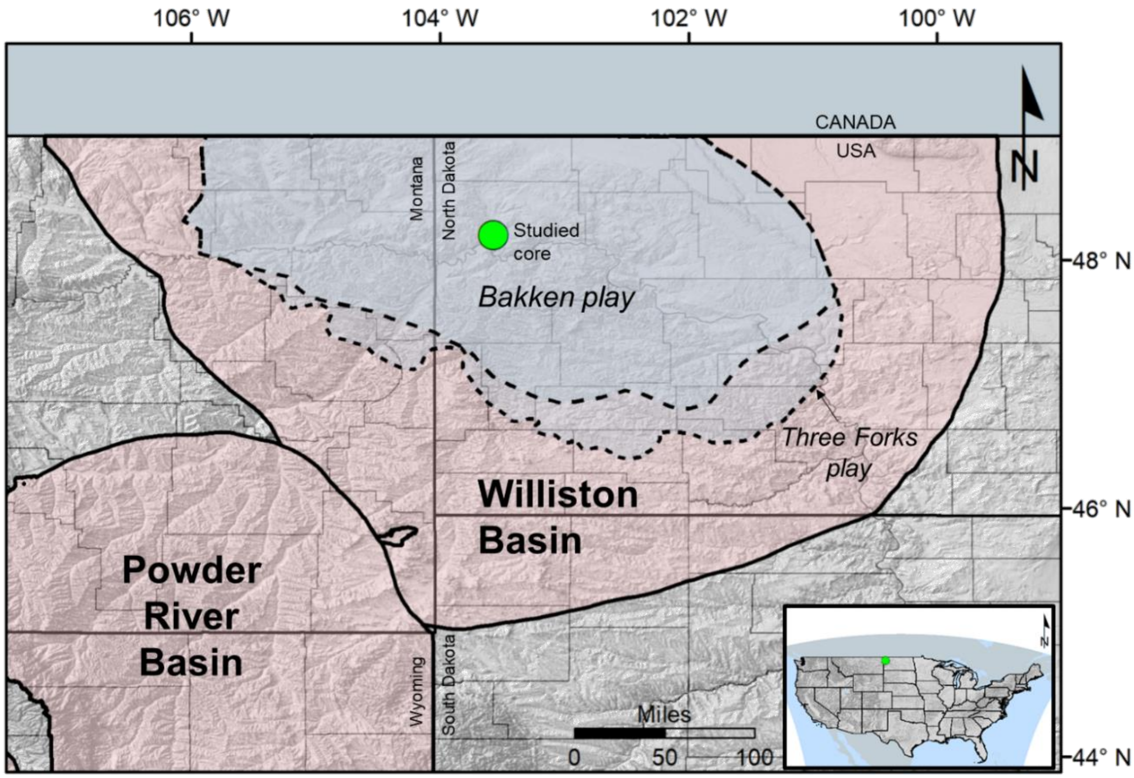

Figure G.1. Map showing the boundaries of the Williston Basin in the USA.

The studied core is in the central area of the Bakken play (green circle). Boundaries of the elements shown in the map are from EIA (2011).

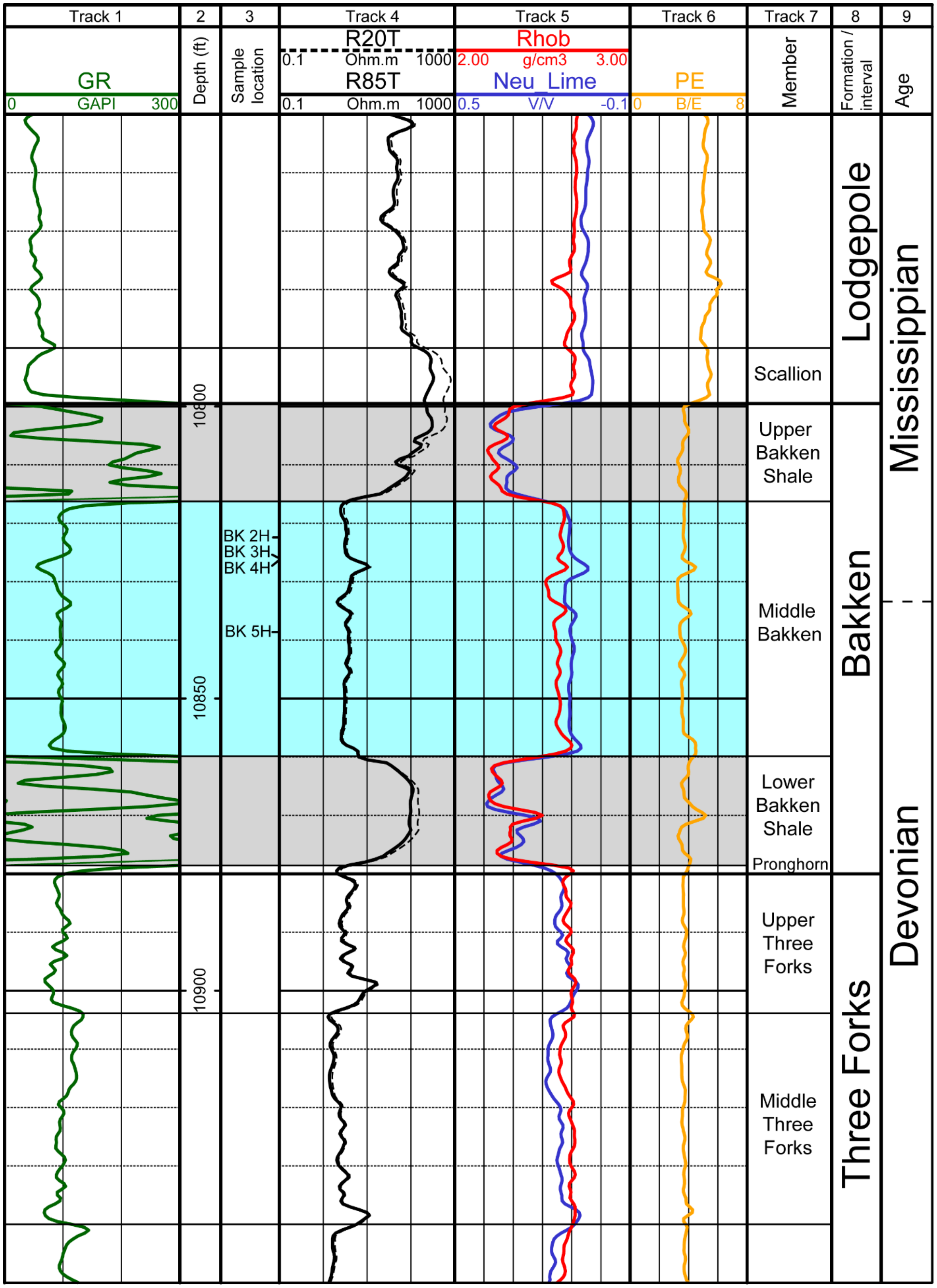
Track 1
2
3
Track 4
Track 5
Track 6
Track 7
8
9
GR
0 GAPI 300
Depth (ft)
Sample location
R20T
0.1 Ohm.m 1000
R85T
0.1 Ohm.m 1000
Rhob
2.00 g/cm3 3.00
Neu_Lime
0.5 V/V -0.1
PE
0 B/E 8
Member
Formation / interval
Age
10800
10850
10900
BK 2H
BK 3H
BK 4H
BK 5H
Scallion
Upper Bakken Shale
Middle Bakken
Lower Bakken Shale
Pronghorn
Upper Three Forks
Middle Three Forks
Lodgepole
Bakken
Three Forks
Mississippian
Devonian

Figure G.2. Wireline log of the studied well.

Wireline log of the cored well in the Williston Basin (Figure G.1) displaying the tops for the four members defined in the Bakken Formation. Tops shown in this figure are based on the correlation with the Whiting 11-11H Braaflat well presented by Sonnenberg (2020). Track 1: wireline gamma ray curve. Track 2: wireline log depth. Track 3: sample depth. Track 4: deep (solid) and shallow (dashed) resistivity curves. Track 5: bulk density (red) and neutron porosity (blue) curves. Track 6: photoelectric effect curve. Track 7: member names. Track 8: Formation or interval names. Track 9: Geological age.

G.3 Materials and methods

G.3.1 Samples

I extracted four 1.5" diameter core plugs oriented parallel to the bedding plane from a wax-preserved core recovered from a well in Williams County, North Dakota (Figure G.1). All four core plugs correspond to the middle member of the Bakken Formation (Figure G.2).

I sub-sampled the core plugs to conduct porosity and permeability measurements and to perform the following analyses: a) optical microscopy in thin sections to describe the texture; b) X-ray powder diffraction (XRPD) to determine the whole rock and <2 um clay fraction mineralogy; c) Non-extracted LECO TOC to determine the organic matter content; and d) mercury injection capillary pressure (MICP) using crushed samples to study the pore throat size distribution. The thin sections were impregnated with blue-dyed epoxy to highlight the pore spaces, and one-half of the thin section was impregnated with dual carbonate staining to ease the identification of carbonate minerals.

G.3.2 Porosity measurements

I determined the total porosity in my core plugs at 'as received' conditions. First, I conduct helium porosimetry (HeP) measurements to compute the pore volume accessible by helium gas. Then, I use nuclear magnetic resonance (NMR) to measure the pore volume occupied by liquids. I divide each pore volume by the bulk volume of the core plug to calculate the helium porosity ($Ø_{HeP}$) and the NMR porosity ($Ø_{NMR}$). The sum of both porosities corresponds to the total porosity ($Ø_{total}$) of the core plug:

$$Ø_{total} = Ø_{HeP} + Ø_{NMR}$$

G.3.3 Steady-state liquid permeability measurements

Once I measured the total porosity of the core plugs, I conducted steady-state liquid permeability measurements. I used the same equipment used by Bhandari et al. (2019) and Ramiro-Ramirez et al. (2020).

I designed my test program (Figure G.3) to document the permeability behavior with stress in my samples and interpret their matrix permeability. I first saturated the sample with dodecane in a vacuum chamber for 24 hr. I then loaded the sample in the permeability cell, where saturation with dodecane continues for 5 days at a confining pressure (P_c) of 1000 psi and a pore pressure (P_p) of 750 psi (Figure G.3) in both the upstream and downstream sides of the core plug. Once the saturation stage is completed, I measured the permeability (Test 1 to Test 10) using the steady-state method at varying stress conditions (e.g., Bhandari et al., 2019; Ramiro-Ramirez et al., 2020) while maintaining a constant pore pressure of ~1000 psi.

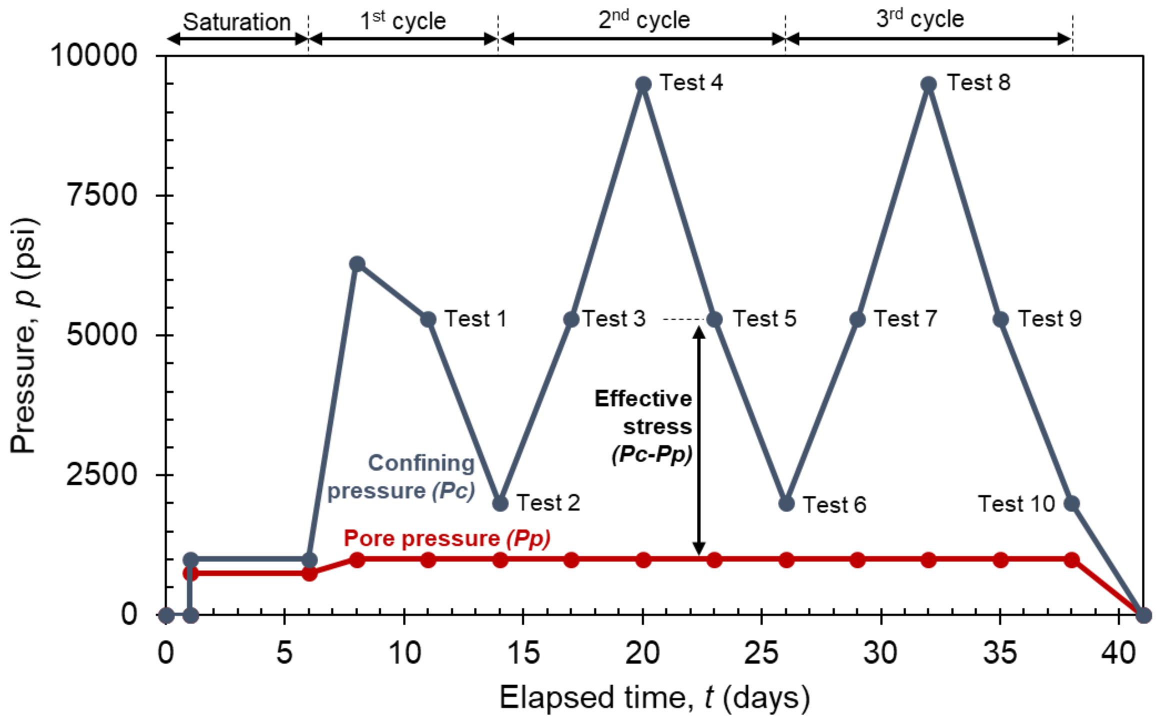

Figure G.3. Permeability test program.

Permeability test program consisting of a sample saturation stage (~6 days) followed by three loading-unloading cycles (~35 days). The pore pressure (Pp, red curve) is maintained constant at ~1000 psi. The confining pressure (Pc, blue curve) is changed throughout the test program to control the effective stress (Pc – Pp) condition at each steady-state permeability test (Test 1 to Test 10). The average total time to complete the test program is ~41 days per sample.

My experimental protocol to conduct the steady-state liquid permeability measurements was as follows:

1. I inject dodecane from the upstream side of the core plug at a constant pressure of 1050 psi while maintaining the pressure constant on the downstream side at 950 psi. I record the upstream and downstream pressures (Figure G.4A) and the volume change of the pump cylinders (Figure G.4B) for at least 24 hr. The slope of the injected pore volume (blue curve, Figure G.4B) corresponds to the flow rate (q).

2. I conduct a second steady-state test by injecting dodecane at a constant q (calculated in the previous step) in the upstream side while maintaining the pressure in the downstream side constant at 950 psi (Figure G.4A). I record the experimental data for at least 24 hr., and calculate the permeability (k) using Darcy's law equation:

$$k = -\frac{q}{A}\frac{\mu L}{\Delta P}$$

where μ is the viscosity of dodecane, ΔP is the pore pressure differential between the downstream and upstream sides of the core plug, and A and L are the cross-sectional area and the length of the core plug, respectively.

I replicate this steady-state experimental protocol in Test 1 through Test 10 (Figure G.3). I ramp the confining pressure at a constant rate of 25 psi/min between tests to ensure that the core plug is not damaged due to drastic changes in the pressure conditions. When a new stress condition is reached, I let the sample stabilize for 24 hr. before conducting the steady-state permeability test. The average time to complete my multi-stress program is ~40 days (Figure G.3).

G.4 Results

G.4.1 Sample characterization

Sample BK 2H

Sample BK 2H is a dolomitic siltstone (Figure G.5A) primarily composed of detrital silt-sized quartz grains (34.3 wt. %) and dolomite cement (30.2 wt. %) (Table G.1). The clay fraction (11.4 wt.%) is dominated by illite plus mixed layered illite/smectite (I+I/S-ML) (98 %) and minor amounts of chlorite (2%). The TOC is very low (0.52 wt. %). The MICP results (blue, Figure G.6) indicate that this sample has a bimodal pore-throat size distribution. The maximum mercury intrusion occurs at the injection pressures equivalent to the pore throat radii of 0.014 µm and 0.029 µm.

Sample BK 3H

Sample BK 3H is a dolomitic sandy siltstone (Figure G.5B) consisting mostly of detrital silt- and sand-sized quartz grains (46.2 wt.%), and dolomite cement (24.6 wt.%) (Table G.1). Clays (7.4 wt.%) are primarily I+I/S-ML (98 %) and minor amounts of chlorite (2%). The TOC is very low (0.58 wt. %). The MICP results (orange, Figure G.6) indicate that this sample has a bimodal pore-throat size distribution. The maximum mercury intrusion occurs at the injection pressures equivalent to the pore throat radii of 0.014 µm and 0.060 µm.

Sample BK 4H

Sample BK 4H is a calcareous silty sandstone (Figure G.5C) primarily composed of detrital sand-sized quartz grains (45.9 wt.%) and calcite cement (34.9 wt.%) (Table G.1). The clay fraction in this sample (3.6 wt.%) is the lowest of all four samples and consists primarily of I+I/S-ML (99 %) and minor amounts of chlorite (1%). The TOC is very low (0.36 wt. %). The MICP results (grey, Figure G.6) indicate that this sample has a bimodal pore-throat size distribution. The maximum mercury intrusion occurs at the injection pressures equivalent to the pore throat radii of 0.010 µm and 0.170 µm.

Sample BK 5H

Sample BK 5H is a dolomitic siltstone (Figure G.5D) consisting mainly of detrital silt-sized quartz grains (42.5 wt.%) and dolomite cement (19.8 wt. %) (Table G.1). Clays (11.7 wt.%) are in similar abundance to those in Sample BK 2H, and they consist primarily of I+I/S-ML (97 %) and minor amounts of chlorite (3%). The TOC is very low (0.53 wt.%). The MICP results (green, Figure G.6) indicate that this sample has a bimodal pore-throat size distribution. The maximum mercury intrusion occurs at the injection pressures equivalent to the pore throat radii of 0.014 µm and 0.046 µm.

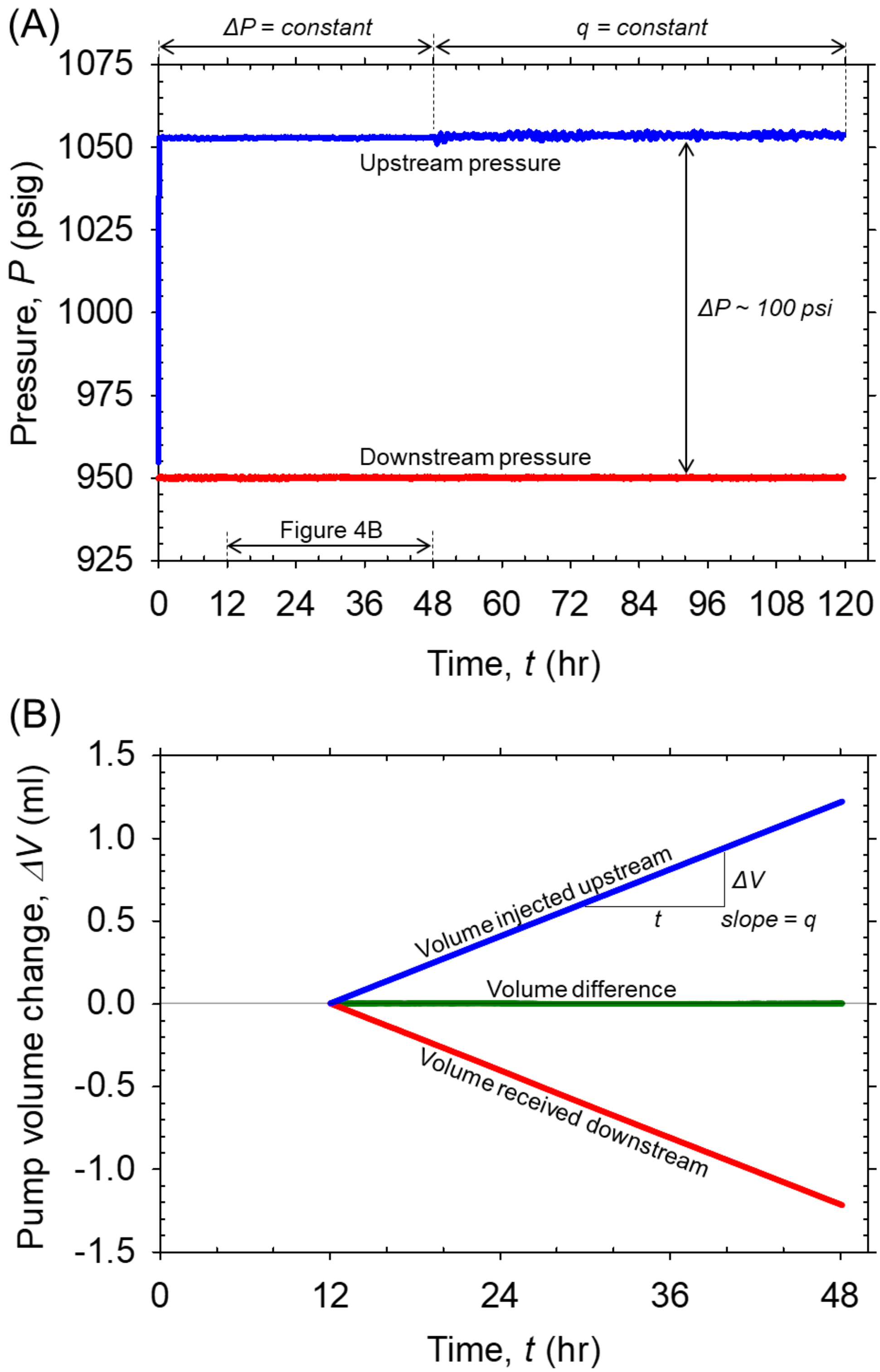
(A)
ΔP = constant
q = constant
1075
1050
1025
1000
975
950
925
Pressure, P (psig)
Upstream pressure
ΔP ~ 100 psi
Downstream pressure
Figure 4B
0
12
24
36
48
60
72
84
96
108
120
Time, t (hr)
(B)
1.5
1.0
0.5
0.0
-0.5
-1.0
-1.5
Pump volume change, ΔV (ml)
Volume injected upstream
ΔV
t
slope = q
Volume difference
Volume received downstream
0
12
24
36
48
Time, t (hr)

Figure G.4. Example of data recorded during a steady-state permeability test.

Example of data recorded during a steady-state permeability test in Sample BK 3H at *Pc* = 9500 psi (Test 8, Figure G.3). (A) Upstream (blue curve) and downstream (red curve) pressures recorded by the pressure transducers located next to the core holder. I run a first steady-state test by setting the pressure in the upstream and downstream sides constant at 1050 psi and 950 psi, respectively. I run a second steady-state test by setting the flow rate (*q*) constant in the upstream side while maintaining the pressure constant at 950 psi in the downstream side. The difference between the upstream and downstream pressures corresponds to the pressure differential (ΔP) that I use to compute the permeability using Darcy's law equation. (B) Volume of dodecane injected (blue curve) and received (red curve) at constant pressure by the upstream and downstream pumps. The slope of the volume injected in the upstream side corresponds to the flow rate (*q*) that I use to conduct the second steady-state permeability measurement. The difference between the injected and received volumes (green curve) corresponds to the system leak. I show data recorded after 12 hr.

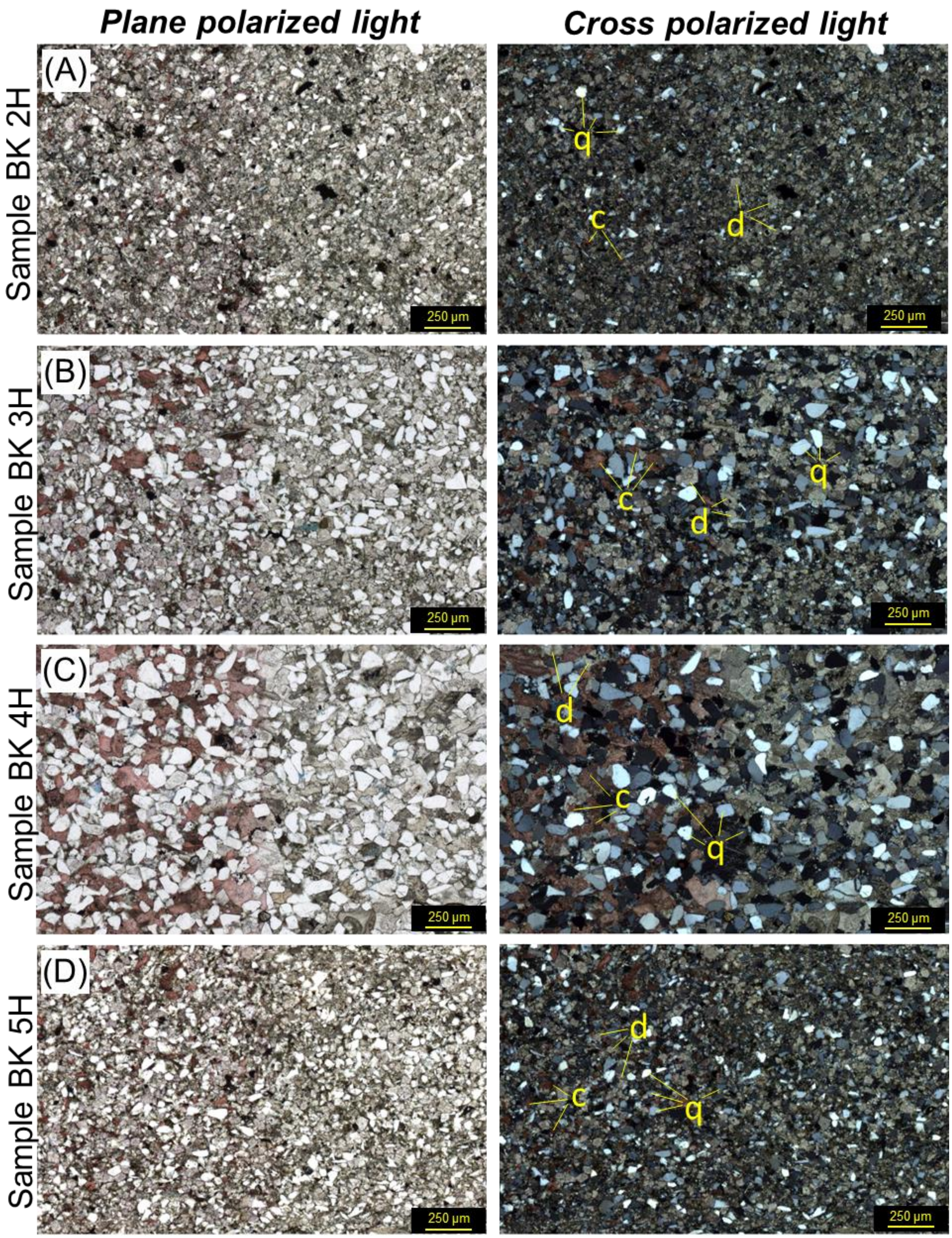
Plane polarized light
Cross polarized light
(A)
Sample BK 2H
q
c
d
250 µm
(B)
Sample BK 3H
c
d
q
250 µm
(C)
Sample BK 4H
d
c
q
250 µm
(D)
Sample BK 5H
d
c
q
250 µm

Figure G.5. Plane polarized light and cross polarized light photomicrographs

Plane polarized light (left) and cross polarized light (right) photomicrographs of (A) Sample BK 2H, (B) Sample BK 3H, (C) Sample BK 4H, and (D) Sample BK 5H. Thin sections were impregnated with blue-dyed epoxy. The left half of the thin section is impregnated with dual carbonate staining to distinguish between calcite (red-stained) and dolomite (non-stained). q = quartz, d = dolomite, c = calcite.

Table G.1. Summary of XRPD and LECO TOC analyses.

Summary of XRPD-determined mineralogy and LECO TOC content of the middle Bakken samples tested for permeability

Sample	Quartz[a] (wt. %)	Feldspars[a] (wt. %)	Calcite[a] (wt. %)	Dolomite[a] (wt. %)	Clays[a] (wt. %)	Others[a] (wt. %)	TOC[b] (wt. %)
BK 2H	34.3	9.6	8.2	30.2	11.4	5.7	0.52
BK 3H	46.2	10.6	7.4	24.6	7.4	3.3	0.58
BK 4H	45.9	5.9	34.9	7.5	3.6	1.9	0.36
BK 5H	42.5	11.5	8.2	19.8	11.7	5.8	0.53

[a] Determined with XRPD analyses by The James Hutton Institute. Feldspars include K-feldspars and plagioclase; dolomite includes Mg-dolomite and ankerite; clays include illite, smectite-illite mixed layer and chlorite

[b] Determined using LECO TOC analyzer by GeoMark research Limited.

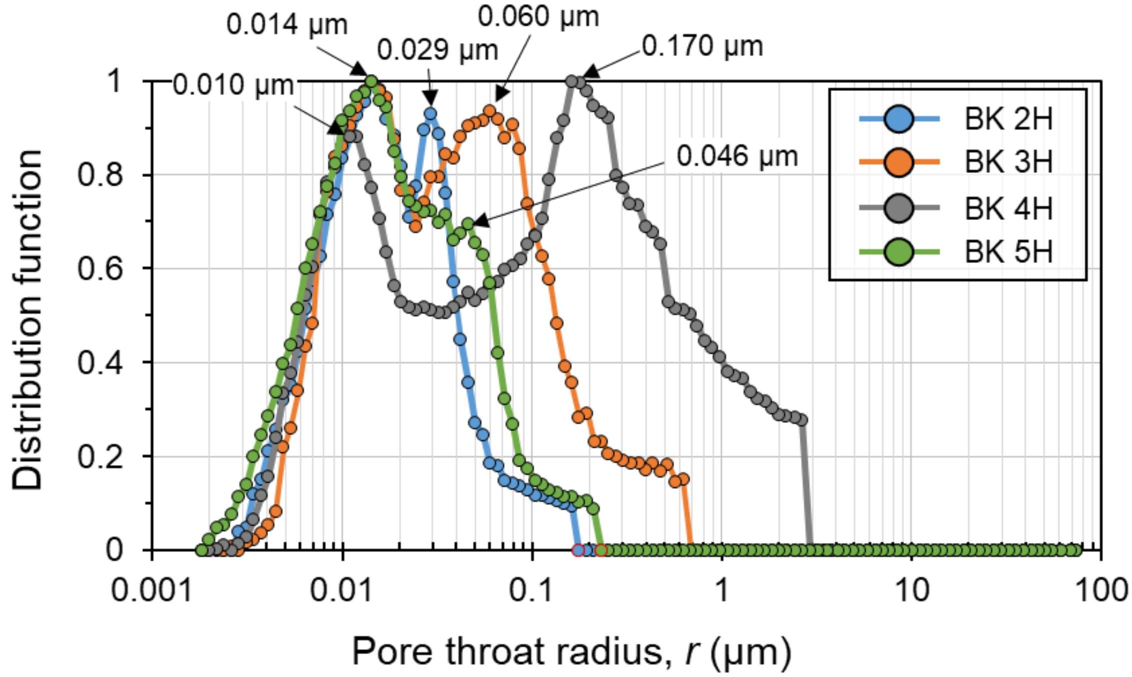

Figure G.6. Pore throat size distributions

Pore throat size (radius) distributions computed from MICP in samples BK 2H (blue), BK 3H (orange), BK 4H (grey) and BK 5H (green). The mercury surface tension and contact angle used in the Washburn (1921) equation to calculate the pore throat radius were 485 dynes/cm and 140°, respectively.

G.4.2 Total porosity

The porosity results for each sample are shown in Figure G.7. Samples BK 2H, BK 3H, and BK 5H exhibit a similar NMR porosity (black, Figure G.7) of $Ø_{NMR}$ = 6.1 %. In contrast, Sample BK 4H exhibits a lower NMR porosity of $Ø_{NMR}$ = 3.3 %.

The HeP porosity (grey, Figure G.7) is very similar in samples BK 2H ($Ø_{HeP}$ = 1.7 %), BK 3H ($Ø_{HeP}$ = 1.4 %) and BK 4H ($Ø_{HeP}$ = 1.6 %). In contrast, the HeP porosity in sample BK 5H ($Ø_{HeP}$ = 2.7 %) is almost twice the HeP measured in the other three samples.

The sum of the HeP and NMR porosities indicates that Sample BK 4H is the least porous ($Ø_t$ = 4.9 %), whereas Sample BK 5H is the most porous ($Ø_t$ = 8.8 %). Samples BK 2H and BK 3H exhibit similar total porosities of $Ø_t$ = 7.8 % and $Ø_t$ = 7.5 %, respectively.

G.4.3 Permeability behavior with stress

Figure G.8 shows the permeability versus effective stress for the four samples. I present the results for samples BK 2H, BK 3H, and BK 4H in the same plot (Figure G.8A) because they exhibit a similar permeability behavior with stress. The results for Sample BK 5H are plotted separately (Figure G.8B) because it behaves differently than the other three samples.

The initial permeability in samples BK 2H, BK 3H, and BK 4H at the effective stress condition of $P_c – P_p$ = 4300 psi is 63 nD, 383 nD, and 701 nD, respectively (Test 1, Figure G.8A). Upon unloading, their permeability increases to 80 nD, 530 nD, 1323 nD in Test 2. When loading to the maximum effective stress of 8500 psi (Test 4), the stress dependence of permeability is slightly different between these samples: the permeability declines by 25 % in Sample BK 2H, by 40 % in sample BK 3H, and by 60 % in sample BK 4H. When unloading back to 1000 psi (Test 6), the hysteresis effect in all three samples is minimal: the permeability decreases by ~10 % on average compared to the permeability measured in Test 2 at the same stress condition. These three samples behave almost perfectly elastically throughout the last stress cycle as the hysteresis effect is negligible (Figure G.8A).

In contrast, Sample BK 5H (Figure G.8B) exhibits a more significant permeability hysteresis throughout the test program. Its initial permeability is 741 nD (Test 1), and it increases to 1649 nD at the effective stress condition of 1000 psi (Test 2). Upon loading to 8500 psi (Test 4), the permeability declines by ~80 %. When unloaded to 1000 psi (Test 6), the permeability does not recover to the value previously measured in Test 2; instead, the permeability is ~24 % lower. During the last stress cycle, the hysteresis effect is similar to that described for the first two cycles. Overall, I observe that the permeability in Test 10 is ~40 % lower than that in Test 4, both conducted at the effective stress condition of 1000 psi.

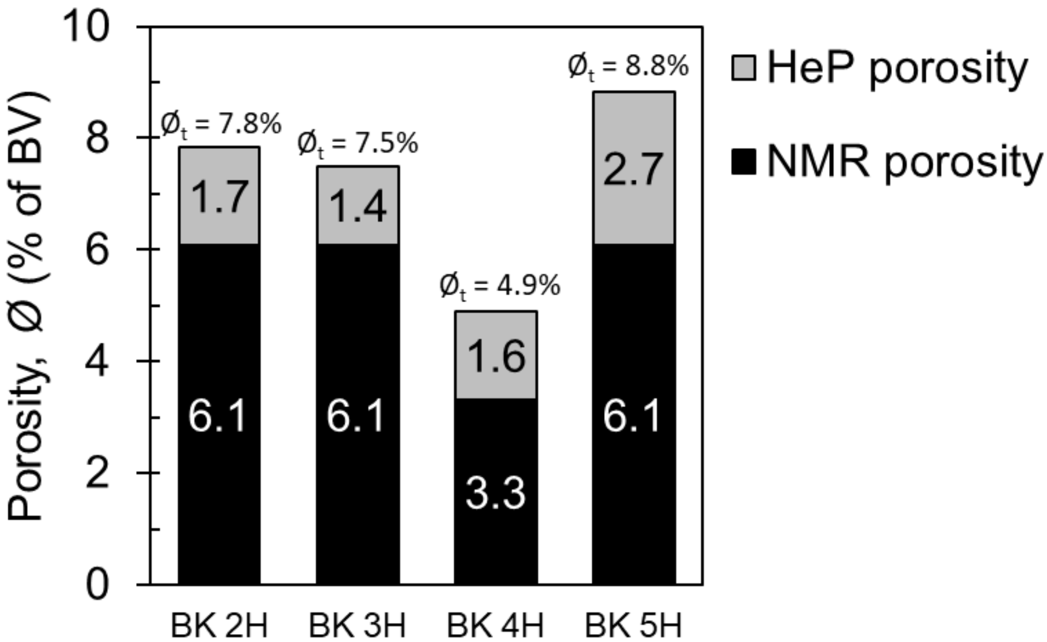

Figure G.7. Porosity results.

Summary of porosity results in middle Bakken samples. Nuclear magnetic resonance porosity (ØNMR, black) corresponds to the pore volume filled by liquids. Helium porosimetry porosity (ØHe , grey) correspond to the pore volume accessible by helium gas. The sum of ØHe and ØNMR correspond to the total porosity (Øt) of the sample. The HeP porosity in sample BK 3H was back calculated from the NMR measurements conducted in the core plug before and after the permeability test.

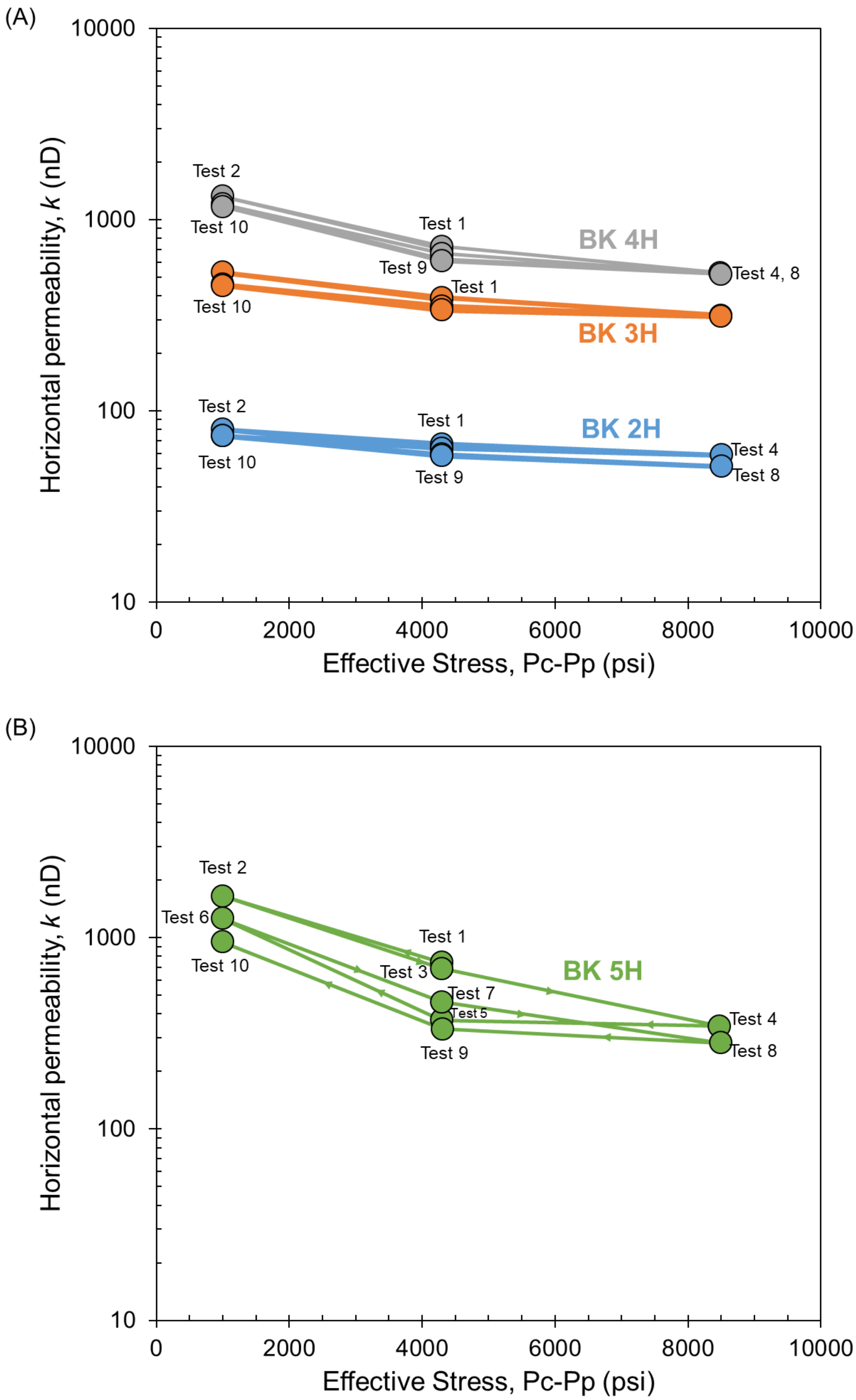

(A)
10000
1000
100
10
Horizontal permeability, k (nD)
0
2000
4000
6000
8000
10000
Effective Stress, Pc-Pp (psi)
Test 2
Test 10
Test 1
Test 9
BK 4H
Test 4, 8
Test 1
Test 10
BK 3H
Test 2
Test 1
BK 2H
Test 10
Test 9
Test 4
Test 8
(B)
10000
1000
100
10
Horizontal permeability, k (nD)
0
2000
4000
6000
8000
10000
Effective Stress, Pc-Pp (psi)
Test 2
Test 6
Test 10
Test 1
Test 3
BK 5H
Test 7
Test 5
Test 9
Test 4
Test 8

Figure G.8. Permeability results.

(A) Permeability results as a function of effective stress for core plugs BK 2H (blue), BK 3H (orange) and BK 4H (grey). (B) Permeability results as a function of effective stress for core plug BK 5H (green).

G.5 Discussion

G.5.1 Interpretation of matrix permeability

My steady-state liquid permeability measurements show that samples BK 2H, BK 3H, and BK 4H exhibited a nearly elastic behavior throughout the test program (Figure G.8A). In contrast, Sample BK 5H experienced a more significant permeability hysteresis (Figure G.8B). I interpret that sample quality controls this hysteresis effect. The micro-CT scans acquired in the pre-tested twin core plugs of samples BK 2H (Figure G.9A), BK 3H (Figure G.9B), and BK 4H (Figure G.9C) indicate that they are intact (at the micro-CT resolution of ~24 voxels). In contrast, the micro-CT scan acquired in the pre-tested twin core plug of sample BK 5H (Figure G.9D) indicates that it has multiple open artificial microfractures. I interpret that these microfractures close when I increase the effective stress applied on the sample. When I decrease the effective stress, these microfractures may partially reopen and then close again when the effective stress in increased. Therefore, I interpret that the permeability hysteresis observed in Sample BK 5H results from the microfractures closure throughout the loading-unloading cycles in my test program (Figure G.8B).

The micro-CT scans acquired on the core plugs after they were tested for permeability (Figure G.9) confirm that samples BK 2H, BK 3H and BK 4H have no visible microfractures, and that most microfractures in Sample BK 5H are irreversibly closed. Hence, for the intact samples, I interpret that the permeabilities measured in Test 8, Test 9, and Test 10 (Figure G.8A) are representative of their horizontal matrix permeabilities to dodecane (Table G.2). For sample BK 5H, the permeabilities measured in Test 8 and Test

9 are representative of its horizontal matrix permeability (Table G.2), whereas the permeability measured in Test 10 is probably a combination of the matrix and microfracture permeabilities.

My interpretation for the permeability hysteresis observed in these middle Bakken samples is similar to that made by Bhandari et al. (2019) in permeability measurements conducted in Wolfcamp mudstones at multiple stress conditions.

G.5.2 Lithologic control on porosity and matrix permeability

My results indicate that samples BK 2H, BK 3H, and BK 5H have high total porosity ($Ø_t$ = 7.5 % to 8.8 %), and they consist primarily of quartz and dolomite. In contrast, sample BK 4H has much lower porosity ($Ø_t$ = 4.9 %) and it is primarily quartz and calcite. This indicates that mineralogy correlates with porosity; calcareous samples have low porosity, whereas dolomitic samples have high porosity.

The low TOC content in my samples (TOC = 0.36 wt.% to 0.58 wt.%) indicates porosity within the organic matter (e.g., Loucks et al., 2012; Ramiro-Ramirez, 2016) relative to the total pore volume is minimal. Hence, the measured pore volume must occur as non-organic intraparticle pores (e.g., dissolution pores within carbonate grains and cement) and interparticle pores (e.g., pores lying between detrital quartz grains and cement) (e.g., Loucks et al., 2012; Ramiro-Ramirez, 2016; Ramiro-Ramirez et al., 2020). Fluid flow must therefore occur primarily through these pores.

The MICP results show that the pore throat sizes in my samples have a bimodal distribution. Each mode may represent characteristic pore types (e.g., Li et al., 2015) that form effectively connected pathways for fluid-flow through the rock matrix. The first mode comprises pore throat radii between 0.010 µm - 0.014 µm, and it is common to all four samples. However, the second mode comprising larger pore throat radii is different between samples. I interpret that the pore throats measured in the second mode are controlling my measured permeabilities. Sample BK 4H exhibits the largest pore throats (r ~0.170 µm) and has the highest matrix permeability (k = 520 nD at Pc – Pp = 8500 psi). In contrast, Sample BK 2H has the smallest pore throats (r~0.029 µm) and the lowest matrix permeability (k = 50 nD at Pc – Pp = 8500 psi). The other two samples have intermediate pore throat sizes and matrix permeabilities, which further supports my interpretation.

Lastly, the texture of the samples also correlates with the measured permeabilities. The most permeable sample (BK 4H) has the coarsest (sand-sized) quartz grains, whereas the least permeable sample (BK 2H) shows the finest (silt-sized) quartz grains of all four samples.

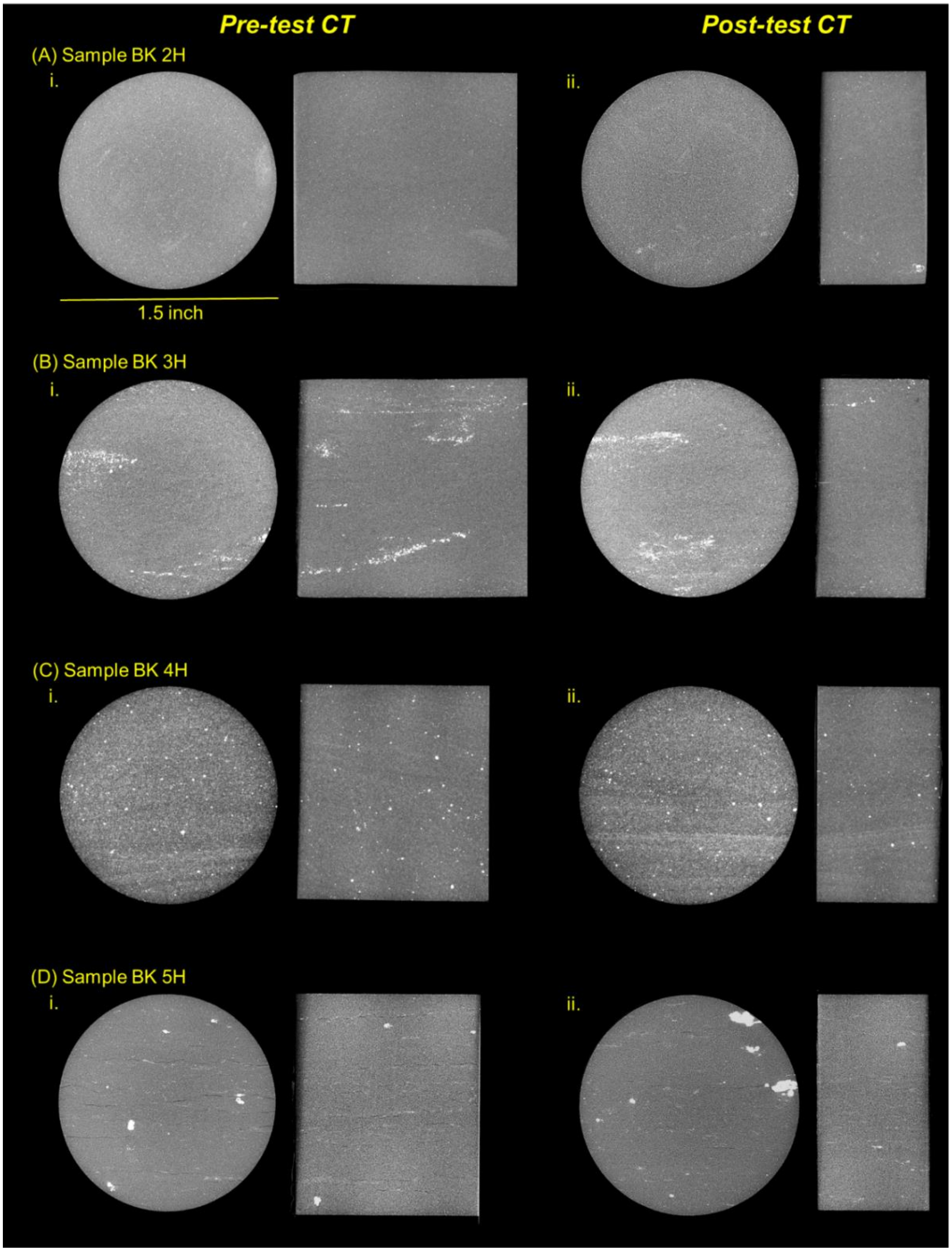
Pre-test CT
Post-test CT
(A) Sample BK 2H
i.
ii.
1.5 inch
(B) Sample BK 3H
i.
ii.
(C) Sample BK 4H
i.
ii.
(D) Sample BK 5H
i.
ii.

Figure G.9. Micro-CT images of tested samples.

Pre-test (left column) and Post-test (right column) micro-CT images of (A) Sample BK 2H, (B) Sample BK 3H, (C) Sample BK 4H, and (D) Sample BK 5H showing diametrical and longitudinal cross-sections. Pre-test images were acquired in twin core plug, and Post-test images were acquired in the tested core plug. The samples were CT scanned without confinement.

Table G.2. Summary of permeability results.

Summary of interpreted horizontal matrix permeability to dodecane at three different effective stress conditions during the third unloading segment (Test 8, Test 9, Test 10) (Figure G.3) for the four middle Bakken samples. (*) The permeability measured in Sample BK 5H at Pc – Pp = 1000 psi may have an influence from the microfractures present initially in the sample.

Sample	Permeability (nD)		
	P_c - P_p = 8500 psi	P_c - P_p = 4300 psi	P_c - P_p = 1000 psi
BK 2H	51	58	74
BK 3H	312	337	453
BK 4H	519	608	1167
BK 5H	282	333	951 (*)

G.6 Conclusions

1. I show sample (core plug) quality controls the permeability hysteresis behavior. A multi-stress permeability test program is necessary to interpret the matrix permeability.

2. I document there is one order of magnitude permeability heterogeneity in the middle Bakken. The matrix permeability to dodecane (oil) of the tested samples is between ~50 nD and ~520 nD.

3. My permeability measurements, when combined with additional characterization analyses, indicate that permeability correlates primarily with rock texture, mineralogy, and pore-throat size distribution. Total porosity and TOC do not correlate with permeability.

Acknowledgements

I thank Equinor for funding this research under the University of Texas - Equinor Fellows Program. I am grateful to Dr. Bruce Hart and Nigel Bedrock for guidance and fruitful discussions. Lastly, I thank NSF for supporting the University of Texas High-Resolution X-ray Computed Tomography Facility (UTCT) through the grant EAR-1762458.

References

Assady, A., H. Jabbari, A. M. Ellafi, and B. Goudarzi, 2019, On the characterization of Bakken Formation: oscillating-pulse, pulse-decay permeability measurement & geomeachanics, U.S. Rock Mechanics/Geomechanics Symposium, New York City, New York, p. 11.

Bhandari, A. R., P. B. Flemings, S. Ramiro-Ramirez, R. Hofmann, and P. J. Polito, 2019, Gas and liquid permeability measurements in Wolfcamp samples: Fuel, p. 1026–1036.

Chhatre, S. S., E. M. Braun, S. Sinha, M. D. Determan, Q. R. Passey, T. E. Zirkle, A. C. Wood, J. A. Boros, D. W. Berry, S. A. Leonardi, and R. A. Kudva, 2015, Steady-state stress-dependent permeability measurements of tight oil-bearing rocks: Petrophysics, v. 56, p. 116-124.

EIA, 2011, Maps: Oil and gas exploration, resources, and production.

EIA, 2021, Tight oil production estimates by play.

He, J., and K. Ling, 2016, Measuring permeabilities of Middle-Bakken samples using three different methods: Journal of Natural Gas Science and Engineering, v. 31, p. 28-38.

King, H., M. Sansone, P. Kortunov, Y. Xu, N. Callen, S. Chhatre, H. Sahoo, and A. Buono, 2018, Microstructural Investigation of Stress-Dependent Permeability in Tight-Oil Rocks: Petrophysics, v. 59, p. 9.

Kurtoglu, B., 2013, Integrated reservoir characterization and modeling in support of enhanced oil recovery for Bakken, Colorado School of Mines, 239 p.

Li, H., B. S. Hart, M. Dawson, and E. Radjef, 2015, Characterizing the middle Bakken: laboratory measurements and rock typing of the middle Bakken Formation, Unconventional Resources Technology Conference (URTeC), San Antonio, Texas, USA, p. 13.

Loucks, R. G., R. M. Reed, S. C. Ruppel, and U. Hammes, 2012, Spectrum of pore types and networks in mudrocks and a descriptive classification for matrix-related mudrock pores: AAPG Bulletin, v. 96, p. 1071-1098.

Mathur, A., C. H. Sondergeld, and C. S. Rai, 2016, Comparison of Steady-State and Transient Methods for Measuring Shale Permeability, SPE Low Perm Symposium, Denver, Colorado, USA, p. 22.

Ramiro-Ramirez, S., 2016, Petrographic and petrophysical characterization of the Eagle Ford Shale in La Salle and Gonzales counties, Gulf Coast Region, Texas: Master thesis, Colorado School of Mines, Golden, Colorado, USA, 126 p.

Ramiro-Ramirez, S., A. R. Bhandari, P. B. Flemings, and R. M. Reed, 2020, Porosity and Permeability Heterogeneity in the Upper Wolfcamp, Delaware Basin, West Texas: Implications for Production, SPE/AAPG/SEG Unconventional Resources Technology Conference, Virtual, Unconventional Resources Technology Conference, p. 8.

Schmoker, J. W., and T. C. Hester, 1986, Organic carbon in Bakken Formation, United States portion of Williston Basin: AAPG Bulletin, v. 67, p. 2165-2174g.

Sonnenberg, S. A., 2020, The Bakken–Three Forks super giant play, Williston Basin: AAPG Bulletin, v. 104, p. 2557-2601.

Sonnenberg, S. A., and A. Pramudito, 2009, Petroleum geology of the giant Elm Coulee field, Williston Basin: AAPG Bulletin, v. 93, p. 1127-1153.

Teklu, T. W., X. Li, Z. Zhou, and H. Abass, 2018, Experimental investigation on permeability and porosity hysteresis of tight formations: SPE Journal, v. 23, p. 672-690.

Tran, T., P. Sinurat, and R. A. Wattenbarger, 2011, Production characteristics of the Bakken shale oil, SPE Annual Technical Conference and Exhibition, Denver, Colorado, USA, p. 14.

Washburn, E. W., 1921, The dynamics of capillary flow: Physical Review, v. 17, p. 273-283.

Yu, W., H. R. Lashgary, and K. Sepehrnoori, 2014, Simulation study of CO_2 huff-n-puff process in Bakken tight oil reservoirs, SPE Western North American and Rocky Mountain Joint Regional Meeting, Denver, Colorado, USA, p. 16.

Vita

Sebastian Ramiro Ramirez was born in Madrid, Spain. He attended the Universidad Complutense de Madrid to pursue two university degrees at master's level. He earned a degree in Geological Engineering and a degree in Geological Sciences in 2012. He also attended the Colorado School of Mines and earned a Master of Science in Geology with a minor in Petroleum Engineering in 2016. After graduation, he started his Ph.D. program at the Jackson School of Geosciences at the University of Texas at Austin.

Email address: sramiro.r@gmail.com

This dissertation was typed by Sebastian Ramiro Ramirez.